

ABSTRACT

MARX, JACOB CHARLES. Composite Metal Foam in Extreme Environments (Under the direction of Dr. Afsaneh Rabiei).

Extreme environments require advanced materials that operate well in a variety of conditions while maintaining their structural integrity and safety. Today's transportation vehicles undergo extreme loading under accident conditions. For instance, tank cars carrying hazardous materials can be punctured during derailment leading to injury and death. Military systems also undergo severe loading at high strain rates brought on by ballistic impact and explosives. The purpose of this work is to further study composite metal foam (CMF) as an advanced energy absorption material under extreme loading presented by puncture, ballistic, blast, and fragment impact and understand their benefit over conventional bulk metals.

In the first part of this study, steel-steel composite metal foam core sandwich panels (SS-CMF-CSP) were characterized under quasi-static loading for their potential use in future tank car structures for puncture resistance. SS-CMF-CSP were manufactured and tested under compression and tension. Stainless steel face sheets were attached to the SS-CMF core using two methods: diffusion and adhesive bonding. The bond line between the core and face sheets was analyzed under scanning electron microscope. The mechanical strength of the CMF core sandwich panels was compared to bare CMF samples. The face sheets were found to not greatly affect the deformation of the SS-CMF core under compression. However, the diffusion bonded SS-CMF-CSP yielded a stronger product primarily due to microstructural changes in the sphere wall. In tension, the face sheets support the core and improve the strain to failure while microstructural changes were found to impact the failure mode of the SS-CMF.

The use of CMF as a novel military armor is further explored in this work as it presents the opportunity for reduced weight of military vehicles. CMF layered hard armors were

evaluated against ballistic threats of increasing size. In this work CMF armors were tested against 0.50 caliber (12.7 x 99 mm) ball and M2 armor piercing (AP) rounds and 14.5 x 114 mm B32 armor piercing incendiary (API) rounds. The armors stopped 0.50 caliber AP at speeds up to 819 m/s without penetration. The CMF layer was found to absorb 72-75% and 68-78% of the kinetic energy of the ball and AP round, respectively. When compared to rolled homogeneous steel armor (RHA), the CMF hard armors have a mass efficiency of 2.1. Finite element analysis was completed using ANSYS to study the impact. The results are shown to be in good agreement with the experimental findings.

Preliminary tests against the 14.5 mm armor piercing incendiary (API) round were found to outperform the RHA standard with a mass efficiency of 1.5. The CMF hard armors were able to stop an impacting round with an average velocity of 780 m/s and an areal density of 16 g/cm². The CMF layer is calculated to absorb between 70-83% of the bullet's kinetic energy. The results are compared with CMF armors' performance against 7.62 and 12.7 mm armor piercing threats. The energy absorbed by the CMF layer is shown to increase linearly with larger rounds that have a broader impact area and engaged a higher number of hollow spheres, improving the cushion-ability of the foam layer.

SS-CMF panels were manufactured and tested against high explosive incendiary (HEI) rounds to study their resistance against explosive blast pressure and resulting fragments. The bare CMF panels were able to stop the imparted fragments at speeds above 1500 m/s and absorb the blast energy without cracking or bowing. The CMF was also shown to outperform the aluminum plate by locally absorbing the impact of the fragments, reducing the transfer of stress to the surrounding structure.

© Copyright 2020 by Jacob Marx

All Rights Reserved

Composite Metal Foam in Extreme Environments

by
Jacob Charles Marx

A dissertation submitted to the Graduate Faculty of
North Carolina State University
in partial fulfillment of the
requirements for the degree of
Doctor of Philosophy

Mechanical Engineering

Raleigh, North Carolina

2020

APPROVED BY:

Dr. Afsaneh Rabiei
Committee Chair

Dr. Fuh-Gwo Yuan

Dr. Gracious Ngaile

Dr. Alexei Saveliev

DEDICATION

**To my wife, Natasha, for her love and support along the way and to our beautiful
daughter, Layla.**

BIOGRAPHY

Jacob Marx was born in Phoenix, Arizona in 1990 and raised in Pittsburgh, Pennsylvania. He received his bachelor's degree in Physics at Case Western Reserve University and gained an interest in material processing and testing. He followed his interest in materials, physics, and engineering to North Carolina State University and graduated with his master's degree in Nuclear Engineering in 2015. During the last semester of his master's program he was hired by Dr. Afsaneh Rabiei as a Research Assistant in the Mechanical Engineering Department for the Advanced Materials Research Lab. Jacob has since been processing and testing composite metal foams for a variety of advanced engineering applications for tank car designs, aerospace structures, and lightweight vehicle armors. Jacob has learned to operate a variety of material processing and testing equipment through his research that he hopes to apply in engineering applications for developing the next generation of advanced materials.

ACKNOWLEDGMENTS

I would like to first acknowledge and thank Dr. Afsaneh Rabiei for the opportunity to work on such exciting projects and the mentoring I received from her through the years. I am forever grateful for the insight and training she provided me that allowed me to become a better scientist while also develop a confidence in my work and push myself to always strive for the best. I feel very lucky to have been given the chance to learn as much as I have on material manufacturing, process optimization, and mechanical testing and imaging that I would not have otherwise been introduced to. She instilled a drive for perfection that has taught me there is always room for improvement and how to apply it in various aspects of my life.

I would like to thank Dr. Fuh-Gwo Yuan, Dr. Gracious Ngaile and Dr. Alexei Saveliev for their time and effort as members of my committee. I appreciate their support, input, and individual expertise they offered along the way.

I would like to thank the agencies that have funded my research along the way. The Joint Aircraft Survivability Program (JASP) under award #W911W6-15-D-0001-0001 for armor manufacturing and testing. I would also like to thank the team who facilitated the testing at the CCDC AvMC Aviation Development Directorate (ADD) for their expertise and support during experimental procedures. The Department of Transportation (DOT) Pipeline and Hazardous Materials Safety Administration (PHMSA) under project number #DTPH5616C00001 for funding work on CMF sandwich panels under various loading conditions. NASA Langley Research Center IRAD program, project #NNX17AD67A for the work done on polymer-infused Composite Metal Foam.

I also want to recognize and thank Steve Cameron and Vincent Chicarelli for their work and guidance in the Mechanical and Aerospace Engineering graduate machine shop. The shop

is constantly busy, and I appreciate them both taking the time to not only help me with my work but teach me along the way. Steve and Vince both spent countless hours machining molds and helping me learn the best way to design parts for easier machining and improving sample molds given their tight tolerances. This project would not have progressed as well as it did without their help and willingness to fit me into their schedules. Thanks also to Gary Lofton and Chris Anderson of the undergraduate machine shop for their help when moving equipment and receiving materials.

I would like to thank the other members of the Advanced Materials Research Lab with whom I have had the pleasure of working with throughout the years. Dr. Shuo Chen for her help introducing me to CMF, Dr. John Durham for his friendship as well as Swathi Upadhyay, Amrita Lall, and Siddhartha Sarkar.

I would like to acknowledge and thank the undergraduates and volunteers who have helped me along the way preparing molds and samples for manufacturing and testing. Their ability to learn and apply themselves was greatly appreciated throughout my work. Thanks to Jesse Dannenberg, Wyatt Peterson, and Jerod Schwandt for always being available when needed. Thank you to Kamellia Karimpour for your efforts in data analysis and creating plots. Your ability to meet the required level of perfection in the lab was a great help and support throughout my research.

I also want to thank the people who helped along the way to make this project possible: Dr. Marc Portanova and his team at ADD for their help and advice when running the ballistic and blast tests; Joel Alexa and Pete Messick for their help running the vacuum hot press at NASA Langley; Dr. Greg Lucier, Johnathan McEntire, and Jerry Atkinson for your help while working at the Constructed Facilities Laboratory (CFL) at NCSU.

Last, I would like to acknowledge and thank my family for their constant support, love, and encouragement throughout this journey.

TABLE OF CONTENTS

LIST OF TABLES	x
LIST OF FIGURES	xiii
CHAPTER 1: INTRODUCTION.....	1
1.1. Extreme Environments	1
1.1.1. Extreme Mechanical Loading	1
1.2. Tank Car Structure	3
1.2.1. Tank Car Materials	7
1.3. Military Environments	13
1.3.1. Military Armors	13
1.3.2. Ballistic, Blast and Fragment Threats	18
1.4. Armor Materials.....	27
1.4.1. Metal Armors	27
1.4.2. Layered Composite Armors	41
CHAPTER 2: LITERATURE REVIEW OF COMPOSITE METAL FOAM.....	44
2.1. Metal Foams	44
2.1.1. Manufacturing of Metal Foams	44
2.1.2. Properties of Metal Foams	48
2.2. Composite Metal Foams at a Glance	50
2.2.1. Preparation of CMF	50
2.2.2. Basic Properties of Composite Metal Foams	54
2.3. Established Properties of Composite Metal Foam under Extreme Environments.....	65
2.3.1. Radiation Shielding Properties of CMFs	65
2.3.2. Thermal Properties of CMFs.....	71
2.3.3. High Strain Rate Impact and Energy Absorption	75
2.4. Summary of Composite Metal Foam	82
2.5. Research objectives.....	82
CHAPTER 3: MATERIALS AND MANUFACTURING	85
3.1. Manufacturing of Steel-Steel Composite Metal Foam	85
3.2. Manufacturing of Steel-Steel Composite Metal Foam Core Sandwich Panels	87
3.2.1. Composite Metal Foam Core Sandwich Panels with Metal Face Sheets	88
3.2.2. Composite Metal Foam Core Sandwich Panels for Armor Applications	89
CHAPTER 4: COMPRESSION OF COMPOSITE METAL FOAM SANDWICH PANELS.....	91
4.1. Material Processing.....	91
4.2. Experimental Compression Setup.....	93
4.3. Compression Modeling Setup Conducted by an External Company	93
4.4. Results and Discussion	96
4.4.1. Compression Structural Properties	96
4.4.2. Compression Mechanical Properties.....	107
4.5. Compression Modeling Results Conducted by an External Company	115
4.6. Summary of SS-CMF and SS-CMF-CSP under Compression.....	116

CHAPTER 5: TENSION OF SS-CMF AND SS-CMF-CSP	118
5.1. Materials Processing	118
5.2. Tension Testing Setup	119
5.3. Tension Results and Discussion of SS-CMF and SS-CMF-CSP	120
5.3.1. Sample Images	120
5.3.2. Bare SS-CMF Under Tension	121
5.3.3. SS-CMF Core Sandwich Panels Under Tension	130
5.3.4. Analytical Approximation	136
5.4. Summary of SS-CMF and SS-CMF-CSP under Tension	137
CHAPTER 6: BALLISTIC PERFORMANCE OF COMPOSITE METAL FOAM AGAINST LARGE CALIBER THREATS.....	139
6.1. Experimental Procedure.....	139
6.1.1. Materials and Processing	139
6.1.2. Ballistic Testing Procedure	141
6.1.3. Analytical Energy Absorption Analysis	144
6.1.4. Finite Element Analysis.....	145
6.2. Results and Discussion	156
6.2.1. Ballistic Results	156
6.2.2. Computational Results	167
6.3. Summary of CMF Armors Against Large Ballistic Threats (0.50 Cal).....	174
CHAPTER 7: COMPARING THE PERFORMANCE OF COMPOSITE METAL FOAM ARMORS AGAINST VARIOUS THREAT SIZES.....	175
7.1. Materials and Processing	175
7.2. Ballistic Testing and Procedures.....	178
7.3. Results and Discussion	182
7.3.1. 14.5 mm Test Results.....	182
7.3.2. Mass Efficiency Ratio (MER).....	188
7.3.3. Analytical Energy Absorption	190
7.3.4. Comparison of CMF Armors against Various AP Threats	192
7.4. Summary of CMF Armors Against Increasing Ballistic Threat Size	198
CHAPTER 8: A STUDY ON BLAST AND FRAGMENT RESISTANCE OF COMPOSITE METAL FOAMS THROUGH EXPERIMENTAL AND MODELING APPROACHES	200
8.1. Materials and Processing	200
8.2. Experimental Set Up and Testing Procedures	203
8.3. Finite Element Model Conducted by an External Company to Initialize and Run the Model	209
8.3.1. Material Model Conducted by an External Company	209
8.3.2. Fragment Model Conducted by an External Company.....	212
8.3.3. Particle Blast Model Conducted by an External Company.....	212
8.4. Results and Discussion	214
8.4.1. Experimental Results	214
8.4.2. Modeling Results Conducted by an External Company	220
8.5. Summary of Blast and Frag Testing of SS-CMF.....	223

CHAPTER 9: CONCLUSIONS	225
9.1. Mechanical Testing of SS-CMF and SS-CMF-CSP.....	225
9.2. Ballistic Performance of Composite Metal Foam Armors	226
9.3. Blast and Fragment Resistance of CMF	227
CHAPTER 10: INSIGHT FOR FUTURE WORK	228
LIST OF PUBLICATIONS	230
REFERENCES.....	231

LIST OF TABLES

Chapter 1

Table 1-1: Chemical composition of tank car steels, TC128 B and A516 70, as outlined by the Association of American Railroads [11].....	7
Table 1-2: Weight of the M1 Abrams tank from 1980-1999 showing the increase in overall weight due to armor improvements to protect against more penetrating threats [23].	17
Table 1-3: Projectile core properties and kinetic energy density of various ballistic threats [24].	21
Table 1-4: Heat of detonation and TNT pressure and impulse mass equivalents for various explosive materials [28]–[30].....	25
Table 1-5: Chemical composition for manufacturing of RHA as required by MIL-A-12560K [35].	30

Chapter 2

Table 2-1: Chemical compositions of spheres and matrix materials used in manufacturing close-cell CMFs (wt%) [73], [94], [103].	53
Table 2-2: Comparison of metal foams and their mechanical properties under quasi-static loading.....	57
Table 2-3: Sources used in gamma radiation shielding test and their equivalent photon energies [113].....	69
Table 2-4: Experimental results of thermal testing of CMF and comparable bulk materials [102].	74
Table 2-5: CMF samples subjected to dynamic loading for varying sphere sizes and strain rates [107].....	76

Chapter 3

Table 3-1: Chemical composition (wt%) of the material components that make up the SS-CMF and SS-CMF-CSP.	85
---	----

Chapter 4

Table 4-1: Measured grain size of the matrix and sphere wall for the base SS-CMF and diffusion bonded SS-CMF-CSP.	103
Table 4-2: Mechanical properties of the scaled base SS-CMF and SS-CMF-CSP under compression compared to prior small-scale SS-CMF and the improved/ optimized scaled samples.....	114

Chapter 5

Table 5-1: Average mechanical properties for SS-CMF and SS-CMF-CSP tested under quasi-static tension. The values from other metal foams are presented for comparison.....	124
---	-----

Table 5-2: Normalized mechanical properties for SS-CMF and SS-CMF-CSP tested under quasi-static tension. The values from other metal foams are presented for comparison.....	125
--	-----

Chapter 6

Table 6-1: Dimensions of the impacting rounds and their inner core used in ballistic testing [24].....	142
--	-----

Table 6-2: Material Parameters for the projectile and the aluminum backing plate of the CMF hard armor.....	147
---	-----

Table 6-3: Johnson-Holmquist 2 material parameters for B ₄ C ceramic panel [162], [163].	152
---	-----

Table 6-4: Properties of the ballistic tests organized by projectile type and impact velocity. The areal density, kinetic energy, and whether the test was partial penetration (PP) or complete penetration (CP) is listed.....	156
---	-----

Table 6-5: Percent of energy absorbed by each layer in the CMF hard armor system for all PP impacts.....	167
--	-----

Chapter 7

Table 7-1: Projectile and core sizes for each of the tested ballistic rounds [24].	181
--	-----

Table 7-2: Summary of ballistic testing of CMF armors against the 14.5 x 114 mm B32 round.	182
--	-----

Table 7-3: Percent of energy absorbed by each layer for PP impacts against multiple sized rounds.....	191
---	-----

Table 7-4: Properties of CMF armors against the 12.7 mm and 14.5 mm AP threats when normalized by the 7.62 mm AP armors.....	195
--	-----

Chapter 8

Table 8-1: CMF Panels and their corresponding thickness, density, and sphere diameters used to test against HEI rounds.	202
---	-----

Table 8-2: Simplified Kingery-Bulmash Airblast Coefficients.	209
--	-----

Table 8-3: Material properties for the composite metal foam, aluminum armor, aluminum, low carbon steel, and copper fragments.....	211
--	-----

Table 8-4: HEI blast wave properties arriving at the CMF and aluminum 5083-H116 panels.....	213
---	-----

Table 8-5: Average depth of penetration for each fragment size comparing experimental and numerical modeling findings.....	219
---	-----

LIST OF FIGURES

Chapter 1

Figure 1-1: Images of the aftermath of vehicle accidents involving (a) cars, (b) train cars [2], (c) airplanes [3], and (d) tank cars [4].....	3
Figure 1-2: Hazmat shipment type by class [1].	5
Figure 1-3: DOT-117 tank car designed to replace the DOT-111 used in transportation of hazardous materials [10].....	6
Figure 1-4: Diagram of the two fracture mechanisms, (a) brittle and (b) ductile, in steels [7].....	8
Figure 1-5: Puncture of a TC128 Grade B tank car near Minot, ND carrying anhydrous ammonia [14].....	10
Figure 1-6: Digital images of the manufactured sandwich panels for potential tank car shells [17].....	12
Figure 1-7: (a) Military vehicles shown by their armor class and increasing weight required for protection. (b) Ground capabilities of combat vehicles and their necessary fuel requirements showing the need for improved fuel efficiency with heavy armor vehicles [21].	16
Figure 1-8: Small arms ammunition design of most ballistic threats and a Table showing example threats and their muzzle velocity [19].....	19
Figure 1-9: Image of IED's disarmed in eastern Baghdad in 2005 during the Iraq war [25].....	22
Figure 1-10: Simple schematic of a blast wave propagation [19].	23
Figure 1-11: Pressure time history of an ideal blast wave in open air [27].	24
Figure 1-12: Microstructure of RHA highlighting the carbide precipitations and revealing the slightly martensitic grain structure [37].....	31
Figure 1-13: Armored survivability kit (ASK) developed by the Army Research Lab (ARL), primarily made up of RHA, outfitted onto a HMMWV [22].....	32
Figure 1-14: Microstructure of UHH showing the martensitic grain structure [45].....	33
Figure 1-15: Wrought aluminum alloy designations and their primary alloying element. 5xxx, 6xxx, and 7xxx series alloys have been the focus of recent research of aluminum armors [49].	35
Figure 1-16: Back face spalling comparing the aluminum alloy 7039 and 5083 armor plates impacted by the same round [47].	38
Figure 1-17: The M2 Bradley and M1A2 military vehicles that use titanium for protective armors in regions such as the commander's hatch and top armors [61].	41

Figure 1-18: Impact stages of a ballistic threat into a layered armor showing how the ceramic erodes the bullet and its core and allows the backing plate to absorb the kinetic energy.....	43
---	----

Chapter 2

Figure 2-1: Processing method used to manufacture ERG's DUOCEL foam by investment casting [77].....	46
Figure 2-2: Digital images of the cut section of (a) closed-cell Alporas aluminum foam, (b) steel hollow sphere foam [73].....	48
Figure 2-3: Schematic of the typical stress-strain curve of metal foams [77].	49
Figure 2-4: Digital images of the cut section of (a) sintered composite metal foam with 4mm steel spheres in steel matrix and (b) cast composite metal foam with 4mm steel spheres in an aluminum matrix [73].....	52
Figure 2-5: Quasi-static stress-strain curve for SS- CMF and Al-S CMF compared to other metal foams and bulk steel and aluminum [95], [96], [104]–[106].....	55
Figure 2-6: Typical engineering stress-strain curves for (a) SS-CMF and (b) Al-S CMF under quasi-static compression for different sphere sizes [107].	56
Figure 2-7: Fatigue graphs of (a) ALPORAS aluminum metal foam showing the multiple stages of its collapse [79] and (b) Al-S CMF [73].....	60
Figure 2-8: Maximum strain and stress for cyclic loading of Al-S CMF, SS-CMF and aluminum metal foam at one million cycles ($N=10^6$) [73], [111].	62
Figure 2-9: Sequential digital imaging of CMF sample under fatigue deformation made of (a) Al-S deformed at 65% of its plateau strength and (b) SS-CMF deformed at 50% of its plateau strength [112].....	63
Figure 2-10: SEM imaging of Al-S CMF (a) with four spheres surrounded by matrix and other various phases and (b) a zoom in of the sphere wall-matrix interface and intermetallic precipitations as well as the (c) voids left between spheres [98].....	64
Figure 2-11: (a) SEM imaging of SS-CMF with three spheres on the bottom and sides and the (b) zoomed in area near one sphere showing the (i) sphere wall, and (ii) micro-porosities within matrix [73].	65
Figure 2-12: (a) Gamma-ray transmission as a function of photon energy for both Al-S and SS-CMF in addition to HZ SS-CMF and aluminum A356 sample all with an areal density of 2 g/cm^2 . (b) X-ray transmission of samples tested with lead and aluminum as bulk control materials [73], [117].....	68
Figure 2-13: Transmission of neutrons on tested samples at a constant areal density of 2 g/cm^2 with error bars indicating the variations between samples of different sphere sizes [73], [117].....	71
Figure 2-14: Temperature evolution at the opposite surface of SS-CMF and 304L SS samples during experimental flame test [73], [102].	74

Figure 2-15: Compression testing of CMF under (a) Quasi-static loading and (b) Dynamic Loading at a speed of 112 meters per second of Al-S and SS-CMF shown on the left and right respectively [73], [120].	77
Figure 2-16: Layered model of the ballistic armors produced for testing showing the central CMF layer between a top ceramic plate and Kevlar TM or aluminum backing (thicknesses are not shown to scale) [73].....	78
Figure 2-17: Digital image of the ballistic threats Type III and Type IV on the left and right respectively [73], [122].	79
Figure 2-18: Digital images of tested CMF armor systems that have defeated multi-shot Type III (a) front and (b) back with a Kevlar TM back plate, (c), Type IV with aluminum back plate, and (d) a close up of the impact zone showing (i) collapsed spheres, and (ii) the stopped armor piercing core [122].	81

Chapter 3

Figure 3-1: Digital images of the (a) as-process SS-CMF and (b) a ground SS-CMF panel with a smooth and flat exterior surface.....	87
Figure 3-2: Image of an SS-CMF-CSP armor arrangement curing under vacuum.	90

Chapter 4

Figure 4-1: (a) Image of the 1/8 unit cell arrangement with meshing used to create CMF model, (b) the full compression model used for simulating CMF, and (c) the fully meshed sample used for testing.....	95
Figure 4-2: Digital images of the (a) base SS-CMF, (b) adhesively bonded SS-CMF-CSP, and (c) diffusion bonded SS-CMF-CSP compression samples prior to testing... .	97
Figure 4-3: (a) SEM image of the electropolished base SS-CMF showing the microstructure of the (b) matrix and (c) sphere wall. The outlined areas marked on image (a) in white show the location of the higher magnification images shown in (b) and (c).	98
Figure 4-4: (a) and (b) SEM images of the etched base SS-CMF showing (a) sphere wall-matrix interface, and (b) zoom in area marked in image (a) with marked carbides along the grain boundaries in the sphere wall (white arrows). (c)-(d) show the EDS maps of the area outlined in (b) that confirms higher concentration of (c) Cr and (d) C at the grain boundaries.....	100
Figure 4-5: SEM images of the electropolished diffusion bonded SS-CMF-CSP showing the (a) face sheet interface with the core and (b)-(c) the microstructure of the matrix and sphere wall, respectively. The outlined areas shown in image (a) in white are the location of the higher magnification images shown in (b) and (c). Black arrows in (c) indicate the location of twin boundaries.	101

Figure 4-6: SEM images of the etched SS-CMF-CSP showing the location of the EDS mapping along the sphere wall interface with the matrix. (c)-(d) EDS maps of Cr and C showing carbon rich regions in the matrix and at the interface between the sphere wall and the matrix.....	104
Figure 4-7: (a) High magnification SEM image of the etched SS-CMF-CSP along the face sheet interface with the SS-CMF core. (b)-(c) show the EDS line scan plots for Cr and Ni, respectively, with a slight gradient in the Ni content across the interface. Dotted line marked the location of the interface.....	106
Figure 4-8: Compressive stress-strain curves of scaled SS-CMF and SS-CMF-CSP (unoptimized).....	108
Figure 4-9: Images at 0% strain, left, and 60% strain, right, of the (a-b)SS- CMF base, (c-d) adhesive bonded SS-CMF-CSP, and (e-f) diffusion bonded SS-CMF-CSP.....	111
Figure 4-10: Compressive stress-strain curves of scaled SS-CMF and SS-CMF-CSP compared to the improved/ optimized scaled samples.	113
Figure 4-11: Generated finite element results showing the (a) stress-strain curve obtained using an elastic- perfectly plastic material model paired with the geometric meshing and (b) the simulated SS-CMF sample deformed to 50% strain showing the distribution of displacement throughout.....	116

Chapter 5

Figure 5-1: Digital images of the (a) cross section and (b) top surface, of the dog-bone samples cut from SS-CMF-CSP panels using wire EDM followed by surface machining.....	121
Figure 5-2: (a) Engineering stress-strain curves of the bare SS-CMF samples, and (b) the stress-strain curve normalized by the density of the SS-CMF samples.....	123
Figure 5-3: Digital images of SS-CMF (Sample 1) under tension showing crack initiation and failure (a)-(e). Higher magnification images of the outlined areas are shown below in (b-i)-(e-i).....	126
Figure 5-4: Digital images of the SS-CMF (Sample 1) shown in Figure 5-3 after tensile failure. (a) The side of the sample and (b)-(c) the fractography images showing sphere walls tearing rather than debonding from the surface. 127	
Figure 5-5: Digital images of SS-CMF (Sample 2) under tension with multiple cracks initiating about the same location near failure. The magnified images (b-i)-(e-i) showing crack evolution are highlighted in the respective images above.....	128
Figure 5-6: Digital images of the SS-CMF (Sample 2) shown in Figure 5-5 with detailed information from the failure surfaces under tension. (a)-(b) the side of the sample and (c)-(d) the fractography images showing failure across the sphere walls. The red arrows highlight the location of additional crack formations around the region of failure.....	129

Figure 5-7: Engineering stress-strain curve of (a) SS-CMF-CSP samples. The vertical dotted line divides the CMF core failure region (left) from the additional plastic straining and failure of the face sheets (right). (b) The stress-strain curve normalized by the density of the CMF-CSP samples.	131
Figure 5-8: Digital images of SS-CMF-CSP (Sample 2) under tension. Higher magnification images of the respective strains are shown at the bottom of the figure. The sample was imaged (a) prior to loading, (b) slight debonding occurred just prior to major deformation, and (c) crack initiation at the center of the sample. (d)-(e) Crack growth in the core leads to failure (f) with further debonding and face sheet yielding until (g) failure of the face sheets.	133
Figure 5-9: Fracture surfaces of the SS-CMF-CSP sample imaged in Figure 5-8 (Sample 2) with a mixed mode of failure when compared to the bare CMF. The sample fractures by tearing the sphere walls, but also slight detachment of the sphere walls from the matrix highlighted by red arrows. Removed spheres are shown by the solid arrows and their corresponding dimples by dotted arrows can be seen in the (a) top and (b) bottom fracture surfaces.	135

Chapter 6

Figure 6-1: Digital images of (a) CMF panel prior to assembly showing the surface of the as-processed panel and (b) cut surface showing the internal structure.	140
Figure 6-2: Diagram of the multi-layered hard armor system with the CMF layer bonded between the ceramic faceplate and aluminum 7075-T6 backing. The presented dimensions are not to scale.	141
Figure 6-3: Diagram of the 12.7 x 99 mm ballistic projectile used for testing under MIL-STD-622F standard.	143
Figure 6-4: Diagram of the ballistic testing setup showing the positioning of the Mann gun, velocity chronographs, target, and high-speed camera.	143
Figure 6-5: (a) Cross section of the projectile highlighting the hardened steel core surrounded by the lead filler and encased in the copper jacket. (b) View of the meshed model from above using a 0.75mm fine mesh for the projectile and primary point of impact. The fine mesh is surrounded by a coarser mesh as it transitions away from the center of the plate.	146
Figure 6-6: Stress-strain curves of CMF samples at quasi-static and dynamic loading [107].	155
Figure 6-7: (a, c) Front and (b,d) rear images of CMF hard armor samples tested against the 12.7 x 99 mm ball threat.	158
Figure 6-8: Areal Density and impact velocity of PP (triangle) and CP (circle) tests of the 12.7 x 99 mm AP against CMF armors.	160
Figure 6-9: Front (a and c) and rear (b and d) images of the initial tests run of CMF hard armors against 12.7 mm AP threats.	161

Figure 6-10: Front (a, c, e, g) and rear (b, d, f, h) images of CMF hard armors impacted by 12.7 x 99 mm AP threat with a zoom in of the crushed spheres found below the backplate of AP12 (i)	163
Figure 6-11: Mass efficiency of CMF hard armors and commercially available Bisalloy ultra-high hardness steel plate [45]. The blue dotted line encompasses the samples that were used to calculate the V_{50}	166
Figure 6-12: Images of the residual core fragments and casings retrieved after testing for the (a) ball and (b) AP rounds.....	169
Figure 6-13: Multilinear stress-strain curves used to represent CMF in finite element analysis during ballistic impact of 7.62 [122] and 12.7 mm AP threats.....	170
Figure 6-14: Kinetic energy of the 12.7 x 99 mm AP core resulted from FEA modeling of 800 m/s impact.	172
Figure 6-15: ANSYS maximum principal stress distribution of all layers of the CMF armor during the simulated ballistic impact of the 12.7 mm AP round with a velocity of 800 m/s at (a) 0 μ s, (b) 30 μ s, (c) 60 μ s, (d) 90 μ s, (e) 120 μ s, and (f) 150 μ s.	173

Chapter 7

Figure 7-1: Exploded view diagram showing the arrangement of the CMF armors using (a) a ceramic face sheet, (b) a thin RHA faceplate above the ceramic, and (c) RHA above a layer of individual ceramic tiles. Note that the thicknesses and sizing are not to scale.....	177
Figure 7-2: Digital images of the (a) Mann gun used to fire the rounds and (b) the target sample and high-speed camera setup used to record the impact.	178
Figure 7-3: Cross section drawing of the (a) 7.62 x 63 mm M2 AP, (b) 12.7 x 99 M2 AP, and (c) 14.5 x 114 mm B32 API projectiles [24] that are used for testing CMF armors.....	180
Figure 7-4: Digital images of the front and back (a-f) of Armor 1, 2, and 3 following ballistic testing as well as additional images of the compressed spheres (g) in Armor 3.....	184
Figure 7-5: Results of the 14.5 x 114 mm B32 API testing plotted alongside V_{50} values for both RHA and HHA [35], [42], [46].....	190
Figure 7-6: Fragments of the fractured steel core retrieved from Armor 2 (PP) following testing.....	192
Figure 7-7: Percent of energy absorbed by the CMF layer as a function of the impact energy imparted by each ballistic threat. A linear fit between the 7.62 [122] and 12.7 mm [137] AP data shows how the 14.5 x 114 mm B32 API data currently compares with its higher impact energy.....	194

Figure 7-8: Digital images of the front and back of the layered SS-CMF armors with a highlight of the impact region after testing against a (a)-(c) 7.62 mm M2 AP, (d)-(f) 12.7 mm M2 AP, and (g)-(i) 14.5 mm B32 API	198
---	-----

Chapter 8

Figure 8-1: Manufactured 25 x 25 cm SS-CMF panel with a zoom in of the sphere arrangement on the top corner.....	202
Figure 8-2: Image of 23 x 152 mm high explosive incendiary rounds used to test CMF panels against blast wave and fragment impact.....	203
Figure 8-3: Diagram of the experimental setup for HEI blast against CMF panels.	205
Figure 8-4: Experimental set up showing the positioning of cameras and CMF panels in relation to the thin aluminum target.....	206
Figure 8-5: Initialized blast wave and fragments modeled in IMPETUS Afea Solver.	214
Figure 8-6: Digital images of the surface of SS-CMF panels with thickness of (a)-(d) 9 mm and (e) 16.75 mm following testing against three 23 x 152 mm HEI rounds with a close up (f) of a large fragment impacted on the 16.75 mm thick SS-CMF.	216
Figure 8-7: Fragment depth of penetration based on the area of impact of small (yellow), medium (red) and large (blue) frags for: (a) thin CMF panels and (b) thick CMF panel.	218
Figure 8-8: Comparison of the experimental and modeling results for a 16 mm thick CMF panel and 16.85 mm thick aluminum 5083 armor panel against HEI blast and frag.....	221
Figure 8-9: Comparison of the stress distribution in CMF (a,c) and aluminum 5083-H116 (b,d) panels upon interaction with blast wave and fragment impacts resulted from HEI round at 50 μ s (a,b) and 180 μ s (c,d).	223

CHAPTER 1: INTRODUCTION

1.1. Extreme Environments

A variety of engineering fields place materials and their structures under extreme conditions that are not normally experienced in the natural world. The environments are created in order to achieve a designed outcome, whether it be energy production, high speed travel, or exploration of currently uninhabitable regions. The term “extreme environments” is used to refer to circumstances that modify a material’s capability when exposed to high pressures, temperatures, energetic or magnetic fluxes, radiation exposure, and chemically aggressive environments that cause corrosion and oxidation. The advancement of fields that experience these conditions is primarily limited to the materials that are available to survive the exposure. It becomes apparent that in order to improve efficiency and safety under such harsh environments, a new wave of materials must be manufactured and studied in order to continue to advance human technology. Energy, transportation, and defense require new materials to expand the current technology as new steps are taken to improve plant efficiencies, reduce vehicle weights, and continue to expand understanding of materials that can be useful for national security. A better understanding and constant research into how materials act in extreme environments is crucial to advancing human technology across multiple platforms and providing a safer future.

1.1.1. Extreme Mechanical Loading

The ability to understand and create materials that can withstand high strain rate and stresses is of importance for advancing current technologies for transportation and military defense systems. Severe loads under accidents experienced during operation of transportation vehicles is responsible for damage, injury, and death (Figure 1-1) [1]–[4]. These accidents

occur at high speeds with a large accelerating pulse with rapid loading and unloading of the vehicles. These events place materials under failure modes involving strain hardening and strain rate effects, large plastic deformations, and complex stress states. It is paramount to continually investigate new materials that can replace these structures and absorb energy at a higher efficiency using advanced materials. Transportation is an essential feature of everyday life and requires materials that can perform under extreme conditions such as temperature, pressure, and corrosive environments. Transportation is also dependent on fuel efficiency and safety. Fuel efficiency and safety are thought to be inversely related, as safer structures generally require additions to a vehicle's design. The next generation of vehicles require advanced materials that reduce the overall weight without sacrificing the structural integrity of the vehicle. The materials used for crashworthy vehicle systems and for carrying hazardous waste must be able to absorb energies at high rates of impact in order to protect the passengers and cargo. The materials used for train cars and trucks to transport hazardous waste must safely carry the cargo without risking dangerous spills and exposure to personnel and the environment. From spent nuclear fuel to chlorine for water treatment, freight rail tank cars are one of the most popular means for transporting hazardous materials (hazmat) [1]. Until recently, the current tank car design has not been greatly modified since its standardization.

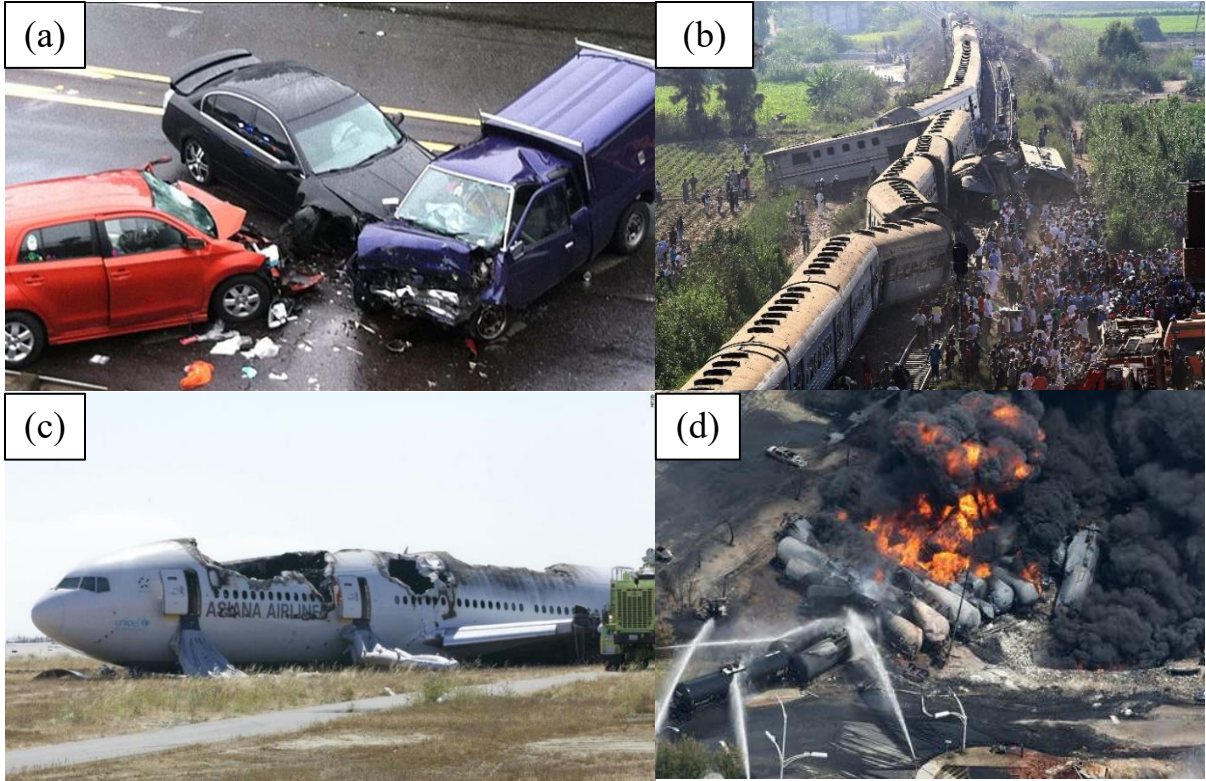


Figure 1-1: Images of the aftermath of vehicle accidents involving (a) cars, (b) train cars [2], (c) airplanes [3], and (d) tank cars [4].

1.2. Tank Car Structure

The current tank structure was established in the 1960's with the development of the DOT-111 tank car design. The design itself has not greatly changed although the importance for hazmat protection has become the focus for the next generation of tank cars and materials used in tank cars [5]. One of the primary concerns under accident conditions is puncture of the tank car containment. Although the tank cars themselves are not directly responsible for accidents, the DOT-111 cars have been prone to puncture and spilling hazardous materials. In incidents such as the Lac-Mégantic, Quebec rail disaster in 2013 where 74 DOT-111 tank cars carrying crude oil derailed, killing 47 residents [6]. The crude oil ignited during the accident, destroying roughly half of the downtown area [6], [7]. These types of accidents have occurred

in other regions involving the DOT-111 tank cars through the years [8]. The DOT-111 tank cars were originally designed with a shell made from 7/16 in. thick steel [1]. Some tank cars are lined with an additional 1/8 in. thick steel jacket to help protect it during derailment [1]. The DOT-111 is a non-pressurized tank car that has been widely used to transport ethanol and crude oil [9]. In 2017, the DOT-111 made up over 50% of the tank car fleet in the United States [1]. In addition, hazardous materials made up 75% of all tank car shipments in 2015 [1]. The class of hazardous materials transported by tank car are shown in the pie chart in Figure 1-2 [1]. It can be seen that flammable liquids make up almost half of the hazardous materials shipped. In order to safely transport these types of materials, the puncture resistance and insulation must be improved for future tank car designs. The DOT-111 tank cars are relatively simplistic compared to more recent designs which include a layered structure for further protection from rupture and combustion.

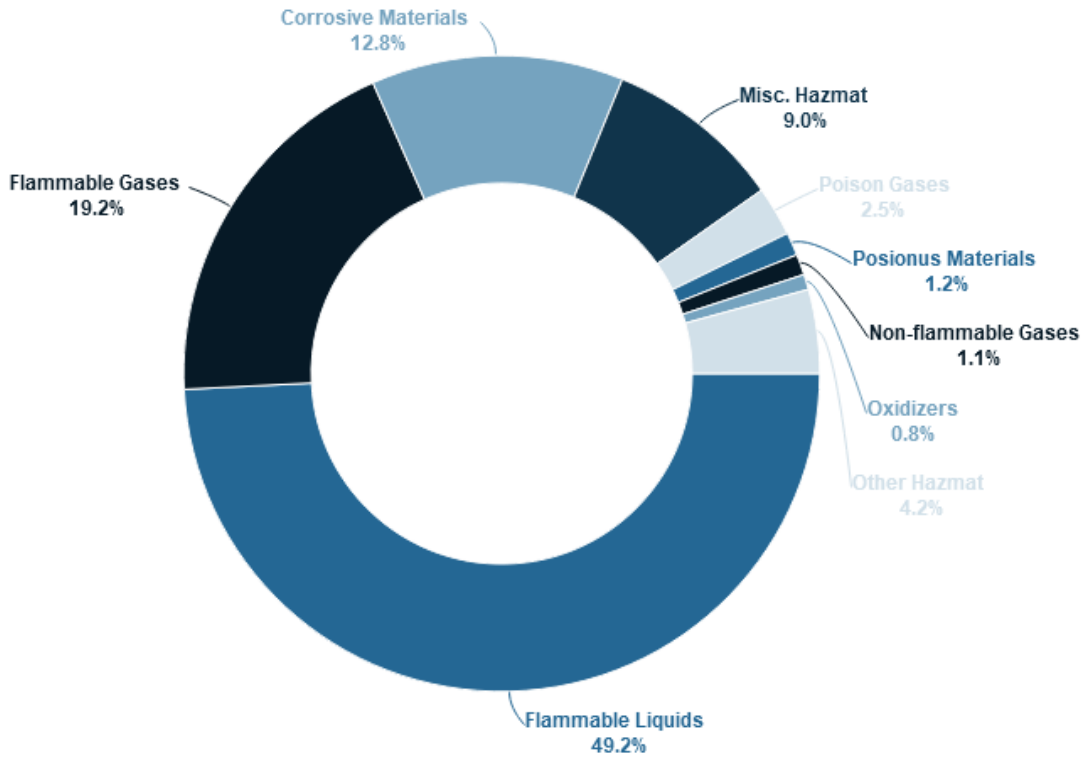


Figure 1-2: Hazmat shipment type by class [1].

A new car design was suggested by the Railway Supply Institute (RSI) in 2014 and adopted by the DOT shortly thereafter [1], [10]. The DOT-117 tank car design that was adopted uses a layered construction in order to give the tank additional protection [1], [10]. The shell consists of five layers that are presented in Figure 1-3 [10]. The outer layers are made of a required 1/8 in. thick steel jacket that is the first layer to protecting the car from leaking during derailment [1], [10]. The jacket also protects the interior layers from weathering and deterioration during the car's lifetime [1], [10]. The car has two head shields at either end made from half inch steel. The head shields are the primary reinforcement for puncture resistance in order to avoid damage during derailment and car pileup. During derailment, a risk of puncture is presented by the coupler of surrounding railcars as well as the crash environment, generally

occurring at either head of the tank car. The head shields can be built into the tank car design or can be made of a separate attachment that can provide further puncture protection [1], [10].

The DOT-117 also uses a 7/16 in. thick shell and also includes a thermal jacket and insulation layer sandwiched between the shell and the jacket [10]. The insulation layer keeps the material contents at an appropriate temperature during shipping and loading. The thermal blanket is intended to protect the contents from exterior fires and reduce the risk of combustion of the car's contents. The thermal blanket is made from a high temperature material such as woven ceramic fibers and is required to be at least $\frac{1}{2}$ in. thick for the DOT-117 tank cars [1], [10]. In addition to the structural design changes, the DOT-117 also includes a new top high-flow pressure relief valve to avoid complete rupture of the tank's shell during puncture accident events. The new valve system and tank structure are all designed to prevent the car from emptying its contents during accident conditions [10].

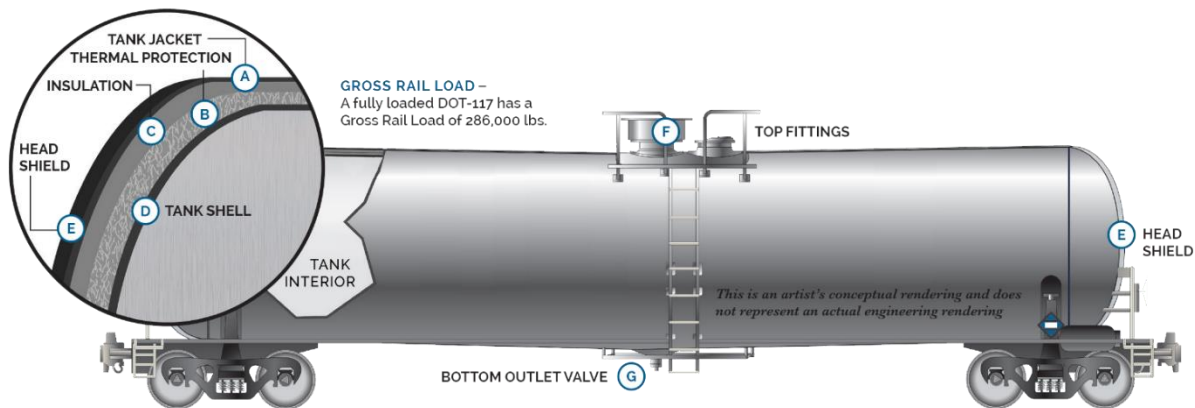


Figure 1-3: DOT-117 tank car designed to replace the DOT-111 used in transportation of hazardous materials [10].

1.2.1. Tank Car Materials

Researchers have been working closely with the railway industry and DOT to help improve the puncture resistance of the current design by comparing it to potential material replacements. The current material requirements for tank car construction are outlined by the Association of American Railroads' (AAR) standards and practices [11]. The two high-strength steels that have been made standard for tank car construction are the AAR TC-128, Grade B and AAR-A516, Grade 70 [1], [10]. The steels are carbon, manganese steels used for pressurized tank car construction. The chemical composition of both grades is listed in Table 1-1 [11]. TC-128 B has become the industry standard for most new tank car production over A516 [10]. The improvements to metal processing and manufacturing have pushed TC-128 B to its metallurgical limits for pressurized tank car construction. Alternative steels with a lower carbon content have been explored for improved toughness and weldability [12].

Table 1-1: Chemical composition of tank car steels, TC128 B and A516 70, as outlined by the Association of American Railroads [11].

Steel Grade	C (wt%)	Mn (wt%)	S (wt%)	Si (wt%)	Nb (wt%)	V (wt%)	Ni (wt%)	Mo (wt%)	Cu (wt%)
TC128 B	0.24	1.00-1.65	0.015	0.15-0.40	0.02	0.08	-	-	-
A516 70	0.23	0.85-1.20	0.015	0.15-0.40	0.02	0.03	0.40	0.12	0.40

TC-128 B steel has been found to fail during rail accidents due to crack initiation and propagation through the tank car shell [7], [13]. Ferritic steels undergo two primary mechanisms of fracture. Brittle fracture is one mechanism of fracture that occurs due to rapid trans granular crack propagation [7], [13]. Ductile fracture is caused by the growth and coalescence of small voids that exist in the material due to intrinsic defects. The voids are

formed around precipitations such as carbides or, in the case of TC-128 B and A516 70, nonmetallic inclusions such as manganese sulfide (MnS) [7]. Images describing the brittle and ductile fracture mechanisms are shown in Figure 1-4 [7]. During the puncture of TC-128 B tank cars, both fracture mechanisms have been documented [7], [13].

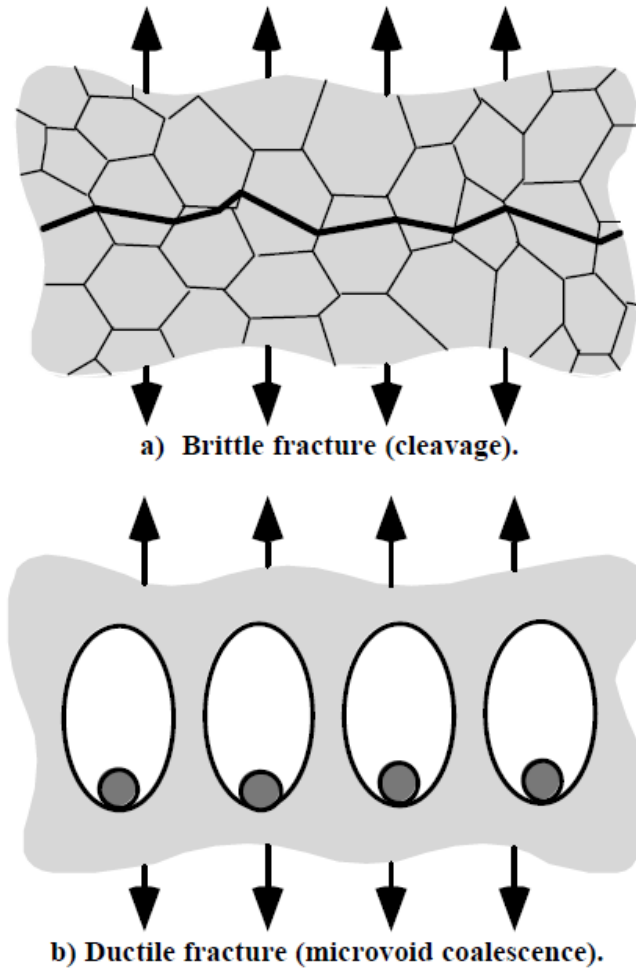


Figure 1-4: Diagram of the two fracture mechanisms, (a) brittle and (b) ductile, in steels [7].

An example of a tank car rupture experiencing both brittle and ductile failure is shown in Figure 1-5 [14]. The car was carrying hazardous anhydrous ammonia at the time of rupture in 2002, near Minot, North Dakota [7], [14]. The shell and steel jacket were unable to contain

the hazardous material, leading to caustic gas release to the surrounding region and delaying rescue operations [7]. The failure of the Minot tank car initiated from ductile rupture due to void coalescence in the steel [7]. The microvoids grow during plastic deformation until a crack is formed and can propagate through the tank car head/shell. Crack propagation continues through the steel via either ductile or brittle fracture depending on the microstructure of the surrounding material [7], [14]. The steel used to manufacture the Minot tank cars met the standardized strength requirements even though it failed to contain the car's lading [7]. This has led to an effort to reimagine the tank car structure using various geometric and material changes to improve their overall puncture and failure resistance.



Figure 1-5: Puncture of a TC128 Grade B tank car near Minot, ND carrying anhydrous ammonia [14].

Current research is built upon understanding the puncture strengths and dynamics of the relatively new tank car designs (DOT-117, DOT-105, etc.) while also evaluating new strategies for maintaining the tanks' integrity under accident conditions [9], [15], [16]. Alternative protection systems for tank car structures incorporate energy absorption materials and engineered metal systems (EMS) that weld geometric cores into a sandwich panel that can be used in tank car designs or placed as an exterior jacket for current cars [17]. The sandwich panels have been tested for their bending stiffness and puncture resistance compared to bulk steel tank car shells, while providing possible weight savings. The cores are designed with various geometries and sizes such as: round tube core, X-core, and diamond core as shown in Figure 1-6 [17]. The 3 inch outer diameter tubes were chosen for full-scale puncture testing and showed improved puncture resistance against a ram imparting 3.13 million ft-pounds [17].

The work presents the opportunity of investigating energy absorption materials that can be placed into a sandwich structure and attached to the exterior of existing tank cars in order to improve puncture resistance during accidents. The exterior protection can be selectively attached to cars at high risk regions such as the head shields and lower half of the tank car where shell punctures are most likely to take place.

6"x2'x5" Pipe Round Tube Core Test Article (P1)



6"x2'x3" Round Tube Core Test Article (P2)



6"x2'x2" Round Tube Core Test Article (P3)



6"x2' X-Core Shell Test Article (X1)



6"x2' Diamond Core Test Article (D2)



Figure 1-6: Digital images of the manufactured sandwich panels for potential tank car shells [17].

High strain rate impacts, similar to those tank cars experience during accidents, also occur in defense systems regularly exposed to high velocity blast and ballistic threats.

Advanced materials that offer lightweight energy absorption capabilities are needed to improve both tank car designs and the future of military armors.

1.3. Military Environments

Military systems are regularly exposed to extreme environments for a number of diverse applications. The military is constantly working on the cutting edge of material for advanced defense systems for the variety of threats that personnel and vehicles are exposed to in war zones. Military vehicles require lightweight materials for improved fuel efficiency and lower carbon emissions while improving their safety against high speed impacts by projectile threats and explosives. This has led to a new wave of advanced materials that can revolutionize energy absorption and be applied to a multitude of engineering structures. One such example is the necessity for advanced materials in defense technologies that undergo rigorous environments and are needed to protect forces during battle. In order to advance armor technology, light-weight alternatives that can perform against a variety of threats and improve upon the current standard's maneuverability, fuel efficiency, and reliability is paramount to protect vehicles and personnel [18], [19].

1.3.1. Military Armors

Armors are a necessity for today's police and military operations to protect vehicles and personnel in dangerous situations. Materials for armors are needed to protect against a variety of extreme threats that include blast, ballistic, and fragment impacts at high rates of speed that can be lethal to exposed personnel [18], [19]. The military's success is dependent on reliable armors for its vehicles and personnel. Light armors are flexible and weight efficient but only protect against small arms fire [18]. Heavy armors are meant to face large caliber threats but decrease the fuel efficiency and maneuverability of the vehicles that use them. The

next generation of vehicle and personal armors must be lightweight, cost effective, and perform well against an array of blast and ballistic threats [18].

Armors can be classified into two material categories: soft and hard armors. Soft armors are made up of flexible composite fabric components that are able to defeat small caliber rounds [20]. Soft armors are widely used as personal body armors due to their light weight and availability. Soft armors are limited to their application against small caliber rounds and low speed fragments but are relatively weight efficient compared to other material alternatives. Hard armors use ceramic and metallic plates that are heavier than soft armors but have improved protection against larger caliber rounds and armor piercing threats at high impact velocities. Hard armors are used for both personal and vehicle protection.

The military has various vehicles used in combat that are outfitted to protect against different threat levels. As the threat increases, so does the weight of the vehicle. Some examples of this trend are shown in Figure 1-7(a) [21]. One of the most agile vehicles, the high mobility, multipurpose, wheeled vehicle (HMMWV) is able to transport troops relatively quickly but does not offer the same protection as the joint light tactical vehicle (JLTV) which is outfitted with two levels of armor protection [22]. Over the past three decades, there has been a constant growth in military vehicle weight in order to defend against larger ballistic threats. For example, the Abrams tank weight has increased from 54.4 to 63 metric tons over 29 years in order to better defend against the advancement in ballistic and explosive threats [23]. The increased weight reduces the vehicle's fuel efficiency and maneuverability making it susceptible to attack and ambush during refueling or when setting up required supply lines. A similar trend exists for personal armors that require advanced protection using heavy metal plates. These armor inserts reduce the user's mobility and can be more cumbersome than

helpful during combat. The next generation of military vehicles and protection for personnel has reached a pivotal point for reevaluating and advancing the current materials used for armors.

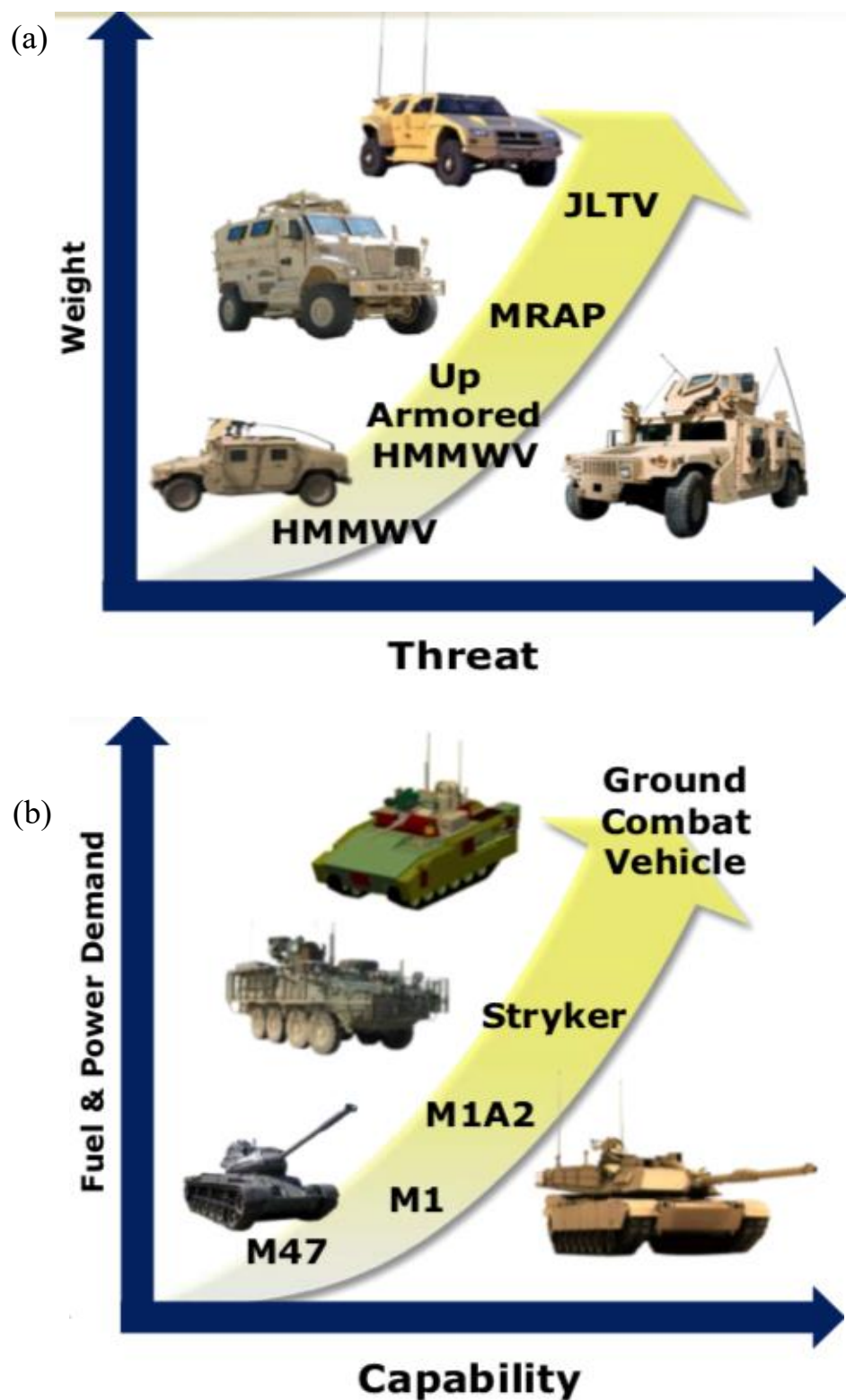


Figure 1-7: (a) Military vehicles shown by their armor class and increasing weight required for protection. (b) Ground capabilities of combat vehicles and their necessary fuel requirements showing the need for improved fuel efficiency with heavy armor vehicles [21].

Table 1-2: Weight of the M1 Abrams tank from 1980-1999 showing the increase in overall weight due to armor improvements to protect against more penetrating threats [23].

Year	Vehicle	Weight [23] (metric tons)
1980	M1	54.4
1984	M1IP	55.3
1988	M1A1	58.9
1990	M1A2	62.1
1999	M1A2 SEP	63

Overall, the future of armors must balance three primary axioms [18], [19]. The first is based on the protection the armors provide as they are designed to defeat up to a certain ballistic and explosive threat. The armors must be cost effective and be able to be manufactured on a large scale that can be easily outfitted to current military vehicle designs. Finally, the armors must be weight efficient when compared to the current military standards without sacrificing protections that are currently in place. Weight is an important factor when considering armors as it can help improve the survivability of the vehicle by improving the speed, agility, range of travel, and transportability, thereby making them easier to maneuver in and out of combat.

The materials that are able to perform such a task must also balance three main features in order to achieve the desired outcome. Most ballistic threats are made up of a piercing core that can be made of hardened steel or tungsten carbide. The armor must be hard enough to fracture the core, breaking it into smaller pieces, and prevent complete penetration of the round. After the core is fractured, the armor must be able to absorb and dissipate the kinetic energy of

the impacting rounds through plastic deformation in order to protect the personnel and payload. As previously discussed, the armors must be made of materials with a lower density than conventional armors in order to reduce their weight and improve the vehicle's maneuverability and fuel efficiency. Prior to discussing the next generation of armors, it is important to first establish and understand the threats that these armors face and the materials currently being used to defeat them.

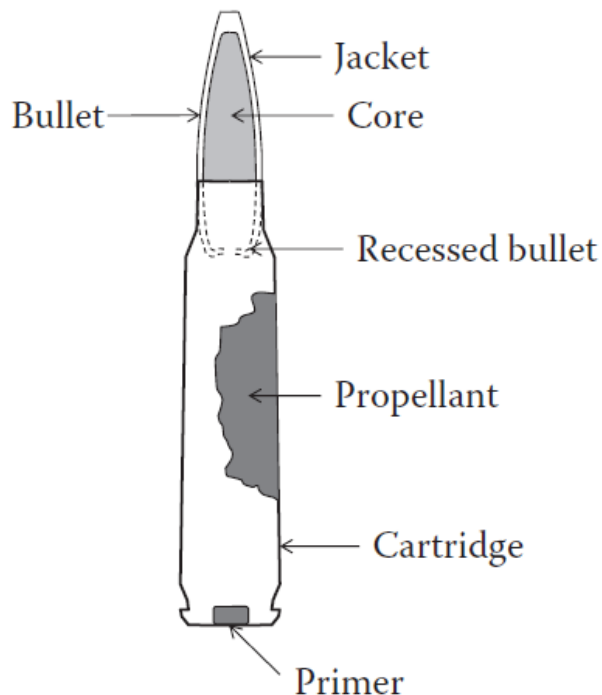
1.3.2. **Ballistic, Blast and Fragment Threats**

Ballistic Threats

Armors outfitted to military vehicles are designed to perform up to a specified level of protection while being resistant to other environmental exposures such as humidity, corrosion, shock, and vibration. Current armors exist to protect the wearer from projectile and fragment impacts created from ballistic threats and explosives in order to reduce injuries and fatalities. Bullets are one of the primary forms of aggression used around the world. Small-arms ammunition is made up of sections that include the cartridge and bullet. The bullet is the projectile that is launched from the threat. The cartridge contains the propellant required to fire the bullet which is initiated by the hammer striking the primer at the base of the cartridge. The bullet that is fired from the round has an outer jacket surrounding the bullet's core which acts as the penetrator on impact. The core is surrounded by a jacket that protects the barrel from the hard core, engages rifling within the barrel and gives the projectile an optimized shape for traveling. A general ammunition design is shown in Figure 1-8 [19].

Bullets are made in various shapes and sizes but are named to describe the threat's size and penetrating type. A bullet, such as the 7.62 x 51 mm ball has a 7.62 mm bullet diameter and an overall length of 51 mm when including the cartridge. The diameter can also be

described as the caliber of the threat, using inch units rather than metric. In this system a 7.62 mm round is commonly known as a 0.30 caliber and a 12.7 mm threat is referred to as a 0.50 caliber round. Larger ballistic threats carry a higher muzzle velocity based on the size of the cartridge and the type of core used in the projectile.



Ammunition	v_0 (m/s)
5.56 × 45 mm SS109	920
7.62 × 39 mm PS Ball	720
7.62 × 51 mm Ball	820
7.62 × 51 mm FFV	950
14.5 × 114 mm BS41	1000

Figure 1-8: Small arms ammunition design of most ballistic threats and a Table showing example threats and their muzzle velocity [19].

The core of the bullet can be made from various materials in order to increase their penetrative qualities. Ball rounds are widely used and are made up of a mild steel core [19]. The ball rounds are relatively soft with a Vickers hardness of 280 [19]. The core, upon impact with armors, will deform along with the lead filler and copper or steel jacket. The mild steel rounds are relatively easy to stop using as little as 12 mm of mild steel when impacted from 10m [19]. Cores made of harder and denser materials such as hardened steel or tungsten carbide can replace the mild steel for increased penetration and impact energy. The hardened steel and tungsten carbide cores are referred to as armor piercing (AP) threats due to their improved piercing qualities [19]. Larger threats can use much harder cores, such as tungsten carbide and have a higher muzzle velocity, such as the 14.4 x 114 mm BS41 shown in the table in Figure 1-8 [19]. The hardened steel and tungsten carbide cores have a higher density and impact with a higher kinetic energy. The kinetic energy, KE, is calculated using the classical mechanics equation of:

$$KE = \frac{1}{2}mv^2 \quad (1)$$

where m is the mass of the projectile and v is the velocity at which it impacts. By increasing either the mass or velocity, the kinetic energy imparted into the armor increases, hence why armor piercing rounds are more damaging than ball rounds. The penetrating quality of a ballistic threat can also be measured by its kinetic energy density, KE_d . The kinetic energy density is calculated by dividing the kinetic energy by the cross-sectional area of the bullet, A:

$$KE_d = \frac{mv^2}{2A} \quad (2)$$

The kinetic energy densities of multiple sized bullets are listed in Table 1-3 [24]. As can be seen, the larger projectiles carry a higher kinetic energy density due to their larger core mass and impact velocity. The tungsten carbide core of the 14.5 x 114 mm BS41 API is smaller

than the BS32, but because of the higher density of the tungsten carbide ($\rho = 14.9 \text{ g/cm}^3$) when compared to the steel ($\rho = 7.8 \text{ g/cm}^3$), the projectile imparts a higher kinetic energy density. The higher kinetic energy density makes a projectile more piercing and requires stronger and thicker armors to stop it.

Table 1-3: Projectile core properties and kinetic energy density of various ballistic threats [24].

Ballistic Threat	Core Material	Core Diameter (mm)	Core Mass (g)	KE_d (MJ/m²)
7.62 x 63 mm M2 AP (0.30 Cal)	Hardened Steel	6.2	5.3	71
12.7 x 99 mm M2 AP (0.50 Cal)	Hardened Steel	10.9	25.9	112
14.5 x 114 mm BS32 API	Hardened Steel	12.4	41.0	170
14.5 x 114 mm BS41 API	Tungsten Carbide	10.9	37.9	211

Blast and Fragment Threats



Figure 1-9: Image of IED's disarmed in eastern Baghdad in 2005 during the Iraq war [25].

Explosive threats such as IED's and shape charges are also known for the blast wave they produce upon detonation. When a detonation occurs, a very fast chemical reaction involving a solid, dust, or gas rapidly releases a surge of hot gases and energy. The gases that are produced expand into the surrounding environment and displace the air, creating a blast wave and shock front. The blast wave propels fragments, damages vehicles and structures, and can cause internal damage to vital organs such as the lungs, brain, and flesh [26]. The physics behind the propagation of blast waves is complicated, but the best protection from injury is to further your distance from the site of detonation. A simple schematic of the propagation of a blast wave in open air is shown in Figure 1-10 [19]. The blast can be seen at three distances from the point of detonation: r_1 and r_1+r_2 . The surface area of the blast wave at both locations

is marked by s_1 and s_2 . As can be seen, the area increases by a factor of r^3 , meaning the energy density and pressure fall off rather quickly [26]. For example, by doubling your distance from the charge, the energy density is reduced to 1/8 of its original value.

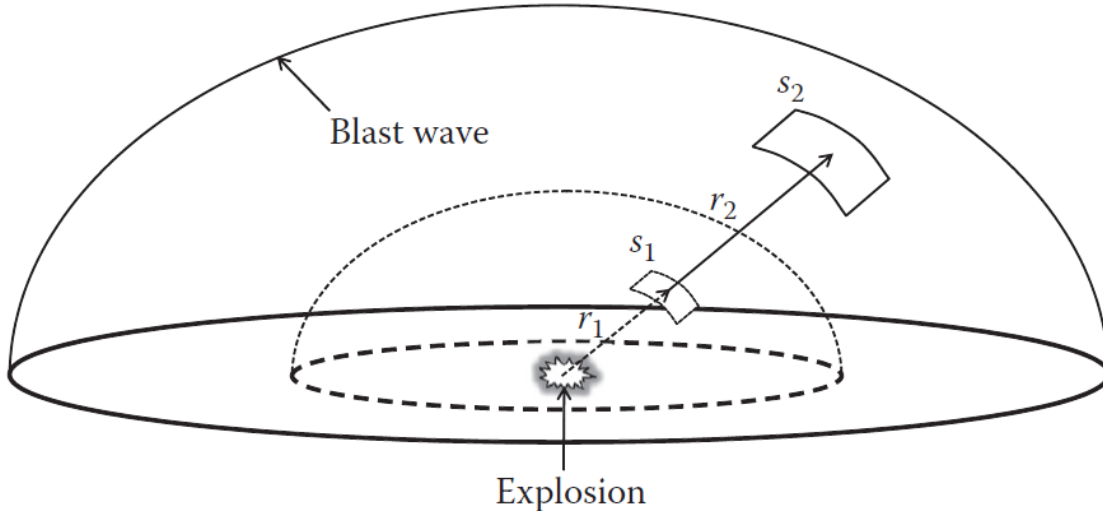


Figure 1-10: Simple schematic of a blast wave propagation [19].

Blast waves create an impulse of pressure to the surroundings over a relatively short time causing an instantaneous rise in pressure that falls off over a short period of time as the blast wave front passes. The ideal pressure profile of an open air blast wave is presented in Figure 1-11 [19]. The pressure at an element away from the ignition point is equal to the environment's ambient pressure P_o . The pressure increases almost instantaneously to a peak pressure, P_p , as the wave arrives at the element at time t_A . The difference between the ambient pressure and peak pressure is referred to as the peak overpressure. The peak overpressure falls off depending on the element's distance from the blast source, as previously discussed. After reaching a peak, the pressure falls off exponentially over the positive duration time, t_o , until it

reaches the ambient pressure value. The pressure impulse, I , of the blast wave is measured by calculating the area under the curve for the positive duration as [19], [27]:

$$I = \int_{t_A}^{t_A+t_o} P dt \quad (3)$$

where P is the pressure. The positive phase is followed by a decrease in pressure, below the ambient pressure value, referred to as the negative impulse. The negative duration is much longer than the positive phase and is responsible for a suction force that pulls structures back towards the point of detonation. The negative pressure profile is much lower than the peak overpressure and are not necessarily considered for structural integrity measurements.

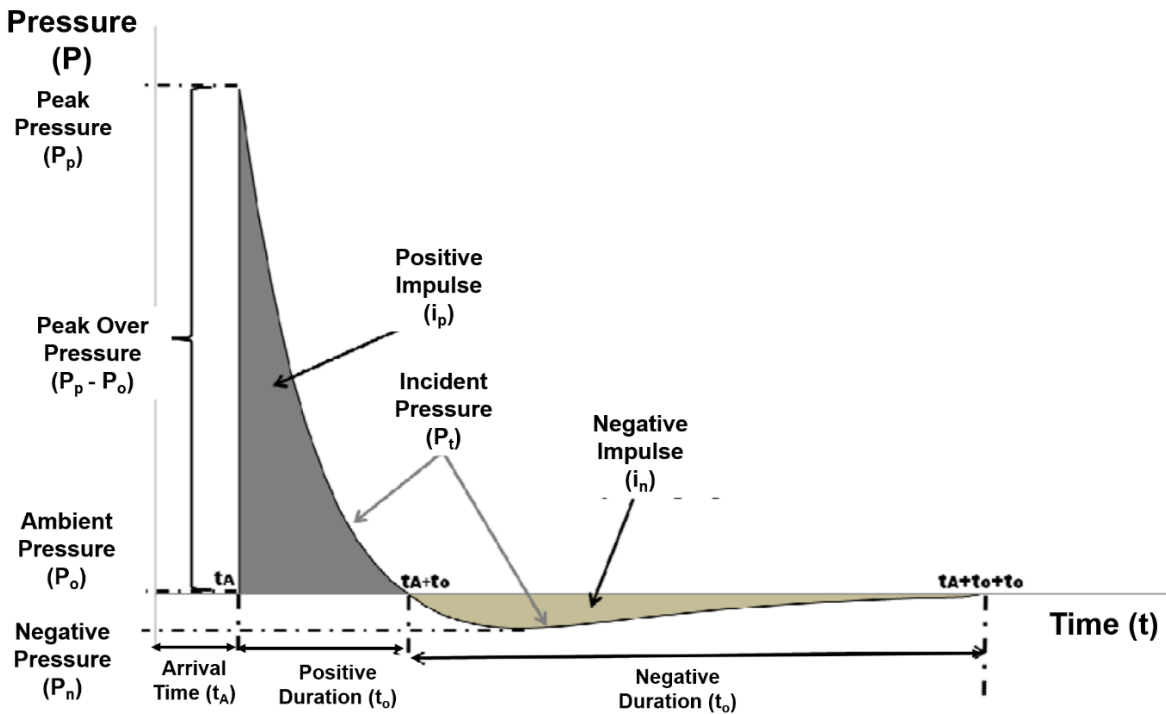


Figure 1-11: Pressure time history of an ideal blast wave in open air [27].

It is first necessary to know the type and amount of explosive material that is detonated in order to approximate the peak overpressure and blast load that will be created. There are

several types of explosives that are used for executing terrorist attacks and igniting IED's. Trinitrotoluene (TNT) has been chosen as a universal quantity for which to compare and quantify the blast characteristics of explosive materials. This is done by calculating the equivalent TNT weight of a chosen explosive media by calculating the ratio of heat produced during detonation and comparing it to that of TNT [27], [28]:

$$W_{TNT} = W_{Exp} \frac{H_{Exp}}{H_{TNT}} \quad (4)$$

where the weight of the TNT and explosive material are W_{TNT} and W_{Exp} , respectively in kg. H_{TNT} is the heat of detonation of the TNT and H_{Exp} is the heat of detonation of the explosive, both measured in MJ/kg [27], [28]. The heat of detonation of various explosive materials has been documented and some are presented in Table 1-4 [28]–[30]. The equivalent weight of TNT can be further simplified to get the TNT equivalent weight factor. The TNT equivalent weight factor can be used to determine the mass of TNT needed to produce an equivalent blast wave created from another explosive media. The TNT equivalent weight factors are also listed in Table 1-4 for both the pressure and impulse values [28], [29].

Table 1-4: Heat of detonation and TNT pressure and impulse mass equivalents for various explosive materials [28]–[30].

Explosive Material	Heat of Detonation (MJ/kg) [30]	TNT Mass Equivalent [28], [29]	
		Peak Pressure	Impulse
TNT	4.10-4.55	1.00	1.00
C4	5.86	1.37	1.19
RDX	5.13-6.19	1.14	1.09
PENTOLITE 50/50	5.86	1.33	1.14

Table 1-4: (continued)

NITROGLYCERIN	6.30	1.54	-
NITROMETHANE	6.40	1.10	-
COMPOSITION B	6.43	1.11	0.98
PETN	6.69	1.27	1.11
NITROCELLULOSE	10.60	1.10	-

Fragment and blast wave impacts are also threats often faced by personnel and vehicle armors. The blast wave and high speed fragments are produced from an exploding charge, pipe bomb, improvised explosive device (IED), high explosive incendiary (HEI) rounds, etc. The fragments that are produced from the explosion vary in velocity, material, and shape depending on the type of detonation. The fragments emitted from most explosive threats are irregularly shaped making them less aerodynamic in flight and reducing their penetrative qualities when compared to ballistic projectiles [19]. The fragmentation can be generated by the shell casing of an explosive round, implanted in the threat like a pipe bomb, or be generated by surrounding debris and material in the case of IED's.

The armors that are designed for vehicle use can also be used to line structures subjected to explosive threats. The armors should be able to mitigate the pressure of the blast wave with appropriate shock resistance and be able to stop incoming fragments. This is especially true for the undercarriage of most armored personnel carriers. IED's have greatly influenced the design and outfitting of armored military vehicles, requiring them to be able to withstand blasts coming from below the main hull. An improvement to current military vehicles has been the outfitting of V-shaped hulls [31]. The JLTV was manufactured by the military with a V-shaped hull that deflects blasts from below, reducing the chance of floor

plate destruction and vehicle lift [19], [31]. In order to maintain consistent protection for military personnel, it is important to consider the blast and fragment protection offered by armors along with their ballistic protection. In order to design and test the next generation of military armors, one must first understand the current armor standards and research that has been completed.

1.4. Armor Materials

Armors have been constantly developed in order to reduce injury and fatalities against projectile threats. For individuals, the armor shields the wearer and must not inhibit their maneuverability and comfort. Vehicles and aircraft require the armor to also be weight efficient and easily incorporated to vehicle designs. Most armors are designed with specific threats in mind, using the projectiles as a baseline for understanding the weight and thickness of each material required to stop it upon impact.

1.4.1. Metal Armors

Metals have been widely used for armors as they are easily attached to existing armor designs. Steels can be manufactured and alloyed to improve their performance under impact while aluminum and titanium alloys can be used to reduce the overall weight. Many studies have been completed on high strain rate impact and energy absorption of metal armors under ballistic impact. Understanding their advantages and disadvantages is important to designing the next generation of advanced materials for armor applications.

Armor Steel

Steel has long reigned as one of the most popular armor materials [32], [33]. It is able to perform against a variety of threats from early small arms projectiles to newly encountered threats such as improvised explosive devices (IED's). Since their early use, steels have been

developed for armor applications due to its commercial availability, ease of fabrication, and industrial production capacity [32]. Homogeneous steel armors were first developed over 100 years ago during manufacturing of some of the first tanks during World War I [33]. The first steel armors were made from a low alloy steel with a low carbon content that could be welded or cast to improve production efficiency [33]. Over the last few decades, cast steels have been replaced by rolled homogeneous armor (RHA) due to reduced production costs [32]. RHA is the current military standard material for the National Institute of Justice (NIJ) ballistic standards for personal and vehicle armor [34], [35]. RHA is a hot rolled steel known for its balance of high hardness, strength, and ductility. RHA is produced under strict specifications using hot rolling followed by heat treatment to create a fine martensitic microstructure as defined by MIL-A-12560K [35]. These standards were developed during World War II and have not changed considerably since.

The chemical composition of RHA steel armors can be varied following the requirements outlined in MIL-A-12560K and shown in Table 1-5 [35]. The carbon content is important for producing the martensitic microstructure created through quenching. The other alloying elements such as nickel, chromium, manganese, molybdenum, and boron all improve the hardenability of the final structure. Silicon helps to delay the onset of martensitic embrittlement and improve the tempering temperature range [36]. The microstructure of the steel armors is highly dependent on the post treatment following hot rolling during manufacturing [37]. Armor steels are quenched and tempered to give them their martensitic microstructure [33], [38]. Quenching of the steel creates a smaller grain structure due to the rapid cooling rate [33], [38]. The tempering phase can vary the hardness and ductility of the final product in order to obtain optimal results [33], [38]. A lower tempering time and

temperature will lead to a harder steel with higher strength at the expense of a lower ductility and toughness [38]. A higher tempering time and temperature allow for further relaxation of the residual stresses created during manufacturing and reduces the hardness of the product while improving its ductility and toughness [38]. The general microstructure of RHA is shown in Figure 1-12 [37]. The figure highlights carbide precipitations that form during quenching of the steel that gives it its improved hardness [37]. The microstructure is a balance of hardness, needed to erode impending rounds, and ductility so the plate does not fail immediately following impact [38].

Table 1-5: Chemical composition for manufacturing of RHA as required by MIL-A-12560K [35].

ELEMENT	COLUMN A MAXIMUM LIMIT for DECLARED CHEMISTRY (WEIGHT PERCENT)	COLUMN B ^{5/} ALLOWABLE RANGE for FUTURE PRODUCTION LOTS (WEIGHT PERCENT)
Carbon	0.27 up to 2" thick, incl 0.29 over 2" up to 4" 0.31 over 4"	± 0.05
Manganese	NONE REQUIRED, HOWEVER IF: ≤ 1.00 > 1.00	± 0.15 ± 0.20
Phosphorus	0.020 ^{1/}	^{4/}
Sulfur	0.010 ^{1/}	^{4/}
Silicon	NONE REQUIRED, HOWEVER IF: ≤ 0.60 > 0.60 to ≤ 1.00 > 1.00	± 0.10 ± 0.15 ± 0.20
Nickel	NONE REQUIRED ^{3/}	± 0.25
Chromium	NONE REQUIRED, HOWEVER IF: ≤ 1.25 ^{3/} > 1.25	± 0.15 ± 0.25
Molybdenum	NONE REQUIRED, HOWEVER IF: ≤ 0.20 ^{3/} > 0.20	± 0.035 ± 0.075
Vanadium	NONE REQUIRED ^{3/}	± 0.05
Niobium	NONE REQUIRED ^{3/}	± 0.05
Boron	... ^{2/}	^{4/}
Copper	0.25 ^{3/}	^{4/}
Nitrogen	0.03 ^{3/}	^{4/}
Titanium	0.10 ^{3/}	^{4/}
Aluminum	0.10 ^{3/}	^{4/}
Lead	0.01 ^{3/}	^{4/}
Tin	0.02 ^{3/}	^{4/}

^{1/} Phosphorus and sulfur total shall not exceed 0.020 wt%.

^{2/} When the amount of boron is specified in the alloy, its content as determined by heat analysis shall not exceed 0.003 percent.

^{3/} When the amount of an element is less than 0.02 percent the analysis may be reported as [< 0.02 wt%].

^{4/} There are no limits on the allowable values for future lots; however, the values may not exceed those listed as the maximum limit.

^{5/} Values are actual tolerance limits NOT percent tolerances.

^{6/} Elements not listed in Table, but intentionally added, shall be reported.

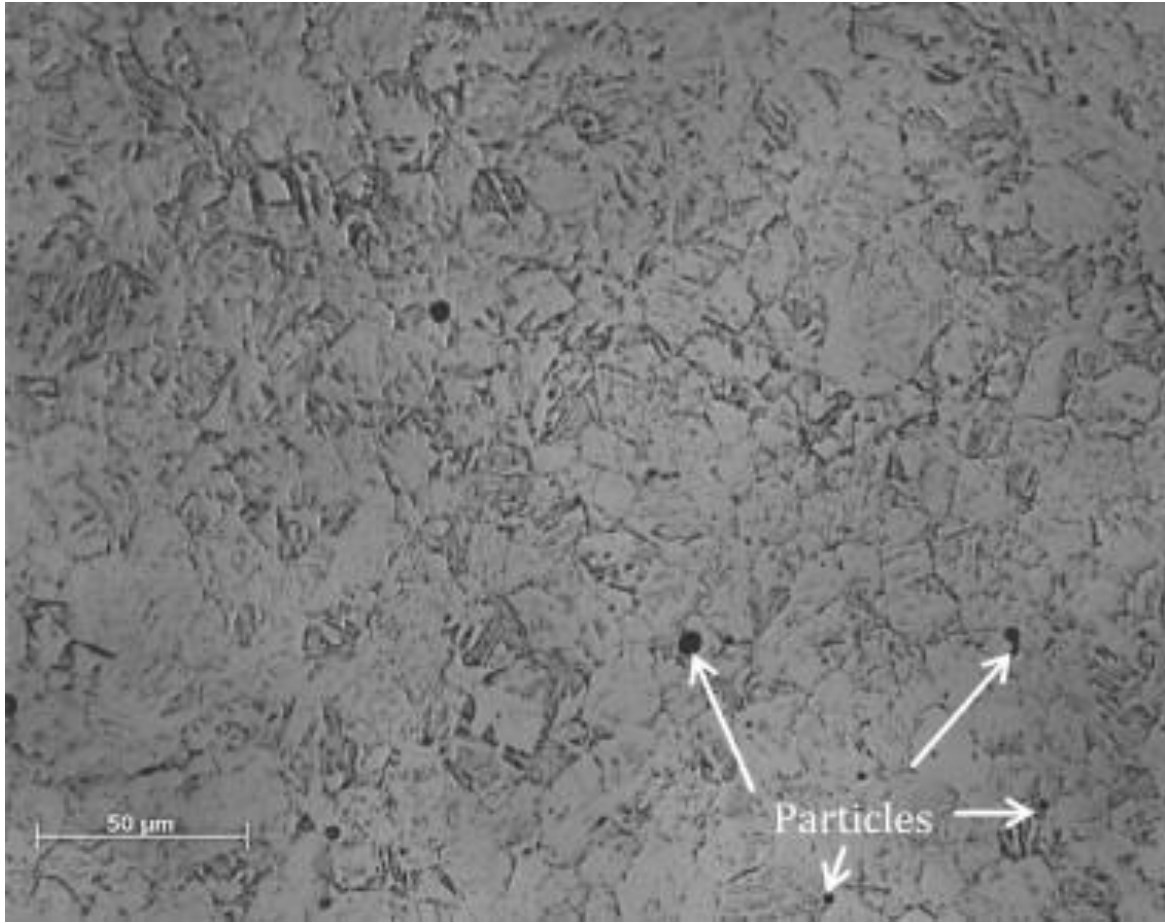


Figure 1-12: Microstructure of RHA highlighting the carbide precipitations and revealing the slightly martensitic grain structure [37].

Due to its initial success and strength, RHA is still widely used as a military armor. The panels are easily incorporated into vehicle design as they can be easily welded and attached to the exterior such as the armor survivability kit outfitted on the high mobility, multipurpose, wheeled vehicle (HMMWV) in Figure 1-13. However, the primary drawback to RHA is its relatively high density (7.9 g/cm^3). As such, RHA is the mass efficiency standard for developing new hard armors and materials as per the MIL-A-12560K specifications. Following the Second World War, ballistic threats have become more penetrating and threatening to conventional armors. Ballistic threats have been developed to use hard steel, tungsten carbide,

and ceramic composite cores that are becoming increasingly destructive [39]. In addition, the military has been seeking alternatives to RHA with a reduced density in order to improve fuel efficiency and maneuverability. This push has led to the development and study of improved steel armors by increasing RHA's hardness [33].



Figure 1-13: Armored survivability kit (ASK) developed by the Army Research Lab (ARL), primarily made up of RHA, outfitted onto a HMMWV [22].

High Hardness and Ultra High Hardness Steel Armors

Monolithic metal armor alternatives to RHA have been studied for over half a decade [40], [41]. There have been a variety of modifications done to the processing of RHA that have yielded harder steel armors. High hardness armors (HHA) and ultra-high hardness (UHH) armor steel plates can provide improved protection against ballistic threats using hardened steel and tungsten carbide armor piercing (AP) cores. The standard for high hardness and ultra-high hardness steel plate armors are governed by MIL-DTL-46100E and MILDTL-32332

respectively [42], [43]. The hardened steel plates are manufactured through a similar quenching process with altered tempering to achieve a fine martensitic microstructure with improved hardness [44], [45]. The chemical compositions of HHA and UHH have a slightly higher carbon content requirement than both RHA with a weight percentage of 0.32 and 0.55 [42], [43]. The increase in carbon content and faster cooling rate creates a martensitic microstructure presented in Figure 1-14 [45]. The additional carbide precipitations and lower tempering temperatures lead to a much harder product.

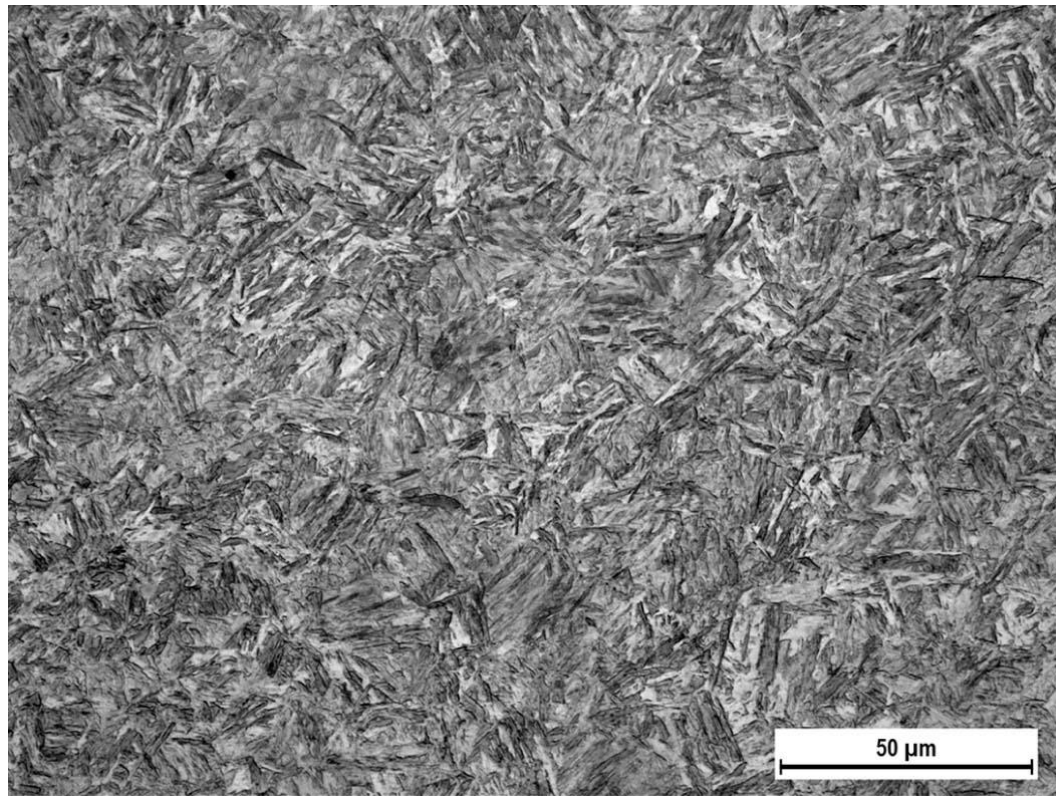


Figure 1-14: Microstructure of UHH showing the martensitic grain structure [45].

The standards require HHA's to have a Brinell hardness between HB 477-534 while UHH armors are required to be above HBW 570 (measured using a tungsten indenter) [42],

[43]. The use of UHH steel plates are still limited as appliqué armors due to their high hardness, limited weldability due to increased carbon content, and weaker structural properties when compared to RHA's and HHA's. The harder armors can allow for weight reduction by reducing the thickness required to stop incoming ballistic threats [24], [45]. Bisalloy's UHH plates tested against 7.62 mm (0.30 caliber) and 12.7 mm (0.50 caliber) AP rounds show much improvement over RHA and achieve the same level of protection with a 33% reduction in overall weight [45]. Yet, against deformable cores and non-AP projectiles, the RHA is more mass efficient due to the reduced piercing nature of the threat and lower hardness required to break down the incoming core. UHH steel armor plates require further processing and therefore are not as cost efficient as RHA but with further study can possibly be used for structural components and offer improved protection for personal armors and vehicles with a lower overall weight and thickness [46].

Aluminum

Recent research has focused on monolithic plate alternatives to homogeneous steel armors with a lower density. Aluminum alloys have a density that is approximately 1/3 that of steel armors ($2.7\text{-}2.8 \text{ g/cm}^3$) and can potentially be used to reduce the overall weight of personnel and vehicle armors [47]. Aluminum offers other advantages over RHA as it is widely manufactured for industrial use and can be processed in large quantities, has high specific strength, and is known for its good corrosion resistance. The use of aluminum as a lightweight armor structure was applied over a century ago in 1895 when Yarrow & Co built an aluminum torpedo boat [48]. The boat used an aluminum frame that was 25% thicker than its steel counterpart but weighed half as much [48]. The weight savings improved the speed of the torpedo boat without sacrificing structural integrity [48]. Aluminum has since been found to

perform well against large blasts loads, impacts by multiple threats, and fragments created from conventional and improvised explosive devices [47]. Recent advancements in alloying and production of aluminum alloys has made it a viable candidate for replacing RHA. Wrought aluminum alloys are separated into seven primary alloying classes depending on the principle alloying elements. The wrought aluminum alloy designations use a four digit number and are shown in Figure 1-15 along with the primary alloying element and their primary attributes [49].

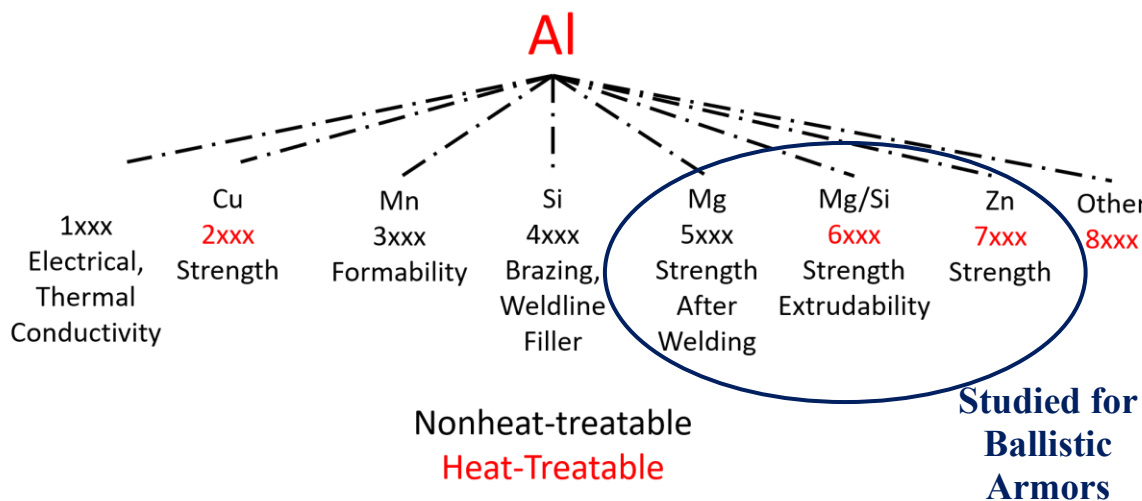


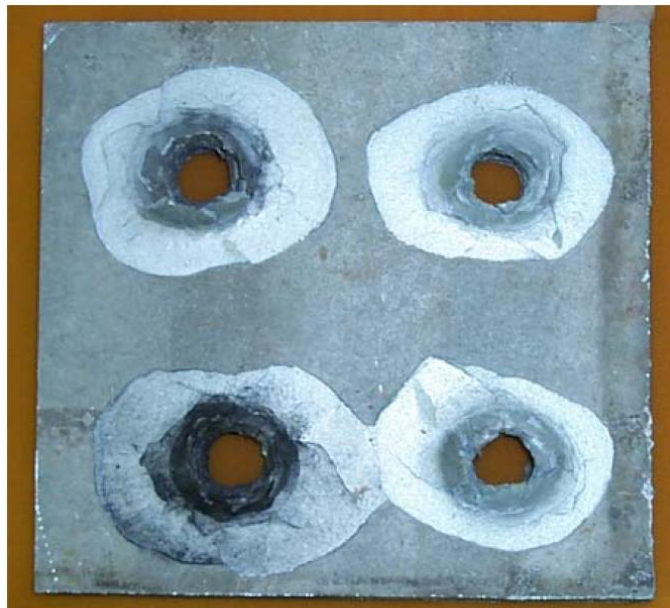
Figure 1-15: Wrought aluminum alloy designations and their primary alloying element. 5xxx, 6xxx, and 7xxx series alloys have been the focus of recent research of aluminum armors [49].

The current wrought aluminum alloy in use for US combat vehicles and aircrafts is an aluminum-magnesium alloy 5083 while alloy 5456 is used for naval applications [34], [47]. Both alloys are known for their weldability and strength following welding as well as improved corrosion resistance over most steels. The US military standards for aluminum armors were developed in the 1960's and have been used to compare various aluminum alloys for their weight savings and performance against various projectiles [47]. The armor grade 5083 and

5456 alloys get their strength over commercial grades by additional strain hardening through rolling and plate tempering [47]. The 5xxx series alloys though are limited in their performance in its wrought form, limiting its overall production and availability [47]. The 7xxx series aluminum alloys are potential improvements to the 5xxx series for their higher strength and hardness [47].

The 7xxx series aluminum alloys have a higher modulus, yield stress and ultimate tensile strength than the 5083 and 5456 armor alloys [47]. Various 7xxx series aluminum alloys are currently being tested to replace 7039 aluminum-zinc alloy, the only 7xxx series given a military specification [50], [51]. Børvik *et al.* have tested multiple aluminum alloys against ballistic impact with 7.62 mm AP core projectiles [52], [53]. The higher strength alloys offer improved ballistic protection but suffer from large backplate fragmentation and spalling. The additional spalling can be seen in Figure 1-16 where the 7039 plate shows large cracking at the back of the armor while the 5083 shows localized plugging with minimal back face spalling [47]. The 7xxx series alloys are also more susceptible to stress corrosion cracking than the 5083 or 5456 armors [47]. Heat treatment and validation of AA6070, AA7055 and other alloy variations followed in attempts to find an alternative solution to the high strength 7039 and 7075 alloys with reduce fragmentation risks from back face spalling [53], [54]. The heat treatment of wrought aluminum alloys is used to enhance the mechanical strength of the sample without drastically changing the crystal structure [55]. More recently, there has been interest in exploring spray formed AA7055. The spray forming process uses nitrogen to atomize aluminum melt and deposit the droplets onto a substrate to form a billet. The billet is hot formed to create a dense product and then quenched in water. Spray forming creates a refined microstructure with hard metastable intermetallic compounds, when compared to conventional

forming methods, due to the higher cooling rate involved in its processing [56]. The development of new high strength aluminum alloys for armor applications has been growing with areal densities almost half that required by the RHA equivalent. The aluminum alloy panels also require almost twice the thickness to stop impending AP rounds and cannot compete with current hardened steel armors at operating muzzle velocities [54].



Back of 50.8mm 7039 aluminum plate



Back of 50.8mm 5083 aluminum plate

Figure 1-16: Back face spalling comparing the aluminum alloy 7039 and 5083 armor plates impacted by the same round [47].

Magnesium

Magnesium alloys are similar to aluminum alloys as a possible weight saving material for ballistic armors. Magnesium is known for its high strength to density ratio and relatively

stable response to shock loading [57]. Magnesium alloy AZ31B has been tested against ballistic threats and compared to 5083-H131 aluminum armor and RHA. AZ31B has similar or greater specific strength values than the 5083-H131 when discussing the ultimate tensile strength, yield strength, and stiffness. The results show that the AZ31B has the ability to outperform the aluminum and steel alloys against lower caliber threats. For larger threats such as the 0.50 caliber APM2, the AZ31B has performance similar to RHA, but is 4.5 times thicker. RHA, in this case, is more desirable for vehicle applications as it has a lower total thickness with a similar areal density. Current magnesium alloys do however have poor corrosion resistance and formability where specific geometries are required. The initial testing of Mg alloys for ballistic armors seem promising and can spark interest in a field of a new armor class that currently has little data.

Titanium

Titanium alloys are another alternative to aluminum and magnesium alloy plates. A variety of titanium alloys make formidable replacements to RHA. Early testing of a dual hardness titanium armor alloy showed good protection against the 7.62 mm M2 AP threat [58]. The dual arrangement used two titanium alloys bonded together, one harder than the other, and was more effective than homogeneous titanium alloy armor. Titanium has a higher density than aluminum but is known for its high strength. One of the most popular grades of titanium is grade 5, also known as Ti6Al4V, which makes up 60% of all titanium alloys in production and is commonly used for titanium armor applications [59]. Titanium as a homogeneous armor offers a 15-35% weight savings over aluminum and RHA when tested against similar threats [60]. The Bradley Infantry Fighting Vehicle and Abrams Main Battle Tank have both accommodated titanium alloys into sections of its hatch and external armor [61]. Titanium,

although an efficient and effective armor material, is expensive to produce and machine. For this reason, using titanium as a bulk armor by itself is much too expensive when aluminum and RHA remain cheaper and widely available. More recently, work on titanium has been expanded due to advancements in metal production and the ability to pair titanium with lighter materials and harder surface coatings [62]. Titanium does have good compatibility with composites and is able to be used in layered armors, where a thin sheet is implemented, for cost effectiveness, to stop ballistic impacts.



M2 Bradley Fighting Vehicle



M1A2 Abrams Main Battle Tank

Figure 1-17: The M2 Bradley and M1A2 military vehicles that use titanium for protective armors in regions such as the commander's hatch and top armors [61].

1.4.2. Layered Composite Armors

Layered hard armors are an arrangement of a ceramic face plate with a composite or metal backing [63]–[65]. Layered armors have become more advantageous over standard monolithic metal or ceramic armors. The layered armors pair two or more materials together

in order to stop piercing rounds. The layers are made up of a disruptor and an absorbing material. A schematic of a layered armor and the impact stages of a bullet are shown in Figure 1-18. The disruptor is used to break down the impacting threat and redirect its energy by either turning the projectile or fracturing its components. The disruptor layer is usually made of a ceramic or high hardness steel. The absorber is placed behind the disruptor to absorb the kinetic energy of the projectile through large plastic deformation without allowing it to fully penetrate the armor. Armors with a metallic backing are heavier than those with a composite backing but are needed for protection from a wider variety of ballistic threats. Layered composite armors can defend against armor piercing threats and consist of a ceramic faceplate backed by a composite or metal panel. The composite backings are generally made with aramid fibers such as Kevlar™ [66], E- and S-glass composites [67], [68], and ultrahigh-molecular weight polyethylene fiber composites such as Dyneema™ [69]. The ceramic layer blunts the core of the projectile and spreads the load of the impact to a larger area, allowing the backplate to absorb the residual energy of the bullet. Ceramic faceplates are desirable for their low density and high hardness. In recent studies, ceramics such as aluminum oxide (Al_2O_3) [70], [71], silicon carbide (SiC) [69], [71], and boron carbide (B_4C) [72] have been effectively used as faceplates.

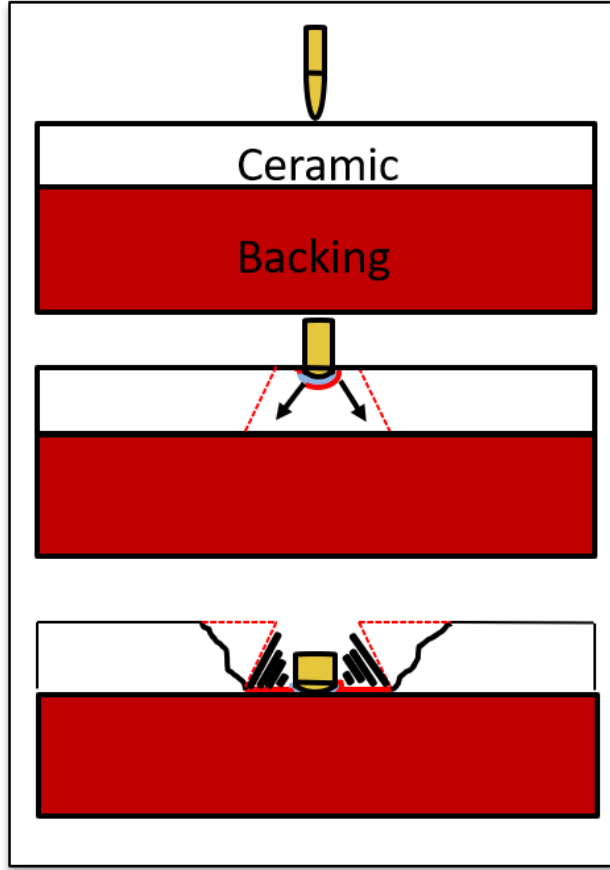


Figure 1-18: Impact stages of a ballistic threat into a layered armor showing how the ceramic erodes the bullet and its core and allows the backing plate to absorb the kinetic energy.

The ceramic layer has been tested as a single panel as well as configurations made up of smaller panels or cylinders [69]. Both geometries have been studied under a wide variety of ballistic threats and configurations. Layered armors have also been studied using metallic backing plates in combination with the composite panels [70]. The layered composite armors can be more effective than monolithic metal armor plates by pairing the high hardness of a ceramic with the ductility of composites and metals rather than relying on a single material for both properties. Layered hard armors can be made using advanced energy absorption materials, such as metal foams, for increased effectiveness and lightweight application for military personnel and vehicles.

CHAPTER 2: LITERATURE REVIEW OF COMPOSITE METAL FOAM

2.1. Metal Foams

In this section a literature review of metal foams and composite metal foam (CMF) is presented in order to fully understand their properties and various applications as well as their potential use in extreme environments [73]. The literature review of CMF included in this chapter can be found published elsewhere [73]. Metal foams are a relatively new class of materials that possess specific thermal, mechanical, acoustic, and electrical properties desirable in many engineering applications [74]–[78]. Metal foams are known for their high strength to density ratio, high specific stiffness, and greatly improved energy absorption capabilities compared to bulk materials [77]. Metal foams are defined by the inherent pores integrated into their metallic structure. They can be split into two primary categories: open and closed cell metal foams. Open cell metal foams are made up of an interconnected network of pores that are easily penetrable by air and other media. Closed cell metal foams are made up of pores that are sealed off from one another. Open and closed cell metal foams are manufactured using a variety of methods.

2.1.1. Manufacturing of Metal Foams

Open Cell Foams

Open cell foams can use placeholders to create porosities in a bulk metal. These placeholders are created by particles that can be washed out from the metal product, such as salt, or polymer preforms designed for use in investment casting. The investment casting method can be engineered to have a range of cell size and shape. Investment casting begins by creating a polymer preform that acts as a space holder and is designed with the desired ligament and cell size. The polymer is then placed in a mold and surrounded with a slurry that is used

to cast around the preform's shape. The polymer preform is then removed through a burnout phase that leaves behind the desired channels and negative space in the casing slurry that will make up the open-cell foam. The molten metal is added to the mold and additional pressure is used to ensure complete filling of the ligaments and overcome the metal's resistance to flow. After cooling, the casting slurry is removed and leaves behind a metal structure with the same shape as the starting polymer. An example of this process is ERG's DUOCEL open cell foam structure as presented in Figure 2-1 [77]. Open cell foams are therefore made up of an interconnected network of ligaments that allow gas and other media to easily pass through the open porosities. This differs from closed cell metal foam, where all of the porosities within the structure are closed off from one another.

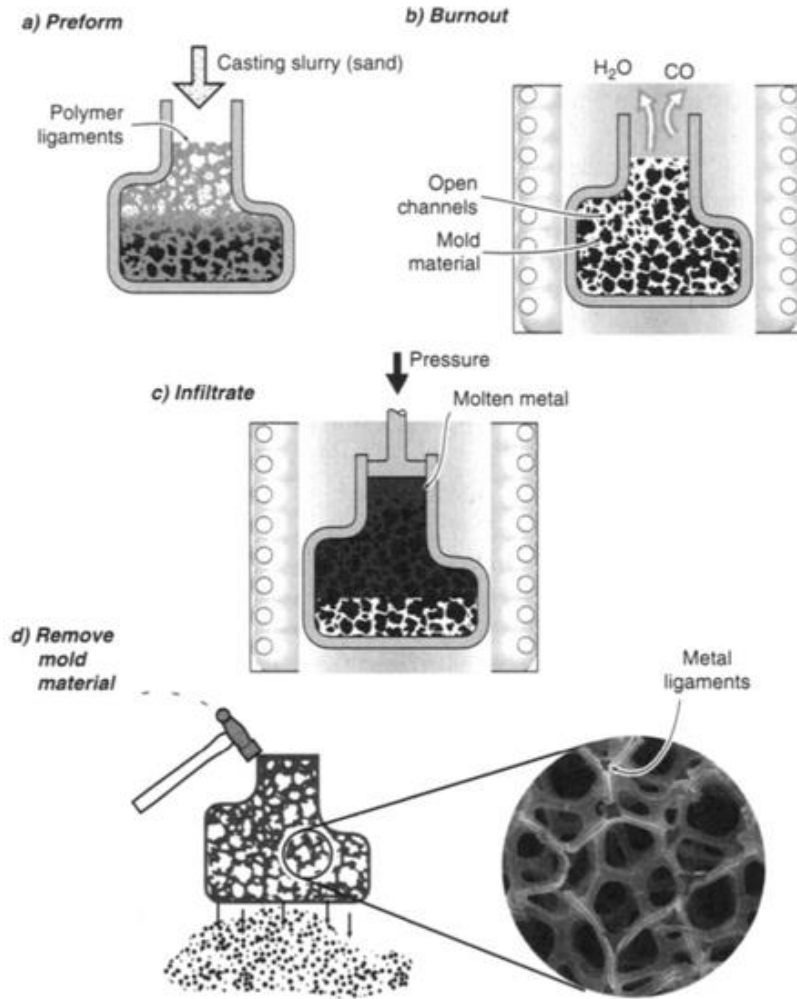


Figure 2-1: Processing method used to manufacture ERG's DUOCEL foam by investment casting [77].

Closed Cell Foams

Closed-cell foams have multiple methods of manufacturing that have become popular for creating sealed off porosities within a bulk metal. The porosities within closed-cell metal foams can be made by bubbling gas through a molten metal (aluminum is popularly used) and cooling the product in such a way to capture the bubbles [77]. In order to do this, gas is injected into a molten metal such as aluminum in a heated crucible. The bubbles float to the top of the melt surface and can be drained from the crucible creating the metal foam. The melt gas

injection process creates a product with variation in pore size ranging from 5 to 20 mm such as CYMAT aluminum metal foam. There are many other methods that can be used to make closed cell metal foam such as gas particle foaming and entrapped gas expansion [77]. These methods generally create products with varying cell size and organization. Though the initial particle size can be controlled, it is difficult to uniformly disperse foaming agents and gas expansion products in the aluminum melt. In order to improve on the random dispersion of porosities throughout the metal structure, metal foams such as hollow sphere foam have been manufactured with a consistent porosity size and shape [77]. Hollow sphere foams (HSFs) are made up of metal hollow spheres manufactured using a lost core technique. This method coats polystyrene spheres in a metal powder slurry and the core is burned off in secondary treatment. The spheres produced have a relatively consistent size, shape, and internal porosity using this process which can improve the metal foam's mechanical properties. Sectioned cuts of Alporas and hollow sphere foam are shown in Figure 2-2 [73].

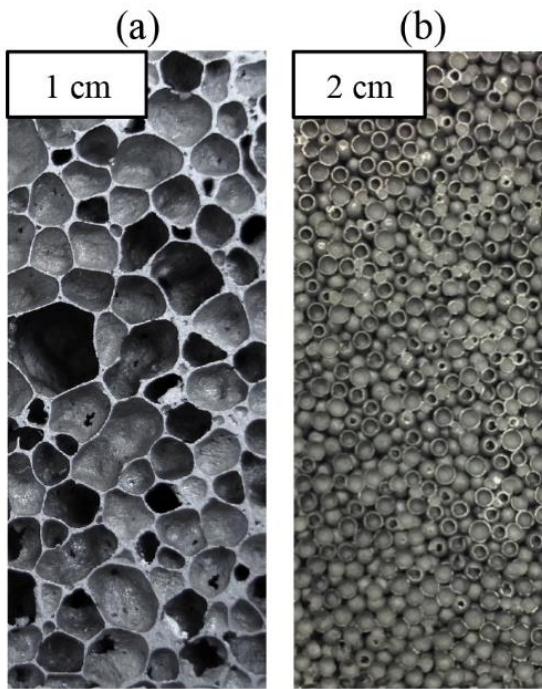


Figure 2-2: Digital images of the cut section of (a) closed-cell Alporas aluminum foam, (b) steel hollow sphere foam [73].

2.1.2. Properties of Metal Foams

Metal foams are able to deform at a relatively constant stress over a broad range of strain under compression as seen by the example stress-strain schematic in Figure 2-3(a). The metal foam experiences an elastic region following its Young's modulus (E) up to yield. Following yield, the cells within the metal foam deform at a constant stress, referred to as the plateau stress (σ_{pl}) until the pores collapse and the densification strain is reached (ε_D). Although useful throughout many engineering applications, metal foams lack consistent and promising performance due to their variation in cell size, similar to the Alporas sample in Figure 2-2(a) [79]–[81]. The non-uniform distribution of cells causes collapse bands to initialize in larger cells under loading [79]. The location and loads at which these collapse bands will form

becomes unpredictable in metal foams with variable cell structure [79], [80], [82]. In order to improve the strength of metal foams, alternate uniform cell structures have been considered.

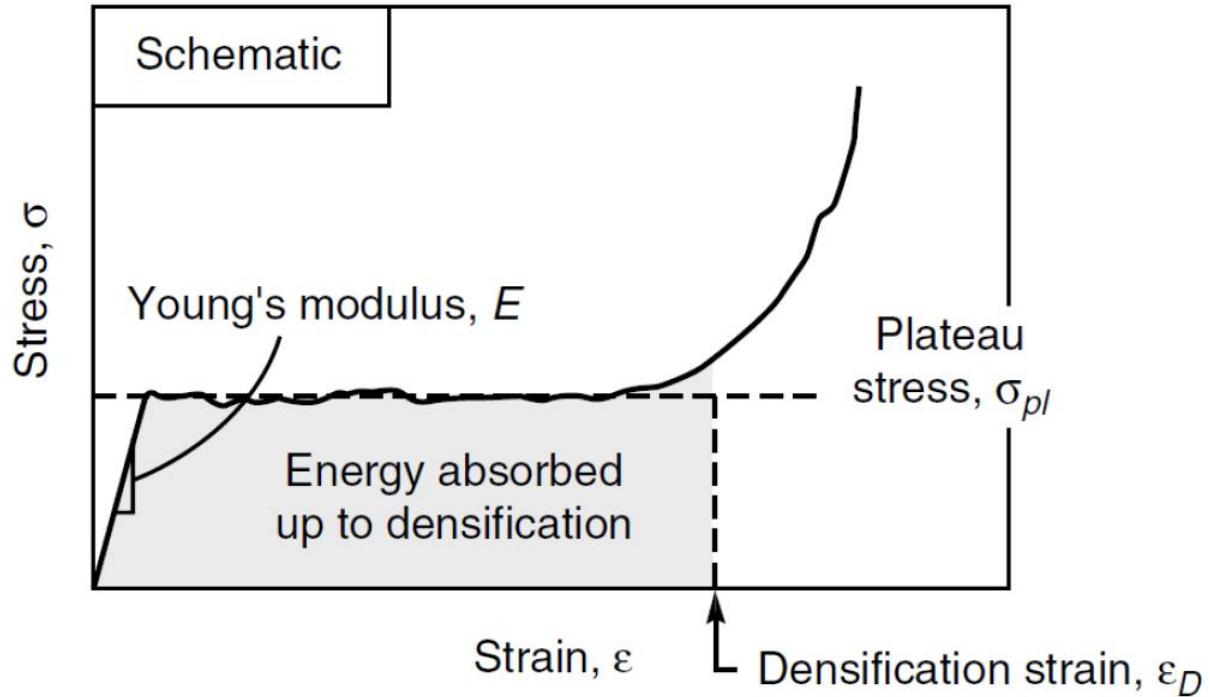


Figure 2-3: Schematic of the typical stress-strain curve of metal foams [77].

Uniform-cell metal foams, such as hollow sphere foam (HSF) shown in Figure 2-2(b), have been designed to increase the uniformity and isotropy of the foam in hopes of overcoming premature failure. Hollow sphere foams are manufactured by sintering hollow metal spheres together using a liquid binder to create a necked region connecting the spheres [83]. The produced HSF has relatively low strength due to the small contact area between the spheres. These randomly packed and sintered structures were found to behave more like open cell foams than closed cell foams with no major stiffness advantage gained [82]. Yet, the organized structure can be used to produce stronger products by filling the void between spheres.

Further research and discovery has led to the creation of composite metal foam (CMF) a closed cell metal foam with higher strength and uniformity than previously manufactured foams [84], [85]. The term composite metal foam refers to a class of metal foam made with hollow metal spheres surrounded by a metallic matrix [73]. Composite metal foam is not to be confused with or classified as syntactic foam; a foam made of non-metallic materials for their matrix or hollow spheres. Prior to the invention of composite metal foam with metallic spheres embedded in metallic matrix [84], [85], there have been some studies on the so called “syntactic foams” based on either polymeric matrix with ceramic hollow spheres, such as cenospheres and microballoons [86]–[88] or metallic matrix with ceramic microspheres [89]–[92]. While CMF has been the first of its kind made with both metallic matrix and metallic hollow spheres [84], [85], [93], some recent studies use different names, such as metal matrix syntactic foam [91], [92], to describe similar materials made with metallic hollow spheres embedded in metallic matrix. Composite metal foam is a novel class of material that is created by combining the benefits of metal matrix composites and metal foams.

2.2. Composite Metal Foams at a Glance

2.2.1. Preparation of CMF

Processing

Composite metal foam (CMF) is a class of metal foam with improved strength and energy absorption than other metal foams. CMF is created by surrounding a set of preform hollow metal spheres with a metallic matrix through casting [93]–[95] or powder metallurgy (PM) technique [96]. The metal matrix surrounds a random loose packing of hollow metal spheres, filling the interstitial spaces between hollow spheres, increasing the stability of the cell walls and structure as a whole. Casting of CMF is performed using gravity casting within

a mold, filling the interstitial space between spheres with a low melting point metal such as aluminum A356 creating an aluminum-steel (Al-S) CMF [93]. Other materials can also be used when casting CMF, as long as the two materials have distinctly different melting temperatures to ensure structural stability of the spheres during casting. The mold used for casting of Al-S CMF is made from steel. The spheres are vibrated within the cavity of the steel mold and molten aluminum is poured into the mold allowing gravity to fill the interstitial spacing between spheres. Aluminum Alloy A356 matrix material is generally used in combination with steel hollow spheres in casting Aluminum-Steel CMF (Al-S CMF) due to its good flow and castability creating a bulk product once cooled. Additional details on the processing steps and casting procedures are given in previous works and patents [84], [85], [93].

Powder metallurgy (PM) technique has also been used to create CMF. PM allows for the use of similar materials for both the spheres and matrix. Using similar metals for both matrix and spheres improves bonding and reduces defects at the interface and intermetallic formations. This technique has been used to create steel-steel (SS-CMF). The spheres are placed into a steel mold. The mold is placed on a vibration table to ensure dense packing of the spheres within the mold, similar to the casting process. The space between the spheres is then filled by a metal powder and vibrated to allow for complete filling of the mold's thickness. The mold is then completely sealed and placed inside a vacuum furnace or hot press for sintering of the metal powder. The mold is then heated to sinter the powder particles to each other and the exterior of the sphere walls, creating a bulk product. Further details of how PM technique is used to process CMF are given in previously published works [96]. Figure 2-4 shows cut sections of both cast and sintered composite metal foam side by side with a conventional metal foam and hollow sphere foam.

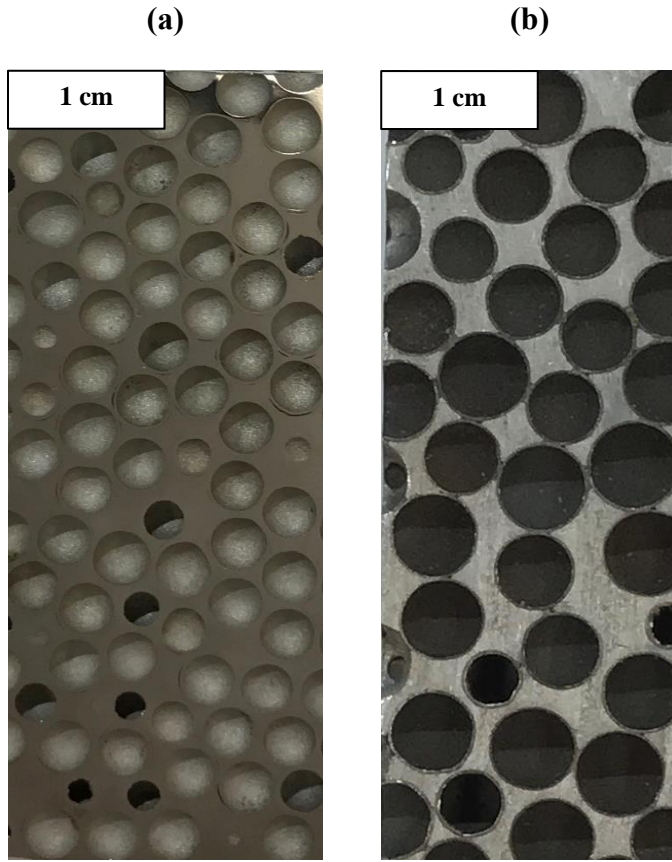


Figure 2-4: Digital images of the cut section of (a) sintered composite metal foam with 4mm steel spheres in steel matrix and (b) cast composite metal foam with 4mm steel spheres in an aluminum matrix [73].

The matrix in CMFs stabilizes the sphere's thin walls, blunts the crack growth in the material, and reduces buckling under loading, which will greatly increase the material's strength and energy absorption [94], [97]–[99]. CMF properties have been shown to vary with sphere size and wall thickness and can be tailored to specific applications [100].

Materials for Manufacturing Composite Metal Foam

The hollow metal spheres used to process composite metal foam are manufactured by Hollomet GmbH located in Dresden, Germany. The spheres are created using powder

metallurgy technique and come in a variety of outer diameters of 2, 4, and 6mm. The wall thickness of each sphere also varies with size but is approximately 5% of the outer diameter. The 316L stainless steel powder used in powder metallurgy processing is supplied by North American Höganäs High Alloys LLC and is sieved to a -325 mesh. The aluminum A356 casting alloy used in manufacturing Al-Steel CMF is supplied by TriAlCo Inc. Table 2-1 shows the elemental compositions of the materials used in creating CMF. The makeup of composite metal foam can also be defined by the volume fraction of sphere wall material, matrix, and air. Knowing that the sphere wall to outer sphere diameter stays relatively constant, the material percentage can be calculated first by relating the densities. These calculations show approximately 16% volume is sphere wall, 26% matrix and 58% air [96], [101], [102].

Table 2-1: Chemical compositions of spheres and matrix materials used in manufacturing close-cell CMFs (wt%) [73], [94], [103].

	Steel Spheres	316L Stainless steel matrix	Aluminum A356.2 matrix
C	0.71 ± 0.15	0.03	-
Mn	0.12 ± 0.04	2	0.28
Si	0.77 ± 0.40	1	7.01
Cr	16.85 ± 0.65	16.00-18.00	0.02
Ni	12.14 ± 0.55	10.00-14.00	-
Mo	2.25 ± 0.11	2.00-3.00	-
P	0.01	-	-
S	<0.003	-	-
Cu	0.04	-	0.11
Co	0.02	-	-
Fe	Balance	Balance	0.5
Mg	-	-	0.39
Ti	-	-	0.09
Zn	-	-	0.06
Al	-	-	Balance

2.2.2. Basic Properties of Composite Metal Foams

Basic Mechanical Properties

Initial studies of CMF from its date of invention yielded many of its basic properties. The material went through years of optimization and testing for all variations properties as a function of their sphere diameter, packing density, matrix and sphere wall porosities and voids for both Al-S and SS-CMF. In addition to sphere size, variations' in the matrix were also tested to optimize CMF performance. The explanation and effect of these variables on CMF can be found in previous works [93]–[101]. CMF has a very high plateau strength under compression when compared to other metal foams [99], as can be seen in the stress-strain curve in Figure 2-5 [95], [96], [104]–[106]. The stress-strain curve is plotted alongside bulk steel, aluminum, and other metal foams. The bulk metals have a much lower failure strain under compression when compared to the metal foam samples. The typical stress-strain curve of AL-S and SS-CMF samples can be seen plotted separately in Figure 2-6. The stress-strain curve of CMF under quasi-static loading shows behavior typical of an elastic-plastic foam under compression. Elastic-plastic foams undergo an initial linear elastic behavior followed by a plateau stress where the material experiences uniform deformation, until complete densification, at a relatively constant stress. Complete densification of CMFs occurs at approximately 60% strain for both Al-S and SS samples. The densification limit of CMF is related to its relative density and amount of air within the material. As the material is compressed and the air within the material is released, CMF acts as its bulk metal.

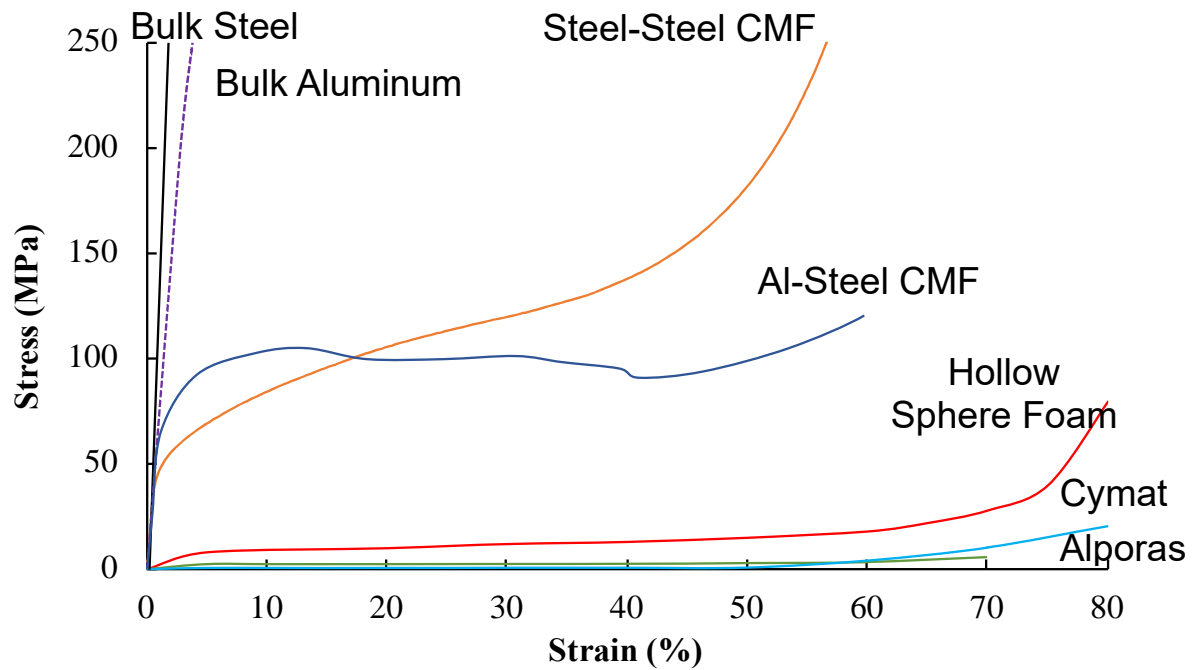


Figure 2-5: Quasi-static stress-strain curve for SS- CMF and Al-S CMF compared to other metal foams and bulk steel and aluminum [95], [96], [104]–[106].

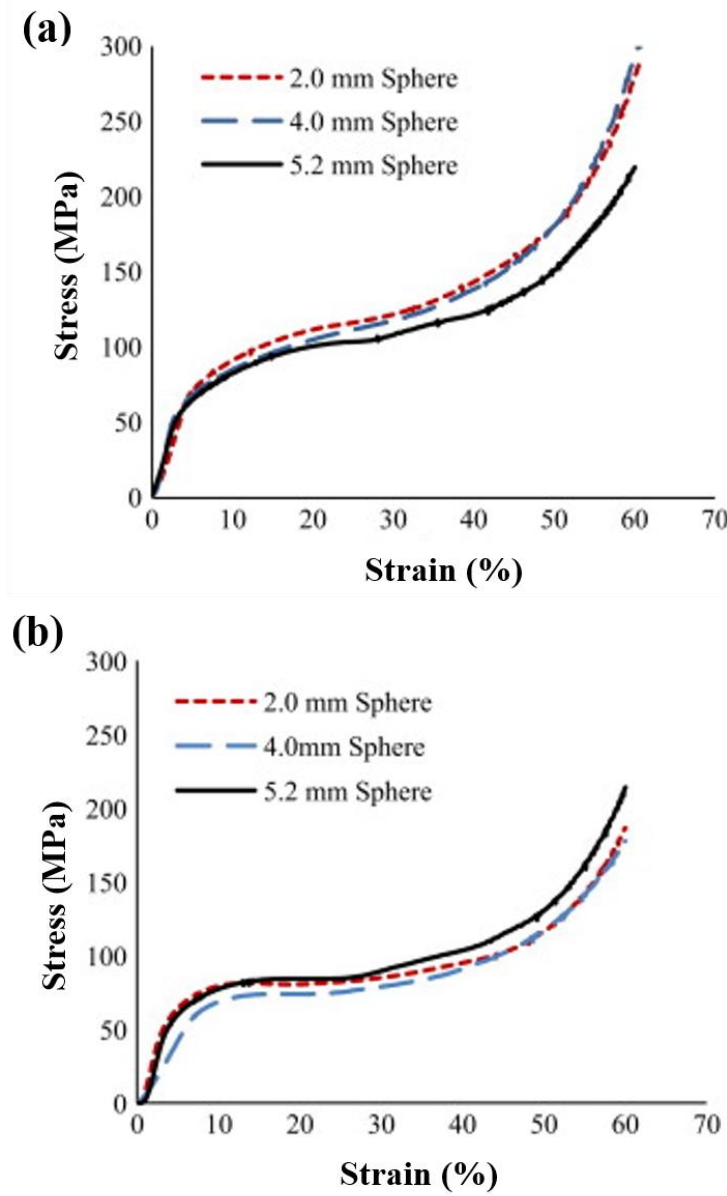


Figure 2-6: Typical engineering stress-strain curves for (a) SS-CMF and (b) Al-S CMF under quasi-static compression for different sphere sizes [107].

The mechanical properties of various metal foams are presented in Table 2-2. Al-S and SS-CMF both have an approximate relative density of 30-40%, as seen in Table 2-2. CMF's higher relative density compared to other metal foams is due to the presence of a matrix filling the space between hollow spheres. Under compression, the porosities within the matrix

collapse completely until the densification strain is reached and after that the CMF acts as its bulk material. The extraordinary high plateau strength of CMFs along with their high densification strain yields a higher energy absorption compared to other metal foams and even bulk metals as the area under the stress-strain curve increases over the broad strain range. CMF lends its higher strength and improved properties to the uniform cell structure that the hollow metal spheres provide. In addition, SS-CMF use the same material for both spheres and matrix that provides a strong bonding between constituents preventing any debonding and defects between the spheres and matrix. On the other hand, the presence of a ductile matrix between hollow spheres further improve the strength of the CMF and its resulted energy absorption. It is also notable that variation of sphere sizes has little to no effect on mechanical performance of CMFs. This is due to the fact that sphere diameter to its wall thickness ratio is maintained constant in all spheres, which leads to the same volume fraction of sphere material in all CMFs.

Table 2-2: Comparison of metal foams and their mechanical properties under quasi-static loading.

	CYMAT Al Foam [105]	Al Microsphere Foam [108]	Al-S CMF [95]	Closed Cell Al Foam [109]	Steel HSF [82]	SS- CMF [96]
Porosity Size/Sphere Outer Diameter (mm)	3	2-4	2,4,6 ...	1-3	2-3	2,4,6 ...
Density (g/cm ³)	0.4	0.8	1.8- 2.4	0.54	1.4	2.5- 3.5
Relative Density (%)	15	30	39	20.2	17.8	37.5

Table 2-2: (continued)

Plateau Stress (MPa)	5	10	80-120	7	23	100-150
Densification Strain (%)	68	55	57	65	60	54
Strength/Density Ratio (MPa/g*cm ⁻³)	12.5	12.5	44	13	16	41
Energy Absorbed at 50% strain (MJ/m ³)	2.6	4	40-50	3.75	13	55-70

Table 2-2 lists multiple properties of various types of aluminum and steel foams in comparison to CMF. The porosity/sphere size refers to the diameter of the openings within the foam either created through placeholders or foaming agents during production. This porosity size will affect the stiffness of the material and influence the failure of the foam. The referenced metal foams listed in the table have similar sizing of porosities but differ in density and strength. Composite metal foam is the densest metal foam listed, but also the strongest. The strength to density ratio of CMF is almost 3 times larger than the other metal foams.

Cyclic Loading

Metal foams are known for collapsing under cyclic loading as strain accumulates within the weaker walls of large cells until rapid failure occurs [110]. This rapid failure leads to large jumps in the strain versus the number of cycles [79]. The strain jump coincides with the formation of collapse bands, as larger cells buckle and lead to large deformations. Composite metal foam, on the other hand, has a fairly flat plateau under cyclic loading without rapid spikes

or jumps as it deforms homogeneously throughout the structure without the formation of collapse bands [101]. The uniform cell structure and consistent cell size in CMF along with the presence of ductile matrix between the spheres eliminates localized failure seen in other metal foams where larger cells initiate buckling and lead to collapse band formation.

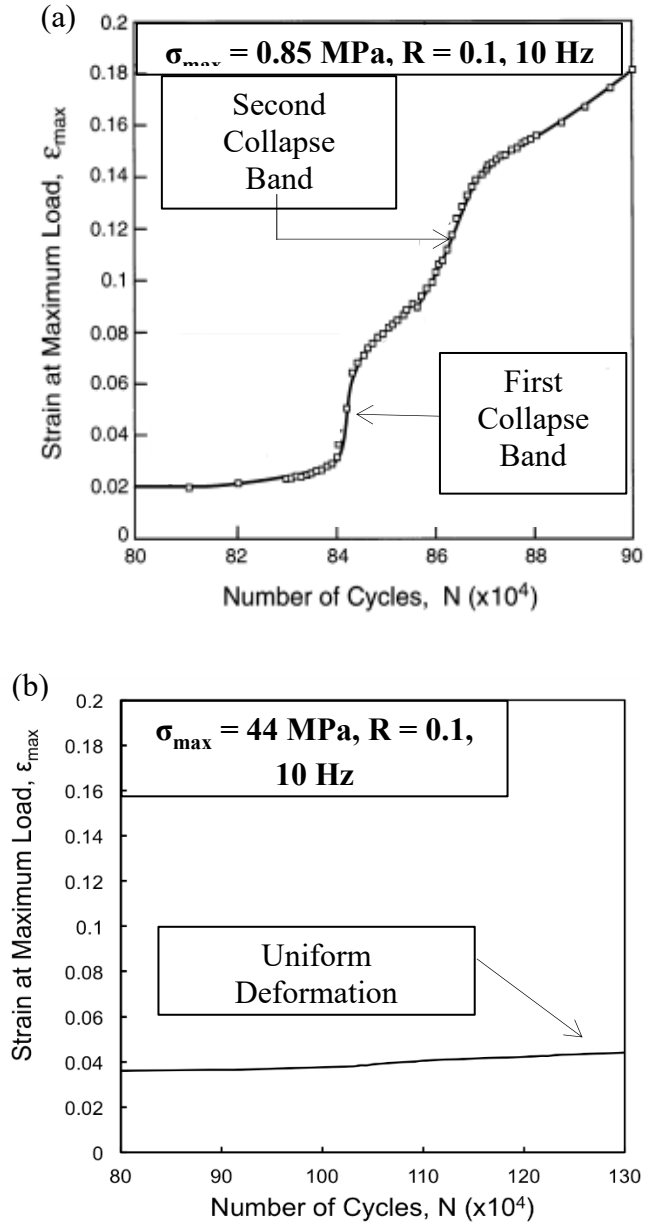


Figure 2-7: Fatigue graphs of (a) ALPORAS aluminum metal foam showing the multiple stages of its collapse [79] and (b) Al-S CMF [73].

Moreover, CMF is able to survive much higher maximum stresses with much lower maximum strains (about one fifth the amount) and deform uniformly through more cycles than other metal foams. This behavior is attributed to the uniform deformation of CMFs during compression resulting from their uniform cell structure as well as the support from the matrix.

The multiple stage failure of conventional aluminum foam is seen in Figure 2-7(a) [79], while the uniform deformation of CMF under higher maximum stress (almost fifty times larger) at a higher number of cycles is shown in Figure 2-7(b) [73]. Figure 2-8 compares the maximum cyclic stress versus maximum strain relation of CMFs and Alporas aluminum foam at one million cycles [73], [111]. In addition to the uniform deformation through fatigue, CMF also has lower strains at higher maximum cyclic stress through the same number of cycles. It was found that the Al-S CMF has slower crack growth as it has a more ductile matrix than the SS-CMF samples. This extends the fatigue life of the samples at stresses up to 75% of the materials plateau stress [112]. When compared to conventional aluminum metal foams such as Alporas, the lifetime of CMFs is longer and does not have multiple bands collapsing consecutively. It was found that in order to induce fatigue strain on Al-S CMF, the maximum induced stress had to be above 65% the plateau stress [112]. The deformation induced by cyclic loading of Al-S and SS-CMF samples can be seen in Figure 2-9. Local deformation occurs all over the samples, and although small, no complete collapse bands are formed through the material. The loading stress for comparable metal foams is much lower than the induced stress for CMF samples, yet CMF has a much longer lifetime.

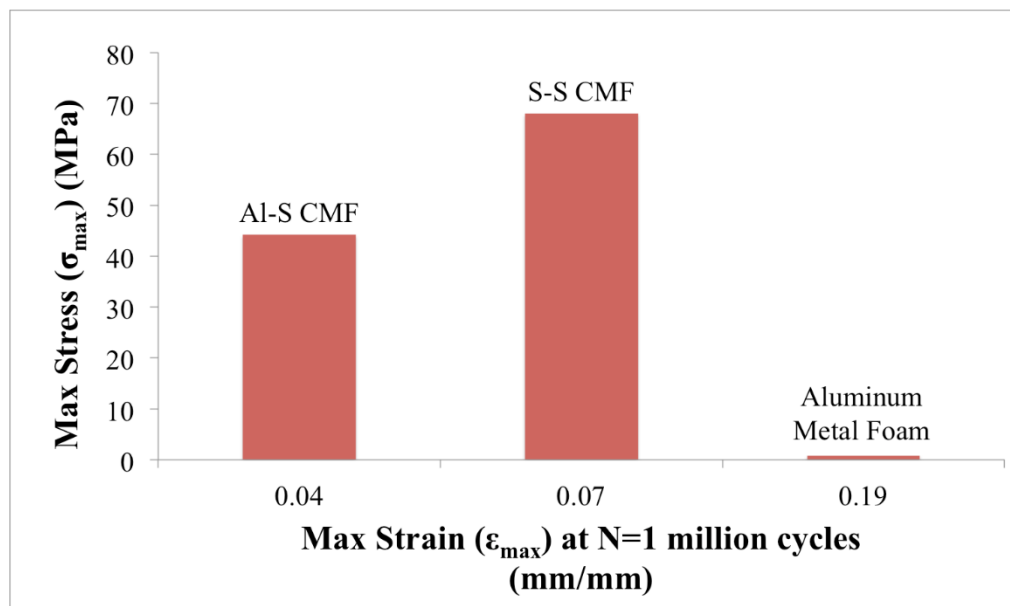


Figure 2-8: Maximum strain and stress for cyclic loading of Al-S CMF, SS-CMF and aluminum metal foam at one million cycles ($N=10^6$) [73], [111].

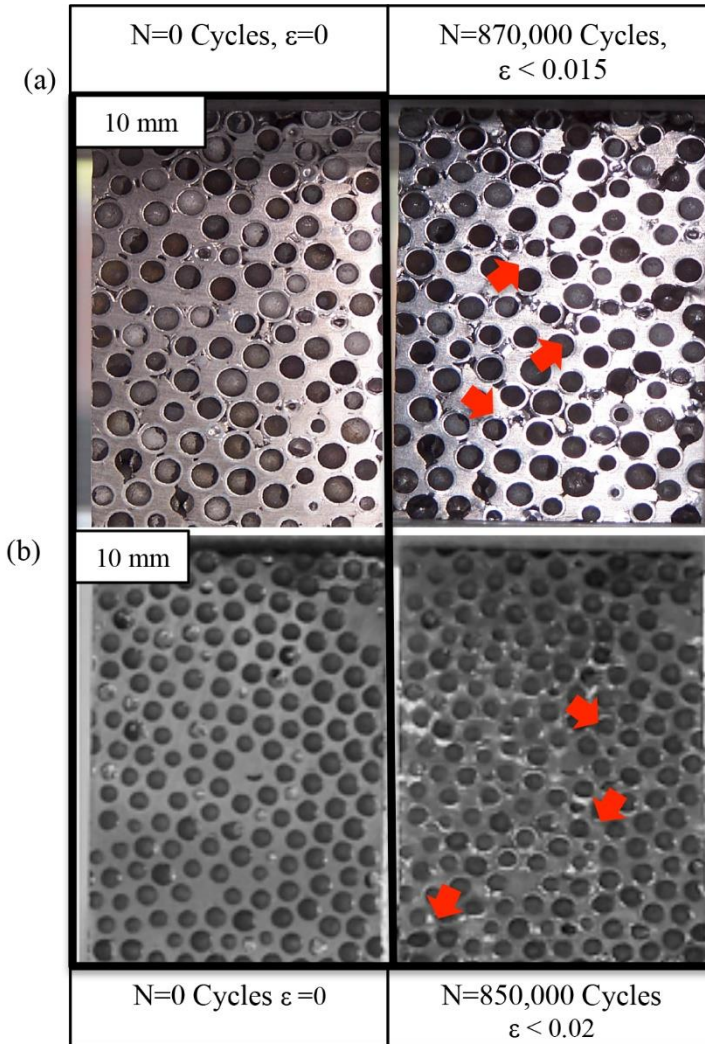


Figure 2-9: Sequential digital imaging of CMF sample under fatigue deformation made of (a) Al-S deformed at 65% of its plateau strength and (b) SS-CMF deformed at 50% of its plateau strength [112].

Microstructural Characterization of CMFs

Scanning Electron Microscopy (SEM) and Energy Dispersive X-ray Spectroscopy (EDS) have been used to characterize and analyze the presence and distribution of all phases in the micro-structure of composite metal foam. SEM imaging of Al-S CMF samples reveal an intermetallic phase present within the matrix surrounding the spheres, as can be seen in Figure 2-10. Iron diffuses into the aluminum matrix and creates brittle β -AlFeSi plates surrounding

the steel spheres. Needle-like α -AlFeSi is also formed in the presence of manganese and silicon found in the aluminum A356 throughout the matrix. These brittle phases in the matrix lead to the debonding of some spheres from the matrix of the Al-S CMF under loading [94], [101]. In addition to the mixed phases, there exist cavities between spheres where the aluminum matrix does not fully penetrate in between spheres and the aluminum melt solidifies along the sphere wall prior to complete flow through the cavity.

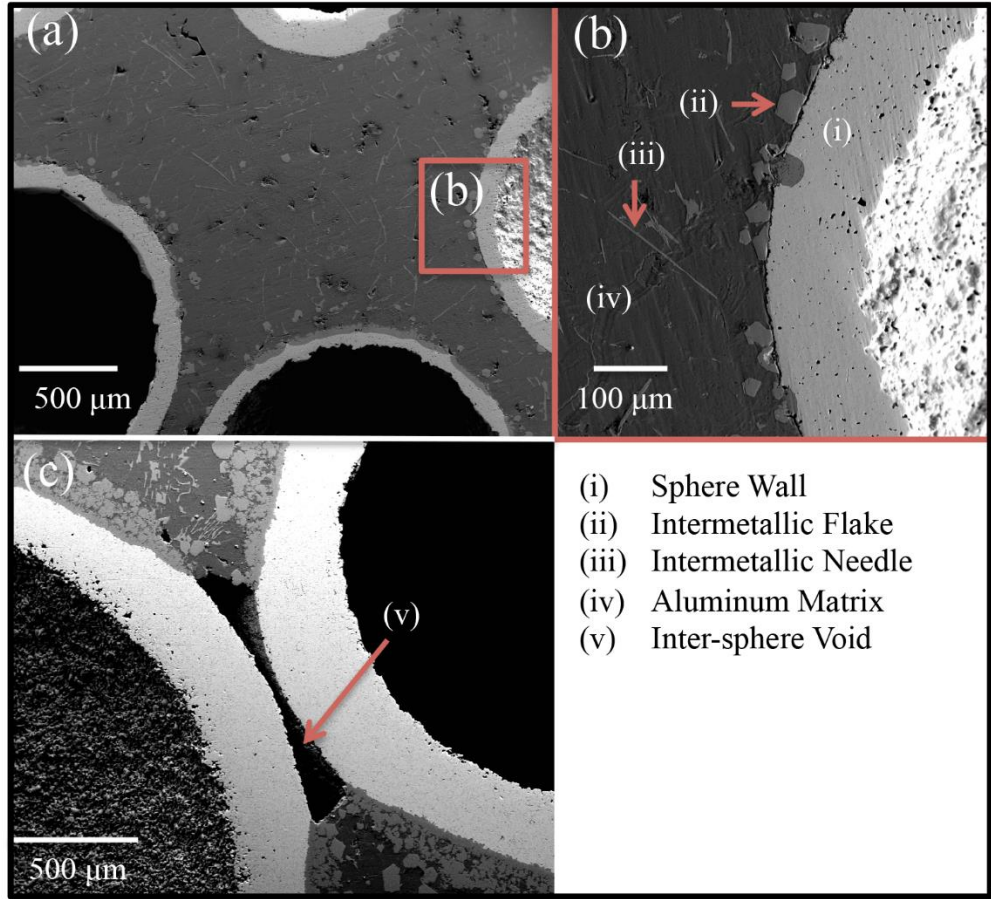


Figure 2-10: SEM imaging of Al-S CMF (a) with four spheres surrounded by matrix and other various phases and (b) a zoom in of the sphere wall-matrix interface and intermetallic precipitations as well as the (c) voids left between spheres [98].

SS-CMF, as previously discussed, is manufactured using powder metallurgy technique. The stainless steel metal powder used in sintering creates a continuous matrix with small micro-porosities spread throughout. These types of micro-porosities are common with sintered metal products and leave small voids between sintered particles [96]. The steel matrix is stronger than the aluminum, making a stronger resultant composite metal foam. SEM images of the micro-porosities within the sintered matrix of CMF can be seen in Figure 2-11 in addition to the porosities within the sphere wall itself.

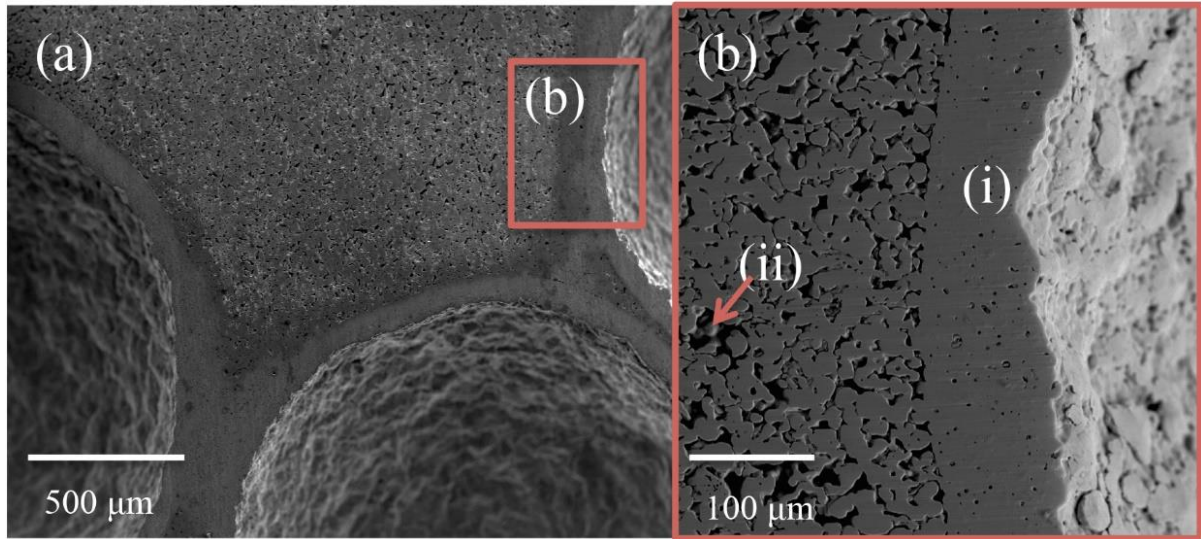


Figure 2-11: (a) SEM imaging of SS-CMF with three spheres on the bottom and sides and the (b) zoomed in area near one sphere showing the (i) sphere wall, and (ii) micro-porosities within matrix [73].

2.3. Established Properties of Composite Metal Foam under Extreme Environments

2.3.1. Radiation Shielding Properties of CMFs

Aside from CMF's specific mechanical traits, it also has other useful physical traits that can be implemented for specific engineering applications. Recent nuclear accidents and reactor

developments have pushed research towards developing novel advanced materials with improved radiation shielding and mechanical performance under accident and operating conditions [113]–[115]. Composite metal foams made from heavy metals such as iron, tungsten, and vanadium can offer reliable radiation shielding, but with the advantage of low density and great mechanical properties. The lower density and high effective atomic number (Z_{eff}) of CMF's components make them a viable candidate for nuclear shielding applications. Materials with a higher atomic number increase the chance of interaction with multiple forms of radiation. CMFs made of steel-steel, aluminum-steel, and a T15 high-speed steel-steel have been tested under X-ray, gamma, and neutron irradiation [113]–[115]. These tests represent the types of radiation that materials used in nuclear waste casks, reactor walls, and radiation medical facilities undergo. Gamma radiation is one of the most prominent forms of radiation from low-level nuclear waste [116]. Neutron radiation occurs primarily within reactor cores and from long-lived isotopes in nuclear waste, while x-rays are primarily seen within the medical facilities for imaging. The samples used were made with equal areal densities to directly compare their shielding capabilities while maintaining a constant shield weight. The shielding properties of CMF exceed that of conventional metals and offer the ability for further advancement and exploration of their use in the field.

The samples analyzed in the radiation testing were:

1. 316 SS-CMF
2. Al-S CMF
3. T15-316 SS-CMF
4. Aluminum A356
5. Lead

The T-15-316 SS-CMF is made from a mixture of high speed T15 steel and 316L steel powder when manufacturing CMF using powder metallurgy technique and is referred to as high-Z SS-CMF (HZ SS-CMF). This mixture of alloys introduces vanadium and tungsten into the material, both with a relatively high Z (atomic number) increasing the probability of interaction and absorption with different forms of radiation while not affecting the material's density nor its physical properties [115].

Gamma Ray Shielding of CMFs

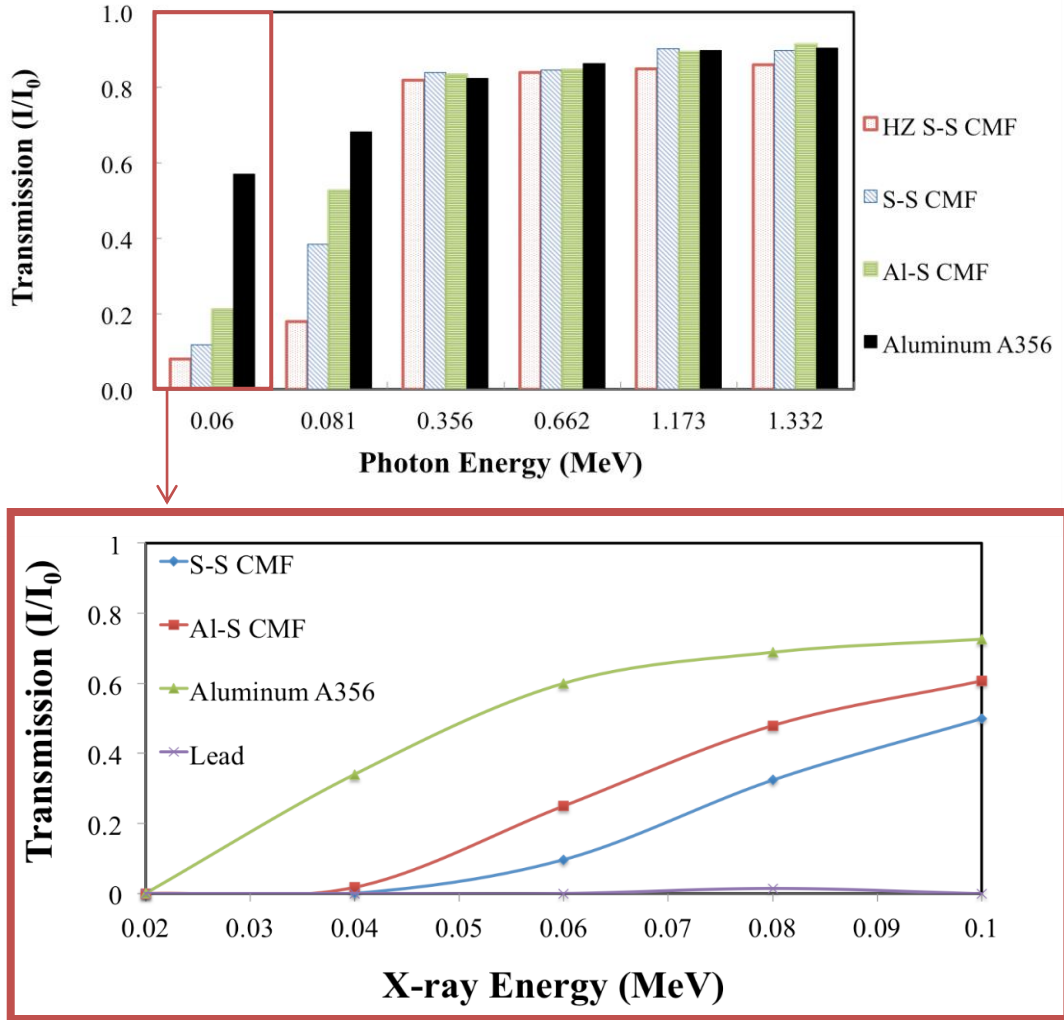


Figure 2-12: (a) Gamma-ray transmission as a function of photon energy for both Al-S and SS-CMF in addition to HZ SS-CMF and aluminum A356 sample all with an areal density of 2 g/cm^2 . (b) X-ray transmission of samples tested with lead and aluminum as bulk control materials [73], [117].

Gamma ray testing was completed using multiple sources that emitted photons at different energy levels. The sources used are listed in Table 2-3 along with their corresponding strength and photon energy levels. The variation in photon energies shows the effectiveness of

competing nuclear interactions. At high energy levels, the measured mass attenuation of the samples is similar throughout. Yet, at low energy levels the $Z_{\text{effective}}$ of the material increases the likelihood of photoelectric absorption dominating the interactions. This occurs due to the increase of electron-photon interactions and more photons are emitted with energies closer to the binding energy of the electrons. At these lower energies, a large difference can be seen between the mass attenuation coefficients of CMF samples and aluminum A356 despite their similar densities. As expected, the HZ SS-CMF has improved gamma ray shielding properties due to its increased Z_{eff} . The data collected can be presented by graphing the transmission of the materials over a range of energies of specific types of radiation. I_0 is the original intensity of the beam arriving at the surface of the sample and I is the transmitted beam measured after passing through the thickness of the sample. As a result, the transmission, I/I_0 , is an indication of the shielding efficiency of the material. Figure 2-12(a) shows the transmission of gamma radiation over a range of energies through CMF samples and bulk control material. Note that the lower the transmission value, the better the material is at shielding that type of radiation. Gamma shielding of CMFs was modeled using XCOM code. The model returned a theoretical mass attenuation coefficient with good agreement to experimentally obtained results for all CMF samples [115].

Table 2-3: Sources used in gamma radiation shielding test and their equivalent photon energies [113].

Source	^{60}Co	^{137}Cs	^{133}Ba	^{241}Am
Photon Energies	1.332 MeV 1.173 MeV	0.662 MeV	0.356 MeV 0.081 MeV	0.060 MeV

X-Ray Shielding of CMF

X-rays are photons of a specific wavelength used for their penetrating abilities in imaging. The x-ray shielding efficiency of CMFs was measured using a high-resolution micro-computed tomography (micro CT) system and compared to aluminum A356 and lead. The transmission of x-rays can be determined by measuring the gray value of the images from the exposed material indicating how much of the incident beam penetrates the given thickness. In previous works the grey value was analyzed, [115] here the transmission values are presented as a function of the x-ray's incident energy shown in Figure 2-12(b). The results show improved x-ray shielding of CMF when compared to aluminum A356. The HZ SS-CMF shows further improved x-ray shielding compared to aluminum, Al-S, and SS-CMF primarily due to the presence of heavy elements such as tungsten, vanadium, and iron. The results for x-ray transmission of the samples were also modeled using XCOM to calculate a mass attenuation coefficient. The calculated results showed a good agreement with experimental findings while the slight variation was attributed to multiple scatters and the non-homogeneous structure of CMFs [115].

Neutron Shielding of CMF

Neutron transmission of CMF was measured using the Neutron Powder Diffractometer beam created from the 1.0MW PULSTAR reactor at North Carolina State University [115]. The reactor beam intensity measured at the guide aperture was 0.64×10^5 n/cm²/s. The intensity of the beam is less than what would be experienced within a reactor core but is useful for testing the radiation shielding efficiency of materials without submerging them into an operating reactor. The background intensity and transmitted intensity were measured for each individual sample to obtain consistent measurements. Figure 2-13 shows the HZ SS-CMF has

the best shielding capacity for neutron radiation than the other manufactured CMFs. All of the samples tested are better at shielding than bulk aluminum A356 of a similar areal density. This is primarily due to the specific geometric form of CMF and its inclusion of air and higher Z elements within the matrix. The trend of improved shielding shown in Figure 2-13 opens up room for more studies to further the shielding capabilities of CMFs.

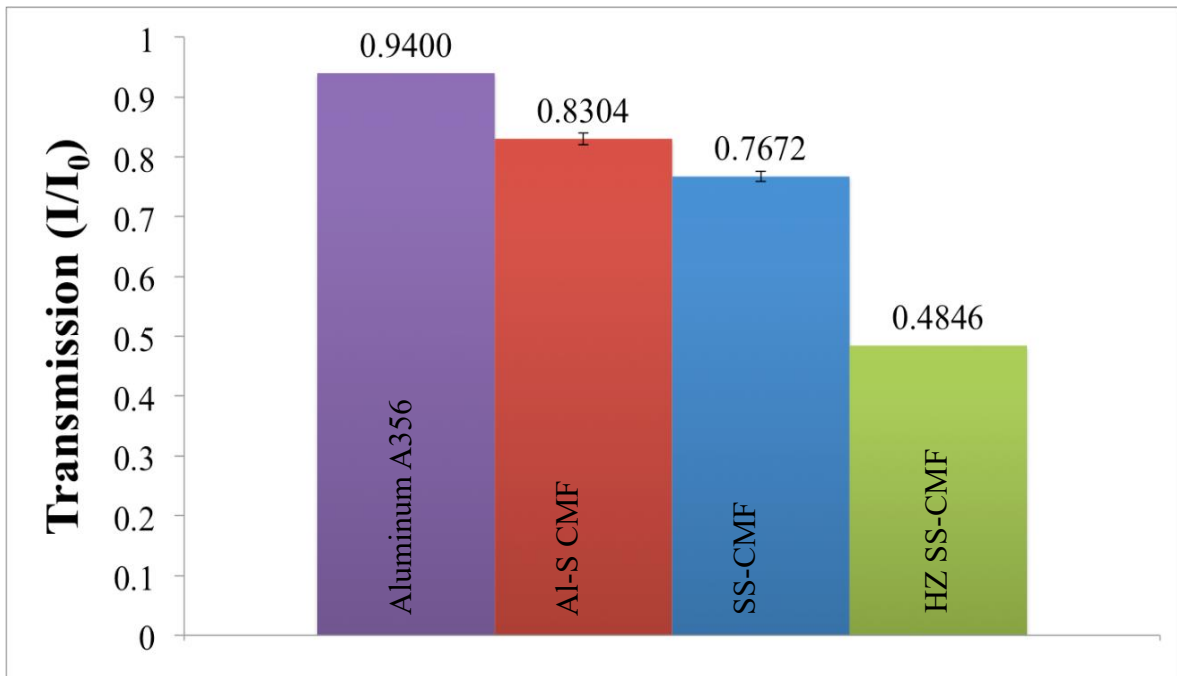


Figure 2-13: Transmission of neutrons on tested samples at a constant areal density of 2 g/cm² with error bars indicating the variations between samples of different sphere sizes [73], [117].

2.3.2. Thermal Properties of CMFs

Metal foams have been known to make efficient and effective heat sinks due to their large surface area resulted from the presence of porosities [118]. The thermal characterization of CMFs including their specific heat, effective thermal conductivity (ETC), and coefficient of

thermal expansion (CTE) have been studied [102]. The results of this study can be found in Table 2-4. The effective thermal conductivity measurements of steel-steel composite metal foam showed a reduction in heat transfer compared to bulk stainless steel. The air trapped within the spheres randomly dispersed through the matrix insulates against heat and provides increased thermal protection. These randomly packed pockets of air within the matrix help disrupt flow of heat through the material that can be seen in bulk stainless steel samples. This effect of porosities and their insulation can be used in many high temperature applications and heat shielding, creating a safer and lighter option than what is currently used in the field.

The measured specific heat of both Al-S and SS-CMF has a lower value than bulk aluminum at room temperature due to the existence of the steel spheres in the material. This type of measurement was done using shavings of the matrix and sphere material, not taking into account the effect of the sphere spacing and CMF specific geometry which aids in its thermal properties [102].

Thermal conductivity was also measured to determine to what extent the porosities increased the materials insulation properties. The thermal conductivity of CMF showed much lower values for both Al-S and SS-CMF than their bulk counterparts due to the air trapped inside the material, acting as an efficient thermal insulator. In addition to a reduction in thermal conductivity, the property remains stable between multiple sphere sizes as long as the sphere wall to diameter ratio remains constant [102]. In addition, the SS-CMF samples have little variation in their thermal conductivity across a broad temperature range, making it a practical material for application and reliable under accident conditions.

Coefficient of thermal expansion (CTE) was measured on SS-CMF samples over a temperature range of 0-400°C. The thermal induced strain in CMF was found to be linear over

the given temperature range, correlating to a constant CTE. CMF not only has a stable CTE across a broad range of temperatures, but it also has a CTE much lower than bulk stainless steel. Under rising temperatures, CMF has limited expansion and is less likely to fail due to thermal stresses and maintains a constant, predictable expansion rate. The stable CTE is attributed to both the micro and macro porosities spread throughout the matrix and the spheres. The porosities accommodate local thermal expansion, which reduces the amount of strain experienced by the material as a whole. The experimental results of specific heat, thermal conductivity, and CTE were all verified using analytical models and ensured the reliability of the findings [102].

In order to obtain a better understanding of the material's overall performance to extreme heating conditions, a flame test was conducted and modeled using FEA. The flame test was performed using propane fuel with an average flame temperature of approximately 800°C at the sample surface. This test provides insight to the stability of composite metal foams when exposed to extreme temperatures. An open flame is placed at the bottom surface of 2.5 cm thick SS-CMF sample, and an IR camera is used to capture the temperature gradient through the thickness for 30 minutes of exposing CMF to 800°C. A 304L stainless steel block cut to the same thickness as the CMF was also tested to compare the time it takes for each material to reach thermal equilibrium. Further detail of the experimental procedures can be found in the published work [102]. The air trapped within the spheres abates the spread of heat through CMF, as air's thermal conductivity is much lower than metals. When compared to 316L stainless steel at 500°C, air has a thermal conductivity of 0.051 W/m°C while 316L steel is 15.2 W/m°C [102] as seen in Table 2-4. Figure 2-14 graphs the temperature rise at the opposite side of the samples. The CMF takes twice as much time to reach equilibrium.

Table 2-4: Experimental results of thermal testing of CMF and comparable bulk materials [102].

Material	Specific Heat (J/g-°C)	Thermal Conductivity (W/m-°C) @500°C	Coefficient of Thermal Expansion (°C ⁻¹)
4 mm Al-S CMF	0.790	30.3	-
4 mm SS-CMF	0.551	5.0	3.00E-6
Aluminum A356	0.963	210	21.4E-6
316L SS	0.50	15.2	10.0 E-6
Air	1	0.051	3.4E-3

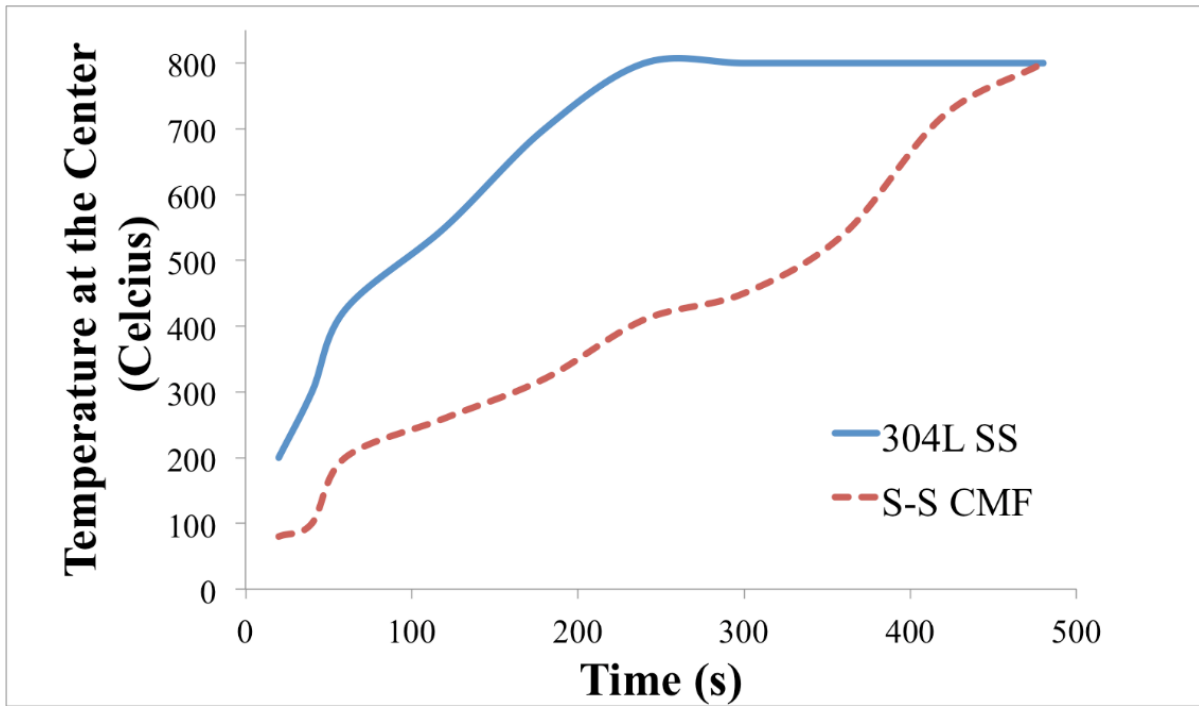


Figure 2-14: Temperature evolution at the opposite surface of SS-CMF and 304L SS samples during experimental flame test [73], [102].

The experimental findings of the flame test were verified using FEA modeling to replicate the flame test. The model shows the flow of heat through CMF and the temperature evolution. The model was completed using ANSYS Workbench and compared CMF to bulk stainless steel under the same conditions. The CMF model was made using the same packing geometry described earlier and also assumed perfect bonding between sphere walls and matrix. A constant heat source was applied to the base of the blocks in the model and heated the material until equilibrium was reached. The CMF has a slower temperature evolution than the 304L stainless steel lending to the air trapped within the spheres acting as an insulator.

2.3.3. **High Strain Rate Impact and Energy Absorption**

Split Hopkinson Pressure Bar

The first studies of composite metal foams showed its ability to maintain a relatively uniform plateau stress over large amounts of strain under quasi-static compression [94], [101]. This behavior offers higher strength under quasi-static and cyclic loading when compared to other metal foams due to the regularity of CMF's structure, uniform deformation under compression, and the presence of a matrix between the porosities. Further studies of composite metal foam showed an increase in performance under higher loading rates [119]. The increase in strain rate showed a rise in the yield and plateau strength of the material. In addition, initial studies found the energy absorption of SS-CMF under dynamic loading rates increased up to 30% [119]. The tests were done using a Split Hopkinson Pressure Bar (SHPB) apparatus that loaded the samples at varying speeds and recorded the stress-strain relationship. The results showed that the initial strengthening occurred at lower strains and the increase was independent of sphere size. All samples showed a rise in energy absorption under the increased loading

rates. In order to study the performance of CMF at high strain rates, a set of direct impact tests were used. The findings of the study are shown in Table 2-5.

Table 2-5: CMF samples subjected to dynamic loading for varying sphere sizes and strain rates [107].

	Strain Rate	Yield Strength (MPa)	Energy Absorption Normalized with Respect to Quasi-Static
2mm SS-CMF	Quasi-Static	100	1
	1523 1/s	160	1.09
	2629 1/s	175	1.26
	3728 1/s	230	1.33
2mm Al-S CMF	Quasi-Static	75	1
	1465 1/s	115	1.05
	1780 1/s	120	1.05

This data laid promising groundwork to use composite metal foams in crash management systems to mitigate and absorb impact energies. Further high strain rate studies using direct impact experiments revealed the strain rate sensitivity for both Al-S and SS-CMFs. The failure of CMFs under dynamic loading was analyzed to determine the mechanism by which the strengthening of the material under higher loading rates occurs. Post analysis of the experiments showed two types of crack propagation in the samples [107]. The first crack type (type I), shown in quasi-static loading, are related to the channels created within the matrix. Type II cracks form about the sphere walls, showing a bursting behavior of the spheres. Under quasi-static compression, the air trapped inside the spheres is compressed and pressurized, resisting further deformation. The reaction creates channels within the matrix to allow the escape of the air. However, during dynamic loading the spheres are rapidly compressed creating a fast increase in their internal pressure leading them to burst about the sphere wall,

giving the material a greater resistance to compression. This resistance continues until 30% strain, at which the majority of the spheres will burst and the samples strength converges to that of one under quasi-static loading [107]. The strengthening that CMF undergoes at higher strain rates was not found to have an upper limit under initial testing. The backpressure caused by the spheres increases the bulk materials strength and energy absorption capabilities drastically. Figure 2-15 shows the products of both Al-S and SS-CMF after being tested under quasi-static and dynamic loading up to 112 meters per second. Both samples show the benefits of CMF's uniform deformation, even at elevated loading rates. There are many parameters affecting the strain rate sensitivity of CMFs, including the strain rate sensitivity of the parent material, micro-inertia effects, shockwave propagation, and air trapped inside porosities. The effect of each parameter is investigated numerically in order to find the most important factor affecting the high strain rate sensitivity of CMFs.

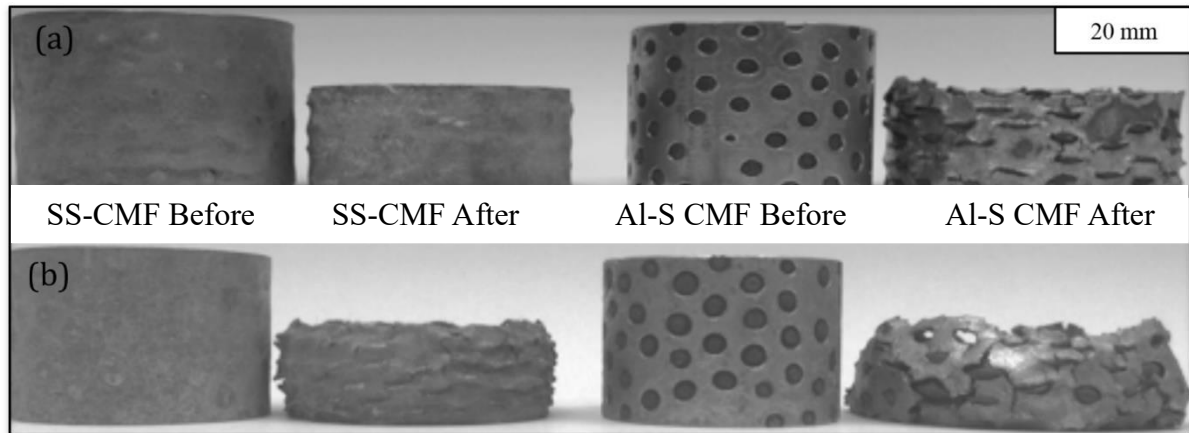


Figure 2-15: Compression testing of CMF under (a) Quasi-static loading and (b) Dynamic Loading at a speed of 112 meters per second of Al-S and SS-CMF shown on the left and right respectively [73], [120].

Ballistic Performance of CMFs

In addition to its potential for improving collisional forces in transportation, CMF has been studied for its potential application in lightweight ballistic armors. CMF can be used to absorb the kinetic energy of impacting rounds in a layered hard armor system. Although a variety of armors currently exist, implementing composite metal foam into these armors offers major weight reduction and performance improvement. Current hard armor systems using woven fibers and bulk metals as energy absorption undergo large deformations when struck. These armor systems may stop the bullet, but the risk of injuring the wearer through behind-armor blunt trauma (BABT) is the main drawback [121]. The bullet is stopped by the woven fiber layer, but the fabric becomes strained and allows the residual energy to impact the wearer. CMF has been studied for use in the structure of layered armors to reduce the depth of penetration by absorbing the energy through uniform compressive deformation of hollow spheres, and further limit BABT injuries.

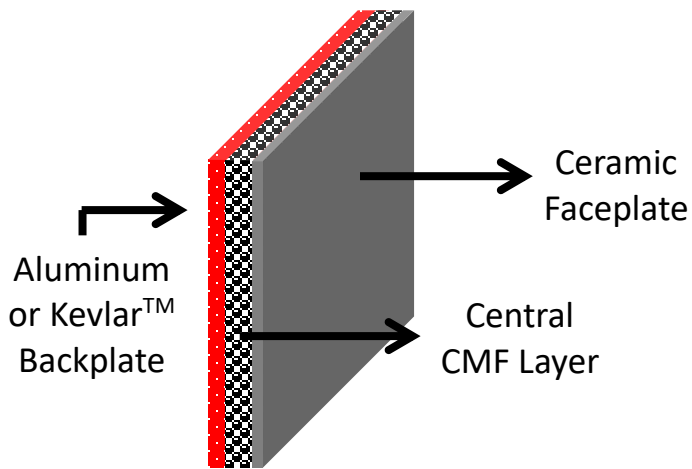


Figure 2-16: Layered model of the ballistic armors produced for testing showing the central CMF layer between a top ceramic plate and KevlarTM or aluminum backing (thicknesses are not shown to scale) [73].



Figure 2-17: Digital image of the ballistic threats Type III and Type IV on the left and right respectively [73], [122].

Ballistic testing of CMF was first published on in 2015 [122], [123]. In these tests, multi-layered composite armor panels were assembled using a ceramic strike face atop CMF with a thin layer of aluminum or KevlarTM backing. A model representing the layering of these materials is given in Figure 2-16, note that the thicknesses in this model are not to scale. Additional details of the sizing and assembly of the armor system can be found elsewhere [122]. Ballistic testing was performed following the National Institute of Justice (NIJ) standards for Type III (7.62 x 51mm M80 Ball) and Type IV (7.62 x 63mm M2 AP) [124]. An image of the ballistic threats can be seen in Figure 2-17. These tests indicated that composite

metal foam armors were able to defeat both Type III and Type IV threats with very minimal back plate indentation.

Samples were able to undergo multiple shots and maintain performance properties. Tested panels of both threats are shown in Figure 2-18, note that neither threat completely penetrates the armor and CMF's ability to consistently stop multiple shots. The multi-shot capabilities of CMF armor panels surpasses that of other ceramic based hard armor systems which are only good for single shot use while their minimal back plate indentation surpasses that of other soft armors and is well below the maximum allowed by NIJ 0101.06 standards. Post analysis of the samples shows the composite metal foam layer absorbs up to 60% of the bullets energy [122]. CMF can be used to replace steel and aluminum in these energy-absorbing applications reducing the overall weight of the system in addition to improving their performance through its high energy absorption capabilities. Replacing these bulk materials with a layer that absorbs energy, instead of transferring it, creates an overall safer armor. These first steps to creating lightweight high performance armors show promising results and further expand the many applications of composite metal foam in fields not previously explored with metal foams.

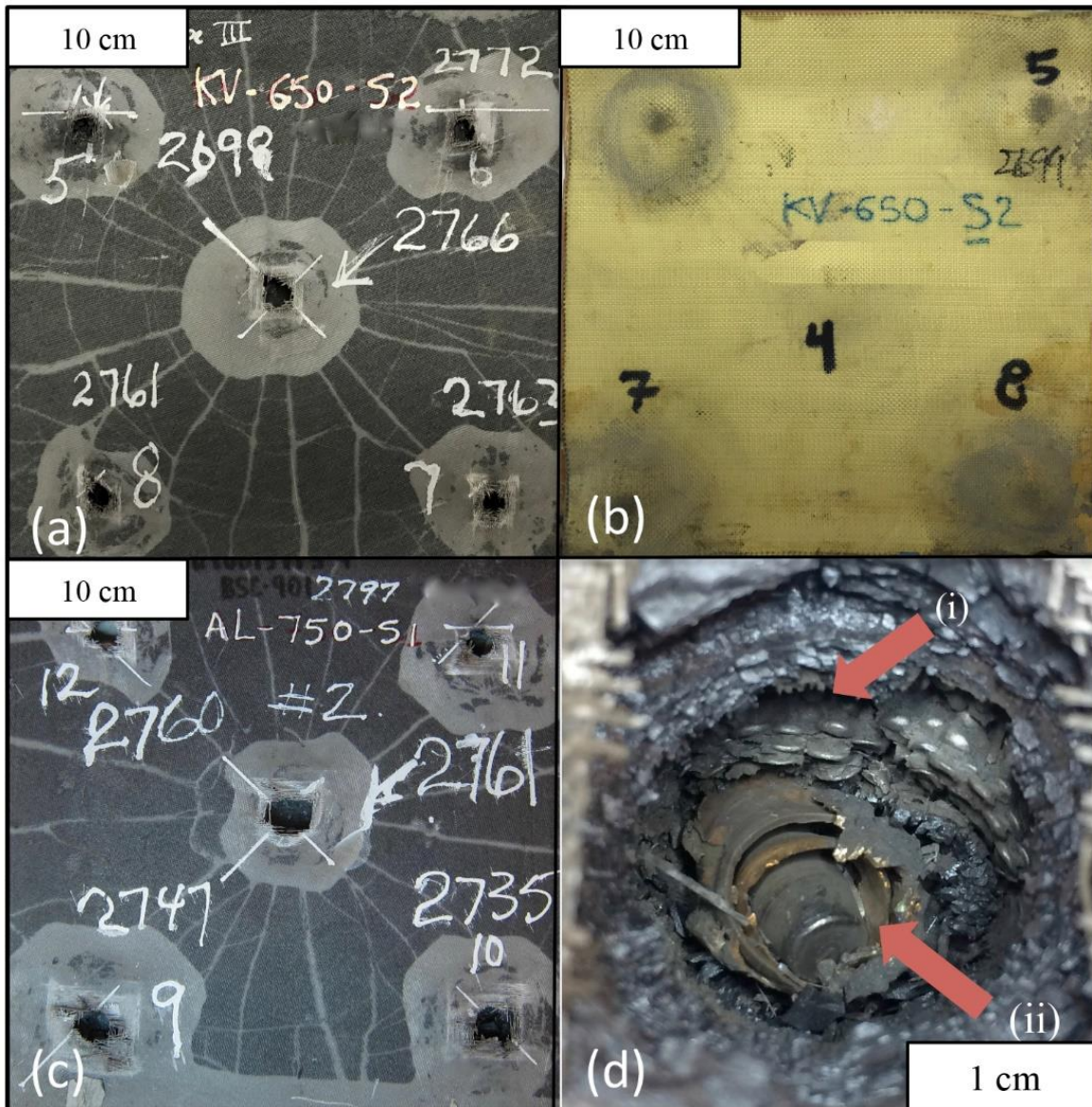


Figure 2-18: Digital images of tested CMF armor systems that have defeated multi-shot Type III (a) front and (b) back with a KevlarTM back plate, (c), Type IV with aluminum back plate, and (d) a close up of the impact zone showing (i) collapsed spheres, and (ii) the stopped armor piercing core [122].

Finite element analysis was also built using ABAQUS/Explicit for modeling the behavior of CMFs under ballistic loading. The model used the same above-mentioned principles as the high strain model including Johnson-Cook constitutive model with an increase in yield behavior for the high-speed impact. The ceramic behavior was used as an input to the

model as it erodes and spreads the bullet tip, allowing the analysis to focus on the mechanism by which the composite metal foam absorbs the energy in the system. As with the high strain rate modeling, the ballistic modeling showed the absorption of energy at the impact zone to be close to that measured in ballistic experimentation [122]. The primary mode by which energy is dispersed is the collapsing of sphere layers below the projectile impact zone.

2.4. Summary of Composite Metal Foam

Composite metal foam has been studied for over a decade since its initial creation in 2004. The mechanical and physical properties of CMF are unique to this novel material. CMF has shown about two order of magnitude higher energy absorption than comparable bulk materials while maintaining a much lower density. Further testing has revealed that CMF strengthens under higher strain rates, making it ideal for car bumpers, helicopter subfloors and train buffer stops as well as other crash worthiness systems. Other high-impact applications include ballistic armors and blast shields, where CMF can be used to replace heavier alternatives. The energy absorption capabilities of these armors can save lives and greatly alter the future of armors. The nuclear and space industry can benefit from the use of CMF for its radiation shielding and thermal insulation benefits to replace standard bulk materials currently being used, leading to lighter and cheaper space exploration.

2.5. Research objectives

Composite metal foam has proven to perform well in a variety of extreme environments through previous testing. It presents itself as a versatile material that can be used for the advancement of nuclear, space, transportation, and military fields. CMF's extraordinary energy absorption capabilities are further studied for use in tank car designs and revolutionary armors in this work.

CMF can be used as core material for sandwich structures for tank car shells and head shields to further improve puncture resistance. CMF can offer passive insulating and radiation shielding for the tank car lading as well as impact energy absorption capabilities without greatly increasing the weight of the tank car. Prior to testing and evaluating the puncture resistance of CMF for tank car structures, sandwich panels using a CMF core must be manufactured and characterized under quasi-static loading. This work presents the first time layered steel-steel composite metal foam core sandwich panels (SS-CMF-CSP) were manufactured and tested under quasi-static loading conditions. The sandwich panels were manufactured by diffusion bonding 316 stainless steel sheets to either side of an SS-CMF core. The sandwich panels were then tested and compared to bare SS-CMF samples under quasi-static compression and tension. The initial testing of the sandwich panels is to explore the effect of bulk metal face sheets when attached to the exterior of the CMF core and apply this knowledge towards manufacturing and testing the layered CMF armors. The loading of SS-CMF was modeled using a newly applied geometry and compared to the experimental results.

In this work, CMF layered armors are tested against various ballistic threat types in order prove CMF's ability to absorb ballistic impacts and potential to replace conventional bulk metal armors. The novel CMF armors can be used to protect against large ballistic threats and improve fuel efficiency and maneuverability of military personnel and vehicles. The goal of this project is to design, manufacture, and test CMF sandwich panels for use in future tank car designs as well as ballistic armor configurations. Both the sandwich panels and armors are made using steel-steel composite metal foam (SS-CMF) that can perform more efficiently than the MIL-A- 12560H RHA standard and other comparable hard armor systems. The first step in this work is to manufacture and test steel-steel composite metal foam (SS-CMF) sandwich

panels under quasi-static compression and tensile loading. SS-CMF armors were also manufactured and tested against various blast and ballistic threats and compared to bulk metal alternatives.

The work by Garcia-Avila *et al.* laid the groundwork for understanding how CMF performs against 7.62 mm ball and AP threats [122]. This project builds upon the initial work by testing SS-CMF hard armor systems against blast waves, metal fragment impacts, and large caliber rounds in an effort to optimize the armor's performance against a variety of threats. The first step in this work was to manufacture and process CMF in panels for testing. The SS-CMF panels used for blast and fragment impact were tested bare sheets. SS-CMF panels were tested against blast and fragment impact through detonation of a 23 mm high explosive incendiary round. The blast and fragment impacts were analyzed individually and simulated using advanced finite element techniques. The finite element results of the SS-CMF panel were compared to a bare aluminum plate with the same overall weight.

CMF ballistic armors were designed and manufactured by layering the SS-CMF panels between a ceramic faceplate and a thin aluminum back plate. The SS-CMF armors were then tested against armor piercing threats larger than those previously studied. Upon ballistic impact the ceramic erodes the hard core of the projectiles and spreads the load of the bullet to a larger area of impact. The CMF layer then absorbs a majority of the bullet's kinetic energy through compression. This differs from bulk metal armors as the kinetic energy is primarily absorbed through compression and cradles the bullet within the armor rather than yielding through tension, causing increased back plate deformation and risk of injury or damage to equipment and personnel. The unique yielding and strength of CMF in compression is much different than other bulk metal alloys and can revolutionize the field of lightweight hard armors.

CHAPTER 3: MATERIALS AND MANUFACTURING

3.1. Manufacturing of Steel-Steel Composite Metal Foam

This work is focused on testing steel-steel composite metal foam under various extreme environments. The CMF samples used in these studies is manufactured using the powder metallurgy technique briefly described in Section 2.2.1. This chapter will discuss the manufacturing process of steel-steel composite metal foam (SS-CMF) in further detail as well as the manufacturing of steel-steel composite metal foam core sandwich panels (SS-CMF-CSP).

Manufacturing of steel-steel CMF using powder metallurgy has been established and optimized through a number of publications [84], [96], [119]. The steel spheres create a random-loose packed arrangement with an approximate packing density of 59% [93]. The molds were vibrated to promote movement of the powder to fill the open volume between the spheres. Steel spheres used for processing the SS-CMF panel were manufactured by Hollomet GmbH located in Dresden, Germany and had an average outer diameter of 2 mm with a wall thickness of 100 μm . The spheres were surrounded with 316L stainless steel powder from North American Höganäs with an average particle size of 44 μm . The elemental composition of the SS-CMF matrix, spheres, and face sheets for SS-CMF-CSP are presented in Table 3-1.

Table 3-1: Chemical composition (wt%) of the material components that make up the SS-CMF and SS-CMF-CSP.

Chemical composition (wt%)							
Material	Fe	C	Mn	Si	Cr	Ni	Mo

Table 3-1: (continued)

2 mm Steel Spheres	Balance	0.68	0.13	0.82	16.11	11.53	2.34
316L Steel Matrix Powder	Balance	0.03	2.00	1.00	16.00-18.00	10.00-14.00	2.00-3.00
316 Stainless Steel Face Sheet	Balance	0.08	2.00	0.75	16.00-18.00	10.00-14.00	2.00-3.00

Multiple molds are packed with the hollow steel spheres and stainless steel matrix powder and then heated within a vacuum hot press that uses a ram to apply pressure to the molds during heating. The molds are heated to 1200°C and sintered for 1 hour at this temperature before being allowed to passively cool. A vacuum pressure of at most 1.3x10-3 Pa was achieved prior to turning on the heating elements to avoid contamination of the sample at high temperatures. Following the heat cycle in the vacuum furnace, the chamber was allowed to passively cool overnight until it reached a temperature below 100°C before the vacuum was released and the molds were removed.

The surfaces of the SS-CMF core panel and the stainless steel face sheets were ground flat using a 35 × 150 cm Gallmeyer & Livingston Co. “Grand Rapids” grinding machine to create smooth surfaces for testing and further processing into SS-CMF core sandwich panels. A picture of the as-processed SS-CMF and the ground surface can be seen in Figure 3-1. The grinding removes any unevenness along the surface and can be ground deep enough to expose the porosities in the material if desired for applications such as sandwich structures. The panels are then placed within an Elma Elmasonic P ultrasonic cleaner filled with water to remove

particles and debris deposited in the SS-CMF's porosities during grinding. The panels are then cleaned with acetone and ready for testing.

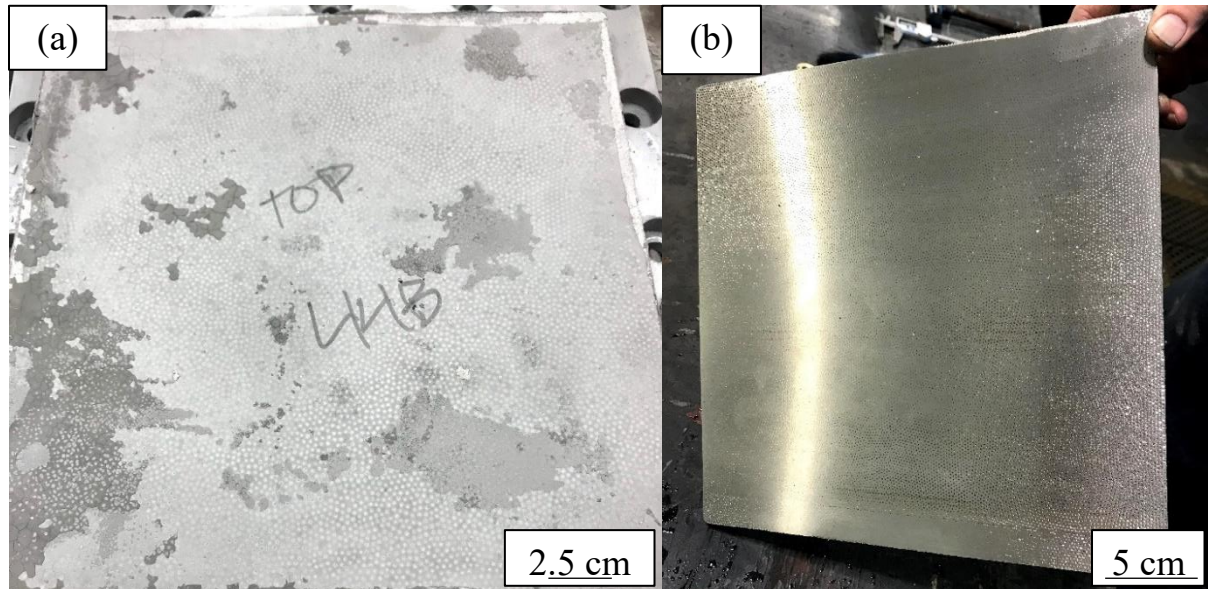


Figure 3-1: Digital images of the (a) as-process SS-CMF and (b) a ground SS-CMF panel with a smooth and flat exterior surface.

3.2. Manufacturing of Steel-Steel Composite Metal Foam Core Sandwich Panels

The SS-CMF panels are able to be assembled into composite metal foam core sandwich panels once they are ground and cleaned. Sandwich panel materials are important in building lightweight and high rigidity structures, such as those which can be used for train car protection and other engineering applications where protection and weight savings are key. Sandwich panels are regularly made with solid face sheets surrounding a porous core that provides strength to the body under flexure without much additional weight. Metal foams can be an optimal material for the core as they provide a porous structure with relatively high strength and low weight [73], [77], [125], [126]. Metal foam core sandwich panels have been made

using a variety of techniques depending on the material makeup of both the core and face sheets. This includes bonding the face sheets to the foam core using adhesive epoxy and traditional metal joining techniques such as welding, brazing, or solid state diffusion bonding [127]–[132]. Each method has its own benefits and drawbacks such as environmental limitations of the epoxy layer, localized heat affected zones within the weldment, and low shear strength of the brazing bond layer. Diffusion bonding can be easily modified for use on metal foams. Until recently, most metal foam sandwich panels have used aluminum foam cores. The structure and bond between the core and the face sheets can be improved by using a high strength foam core, such as composite metal foam. A number of methods can be used for attaching face sheets to the CMF core depending on their material composition.

3.2.1. Composite Metal Foam Core Sandwich Panels with Metal Face Sheets

SS-CMF-CSP using metallic face sheets can be attached using a variety of methods similar to aluminum foam core sandwich panels. Diffusion bonding can be used to maintain porosity within the metal foam core, while also creating a consistent bond where the face sheets and core are in direct contact.

In this work, 316 stainless steel face sheets are attached to SS-CMF cores using the diffusion bonding technique. The chemical composition of the stainless steel face sheets is also listed in Table 3-1. Prior to diffusion bonding, the surfaces of the SS-CMF core panel and the stainless steel face sheets were ground flat using a 35×150 cm Gallmeyer & Livingston Co. “Grand Rapids” grinding machine to create smooth surfaces and ensure continuous contact between the SS-CMF core and the face sheets. The samples are stacked beneath weighted plates to promote close contact of the sandwich panel face sheets and core. The core and face sheets can be placed in the center section of a mold to reduce shifting during the diffusion

bonding process. The assembly is heated to 1200°C and held at that temperature for 1 hour. A vacuum pressure of at most 1.3x10⁻³ Pa is achieved prior to turning on the heating elements to avoid contamination of the sample at high temperatures. Following the heat cycle in the vacuum furnace, the chamber is allowed to passively cool overnight until it reaches a temperature below 100°C before the vacuum is released and the samples are removed.

The stainless steel face sheets can also be attached using adhesive bonding. The adhesive bonding of SS-CMF-CSP using metallic face sheets were assembled using an aerospace grade HYSOL EA 9330.3 two-part epoxy. Stainless steel face sheets are precut and ground to the size of the SS-CMF sample. Small stainless steel spacers with a thickness of 0.5 mm were used to create a consistent bond line thickness between the SS-CMF and face sheets. The epoxy is thixotropic once mixed, making a consistent bond line thickness easier to achieve once the face sheets are affixed. Excess epoxy was removed from the edges of the samples which were then smoothed for testing. The samples were then clamped together and cured at room temperature according to the manufacturer's requirements. These sandwich panels are used to compare to the diffusion bonded SS-CMF-CSP in order to determine their respective benefits and strength.

3.2.2. Composite Metal Foam Core Sandwich Panels for Armor Applications

The CMF core sandwich panels used for armor applications are manufactured by attaching ceramic face sheets and aluminum back plates to the SS-CMF core. The layered arrangements are attached using a high strength aerospace grade epoxy, Loctite EA 9309NA. Thin aluminum spacers are placed between each layer to help hold a consistent bond line in the epoxy. The ceramic is made up of boron carbide (B₄C) and the aluminum alloy used in the armors is 7075-T6 plates. The ceramic layer is ordered to fit the size of the SS-CMF cores

while the aluminum plates are cut from a larger sheet using a waterjet machine. The arrangement is cured at room temperature using a vacuum bagging technique that removes air from the epoxy layer and applies pressure to the layup. The armors are left to cure overnight under vacuum until the epoxy sets, then are left to finish curing in air prior to testing. Excess epoxy that is pulled from the bond layer can be chipped away from the edges of the armor.



Figure 3-2: Image of an SS-CMF-CSP armor arrangement curing under vacuum.

CHAPTER 4: COMPRESSION OF COMPOSITE METAL FOAM SANDWICH PANELS

In this chapter, steel-steel composite metal foam core sandwich panels (SS-CMF-CSP) were manufactured by attaching an SS-CMF core to stainless steel face sheets. The stainless steel face sheets were applied and tested using two attachment methods: adhesive and diffusion bonding. Although the quasi-static compression of SS-CMF has been well reported in the past studies, the results of SS-CMF-CSP under such loading have not yet been reported. The SS-CMF-CSP samples were tested under quasi-static compression and the results are compared to the base SS-CMF and previous testing on small-scale samples. Advanced finite element analysis (Afea) was also developed using IMPETUS and implements a new methodology for modeling CMF under compression. The results of the compression testing can be found published in its entirety elsewhere [133].

4.1. Material Processing

Steel-steel composite metal foam and composite metal foam sandwich panels with metallic face sheets were manufactured using the process outlined in Chapter 3. A panel for compressive testing was manufactured in a 25 x 25 cm size with a thickness of 2.5 cm. The resulting SS-CMF panel had a density of approximately 2.85 g/cm³. The sample panel was manufactured slightly over-sized and ground flat before any post treatment or bonding. Three sample sets were cut from the panel: the first was used to test the properties of the base SS-CMF core, the second for adhesive bonding, and the third for diffusion bonding. In order to manufacture the SS-CMF-CSP, the SS-CMF core was attached to 3 mm thick 316 stainless steel face sheets through adhesive and diffusion bonding. The base SS-CMF samples were cut using a Buehler Isomet 4000 diamond wafering blade with a final size of 25 x 25 x 25 mm.

The faces of the cut samples were ground square and base SS-CMF samples were set aside for testing. The diffusion bonded panel was manufactured using the process outlined in Section 3.2.1. The diffusion bonded SS-CMF-CSP compression samples were cut using a wire electric discharge machine (EDM). The samples are cut with a 1:1 width to height ratio from the diffusion bonded SS-CMF-CSP with an overall size of 25 x 25 x 25 mm. The compression samples were all tested in the same direction, in line with the manufacturing direction with the face sheets on the top and bottom of the SS-CMF. The adhesive bonded SS-CMF-CSP were assembled using the process outlined in Chapter 3 using an aerospace grade HYSOL EA 9330.3 two-part epoxy. Stainless steel face sheets with a 3 mm thickness were pre-cut to 25 x 25 mm squares using a waterjet and ground flat along their surface. Each adhesively-bonded compression sample was cured individually rather than cutting them from a larger panel to avoid damaging the adhesive layer during machining.

During the diffusion bonding of the SS-CMF-CSP, an additional SS-CMF plate was manufactured with modified sintering conditions in attempts to create an improved product for the large-scale manufacturing process, similar to the optimization process completed in a previous study [134]. While the sintering temperature and hold time maintained the same, an additional ram pressure in a hot press furnace increased the compaction of the matrix powder, creating a higher density of SS-CMF product with better bonding between the matrix powder and sphere walls, without deforming the hollow spheres. Samples cut from this panel were also attached to 316 stainless steel face sheets and prepared using a similar method mentioned above. These samples were also tested under compression for comparison.

A section from the as-processed SS-CMF and diffusion bonded SS-CMF-CSP went through additional preparation for microstructural imaging using a scanning electron

microscope (SEM). The interface between the face sheets and the SS-CMF core were also imaged. The sections were prepared using a Buehler ECOMET 2 grinder/polisher using a progression of 320, 600, 800, 1200, and 2400 grit silicon carbide sandpaper with ultrasonic cleaning in water between paper progressions as outlined in the ASM handbook, Volume 9 [135]. The samples were then electropolished with an ESMA E299-CC at a constant current of 10.5 Amps. Electropolishing was followed by etching with Adler's reagent to expose the grain boundaries and additional microstructural features. The samples were imaged using a Hitachi SU3200 scanning electron microscope (SEM). The microscope was equipped with an energy dispersive spectroscopy (EDS) used to map the chemical composition of the samples.

4.2. Experimental Compression Setup

Quasi-static compressive tests were conducted on an MTS 810 servo-hydraulic universal testing machine equipped with a 980kN load cell using displacement control at a rate of 1.27 mm/min. A digital camera was used to image each sample during loading. Lubrication in the form of polytetrafluoroethylene (PTFE) sheets and vacuum grease were placed at the interface between the sample and the platens in order to reduce friction and barreling effects during compression testing. The displacement and load data were recorded using an attached computer and are used to calculate the appropriate stress-strain curves for each sample. All samples were tested under the same loading conditions to easily compare between the various tests.

4.3. Compression Modeling Setup Conducted by an External Company

Finite element analysis (FEA) offers a broad understanding of material interactions and their limitations. IMPETUS Afea Solver was chosen to model the performance of SS-CMF under compression due to its high order element technology [18]. In this study a quasi-static

compression model of CMF was compiled and run by an outside service provider using IMPETUS Afea software. The model is created by reflecting and expansion of a 1/8 unit cell containing a section of the sphere and matrix shown in Figure 4-1(a). The model uses random-loose packed structure between cubic and body centered cubic (BCC). The final sizing of the spheres inside the SS-CMF is a modified BCC structure of hollow metal spheres with a small spacing was placed between porosities to create a packing fill of approximately 59%, consistent with what is seen in manufacturing of CMF [96]. The sphere walls are considered part of the matrix material as to not create an additional interface between the two bodies. This model uses a baseline construction of the CMF geometry and model and does not incorporate the effects of the air within the spheres into the calculations but does expand upon previous works by including the porous geometry of the CMF structure. IMPETUS Afea is suited for future studies involving high rates of deformation and the effects of air inside the spheres using discrete particle based modeling [17].

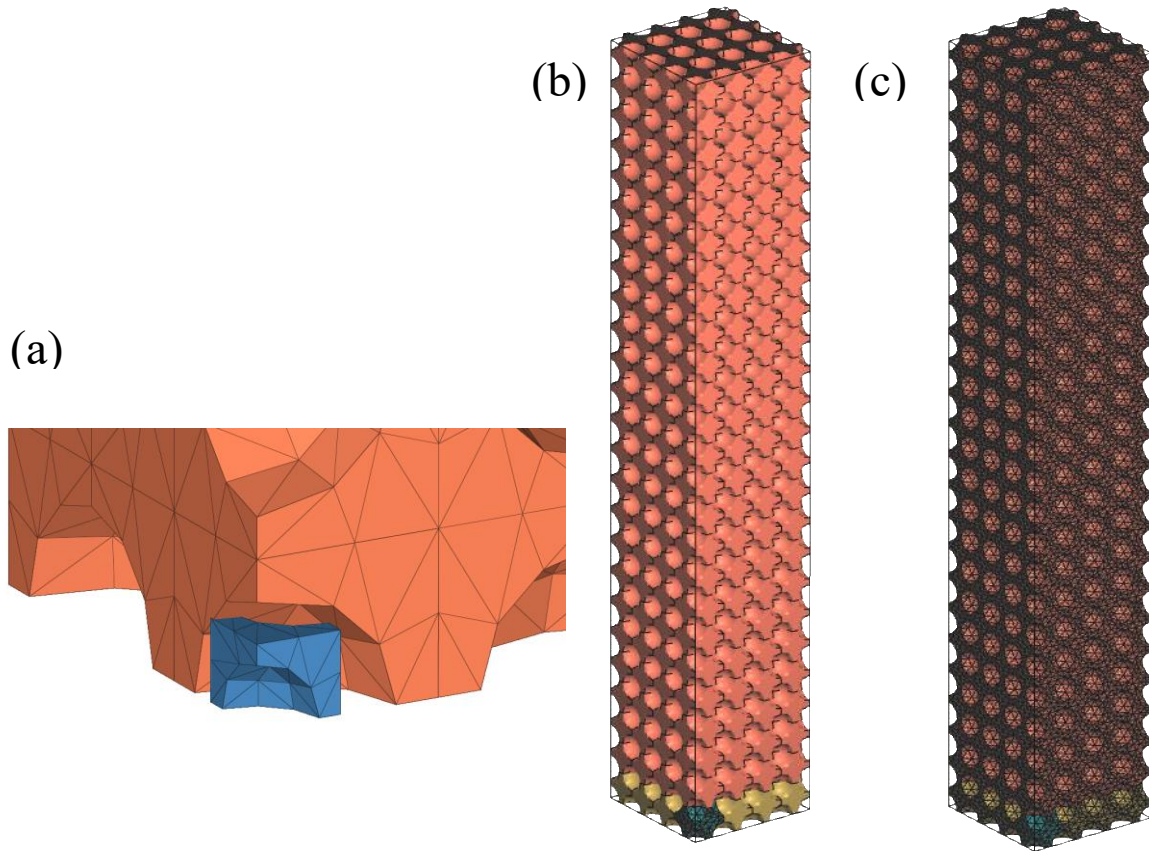


Figure 4-1: (a) Image of the 1/8 unit cell arrangement with meshing used to create CMF model, (b) the full compression model used for simulating CMF, and (c) the fully meshed sample used for testing.

The model was meshed using tetrahedral elements with a length of 0.6 mm, as can be seen in the unit cell in Figure 4-1(a). The sphere wall is shown meshed separately with a smaller element length of 0.3 mm. The smaller element size improves the resolution of the results and avoids compiling errors during deformation of the spherical pores under compression. The two bodies, the sphere and matrix, are modeled with the same material properties and assumed to be in contact during the simulation. The unit cell is reflected within the body to create the compression sample. The model is run in quarter symmetry, as can be seen by the input in

Figure 4-1(b), with a taller sample size than what was tested experimentally to attain reliable results. The entire mesh of the compression sample is presented in Figure 4-1(c).

Modeling materials under quasi-static compression is relatively simplistic, however the porosities within composite metal foam make the finite element analysis more complex. Metal foams show three distinct loading regions: (i) initial elastic region, (ii) plateau region, and (iii) densification. There have been a variety of methods used to model metal foams under compression which work to balance the perfectly plastic realm presented by the plateau stress, and the innate hardening of the material as it approaches densification in order to effectively predict the material's energy absorption [136], [137]. Two constitutive models are paired with the geometric meshing of the sample in order to best approximate the loading of SS-CMF under compression. The CMF is modeled as a perfectly plastic material that assumes a constant stiffness following yield. The material parameters used for the SS-CMF are taken from prior works with a density of 2.9g/cm^3 , a modulus of 13.2 GPa, and a Poisson ratio of 0.1 [122], [138].

4.4. Results and Discussion

4.4.1. Compression Structural Properties

Digital images of the base SS-CMF and the SS-CMF-CSP are shown in Figure 4-2. Figure 4-2(a) shows the base SS-CMF with the sphere openings being exposed following sample cutting. The openings have a varying diameter and depth as the cuts are not at the true center of each sphere. The spheres are sitting in various positions vertically along the sample wall given the inherent packing arrangement obtained during manufacturing of SS-CMF.

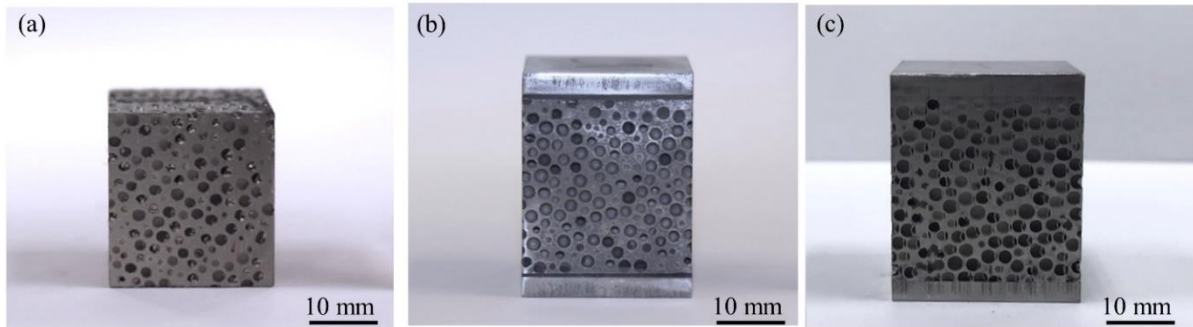


Figure 4-2: Digital images of the (a) base SS-CMF, (b) adhesively bonded SS-CMF-CSP, and (c) diffusion bonded SS-CMF-CSP compression samples prior to testing.

The adhesive bonded SS-CMF-CSP can be seen in Figure 4-2(b). The bond line is seen to be relatively constant across the top and bottom of the sample. The adhesive is able to infiltrate the open sphere porosities on the surface of the sample, improving the strength of the bond to the surface. Previous works on SS-CMF have shown a high infiltration percentage of 88% epoxy infusion into SS-CMF under vacuum curing [139]. These samples were cured under atmospheric pressure but aided by additional clamping force to ensure continuous contact between the core and face sheets. This helps to promote filling of the open spheres but does not necessarily infiltrate the microporosities within the matrix. The epoxy layer creates an efficient bond against the core and face sheets, but it is important to note that its strength can be affected by both heat and moisture while in service, degrading its adhesive properties. On the other hand, the diffusion bond in Figure 4-2(c) will only occur along the surface of the SS-CMF exposed during heating and does not penetrate the open porosities. This means that inherent gaps will exist along the surface where the hollow core of the spheres lie open to the face sheet. The diffusion bonding does have benefits over the adhesive bond as it does not alter the surface porosity of the SS-CMF core. The diffusion bond has similar limitations to the base

metal and does not further restrict the application of the sandwich panel, unlike epoxy adhesives.

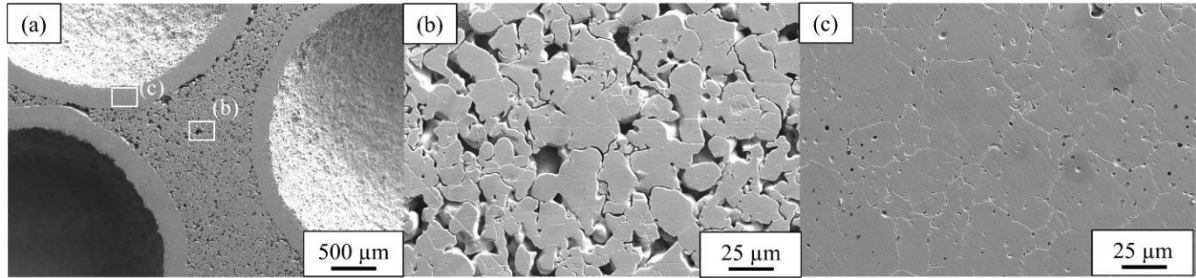


Figure 4-3: (a) SEM image of the electropolished base SS-CMF showing the microstructure of the (b) matrix and (c) sphere wall. The outlined areas marked on image (a) in white show the location of the higher magnification images shown in (b) and (c).

The SEM microstructure of the as-processed SS-CMF is shown in Figure 4-3. Figure 4-3(a) shows a cut section of three spheres intersecting with sintered matrix between them. A small gap can be seen between the two sphere walls located in the top left of the image. These occur in areas where the space between the spheres does not become fully infiltrated with powder during sintering. Good bonding is seen between the spheres walls and matrix surrounding the rest of the spheres. A higher magnification of the outlined sections in Figure 4-3(a) are shown in Figure 4-3(b) and (c). The porosities between the matrix particles (Figure 4-3(b)) and within the sphere wall (Figure 4-3(c)) are apparent in these Figures. Images taken of the matrix and sphere wall grains show that the grains in the sphere wall are larger than those that make up the matrix. The spheres themselves are created using a powder metallurgy process and go through additional heating cycle during the manufacturing of the SS-CMF panel. This leads to additional grain growth in the sphere wall when compared to the matrix as reported in our previous studies [96], [119]. It has been reported that carbide precipitations are mostly formed

at the grain boundaries of the sphere walls due to both the effects of the additional heat cycle during the manufacturing of the SS-CMF as well as the higher starting carbon content of the spheres (Table 3-1) [96], [99]. Previous works have found that the carbide formations within the sphere wall are made up of Cr rich $M_{23}C_6$ carbides known to form in 316 stainless steels [96], [99], [140]. EDS analysis shows the precipitation of carbides along the grain boundaries in the sphere wall of the base SS-CMF sample in Figure 4-4. Figure 4-4(a) and (b) are SEM images of the location used for EDS mapping with Figure 4-4(b) being a zoomed in area represented by the outlined region in Figure 4-4(a). The mapped region is outlined in Figure 4-4(b) and white arrows are used to point towards the location of the carbide formations. The EDS maps of Cr and C in Figure 4-4(c) and (d) verify that these are Cr rich $M_{23}C_6$ carbides forming mostly within the sphere walls.

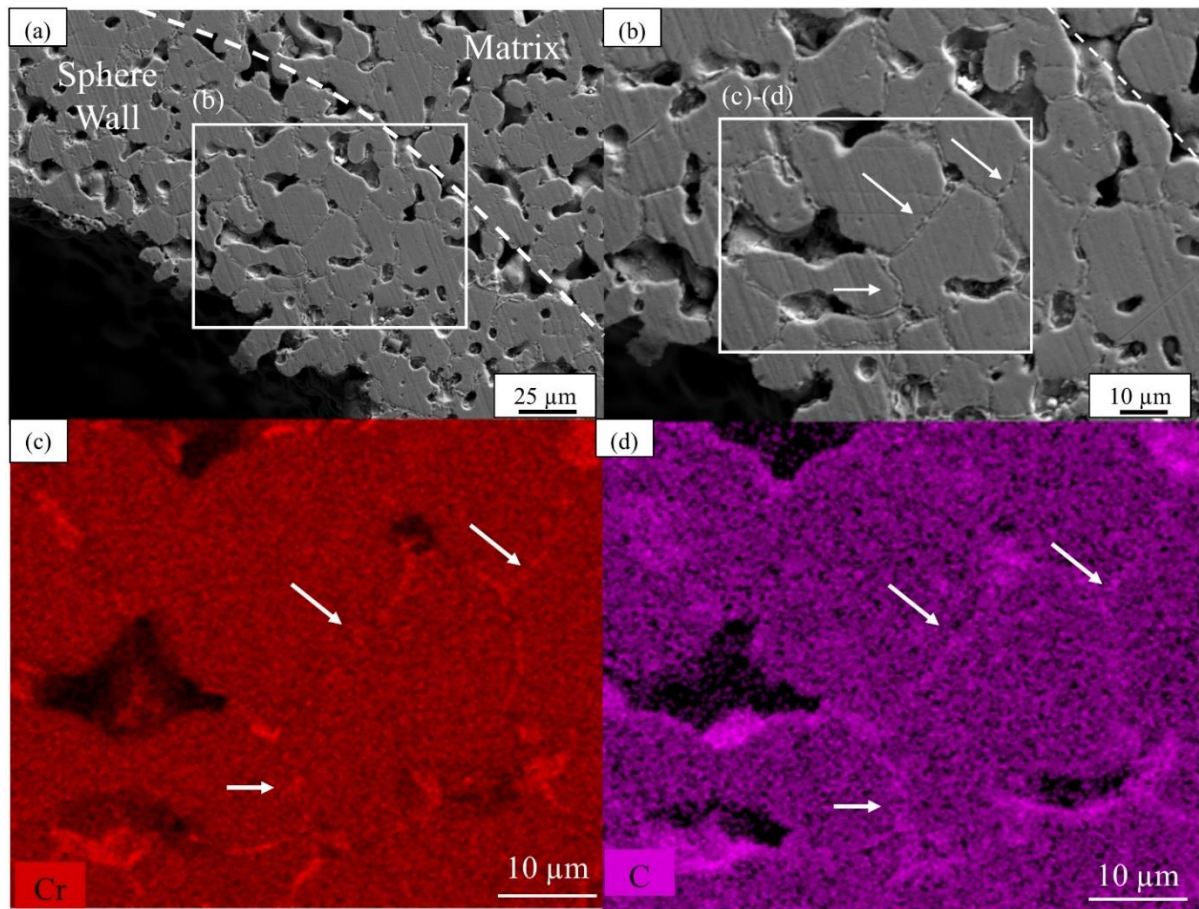


Figure 4-4: (a) and (b) SEM images of the etched base SS-CMF showing (a) sphere wall-matrix interface, and (b) zoom in area marked in image (a) with marked carbides along the grain boundaries in the sphere wall (white arrows). (c)-(d) show the EDS maps of the area outlined in (b) that confirms higher concentration of (c) Cr and (d) C at the grain boundaries.

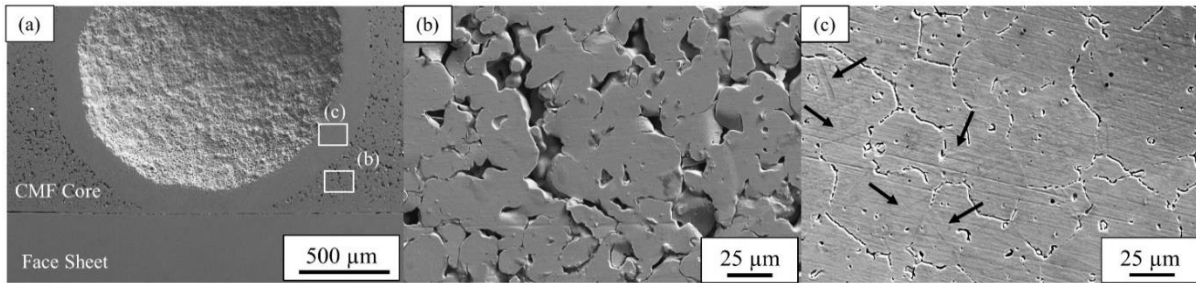


Figure 4-5: SEM images of the electropolished diffusion bonded SS-CMF-CSP showing the (a) face sheet interface with the core and (b)-(c) the microstructure of the matrix and sphere wall, respectively. The outlined areas shown in image (a) in white are the location of the higher magnification images shown in (b) and (c). Black arrows in (c) indicate the location of twin boundaries.

SEM images of the diffusion bonded SS-CMF-CSP sample are shown in Figure 4-5. The bond line between the SS-CMF core and stainless steel face sheets are shown in Figure 4-5(a) with a cross sectional cut of a hollow sphere close to the surface. The contact between the face sheet (bottom) and the SS-CMF core (top) is relatively consistent across the interface, although small gaps exist along the bond line (more easily seen on the left side of the image). The small gaps between the face sheet and the core are suspected to occur during sample cutting and preparation for SEM imaging and do not naturally form during the diffusion bonding process. There are, however, inherent gaps at various points along the interface where the spheres are open to the surface and are not in direct contact with the face sheet. Higher magnification images of the SS-CMF-CSP are shown in Figure 4-5(b)-(c). A similar micro-structure to the base SS-CMF can be seen for both the matrix and sphere wall of the diffusion bonded SS-CMF-CSP. The grains within both the matrix and sphere wall are slightly larger than the base SS-CMF sample. Multiple images were taken at a constant magnification of the base SS-CMF and SS-CMF-CSP and were analyzed using ImageJ to obtain an average of over 100 grain size measurement for the matrix and sphere wall. The average grain size of the matrix and sphere

walls for the SS-CMF and SS-CMF-CSP are listed in Table 4-1. Following the additional heat cycle of manufacturing the diffusion bonded sandwich panels, the average matrix grain size increases from 32 μm to 45 μm and the average sphere wall grain size increases from 39 μm to 49 μm . The grain growth can be seen by comparing Figure 4-3(b)-(c) to Figure 4-5(b)-(c). The SS-CMF-CSP also reveal twin boundaries that have formed following the diffusion bonding heat cycle. The twin boundaries are primarily seen within the larger grains in the sphere wall highlighted by white arrows in Figure 4-5(c) where a majority of the grain growth has occurred. In addition, SEM images and EDS mapping of the SS-CMF-CSP are presented in Figure 4-6. Figure 4-6(a) and (b) show progressive magnification of the mapped region along the sphere wall border with the matrix in the SS-CMF-CSP sample. It can be seen in the lower magnification SEM images that the carbide formations at grain boundaries in the sphere wall are less prominent due to the grain growth. The EDS mapping in Figure 4-6(d) show carbon rich regions along the edge of the matrix grains that reside next to the sphere wall. The higher carbon content is due to diffusion of the carbon from the sphere wall out to the surrounding matrix. The migration of the carbon is primarily due to the additional heat cycle during diffusion bonding of the face sheets and can lead to increased carbide formation within the surrounding matrix and between the two bodies (sphere wall and matrix) rather than primarily just within the sphere wall. Figure 4-6(a) also shows some of the twin boundaries formed in larger grains within the spheres that contribute to the slightly higher strength in SS-CMF-CSP.

Table 4-1: Measured grain size of the matrix and sphere wall for the base SS-CMF and diffusion bonded SS-CMF-CSP.

	Matrix Grain Size (μm)	Sphere Wall Grain Size (μm)
Base SS-CMF	32	39
Diffusion SS-CMF-CSP	45	49

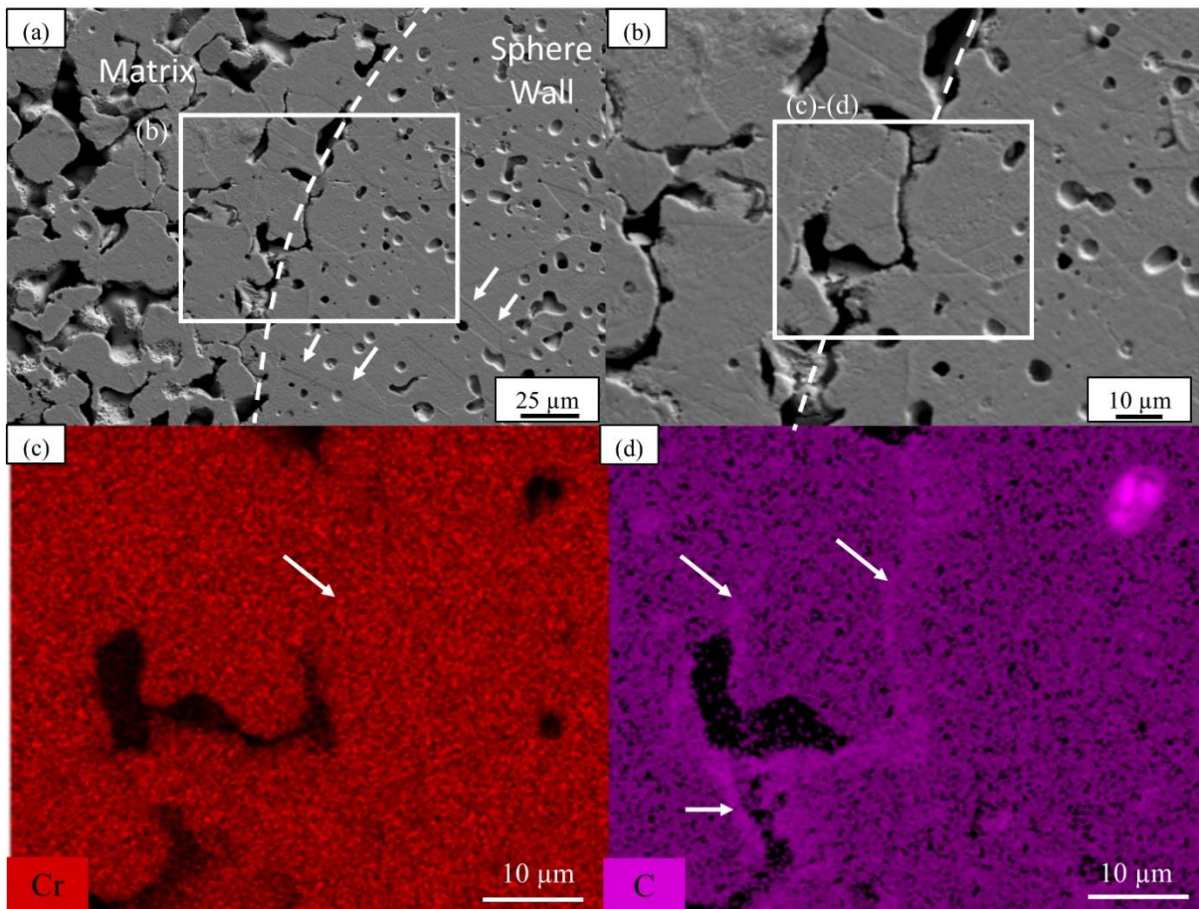


Figure 4-6: SEM images of the etched SS-CMF-CSP showing the location of the EDS mapping along the sphere wall interface with the matrix. (c)-(d) EDS maps of Cr and C showing carbon rich regions in the matrix and at the interface between the sphere wall and the matrix.

EDS line scans were completed across the interface between the face sheets and the SS-CMF core in order to investigate any potential diffusion of elements across the boundary. An example line scan from the face sheet into the matrix is presented in Figure 4-7. The dotted line drawn on the SEM image represents the interface and the solid line represent the line scan length. The line composition plots for Cr and Ni are plotted in Figure 4-7(b) and (c). Both of the Cr and Ni plots show minimal variation in composition, while there is a slight increase in Ni composition when moving into the matrix. This is expected due to the initial slight

compositional difference between the 316 stainless steel face sheets and the 316L matrix of the SS-CMF. The line scans suggest there is minimal diffusion of elements across the diffusion bond given the relatively close elemental compositions of the stainless steel matrix and face sheets.

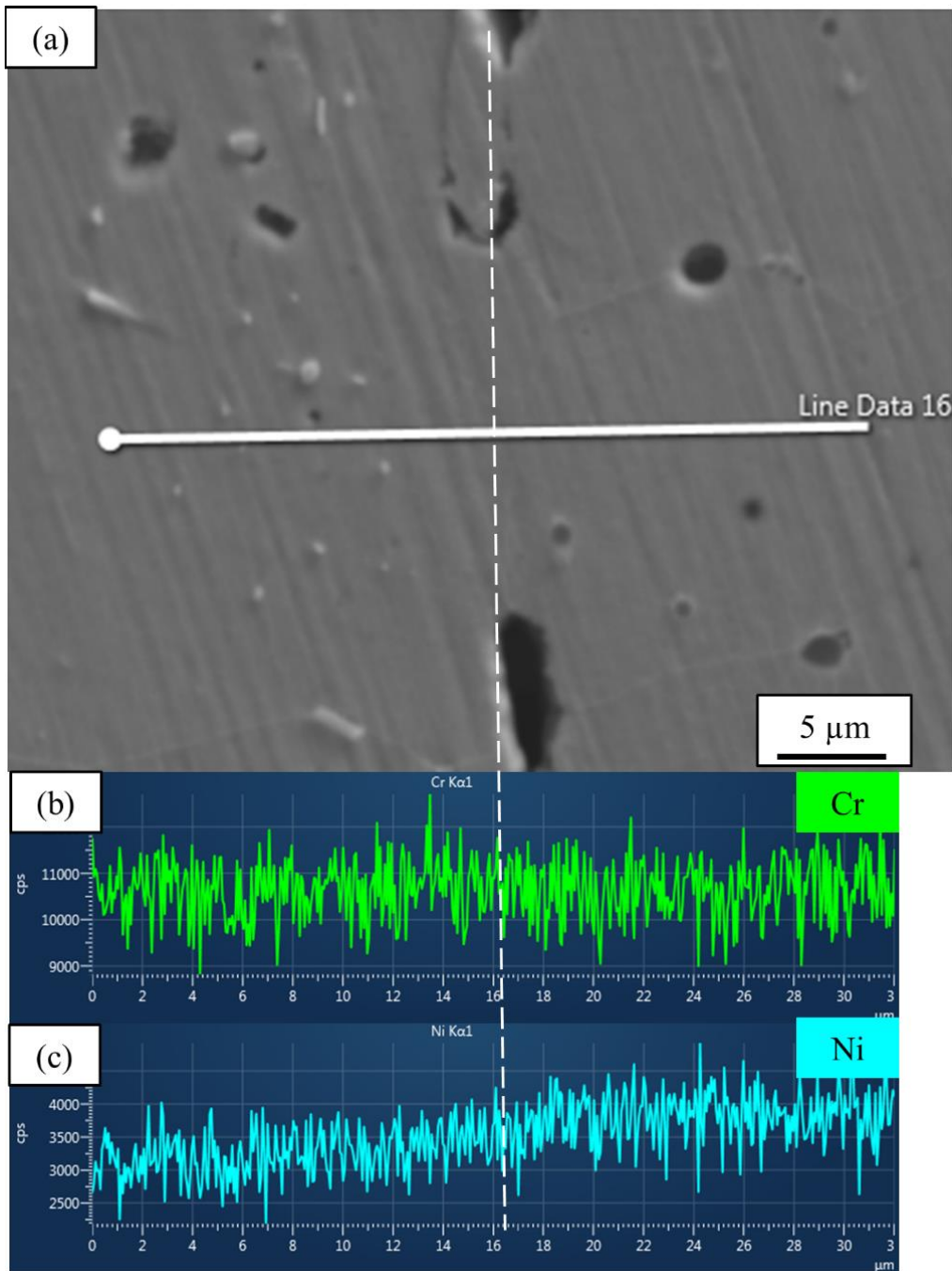


Figure 4-7: (a) High magnification SEM image of the etched SS-CMF-CSP along the face sheet interface with the SS-CMF core. (b)-(c) show the EDS line scan plots for Cr and Ni, respectively, with a slight gradient in the Ni content across the interface. Dotted line marked the location of the interface.

4.4.2. Compression Mechanical Properties

The engineering stress-strain curves for the as-processed SS-CMF and SS-CMF-CSP under compression are shown in Figure 4-8. The plot includes three tests for each sample type compiled into the plot. The strain was calculated using the dimensions of the SS-CMF core, (25 x 25 x 25 mm), as the face sheets were found to not greatly influence the deformation of the core under compression. The plot of the base SS-CMF is represented by the solid lines. The shape of the curve is representative of SS-CMF under compression. The SS-CMF undergoes an initial yield followed by a plateau stress where the hollow metal spheres deform at a constant stress value until densification is reached and the sample stiffens [96], [100], [134].

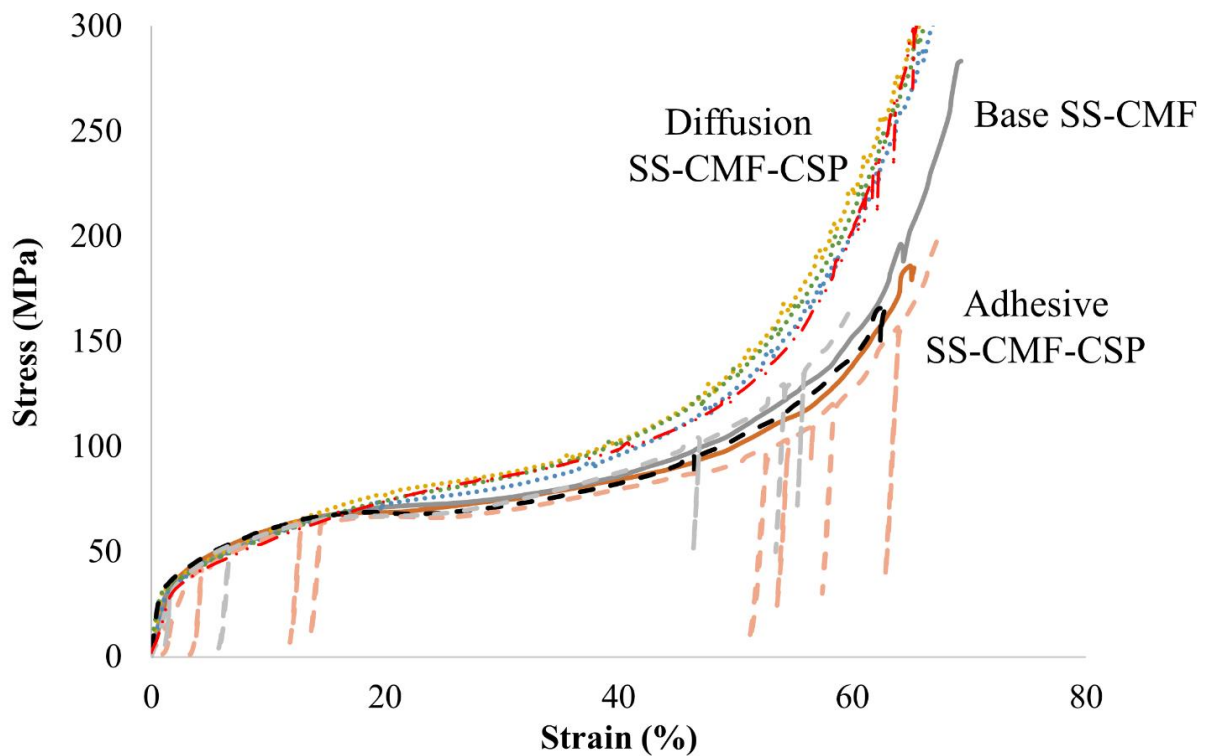


Figure 4-8: Compressive stress-strain curves of scaled SS-CMF and SS-CMF-CSP (unoptimized).

The base SS-CMF sample's curve is overlapped with the adhesive bonded samples shown by the dashed lines in Figure 4-8. The two sets have a very similar stress-strain curve as the face sheets do not have a noticeable effect on the mechanical strength of the SS-CMF-CSP structure under compression. The adhesion bonded samples experience multiple drops in stress at various strains during compression. This is attributed to the shifting of material at the interface of the adhesive bond due to the lateral expansion of the sample under compression and a momentary lapse in the readout registered by the load cell. The drops occur at strains following the initial yield, signifying that it may be due to core motion against the adhesive bond during deformation of the sample. During compression, the porosities within the SS-

CMF core naturally collapse, but the layers in contact with the epoxy layer are held stiff, impeding uniform deformation in the core. This causes momentary shifting of material as additional layers begin to deform and the stress-strain curve returns to its normal path.

The diffusion bonded SS-CMF-CSP samples are shown by dotted lines in Figure 4-8 and were stronger than both the as-processed SS-CMF and adhesion bonded sandwich panels. The strengthening is not necessarily caused by the addition of the face sheets, as the adhesive bonded samples have shown, but is likely caused by the additional heat cycle during diffusion bonding. In order to test this hypothesis, the face sheets of a diffusion bonded SS-CMF-CSP sample were removed and the core itself was tested under the same loading conditions. The results indicated a similar stress-strain curve shown by the red dotted line in Figure 4-8. The test confirms that the strengthening observed in SS-CMF-CSP samples is primarily due to the microstructural changes that occurred during the diffusion bonding process and not necessarily strengthening added directly by the stainless steel face sheets. Generally, the larger grain size in both the matrix and sphere wall is expected to increase the ductility of the material and decrease its hardness. However, a distinct strengthening effect can be seen at strains above 17%. The magnitude of the strengthening is not drastically different from the base SS-CMF but is consistent across all three diffusion bonded SS-CMF-CSP samples. The yield and early plateau stress are not affected, meaning the strengthening is occurring during the deformation and collapse of the hollow metal spheres and its surrounding matrix leading to a steeper slope between 16-50% strain. The twin formations and diffusion of carbon to the matrix from the sphere walls are possible explanations for the strengthening effect following diffusion bonding heat treatment.

The stress-strain curve of the diffusion bonded SS-CMF-CSP also shows a step like shape at strains above 50%. This is thought to occur for a similar reason attributed to the epoxy bonded samples, but to a lesser effect, as the diffusion bond has a lower mechanical impedance than the epoxy interface. The lateral expansion of the core at high strains and subsequent interaction at the bond line causes a rise and fall in the stress measured by the load cell during the densification phase, creating the step like pattern.

Images of the compression samples at 0% strain and 60% strain are shown in Figure 4-9. The base SS-CMF in Figure 4-9(a)-(b) undergoes uniform deformation up to 60 % strain. The adhesive bonded SS-CMF-CSP in Figure 4-9(c)-(d) does show some asymmetric behavior and slight shearing occurring within the core. This is due to the formation of a large dead zone at the top and bottom of the sample. The larger dead zone is created by the stiff interface of the adhesive bond and limits the motion of the core, causing an asymmetric yielding behavior at high strains. The diffusion bonded samples in Figure 4-9(e)-(f) did not experience such limitations and had uniform deformation through densification, similar to the base SS-CMF. The diffusion bonded SS-CMF-CSP were able to uniformly compress up to 70% strain without the core cracking or failing. It can be seen that the SS-CMF core bulges out of the width of the face sheets, yet it does not separate from either of the face sheets. The top and bottom faces are still in contact with the edges of the face sheets. The bond layer created during the diffusion process allows enough motion between the face sheets and the core to accommodate the sample's lateral expansion during compression without separating at the bond interface.

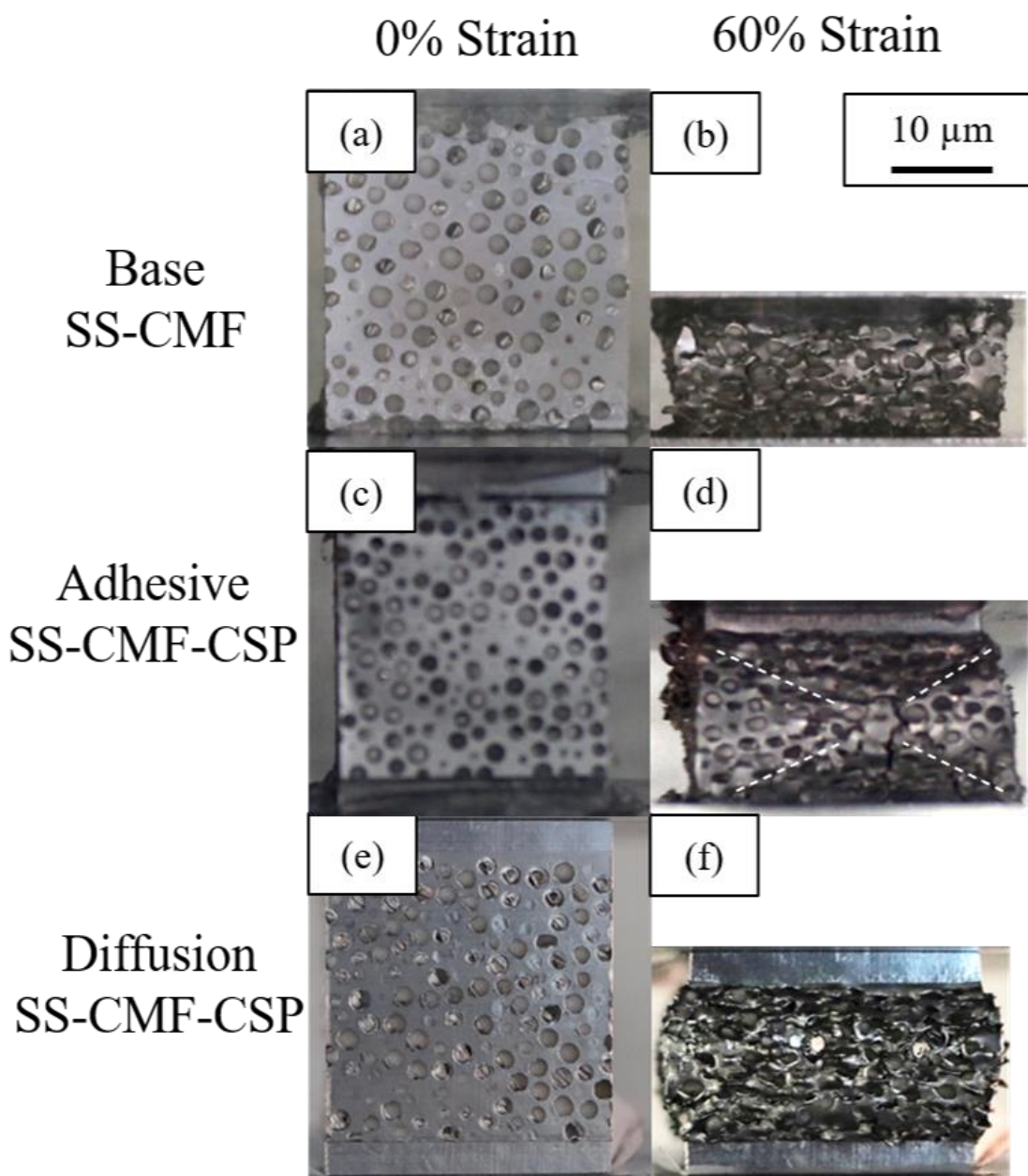


Figure 4-9: Images at 0% strain, left, and 60% strain, right, of the (a-b)SS- CMF base, (c-d) adhesive bonded SS-CMF-CSP, and (e-f) diffusion bonded SS-CMF-CSP.

The initial samples manufactured using the large-scale process have a lower strength than what has previously been established for SS-CMF tested on smaller scale samples [96], [100], [134]. The stress-strain curves of the initial SS-CMF and SS-CMF-CSP compared to the

improved samples are plotted in Figure 4-10. The curves plotted are an average of three tests with the base SS-CMF plotted in a solid red line, the adhesive SS-CMF-CSP in a black dashed line, and the diffusion bonded SS-CMF-CSP in a dotted green line. The improved sample set are all stronger than the initial tests. The improvement in mechanical strength is credited to a superior sintering process that creates a more cohesive matrix and a stronger bond between the matrix and sphere walls. As can be seen in Figure 4-10, a similar divergence of the diffusion bonded sample (shown in dotted green line) occurs with the improved samples between strains of 17-60%. The same strengthening effect is apparent in the improved samples with diffusion bonded face sheets. The strengthening in the improved samples, similar to the unoptimized, does not affect yield strength and early plateau of the material as those properties are mostly controlled by the matrix deformation. This phenomenon occurs at higher strains during the deformation and collapse of the sphere walls. The strengthening continues up through densification to approximately 60% strain, where it begins to converge with the base SS-CMF stress-strain curve.

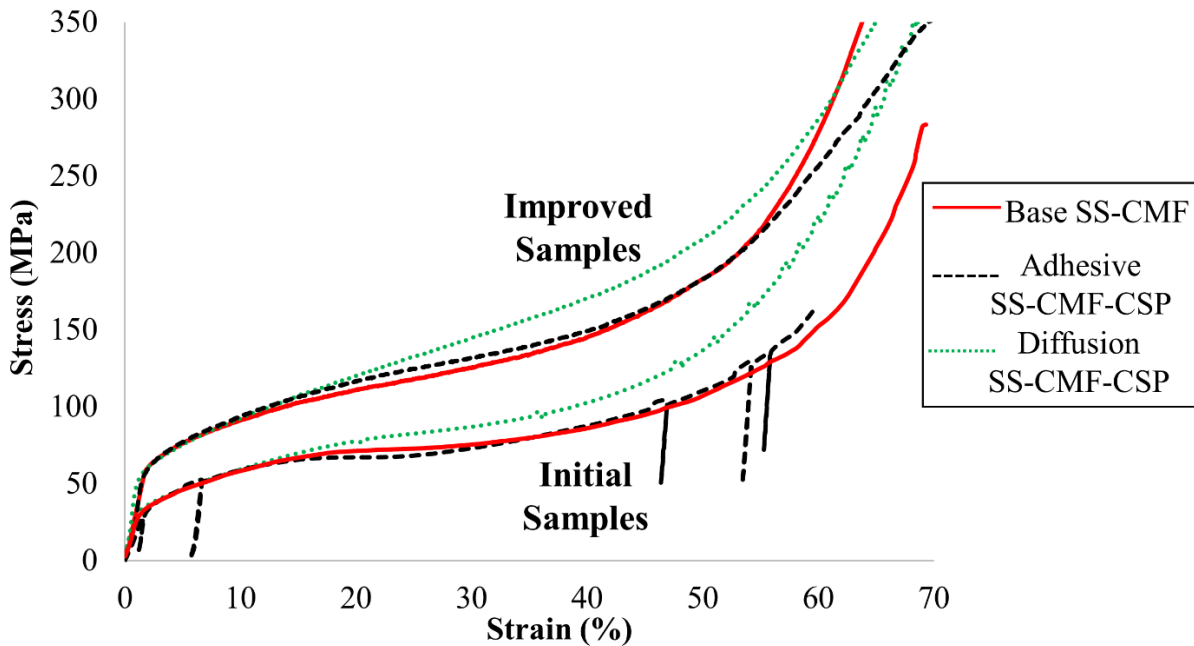


Figure 4-10: Compressive stress-strain curves of scaled SS-CMF and SS-CMF-CSP compared to the improved/ optimized scaled samples.

The mechanical properties of the initial and improved SS-CMF and SS-CMF-CSP are presented in Table 4-2 alongside the compressive properties previously established for small-scale manufactured SS-CMF. The diffusion bonding increases both the plateau stress, measured at 30% strain, and the densification stress of the SS-CMF material under compression for both sample sets. The initial diffusion bonded samples see a 17% increase in plateau stress and 10% densification stress over the base SS-CMF. The improved SS-CMF-CSP set shows a similar increase with a 16% improvement in plateau stress and a 9% rise in densification stress. Meanwhile, both the base SS-CMF and adhesive bonded SS-CMF have similar values for both sets of tests. The energy absorption of the SS-CMF samples can be approximated in MJ/m^3 by calculating the area under the stress-strain curve. The energy

absorbed by each sample is also listed in Table 4-2. It was found that the energy absorbed by the diffusion bonded SS-CMF-CSP increases for both the initial and improved sample sets by approximately 5-7% when compared to their respective base SS-CMF. The improved SS-CMF sample absorbs 35% more energy than the unoptimized samples and is in good agreement with the small scale SS-CMF samples from prior works [96]. This data shows good adaptation of SS-CMF processing to large-scale manufacturing. Future mechanical testing of SS-CMF sandwich panels will use the optimized manufacturing process with a higher strength than originally achieved. The compression results helped to improve the final manufacturing settings for large-scale SS-CMF panel processing as well as investigate the effects of microstructural changes on the final strength of the samples.

Table 4-2: Mechanical properties of the scaled base SS-CMF and SS-CMF-CSP under compression compared to prior small-scale SS-CMF and the improved/ optimized scaled samples.

	Yield strain (mm/mm)	Yield Stress (MPa)	Plateau Stress at 30% (MPa)	Densification Strain (mm/mm)	Densification Stress (MPa)	Specific Energy Absorption (MJ/m³)
Base SS-CMF	1.36	30.51	73.17	61.50	156.44	48.8
Adhesive SS-CMF -CSP	1.68	33.10	73.13	58.06	134.21	42.2
Diffusion SS-CMF -CSP	1.25	31.29	85.13	55.45	170.06	51.2
SS-CMF (Prior Work [96])	1.06	43	127	54	217	67.8
Improved SS-CMF	1.64	54.94	125.71	55.32	217.12	66.5

Table 4-2: (continued)

Improved SS-CMF -CSP	1.63	47.73	132.94	55.84	218.61	68.5
Adhesion						
Improved SS-CMF -CSP	1.51	56.70	145.63	54.53	237.66	71.0
Diffusion						

4.5. Compression Modeling Results Conducted by an External Company

The modeled stress-strain curve of the SS-CMF model under quasi-static compression is shown alongside the experimental results in Figure 4-11(a). The perfectly plastic material model paired with the porous geometry was found to be in good agreement with the experimental results. The model used a multilinear stress-strain relationship up to 15% yield for the initial onset of the plateau stress. After this point, the model assumed a constant stiffness and allowed the geometry of the SS-CMF to dictate the hardening behavior through the plateau region towards densification. The early plateau region is slightly lower than the experimental values between 12-30%, but the model does correct itself relatively quickly as it continues to deform. The geometry gives the displacement curve a relatively consistent slope between 25% to 55% strain that is consistent with experimental data. Densification was appropriately accommodated for by the geometry of the sample as the pores representing the hollow spheres are deformed and stiffen the overall product, as can be seen by the SS-CMF model displaced to 50% strain in Figure 4-11(b). The quarter symmetry representation in Figure 4-11 (b) shows the collapsed spheres throughout the body as densification of the SS-CMF begins. The specific energy absorption of the model up to 50% strain was measured through the finite element analysis as 56.2 MJ/m^3 , similar to the experimental findings reported in Table 4-2. The model's

results are slightly lower than the experimental values as it does underestimate the strength at a few points along the stress-strain curve. Future modeling can aim to incorporate the same geometry used herein and validate it under various loading conditions such as bending and tension as well as consider the air inside the spheres and its effect on the performance of the material under loading using IMPETUS Afea.

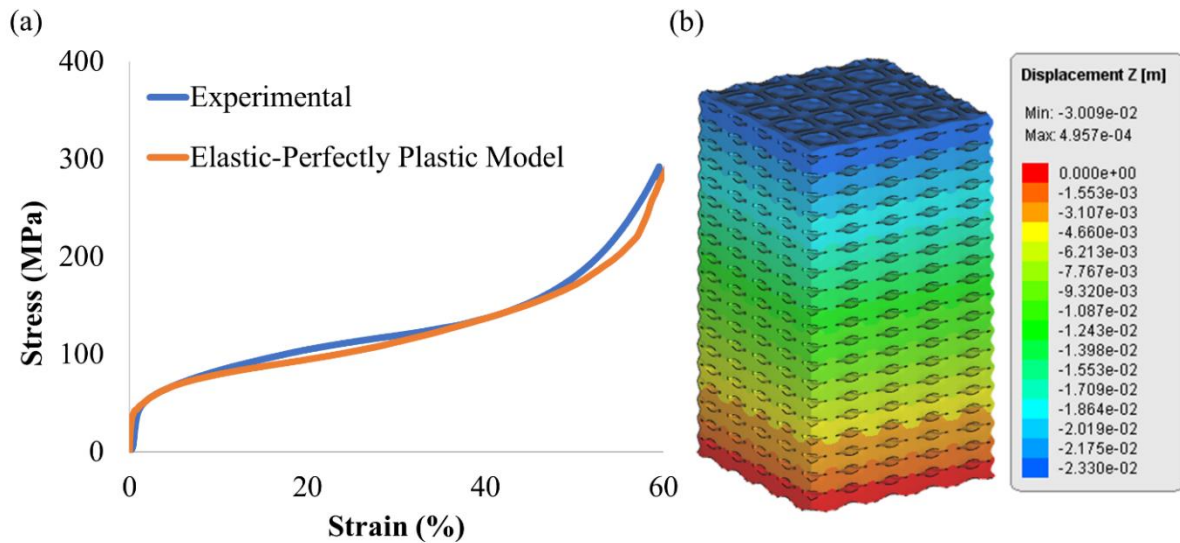


Figure 4-11: Generated finite element results showing the (a) stress-strain curve obtained using an elastic- perfectly plastic material model paired with the geometric meshing and (b) the simulated SS-CMF sample deformed to 50% strain showing the distribution of displacement throughout.

4.6. Summary of SS-CMF and SS-CMF-CSP under Compression

Composite metal foam core sandwich panels were manufactured and tested under quasi-static compression. Two bonding methods, adhesive and diffusion bonding, were tested and compared to the as-processed SS-CMF samples using large-scale manufacturing. It is observed that the face sheets had little effect on the SS-CMF performance under compression, however

it did show the viability of multiple attachment methods for future testing of SS-CMF-CSP. The diffusion bonded SS-CMF-CSP experienced strengthening due to microstructural changes within the CMF core. Finite element analysis was completed using Impetus Afea to model the SS-CMF under compression with a complex geometry. The simulation results show good agreement with the experimental work. The improved processing technique established in this chapter was used for manufacturing SS-CMF and SS-CMF-CSP samples for tensile testing.

CHAPTER 5: TENSION OF SS-CMF AND SS-CMF-CSP

Testing of metal foams has shown their strength in tension is much lower compared to compression [104], [141]–[144]. The network that makes up the foam surrounding the porosities is full of stress concentrations that allow for easy crack formation and propagation [141]–[143]. CMF has one of the highest compressive strengths than any other comparable metal foam, but has yet to be tested under tension [73], [99]. In this section, steel-steel composite metal foam core sandwich panels (SS-CMF-CSP) were manufactured by diffusion bonding stainless steel face sheets to an SS-CMF core, similar to the process used in the previous chapter. The microstructure and bond line of the SS-CMF and SS-CMF-CSP were investigated using SEM imaging. Samples were cut from the panels and tested under quasi-static tension to understand the strength and failure modes of SS-CMF and SS-CMF-CSP. The strengthening provided by the face sheets and the integrity of the diffusion bond are documented and the results are normalized by the sample densities for direct comparison. The results of the tension testing can be found published in its entirety elsewhere [145].

5.1. Materials Processing

Two 25 x 25 cm steel-steel composite metal foam (SS-CMF) panels were manufactured using the powder metallurgy technique outlined in Chapter 3 [84], [96], [119]. One panel was used to test as bare SS-CMF and the other was used to manufacture and test SS-CMF-CSP under tension. The panels were manufactured with a thickness of 13 mm. The resulting SS-CMF samples had a density between 2.9 and 3.1 g/cm³. The sample panels were manufactured slightly over-sized and ground flat to a final thickness of 11.5 mm before any post treatment or bonding to the face sheets. The SS-CMF-CSP was manufactured by attaching one of the SS-CMF panels to two 3 mm thick 316 stainless steel face sheets through diffusion bonding.

Multiple dogbone tensile samples were sized in accordance with ASTM-E8 plate standard and cut using a wire electric discharge machine (EDM) from the SS-CMF and SS-CMF-CSP panels [146]. The tensile dogbone samples were cut with a gauge length of 90 mm and a cross section of approximately 12.7x12.7 mm. Following cutting, the samples were hand ground along the surface to remove particulate and discoloration caused by the wire EDM process. The samples were then cleaned in an ultrasonic bath of water and soap solution followed by another bath of acetone in order to remove loose particles and contaminants before testing.

5.2. Tension Testing Setup

The SS-CMF and SS-CMF-CSP dogbone specimens were tested under quasi-static tension using an MTS QTest TM012 universal testing machine equipped with a 98kN load cell. At least three samples were tested from each of the SS-CMF and SS-CMF-CSP panels. The samples were placed within pneumatic grips and displaced at a rate of 1.27 mm/min at room temperature in accordance with ASTME8 control method B [44]. Aluminum spacers were placed on either side of the grip section to ensure the samples were centered properly in the machine to obtain uniaxial loading. The load and displacement were recorded by a computer connected to the frame's load cell and used to create the stress-strain curves. Images of the samples during tension were taken using a digital camera and analyzed following testing to understand the failure of SS-CMF and SS-CMF-CSP under tension. All samples were tested under the same loading conditions to facilitate easy comparison between the results from various tests.

5.3. Tension Results and Discussion of SS-CMF and SS-CMF-CSP

5.3.1. Sample Images

Digital images of the top surface and cross section of a dogbone sample cut from the base SS-CMF using wire EDM are shown in Figure 5-1(a) and (b). The wire EDM process provides a flat, continuous face at the machined edge, as seen in Figure 5-1(a). The top and bottom of each plate was machined flat to create smooth parallel faces on either side of the samples prior to testing. The surface of the sample shows no open porosities as it was manufactured with added powder on the top and bottom of the panel for post-process machining in order to ensure flat and smooth surfaces as shown in Figure 5-1(b).



Figure 5-1: Digital images of the (a) cross section and (b) top surface, of the dog-bone samples cut from SS-CMF-CSP panels using wire EDM followed by surface machining.

5.3.2. Bare SS-CMF Under Tension

The stress-strain curves resulted from tensile tests of the SS-CMF samples are plotted in Figure 5-2(a). Each sample was cut from the same panel and tested using the same loading conditions. They are labeled as Samples 1-4 in Figure 5-2(a). The shape of the curves is expected for metals and more specifically for metal foams [141], [147]. There exists a relatively small linear elastic region beginning between 0.65-0.75% strain followed by plastic deformation until failure. The relatively low strains are expected for metal foams given the porosities and their resulted stress concentrations under tension. The samples had an ultimate tensile stress consistently above 70 MPa with a failure strain between 7.5-8%. The ultimate tensile strength of the base SS-CMF samples was found to be between 75-85 MPa. The average yield strain, yield stress, ultimate tensile stress, failure strain, and elastic modulus of the tested samples are reported in Table 5-1. The energy absorption by the samples up to failure was

found by calculating the area under the stress-strain curve and is reported in units of MJ/m³ in Table 5-1. As can be seen, the tensile strength of SS-CMF is much higher than those reported for other closed cell metal foams [141]–[144], [148]. Given the variation in relative densities of metal foams, it is best to compare the strengths by normalizing their values by each sample's density.

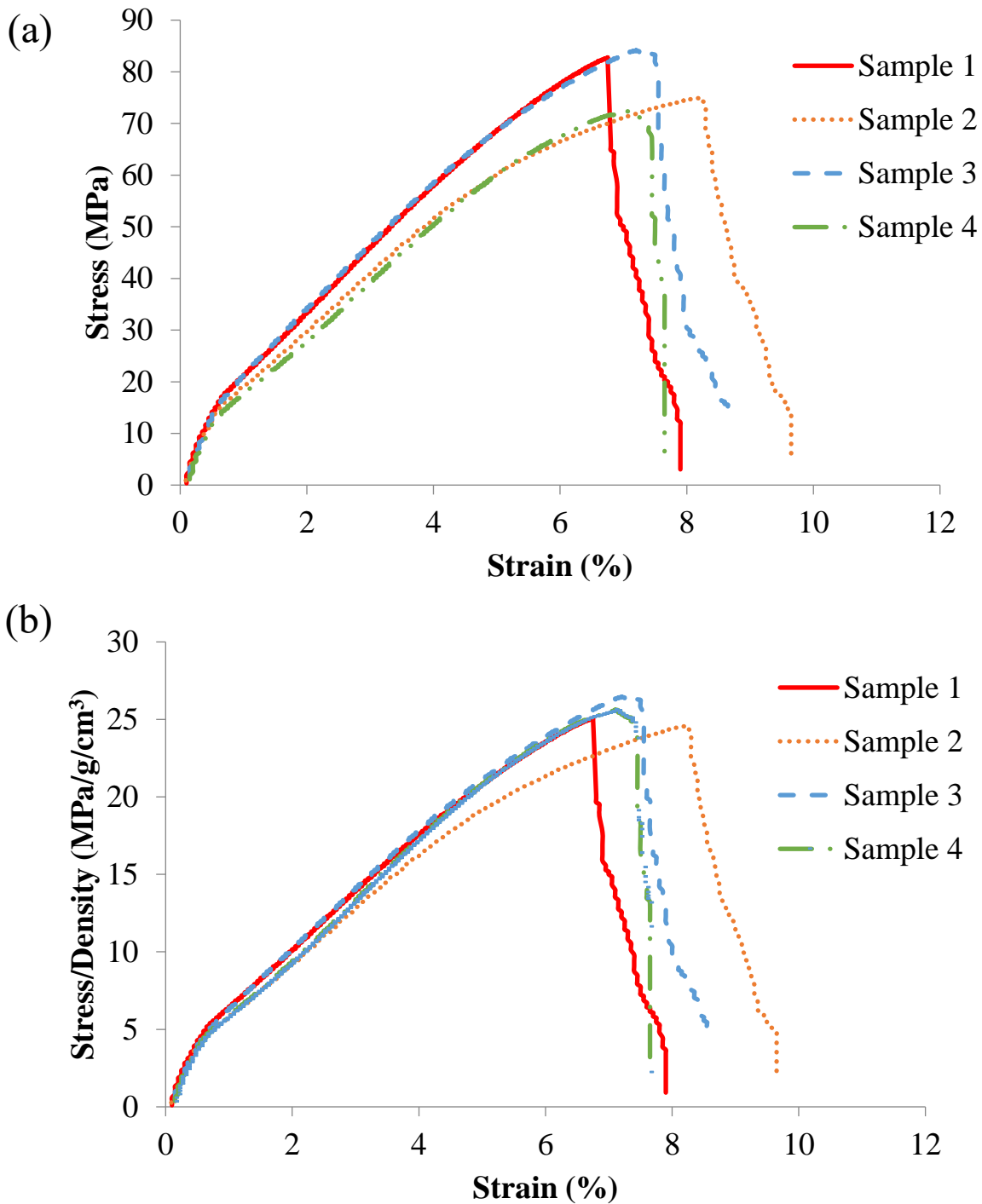


Figure 5-2: (a) Engineering stress-strain curves of the bare SS-CMF samples, and (b) the stress-strain curve normalized by the density of the SS-CMF samples.

Table 5-1: Average mechanical properties for SS-CMF and SS-CMF-CSP tested under quasi-static tension. The values from other metal foams are presented for comparison.

	Tensile Yield Strain (%)	Tensile Yield Stress (MPa)	Ultimate Tensile Stress (MPa)	Tensile Failure Strain (%)	Tensile Young's Modulus (GPa)	Tensile Energy Absorption (MJ/m ³)
SS-CMF	0.63	15.32	77.25	7.75	4.36	2.9
SS-CMF-CSP	5.78	91.66	165	22.9	8.26	20.0
Steel Hollow Sphere Foam (HSF)* [22]	-	3.30	5.35	2.75	3.1	0.15

*The values are approximated from data presented in the respective publications

The normalized stress-strain curves for the bare SS-CMF are plotted in Figure 5-2(b) and show a consistent behavior between the samples given their slight variation in density. When normalized, all of the samples show a maximum tensile stress of approximately 24 MPa/(g/cm³) where other comparable closed cell foams have a maximum normalized strength between 5-10 MPa/(g/cm³) [141]–[143]. The superior strength of SS-CMF compared to other closed-cell metal foams is due to the uniform porosities within the structure and the presence of a matrix that connects and support the spheres. The hollow metal spheres create a consistent porosity size within the SS-CMF's structure compared to other closed-cell metal foams with a larger variation in cell size and cell wall thickness [141], [143]. The unique structure of SS-CMF gives it a normalized tensile strength five times higher than other metal foams and a normalized ultimate tensile strength ten times higher. The specific energy absorption of the SS-CMF under tension was found by dividing the energy absorbed by the density and is

compared to that of other closed cell metal foams in Table 5-2. The specific energy absorption of the SS-CMF is 0.95 J/g whereas other metal foams absorb 0.13 J/g, making SS-CMF a more efficient candidate to be used as the core of sandwich panels.

Table 5-2: Normalized mechanical properties for SS-CMF and SS-CMF-CSP tested under quasi-static tension. The values from other metal foams are presented for comparison.

	Normalized Tensile Yield Stress (MPa/(g/cm ³))	Normalized Ultimate Tensile Stress (MPa/(g/cm ³))	Specific Tensile Energy Absorption (J/g)
SS-CMF	4.79	24.14	0.95
SS-CMF-CSP	20.36	36.67	4.45
Steel Hollow Sphere Foam (HSF)* [22]	1.76	4.73	0.13

*The values are approximated from data presented in the respective publications

Digital images of SS-CMF Sample 1 during tensile testing are shown in Figure 5-3. These images show the failure mode of the base SS-CMF is similar to its parent material (steel), with the cracks initiating and growing along the outer surface and then propagating through the thickness of the dogbone sample. The crack propagation in Figure 5-3(b)-(e) is highlighted by the magnified images at the bottom of the figure. As can be seen in Figure 5-3(b-i), the crack initiated at the surface near a hollow sphere open to the surface. The crack proceeds across the surface of the sample prior to moving through the thickness, as seen in Figure 5-3(d-i). The crack began between 6.0-6.25% strain followed by a rapid progression of failure over a strain percentage of approximately 1% seen by comparing the images in Figure 5-3(c)-(e).

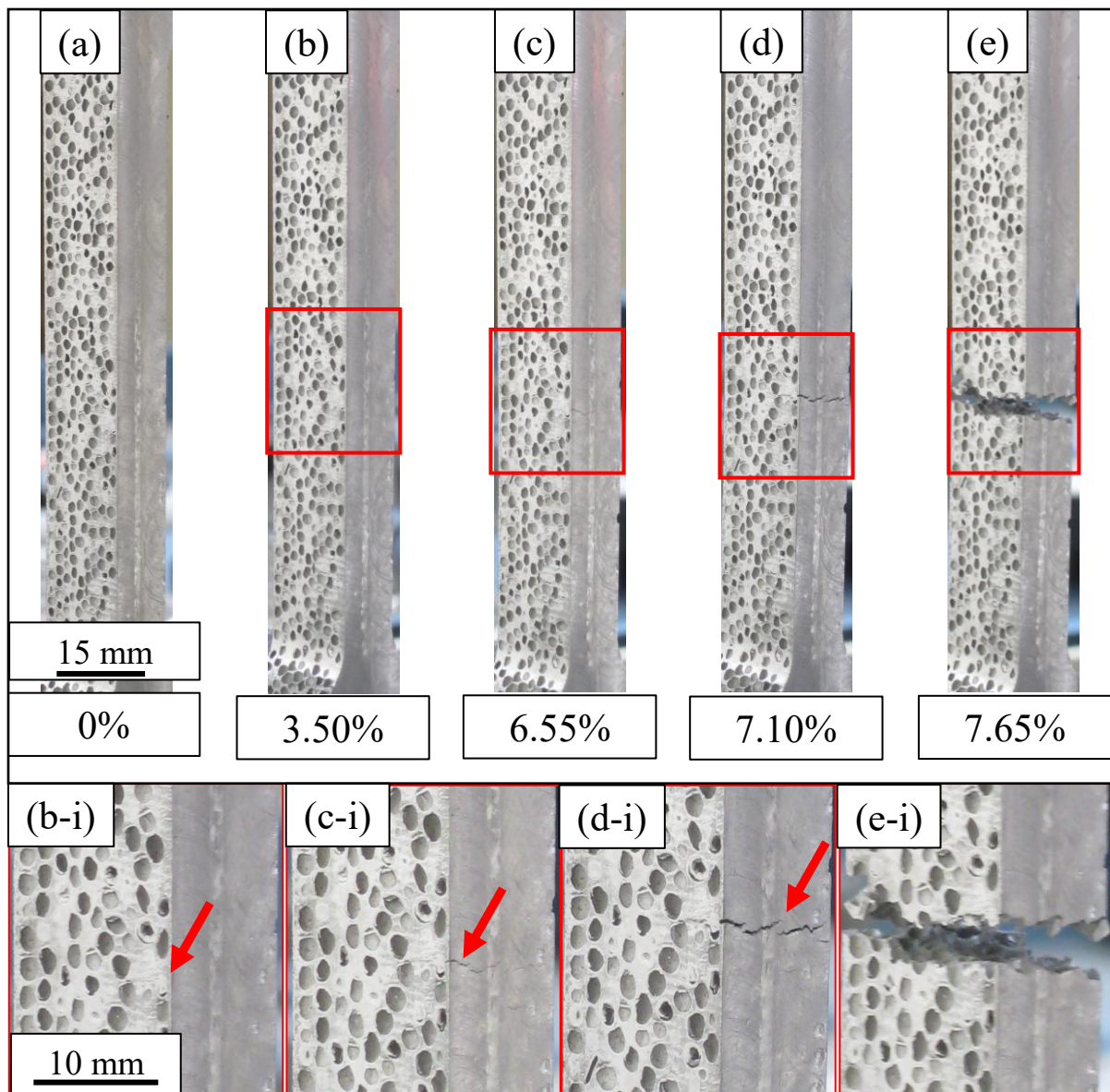


Figure 5-3: Digital images of SS-CMF (Sample 1) under tension showing crack initiation and failure (a) - (e). Higher magnification images of the outlined areas are shown below in (b-i) - (e-i).

Images of the fractured surface of SS-CMF Sample 1 are presented in Figure 5-4. The figure shows that the crack was able to maneuver through the microporosities of the matrix. It seems that the crack propagated mostly through the sphere walls rather than debonding of the spheres from the matrix, as can be seen in the digital fractography images in Figure 5-4(b) and

(c). Debonding of the spheres from the matrix was reported for SS-CMF under four-point bending [97]. However, the fracture across the sphere alludes to a strong bond between the matrix and the sphere walls and indicates optimized processing of SS-CMF. Figure 5-4(a) shows an additional fracture at the far side of the sample where the crack has moved through the sphere wall. There is one sphere that has been removed from the matrix and is highlighted in Figure 5-4(b) as well as the corresponding dimple in Figure 5-4(c). This sphere was pulled from the matrix, most likely due to a slight separation and a weak bond around the sphere wall.

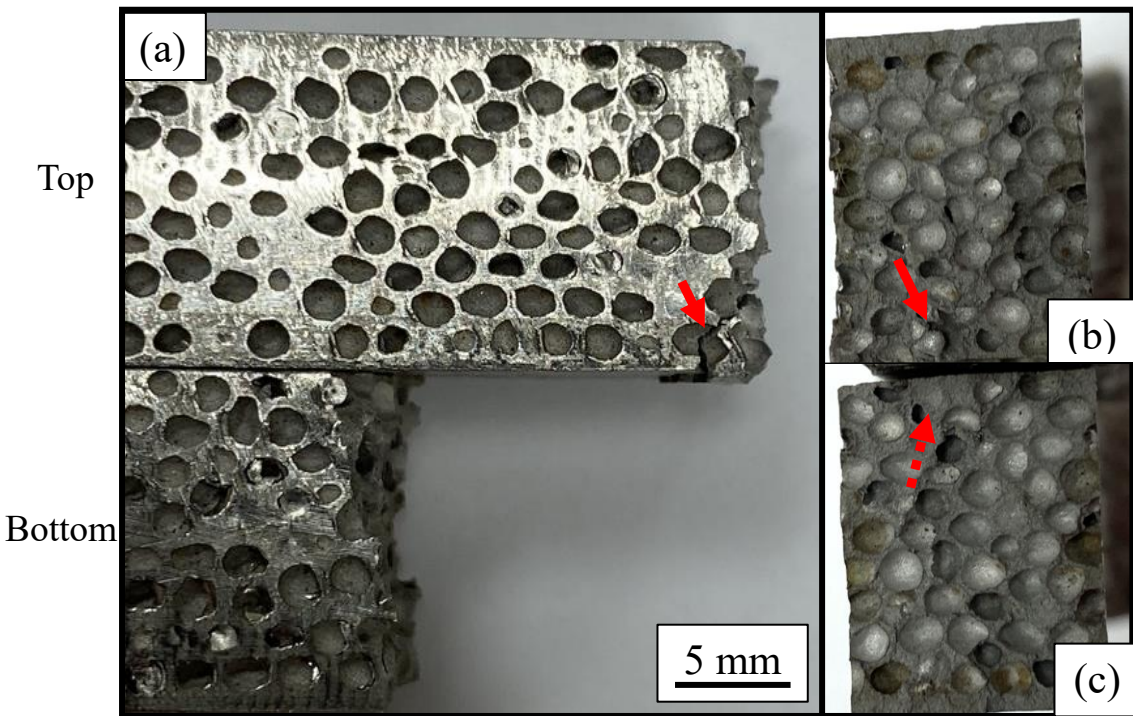


Figure 5-4: Digital images of the SS-CMF (Sample 1) shown in Figure 5-3 after tensile failure. (a) The side of the sample and (b)-(c) the fractography images showing sphere walls tearing rather than debonding from the surface.

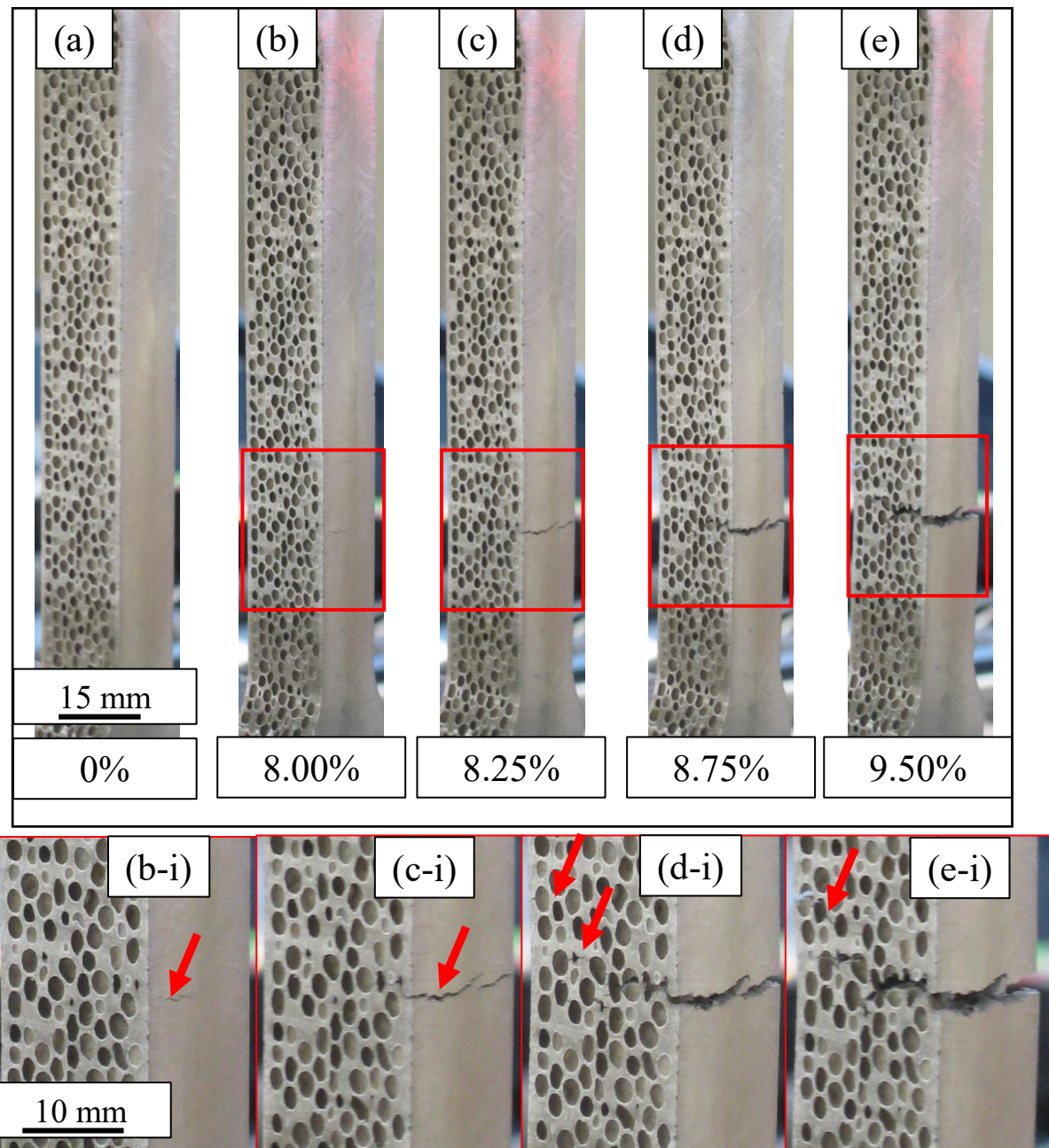


Figure 5-5: Digital images of SS-CMF (Sample 2) under tension with multiple cracks initiating about the same location near failure. The magnified images (b-i)-(e-i) showing crack evolution are highlighted in the respective images above

Images of SS-CMF Sample 2 is shown in Figure 5-5. This sample has a similar failure mode, but with multiple cracks forming at different locations. Higher magnification images of the failure region outlined by the red boxes can be seen at the bottom of the figure. The primary

crack formation can be seen in Figure 5-5(b-i). Additional failure regions separate from the primary crack are seen forming in Figure 5-5(d-i) and Figure 5-5(e-i) on the opposite side of the sample. Failure and cracking across the sphere wall can be seen in Figure 5-5(d-i) at multiple locations. Investigation of the failure surface in Figure 5-6(a)-(d) reveals a similar path of the crack through the sample thickness. The fracture surface in Figure 5-6 shows the broken spheres along the surface as well as additional cracks forming within the sample in Figure 5-6(b) and (d). The sphere highlighted in Figure 5-6(d) shows multiple cracks expanding through the sphere wall along the surface, as well as the secondary crack formation on the opposite face of the sample. The strong bond between the sphere walls and the matrix causes splitting of spheres under tension for the bare SS-CMF.

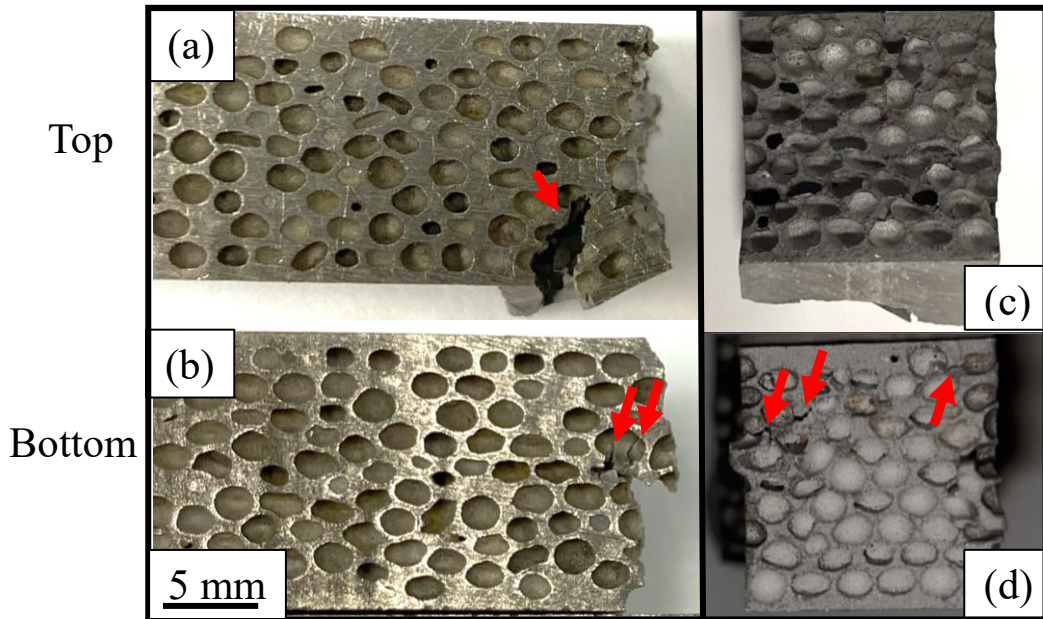


Figure 5-6: Digital images of the SS-CMF (Sample 2) shown in Figure 5-5 with detailed information from the failure surfaces under tension. (a)-(b) the side of the sample and (c)-(d) the fractography images showing failure across the sphere walls. The red arrows highlight the location of additional crack formations around the region of failure.

5.3.3. SS-CMF Core Sandwich Panels Under Tension

The stress-strain curves resulted from tensile testing of SS-CMF-CSP are plotted in Figure 5-7(a). The SS-CMF-CSP samples were all cut from the same panel and loaded using the same conditions. The samples are labeled as Samples 1-3 in Figure 5-7(a). The stress and strain were calculated as a function of the initial total dimensions of the sample, which includes the total thickness of the SS-CMF core and the two face sheets. Digital images taken of the sample during loading indicated that the SS-CMF core fails first while the face sheets continued to elongate further (Figure 9). As such, the first peak of the curve is associated with the failure of the SS-CMF core, followed by the plastic deformation and failure of the stainless steel face sheets at higher strains. These two regions are divided by a vertical dotted line in Figure 5-7(a). The measured mechanical properties of the SS-CMF-CSP are also presented in Table 5-1 below those of the bare SS-CMF properties. The sample had a yield similar to that experienced by the bare SS-CMF between 3.5-4% strain followed by plastic deformation and failure. The yield, prior to core failure, is measured between 90-105 MPa, 500% higher than the bare SS-CMF samples. The ultimate tensile strength of the SS-CMF core increased from 65-80 MPa to 140-175 MPa, 115% stronger than the bare SS-CMF samples. The failure strain of the core also increases from just under 10% to 20-24% with 590% more energy absorbed prior to the failure of the core, not including the additional deformation of the face sheets. The face sheets support the core under tension without completely debonding from its surface. Samples 2 and 3, with their stress-strain curve shown by the dotted and dashed lines, have a very similar strength, whereas Sample 1 represented by a red solid line experienced a lower core failure strength. The lower yield is attributed to the core failing near the fillet area and

close to its radius of curvature due to stress concentrations at the fillet, whereas the other two samples have a very similar yield and failed at the center of the dogbone specimen.

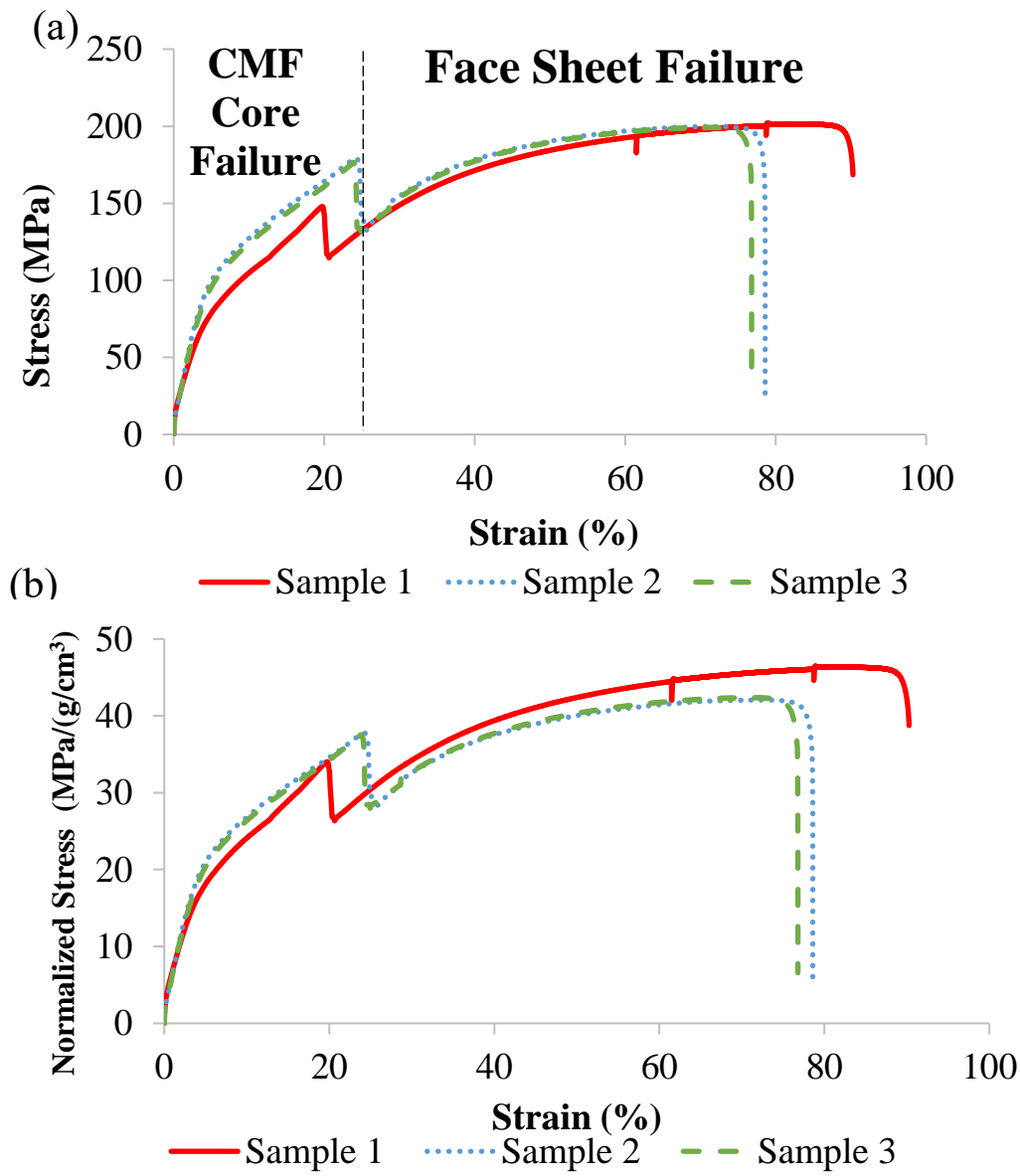


Figure 5-7: Engineering stress-strain curve of (a) SS-CMF-CSP samples. The vertical dotted line divides the CMF core failure region (left) from the additional plastic straining and failure of the face sheets (right). (b) The stress-strain curve normalized by the density of the CMF-CSP samples.

The normalized stress-strain curves are plotted in Figure 5-7(c). All of the SS-CMF-CSP samples have a similar normalized core failure stress between 35-40 MPa/(g/cm³). The average specific energy absorption of the sandwich panels under tension up to the core failure was measured as 4.45 J/g. This is 370% higher than the bare SS-CMF panels. The support of the stainless steel face sheets not only increase the base strength of the core material but also its average normalized values and specific energy absorption, which are listed in Table 5-2. The cores of the SS-CMF-CSP's have a normalized failure stress 52% higher than the bare SS-CMF samples as well as an increased lifetime up to 20% strain to failure, more than double that of the bare samples.

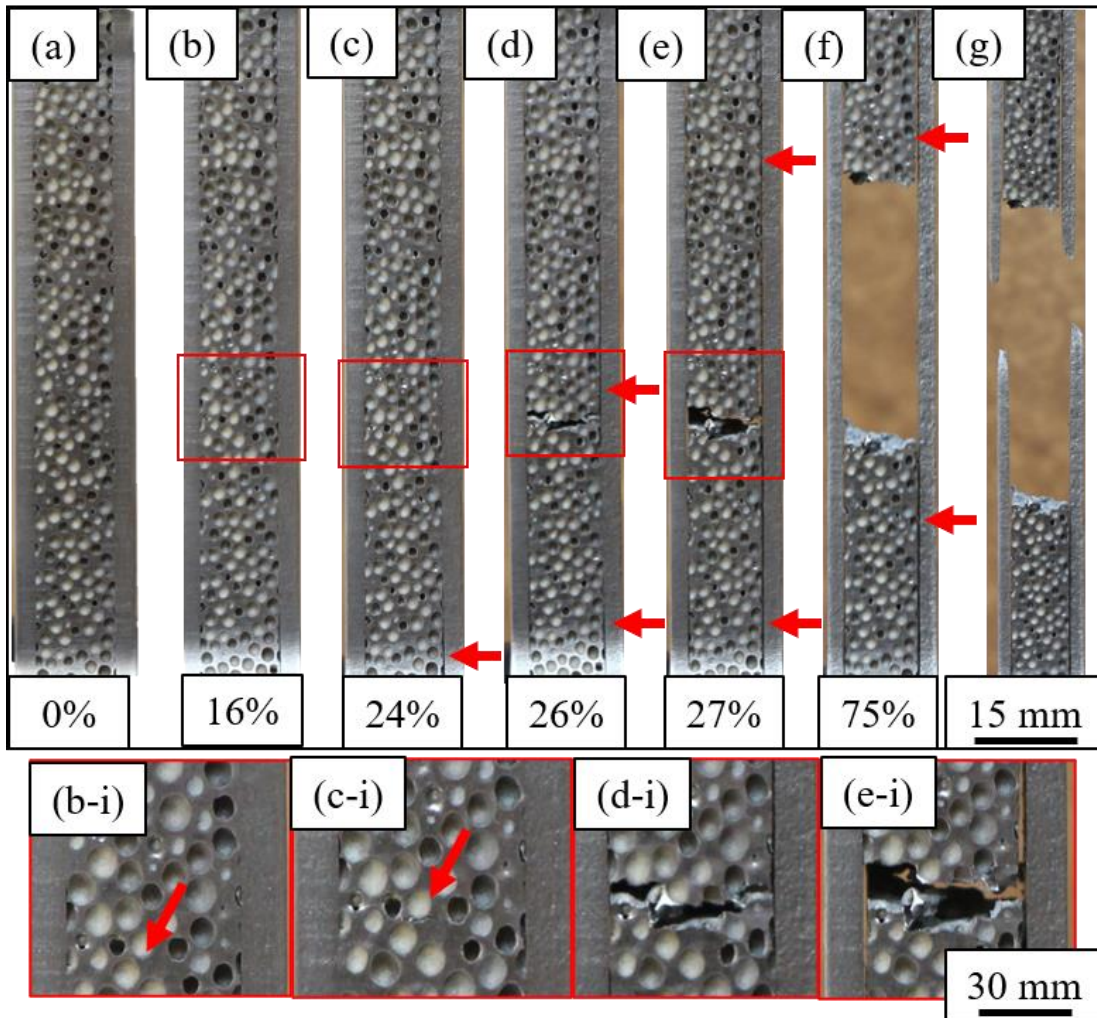


Figure 5-8: Digital images of SS-CMF-CSP (Sample 2) under tension. Higher magnification images of the respective strains are shown at the bottom of the figure. The sample was imaged (a) prior to loading, (b) slight debonding occurred just prior to major deformation, and (c) crack initiation at the center of the sample. (d)-(e) Crack growth in the core leads to failure (f) with further debonding and face sheet yielding until (g) failure of the face sheets.

As can be seen in the digital images of SS-CMF-CSP Sample 2 in Figure 5-8, the diffusion bond between the core and the face sheet maintains its integrity up to the core failure but undergoes slight debonding just outside the grip area at 16% strain (Figure 5-8(b)). Debonding does not spread until after crack initiation in the sample and complete core failure as seen in Figure 5-8(c)-(e). Unlike the bare SS-CMF samples, failure of the SS-CMF-CSP

initiates from within the core's thickness, as can be seen in the highlighted regions at the bottom of the figure. The face sheets lend enough support to delay the core's onset of failure until the crack starts from the center of the core and moves outwards towards the surface, as seen in Figure 5-8(c-i). The crack can be seen forming at the edge of a sphere wall within the center of the core. The crack initiation is most likely due to coalescence of the microporosities that exist in the matrix, similar to that of the bare SS-CMF. The crack then grows towards the surface causing further debonding of the face sheets from the SS-CMF core around the gripped section and at the center of the sample in Figure 5-8(d). Following core failure, the stainless steel face sheets yield up to fracture. Face sheet failure are shown in Figure 5-8(f) and (g) with increased debonding highlighted by the red arrows. The failed sample in Figure 5-8(g) shows necking of the face sheets at the point of failure. It shows that the diffusion bond creates a strong enough interface between the core and face sheets to promote strengthening of the core without limiting the deformation of the face sheets at high strains. The overall strength of the SS-CMF sandwich structure can be further optimized in future testing in order to achieve the desired strength/weight ratio for specific applications.

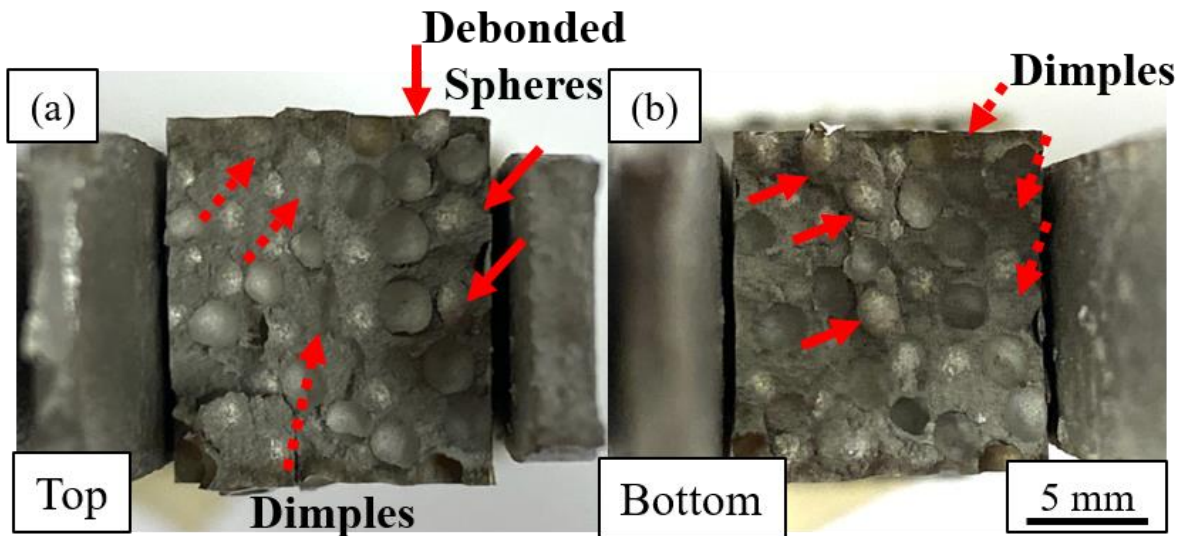


Figure 5-9: Fracture surfaces of the SS-CMF-CSP sample imaged in Figure 5-8 (Sample 2) with a mixed mode of failure when compared to the bare CMF. The sample fractures by tearing the sphere walls, but also slight detachment of the sphere walls from the matrix highlighted by red arrows. Removed spheres are shown by the solid arrows and their corresponding dimples by dotted arrows can be seen in the (a) top and (b) bottom fracture surfaces.

Digital fractography images of SS-CMF-CSP Sample 2 are shown in Figure 5-9. The SS-CMF-CSP's fracture surface is different from the bare SS-CMF samples and shows debonding of the sphere walls from the matrix, much more than the bare SS-CMF, as can be seen in Figure 5-9(a) and (b). The debonded spheres are highlighted by solid red arrows and their corresponding dimples are pointed to by dotted arrows in Figure 5-9(a) and (b). The debonding of the sphere walls from the matrix occurred similarly in all SS-CMF-CSP due to microstructural changes experienced during the diffusion bonding process. The heat cycle causes grain growth within the sphere wall, as seen in the SEM images in Figure 2. This will increase the ductility of the spheres when compared to the bare SS-CMF. The heat cycle also allows for diffusion of elements between the sphere walls and the matrix. During the diffusion bonding process, carbon diffuses out from the sphere wall into the surrounding matrix, due to

its higher starting carbon content. This allows for additional carbide formations within the matrix and along the matrix interface with the sphere wall. The carbides create a more brittle bond with the outside of the sphere walls. The brittle interface, in conjunction with improved ductility within the sphere walls, causes debonding of the sphere walls from the matrix in some locations of the SS-CMF-CSP during tensile failure. This causes the mixed failure mode seen in the SS-CMF-CSP samples in Figure 5-9.

5.3.4. Analytical Approximation

Rule of Mixtures

The rule of mixtures can be used to approximate the properties of the SS-CMF by proportionally combining the properties of the hollow steel spheres and sintered 316L stainless steel matrix. The volume fraction of the hollow spheres and matrix have been previously measured as 59% and 41% respectively given the random-loose packed arrangement of the hollow metal spheres within the SS-CMF [103]. The Young's modulus of the closed-cell hollow sphere foam (HSF) that makes up the macro-porous structure inside the SS-CMF has previously been approximated as 2.047 GPa using Eq. (1) [101]. This value is relatively consistent with what has been found experimentally for hollow sphere foams made with a variety of steels [144], [149]. As for the matrix, Falkowska and Seweryn have reported the elastic modulus of sintered 316L stainless steel for a variety of porosities under tension [150]. The tap density of the SS-CMF matrix has previously been measured as 4.25 g/cm³, which is equivalent to a porosity percentage of approximately 46% [96]. The measured modulus of 316L sintered stainless steel with a porosity of 41% was reported as 32.9 GPa and was used for calculation of the SS-CMF modulus. The rule of mixtures gives the elastic modulus of SS-CMF as:

$$E_{SS-CMF} = [V_{HSF} \times E_{HSF}] + [V_M \times E_M] \quad (3)$$

$$E_{SS-CMF} = 14.74 \text{ GPa} \text{ (upper bound)}$$

where V_{HSF} and V_M are the volume fraction of the hollow spheres and matrix, respectively. E_{HSF} and E_M are the values used as the Young's modulus inputs for the spheres and matrix. Eq. (3) gives the upper bound of the rule of mixtures and the inverse rule of mixtures is used to evaluate the lower bound values as:

$$E_{SS-CMF} = \left[\frac{V_{HSF}}{E_{HSF}} + \frac{V_M}{E_M} \right]^{-1} \quad (4)$$

$$E_{SS-CMF} = 3.33 \text{ GPa} \text{ (lower bound)}$$

The experimentally measured modulus of elasticity of the bare CMF samples under tension was 4.36 GPa. This falls between the upper and lower bounds calculated using the rule of mixtures. The rule of mixtures can also be used to approximate the modulus of the SS-CMF-CSP since it has the addition of the face sheets. The lower and upper bound can be calculated using the bulk metal properties of 316 stainless steel and the experimental values achieved for bare SS-CMF. The volume fractions are changed from the matrix and sphere walls to the bare SS-CMF and the bulk stainless steel face sheets. The face sheets of the SS-CMF-CSP had a volume fraction of 65% SS-CMF core and 35% face sheets. Using the above values for 316 stainless steel reported in the ASM handbook and the experimental values of the bare SS-CMF, the lower and upper bound of the elastic modulus are 6.6 - 71 GPa. The experimental value of 8.3 lies within the calculated range closer to the approximated value from the inverse rule of mixtures.

5.4. Summary of SS-CMF and SS-CMF-CSP under Tension

The mechanical properties of SS-CMF and SS-CMF-CSP were explored through quasi-static tension testing. The face sheets were found to improve the failure stress and strain of the

SS-CMF-CSP samples. Failure analysis of the tension samples revealed the primary reason for crack initiation and growth in the bare SS-CMF and the sandwich panels. The elastic modulus of the bare SS-CMF and SS-CMF-CSP were approximated using the rule of mixtures. The rule of mixtures gives a good approximation for the Young's modulus with the measured values of both the SS-CMF and the SS-CMF-CSP being between the approximated lower and upper bound. The face sheets on the SS-CMF-CSP not only improve the mechanical performance of the SS-CMF core, but also provide a non-porous surface that can protect against corrosion and be used in a variety of engineering applications, including the head shield and shell of tank cars.

CHAPTER 6: BALLISTIC PERFORMANCE OF COMPOSITE METAL FOAM AGAINST LARGE CALIBER THREATS

The previous chapters investigated the quasi-static mechanical properties of CMF core sandwich panels primarily for their potential application in train car head shields and shells for improved puncture resistance. This section moves on to testing and reporting on CMF armors facing various ballistic threats [138]. Initial testing of CMF hard armor systems facing 7.62 x 51 mm ball and 7.62 x 63 mm armor piercing rounds (AP) has previously been reported [122], [123]. The preliminary data showed promising results using CMF hard armors to effectively defeat both ball and AP threats. This study builds on the prior work and explores the use of CMF hard armors to defeat larger caliber ballistic threats such as the 12.7 x 99 mm ball and AP rounds, also known as the 0.50 caliber ball and AP. A finite element analysis of the AP ballistic impact was used to validate the experimental findings and build upon the current model for CMF armor systems.

6.1. Experimental Procedure

6.1.1. Materials and Processing

The CMF panels were manufactured using the powder metallurgy technique developed in previous works and outlined in Chapter 3 [96], [97]. The CMF panels were manufactured in 25 x 25 cm and 30 x 30 cm sizes with a variety of thicknesses. A digital image of a CMF panel prior to assembly is shown in Figure 6-1 with a cross-sectional view of the internal structure created by the hollow spheres (Figure 6-1(b)). The CMF panels were layered with a ceramic faceplate and a thin aluminum 7075-T6 backplate. The ceramic tiles were purchased in two sizes from separate companies, Saint-Gobain and M Cubed Technologies Inc.

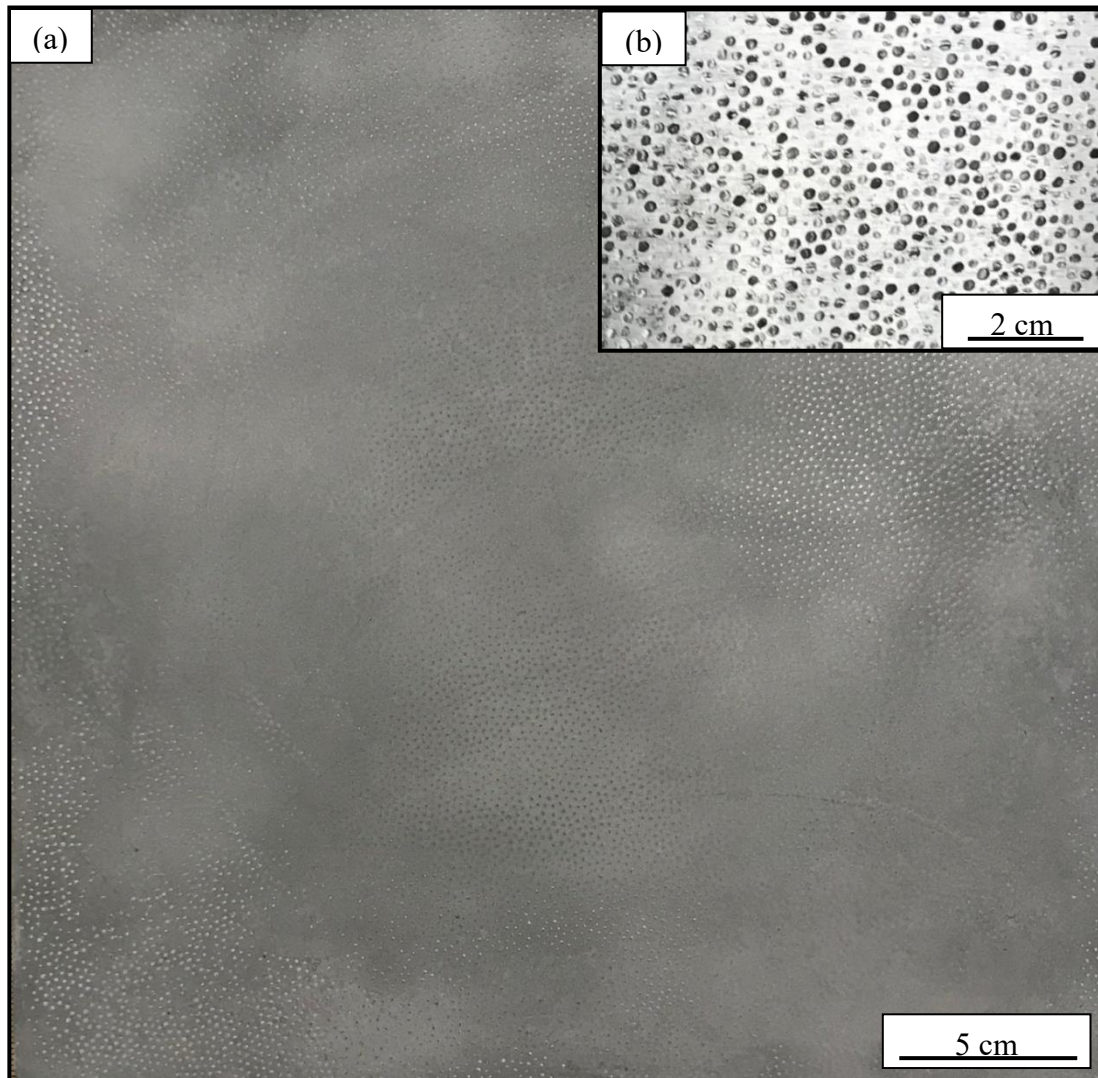


Figure 6-1: Digital images of (a) CMF panel prior to assembly showing the surface of the as-processed panel and (b) cut surface showing the internal structure.

The sandwich panels were assembled following the manufacturing process outlined in Section 3.2.2. A diagram of the hard armor layering and the direction of impact is labeled in Figure 6-2, note that the thicknesses in the figure are not to scale. The thickness of each individual layer was varied to maintain a small range of areal densities for testing against ball and AP threats.

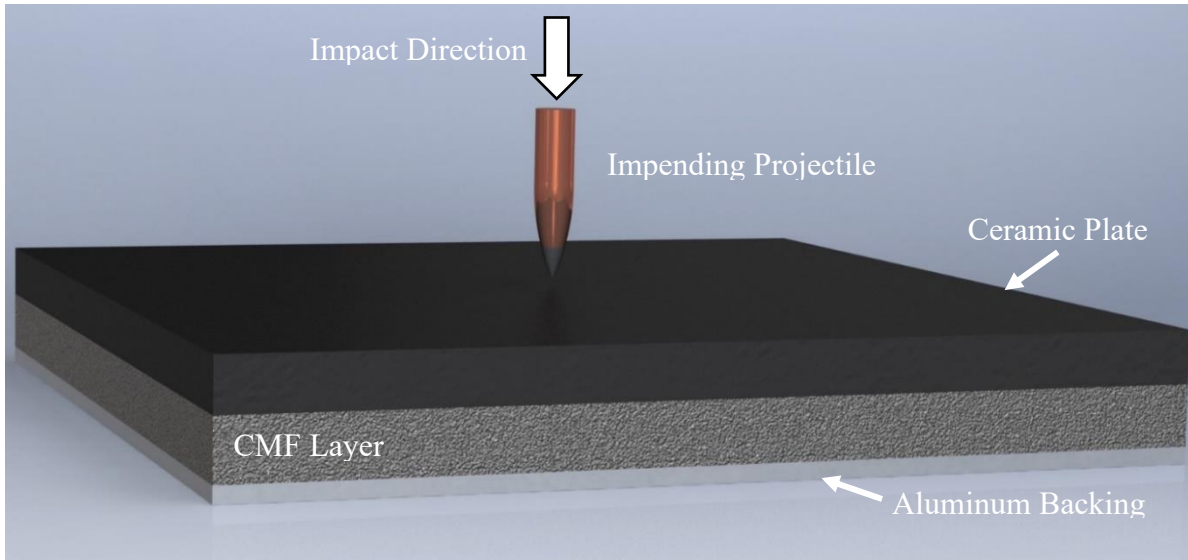


Figure 6-2: Diagram of the multi-layered hard armor system with the CMF layer bonded between the ceramic faceplate and aluminum 7075-T6 backing. The presented dimensions are not to scale.

6.1.2. Ballistic Testing Procedure

The ballistic tests were performed at the Aviation Development Directorate following the MIL-STD-662F [151]. The projectiles tested in this study were the 12.7 x 99 mm ball and 12.7 x 99 mm AP. Both rounds consist of a copper jacket and lead filler surrounding the core. The ball projectile has a mild steel core at its center, whereas the AP round has a hardened steel core. The physical properties of the projectiles are listed in

Table 6-1 and a diagram of their size is presented in Figure 6-3 [24]. The projectiles were fired from a Mann gun placed 5m away from a heavy-duty steel frame used to clamp the armors into place. The armors are supported along their outer edges where they are attached to the steel frame. The samples are impacted at the center of the armor as to reduce the amount of energy transferred to the fixture. Figure 6-4 shows a schematic of the testing setup. The velocity was accurately measured using three velocity chronographs placed between the Mann

gun and the sample. A high-speed camera was set facing the front of the target to verify the speed of impact of the round. The rounds were fired at a 0° obliquity between the projectile and the normal to the armor surface. The direct impact presents the worst-case scenario of impact and the highest risk of penetration.

Table 6-1: Dimensions of the impacting rounds and their inner core used in ballistic testing [24].

Projectile	Length (mm)	Projectile Diameter (mm)	Mass (g)	Core Length (mm)	Core Diameter (mm)	Core Mass (g)	Core Material
12.7 mm Ball	58.7	12.98	42	47.5	10.9	22	Mild Steel
12.7 mm AP	58.7	12.98	45.9	47.5	10.9	25.9	Hardened Steel

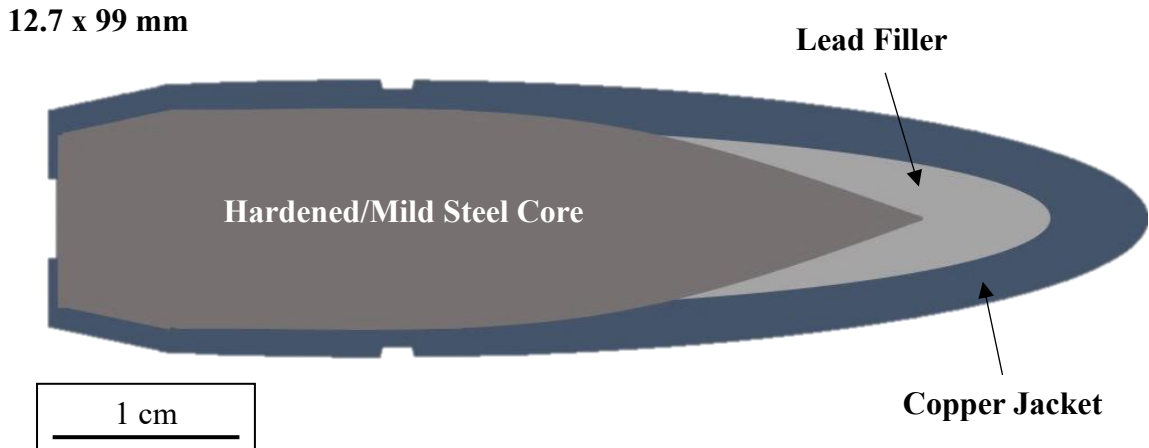


Figure 6-3: Diagram of the 12.7 x 99 mm ballistic projectile used for testing under MIL-STD-622F standard.

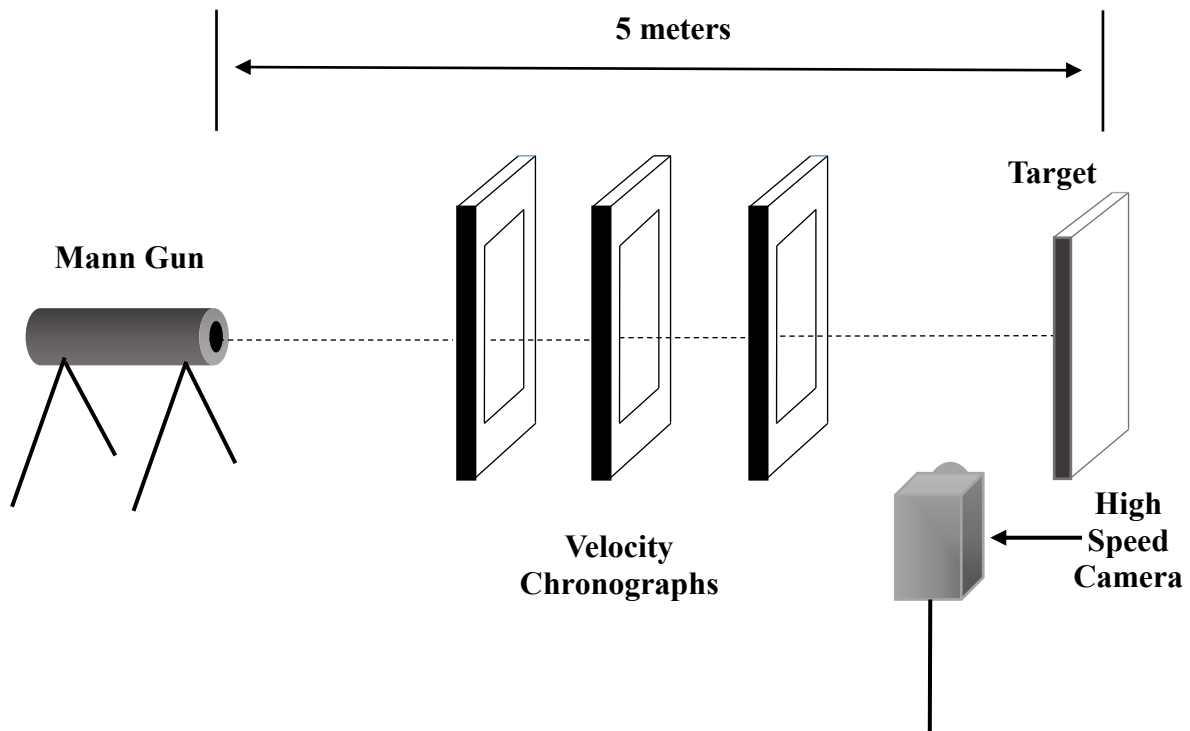


Figure 6-4: Diagram of the ballistic testing setup showing the positioning of the Mann gun, velocity chronographs, target, and high-speed camera.

The MIL-STD-622F standard is widely used for V₅₀ and armor penetration analysis of potential vehicle armors. The V₅₀ of an armor is defined as the impact velocity at which the

projectile has an equal chance of penetrating the armor as it is to be stopped. For this testing, an impact was considered complete penetration (CP) if the core pierced the armor creating a hole large enough that light could be seen through. If a hole was not created through the armor, the projectile was considered stopped and is referred to as a partial penetration (PP). According to MIL-STD-622F, the V_{50} is calculated by finding the arithmetic mean of an equal number of CP and PP tests. At least two of the lowest speed CP and two highest speed PP impacts are needed to find a consistent V_{50} value [151]. The V_{50} can be used to compare the performance of CMF hard armor to commercially available armors against the same threat.

6.1.3. Analytical Energy Absorption Analysis

An analytical method, similar to that used in previous publications, was implemented to calculate the energy absorption of each layer of the CMF armors [123], [152]. The energy of an impacting round was dissipated through compression and fracture of the ceramic faceplate followed by compression in the CMF layer and slight deformation of the aluminum backplate. In order to estimate the energy absorption of each layer in the CMF hard armor, a strain energy approximation is used. Under a partial penetration of the hard armor, the total kinetic energy of the bullet (E_{KE}) is shared between the compression and fracture of the ceramic face ($E_{Ceramic}$), compressive yielding of the CMF (E_{CMF}), ductile yielding of the aluminum backing plate (E_{BP}), and fracturing/erosion of the bullet's core (E_{Bullet}). An energy balance equation was used to back-out the energy absorption of the CMF layer:

$$E_{KE} = E_{Bullet} + E_{Ceramic} + E_{CMF} + E_{BP} \quad (1)$$

The strain energy of each material was calculated using the respective stress-strain curves by approximating the area under the curve and multiplying by the volume of deformed material. The volumetric strain energy (w_p) was calculated in J/m³ by Eq. (2):

$$\omega_p = \int_0^{\varepsilon_f} \sigma d\varepsilon \quad (2)$$

The stress-strain curves needed to approximate the volumetric strain energy for the ceramic and aluminum are taken from previous work [123] while the mild steel ball parameters are approximated using data by Iqbal et al. [153]. Brittle fracture of the hardened steel AP core is expected and a 2GPa fracture stress was used to calculate the energy absorbed during impact, consistent with previous studies [154]. The volume of deformed material of the ceramic faceplate and backing plate can be measured from the tested panels. The volume was then multiplied by the material's plastic strain energy to determine the approximate energy absorbed by that layer during impact. These values were subtracted from the total kinetic energy of the impact (E_{KE}) where the residual energy can be attributed to the CMF layer (E_{CMF}).

6.1.4. Finite Element Analysis

Finite element analysis (FEA) was implemented to validate the experimental findings and can be used to optimize the armors for future ballistic testing. A variety of computational procedures and hydrocodes can be used to model such an impact. ANSYS/AUTODYN Explicit Dynamics solver was chosen in this study to validate the experimental findings. ANSYS/AUTODYN offers both Lagrange and Smooth Particle Hydrodynamic (SPH) solvers, both of which can be used for ballistic impact modeling. SPH is a meshless solver effective at modeling ceramic interactions but is more computationally intensive than the Lagrangian solution. For this reason, the Lagrange formulation was preferred as it was able to model various layers and reduce the overall computational time.

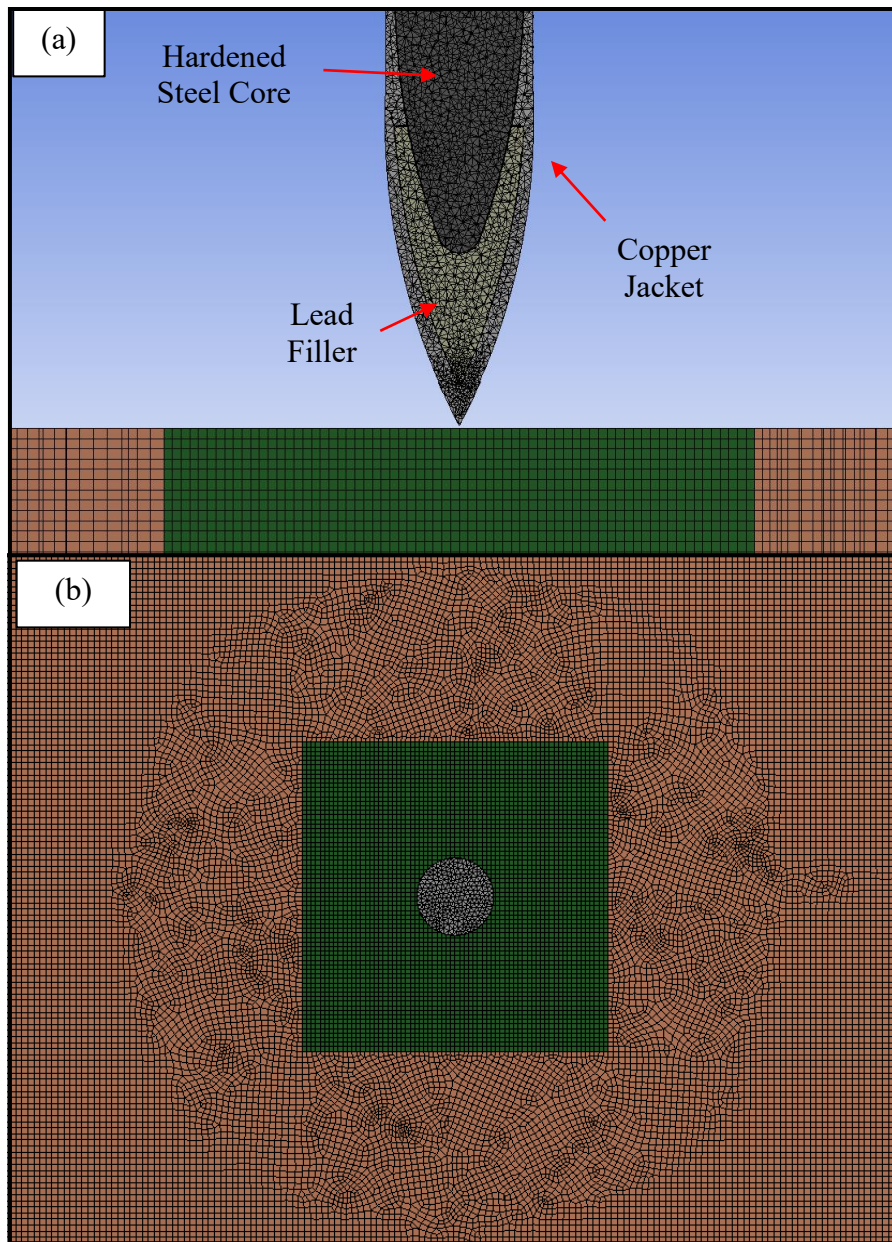


Figure 6-5: (a) Cross section of the projectile highlighting the hardened steel core surrounded by the lead filler and encased in the copper jacket. (b) View of the meshed model from above using a 0.75mm fine mesh for the projectile and primary point of impact. The fine mesh is surrounded by a coarser mesh as it transitions away from the center of the plate.

The ballistic model was built to replicate testing of the 12.7 x 99 mm AP round with an impact velocity of 800 m/s. The 3D model included the three layers of the CMF hard armor

(ceramic faceplate, CMF, and aluminum backplate) as well as the core, casing, and lead filler of the 12.7 x 99 mm AP projectile. The bullet's geometry matches the sizing presented in Table 6-2. The modeled projectile was considered to have a total mass of 49 g with the hardened steel core accounting for 24.4 g. The projectile was placed directly above the ceramic faceplate and assigned an instantaneous velocity of 800 m/s. Figure 6-5(a) shows a cross section view of the projectile and the components that make it up. The core of the round was made to be ogive at the end as a sharp point would receive errors when solving. The projectile was meshed using 0.75 mm size tetragonal elements. Frictionless body interactions were implemented to achieve a conservative impact result [155].

Table 6-2: Material Parameters for the projectile and the aluminum backing plate of the CMF hard armor.

	Density (g/cm ³)	E (GPa)	Poisson Ratio	A (MPa)	B (MPa)	n	c	m	T _{melting} (°C)	Tangent Modulus (GPa)	Erosion Strain
Copper (OHFC) [156], [157]	8.9	115	0.31	206	505	0.42	0.01	1	1100	-	0.3
Lead [157], [158]	11	17	0.29	10	61	0.163	0.41	1	400	-	0.15
Hardened Steel Core [159]	7.85	210	0.33	1,400	-	-	-	-	-	15	0.12
Al 7075 [160]	2.8	72	0.33	546	678	0.71	0.024	1.56	650	-	2

The armor was modeled as a full 25 x 25 cm panel with an areal density of 10 g/cm² based on the average arrangement that resulted in partial penetration in our experimental studies. The armor layers were meshed using two primary regions of hexagonal shaped elements across the armor. A fine meshed region was created about the center of the armor as a 25 cm² square area with a mesh size of 0.75 mm. The area away from the center of the plate was meshed using a maximum element size of 1 mm. A smooth transition mesh was created to connect the two regions. The meshed plate and the smooth transition between the two regions are shown in Figure 6-5(b). The same meshing protocol was used for the ceramic, CMF, and aluminum layer. The armor system was constrained using fixed supports on all outer edges to match the boundary conditions of the experimental work.

An important constraint of solving a high speed Lagrangian problem is the erosion criteria of elements. Without the proper criteria, elements may become eroded too quickly or not at all and cause computational errors while solving [72], [153]. High speed impact models use a variety of erosion techniques in order to achieve a coherent solution [72], [155]. The erosion of the elements in this model was defined by a principal erosion strain for each material paired with a minimum global time step erosion. The erosion criteria of each layer were defined by a material failure strain as well as a minimum time step of 3E-9 seconds. If a given element's time step was smaller than the 3E-9 seconds, the element would be considered too distorted and be eroded from the model. The principal erosion strain is presented alongside the constitutive material parameters.

Material Models

Two constitutive models, the Johnson-Cook and Johnson-Holmquist strength models, were used to describe the behavior of the materials that make up the bullet and various

components of the CMF armor in the finite element analysis. The Johnson-Cook (JC) relation is a visco-plastic model designed for ductile materials at high strain rates [156]. The constitutive model calculates the flow stress, σ_Y , as a function of plastic strain, ε_p , and strain rate, $\dot{\varepsilon}^*$, given by:

$$\sigma_Y = [A + B\varepsilon_p^n][1 + C \ln \dot{\varepsilon}^*][1 - T_H^m] \quad (3)$$

The material constants include the yield strength, A, the strain hardening constant, B, strain hardening exponent, n, and the strain rate sensitivity constant C. T_H and m are the homologous temperature $\{T_H = (T-T_{ref})/(T_{melting}-T_{ref})\}$ and thermal softening exponent respectively. Since the JC model is widely used for predicting the behaviors of various materials under high strain rates, most material parameters can easily be found in literature. The Johnson-Cook parameters used to simulate the bullet's shell and lead filler are presented in Table 6-2 [157], [158]. The harden steel core uses a simplified bilinear kinematic hardening model up to a prescribed fracture strain previously reported in literature and includes calibration of the erosion strains for the bullet's components and boron carbide ceramic [72]. The aluminum backplate also uses the JC strength model and the parameters are included in Table 6-2 [160].

Due to the brittle nature of the ceramic faceplate, it cannot be well represented by the JC model. For this reason, a separate model is needed to simulate the ceramic layer in the armor model. The Johnson-Holmquist (JH) model was first proposed to describe the brittle response of ceramic materials undergoing large deformations [161]. The JH2 model is an improvement of the original JH equations and is used to represent the progressive damage evolution of ceramics through a strength and pressure relationship [162]. The material is modeled by an intact strength, σ_i^* , a fractured strength, σ_f^* , and a pressure to volumetric strain relationship that

mitigates the transition between both states defined by the set of equations below [162]. The normalized equivalent stress, σ^* , is calculated from the normalized intact strength and fractured strength, as well as the damage parameter, D ($0 < D < 1$) [162].

$$\sigma^* = \sigma_i^* - D(\sigma_i^* - \sigma_f^*) \quad (4)$$

where the normalized intact and fracture strength are given by [162]:

$$\sigma_i^* = A[P^* + T^*]^N[1 + C \ln \varepsilon^*] \quad (5)$$

$$\sigma_f^* = B[P^*]^M[1 + C \ln \varepsilon^*] \quad (6)$$

The material constants are the intact strength (A), fracture strength (B), strain rate constant (C), fracture strength exponent (M), and intact strength exponent (N), while P^* and T^* are the normalized pressure and maximum hydrostatic tensile strength of the ceramic [162]. P^* and T^* are normalized by the pressure at the Hugoniot elastic limit (HEL) [163]. The HEL is the pressure at which the material undergoes a transition from an elastic state to an elastic-plastic state [163]. Above the HEL, the material loses its strength and becomes fluid in nature.

The damage for fracture is determined by the plastic strain increment, $\Delta\varepsilon_p$:

$$D = \sum \frac{\Delta\varepsilon_p}{\varepsilon_f^p} \quad (7)$$

and the plastic strain to fracture is calculated from the expression:

$$\varepsilon_f^p = D_1[P^* + T^*]^{D_2} \quad (8)$$

Where D_1 and D_2 are the damage constants of the ceramic material. The hydrostatic pressure before the onset of damage is defined by the linear equation of state (EOS) [162]:

$$P = K_1\mu + K_2\mu^2 + K_3\mu^3 \quad (9)$$

In which μ is the current density, $\mu = \frac{p}{p_0}$, while K_1 , K_2 , and K_3 are the equation of state material constants.

The boron carbide ceramic faceplate was modeled using the JH2 model paired with a linear shock equation of state [164], [165]. The model parameters are listed in Table 6-3. The erosion strain for the ceramic model against an AP core using a similar mesh size was previously calibrated by Krishnan et al. [72].

Table 6-3: Johnson-Holmquist 2 material parameters for B₄C ceramic panel [164], [165].

Property		Units	Value
Density	ρ	g/cm ³	2.63
Hugoniot Elastic Limit	HEL	GPa	19
Intact Strength Constant	A	GPa	0.97
Intact Strength Exponent	N	GPa	0.67
Strain Rate Constant	C		0.005
Fracture Strength Constant	B		0.73
Fracture Strength Exponent	m		0.85
Maximum Fracture Strength	SF _{MAX}	GPa	3
Damage Constant 1	D1		0.001
Damage Constant 2	D2		0.5
Bulking Constant	b		1
Hydrodynamic Tensile Limit	T _{MAX}	GPa	0.26
Pressure Coefficient 1	K1	MPa	233
Pressure Coefficient 2	K2	MPa	-593
Pressure Coefficient 3	K3	MPa	2800
Erosion Strain			8

The CMF model has a unique stress-strain curve and strain rate sensitivity that is not easily represented by the JC or JH2 constitutive relations. CMF is known for its large plateau stress, under compressive loading, that expands across a large strain range from 5-55% [96], [98], [99], [107], [119]. CMF also undergoes strengthening at high strain rates that increases the yield strength and energy absorption of the material [107], [119]. In order to save computational time, the CMF layer was modeled as a solid homogeneous material with the same physical and mechanical properties as the porous CMF, disregarding the geometry created by the hollow metal spheres and the effect of air within its porosities. CMF has been modeled in the prior works using a multilinear stress-strain curve [122], [166]. The defined multilinear stress-strain curve is preferred as the strengthening, strain rate sensitivity, and unique load path of CMF at high strain rates are inherently built into the model.

The bulk modeling properties for the composite metal foam layer remains consistent with previous works [122], [166]. The density of CMF was considered as 2.8 g/cm^3 and the Youngs modulus and Poisson ratio are 13.2GPa and 0.2 respectively [101]. The experimentally achieved quasi-static and dynamic stress-strain curves of CMF are shown in Figure 6-6 [107]. The strengthening of CMF can be seen by the higher stresses induced at increasing strain rates in Figure 6-6 [107]. Interestingly, after a sharp rise in the yield strength, the stress-strain curve of CMF under high speed impact returns to a relatively quasi-static curve above 30% strain as can be seen in Figure 6-6 [107]. The percent increase in volumetric energy absorption (MJ/m^3) of CMF for impacts at 1523 1/s (27 m/s), 2629 1/s (47 m/s), and 3728 1/s (67 m/s) were 108%, 126%, and 133% respectively [107]. The strain rate equivalent to CMF under ballistic impact (800 m/s) is more than ten times larger than the presented stress-strain curves, hence a much larger strengthening effect is expected. The multilinear stress-strain curve used to model CMF

is based on the energy absorption capabilities of the material calculated using the analytical approximation equations based on the experimental findings. For implementation in the ANSYS/AUTODYN material model, the software requires an ever-increasing stress with a positive slope. In order to accommodate for the initial peak in yield stress, the stress-strain curve is built to replicate the overall shape of the experimentally obtained high strain rate curves and a positive slope without a return to the quasi-static shape at 30% strain. However, the total strain energy of the material is kept constant. The multilinear material model for simulating the CMF armor against impact of the 12.7 mm AP round requires further input from the energy absorption calculations derived from the experimental results.

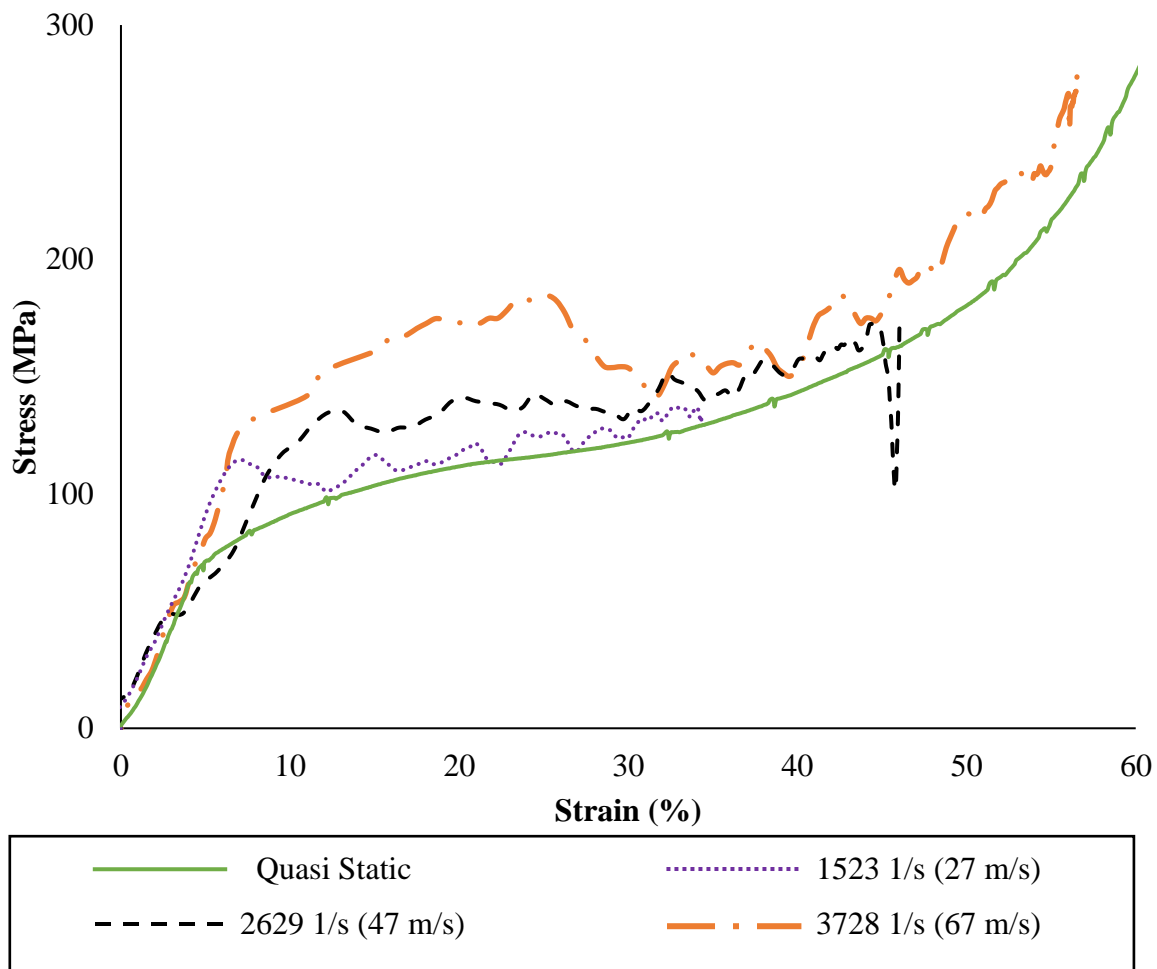


Figure 6-6: Stress-strain curves of CMF samples at quasi-static and dynamic loading [107].

6.2. Results and Discussion

6.2.1. Ballistic Results

12.7 x 99 mm Ball Results

Table 6-4: Properties of the ballistic tests organized by projectile type and impact velocity. The areal density, kinetic energy, and whether the test was partial penetration (PP) or complete penetration (CP) is listed.

Panel	Projectile Type	Areal Density (g/cm ²) [lbs./ft ²]	Impact Velocity (m/s)	Bullet Kinetic Energy (J)	PP/CP	Note
B1	Ball	8.87 [18.2]	717.19	10802	PP	
B2	Ball	9.96 [20.4]	730.30	11200	PP	Ball
B3	Ball	9.13 [18.7]	790.35	13118	CP	
AP1	AP	7.42 [15.2]	496.52	5793	CP	AP: First Set
AP2	AP	7.76 [15.9]	514.20	6213	PP	
AP3	AP	10.36 [21.2]	718.11	12118	PP	
AP4	AP	10.23 [21.0]	773.28	14052	PP	
AP5	AP	10.13 [20.7]	787.00	14555	PP	AP: Second Set
AP6	AP	10.40 [21.3]	792.48	14759	PP	
AP7	AP	10.00 [20.2]	793.39	14793	PP	
AP8	AP	10.23 [21.0]	801.01	15078	PP	
AP9	AP	10.53 [21.6]	815.64	15634	PP	
AP10	AP	10.48 [21.5]	819.30	15775	PP	Tests used to Calculate V ₅₀
AP11	AP	10.20 [20.9]	828.75	16140	CP	
AP12	AP	9.71 [19.9]	844.30	16752	CP	
AP13	AP	9.64 [19.7]	885.75	18437	CP	
V ₅₀	AP	10.06 [20.6]	830	16189	-	V ₅₀

Table 6-4 lists the results of the ballistic testing with the samples organized by the type of threat, areal density, and impact velocity. Out of the three panels tested against 12.7 x 99 mm ball rounds, one had a series of nine 10 x 10 cm ceramic faceplates arranged over the surface to cover the 30x30 cm CMF panel. The other two samples had a single 30 x 30 cm ceramic faceplate and are used to compare the performance between the two arrangements. Images of the front and back of B1 and B2 CMF armors following testing of a 12.7 x 99 mm ball round are presented in Figure 6-7. B1 used a single ceramic panel and had the lowest areal density and impact velocity of the three tests. It can stop the impacting round, but experiences fracture within all three layers, including the aluminum backing. B2 has a higher areal density and impact velocity but shows no sign of the impact on the aluminum backing (Figure 6-7(d)). It indicates that the CMF layer was able to absorb the residual kinetic energy of the round after it was eroded by the ceramic faceplate. The region of impact in B2 is isolated to the center ceramic tile, showing the benefit of the multiple tile arrangement over a single ceramic layer. The tiles surrounding the center are still intact and able to be tested for multi-impact capabilities. This effect is inherent to CMF armors as it cushions the bullet's impact and begins to compress and densify in a localized region. The same mechanism can be seen during impact of CMF panels against blast waves with high speed metal fragments [166]. The compressibility of the CMF layer preserves the ceramic faceplates from excessive damage. The speed of impact for B3 was too great for the sample's ceramic and CMF thickness and experienced a complete penetration. The ball round tests yielded initial results that compare the effectiveness of a multiple tile arrangement over a single faceplate and the efficacy of the CMF hard armors against mild steel core threats. The AP rounds, however, are more piercing and challenging to defeat.

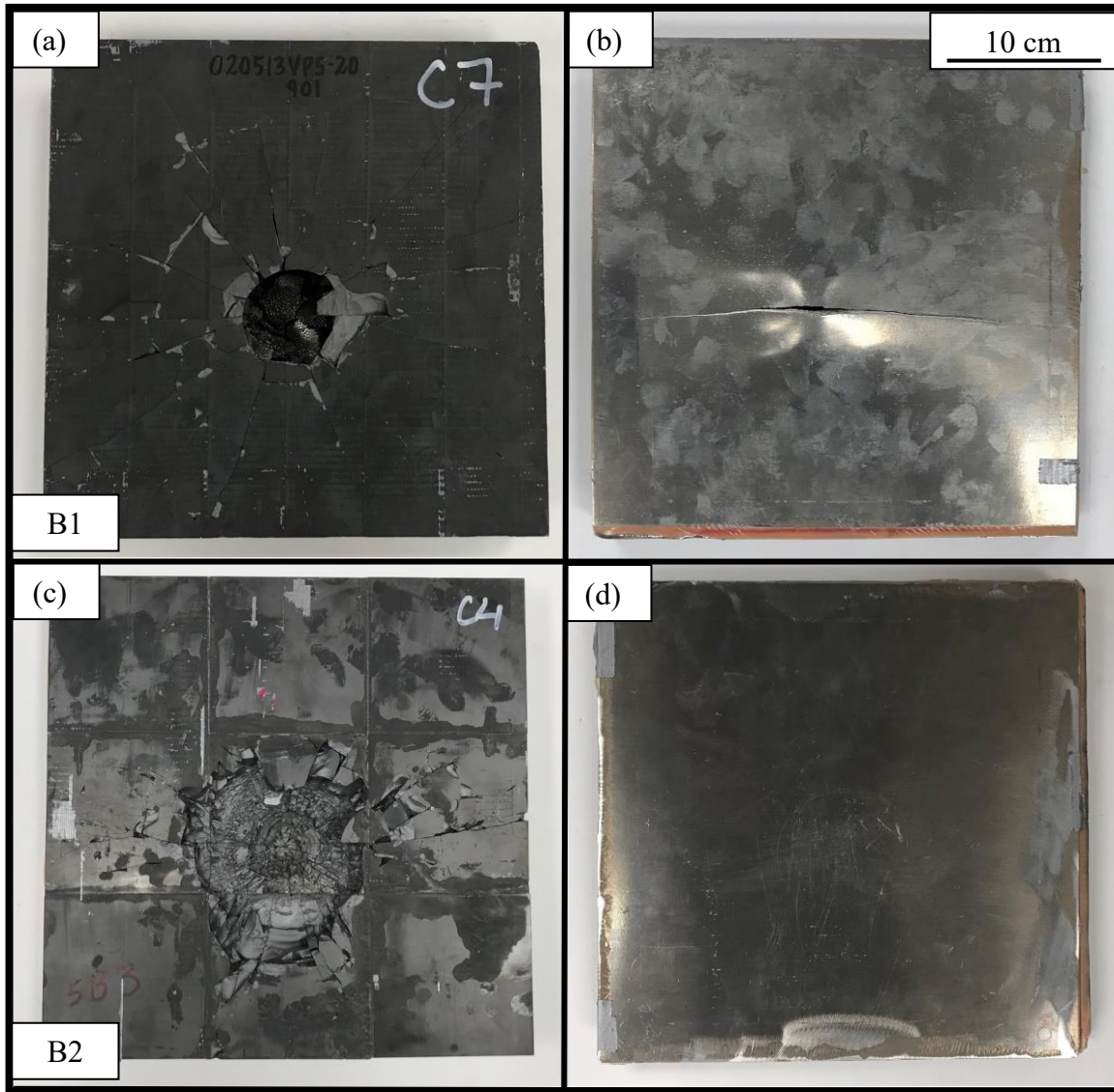


Figure 6-7: (a, c) Front and (b,d) rear images of CMF hard armor samples tested against the 12.7 x 99 mm ball threat.

12.7 x 99 mm AP Results

The areal density, impact velocity, and penetration of the AP tests are also listed in Table 6-4. The areal densities of the of the 12.7 x 99 mm AP tests and their impact velocity are plotted in Figure 6-8. The samples are plotted as PP (triangle) or CP (circle). Overall, fourteen samples were tested against the AP threats, with 9 PP and 5 CP. The tests

were completed in two sets. In the first set (AP1-AP2) the CMF armors were tested at lower impact speeds with areal densities below 8g/cm^2 to verify the ability of the hard armors to defeat the 12.7 mm AP rounds. AP1 was the first 12.7 x 99 mm AP test completed on a CMF hard armor. The complete penetration of AP1 can be attributed to the low areal density of the panel and early failure of each layer. Figure 6-9(a)-(d) shows the front and back surfaces of AP1 and AP2 after testing. AP1 was manufactured with a slightly lower areal density and tested at a similar velocity. The outcome shows cracking and shear plugging of the aluminum backplate in Figure 6-9(a-b). This test suggests that the armor requires a thicker ceramic and CMF layer to stop impacts at higher speeds. AP2 was able to stop a 514 m/s round with no visible bulging on the back panel. The bulging and deformation of the aluminum backplate is also referred to as the backface signature (BFS) of the armor. The BFS is measured through post analysis of the armor and is defined by the diameter and height of the deformed material. The initial tests were essential in determining approximate areal densities required to stop the AP threat at higher impact velocities.

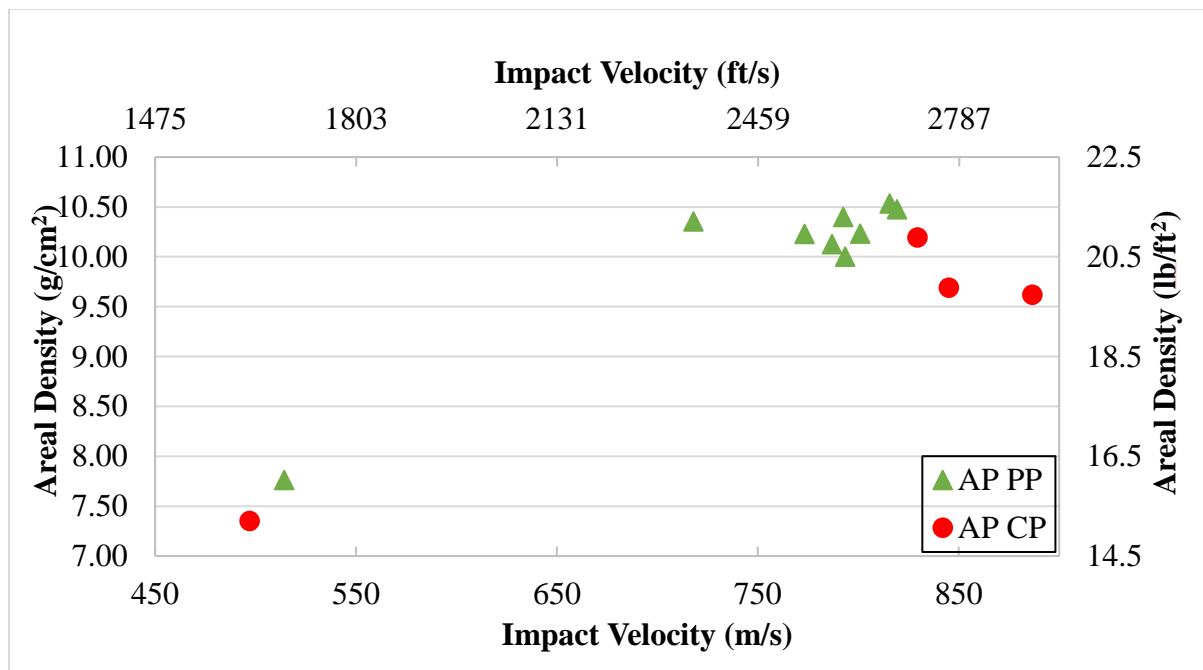


Figure 6-8: Areal Density and impact velocity of PP (triangle) and CP (circle) tests of the 12.7 x 99 mm AP against CMF armors.

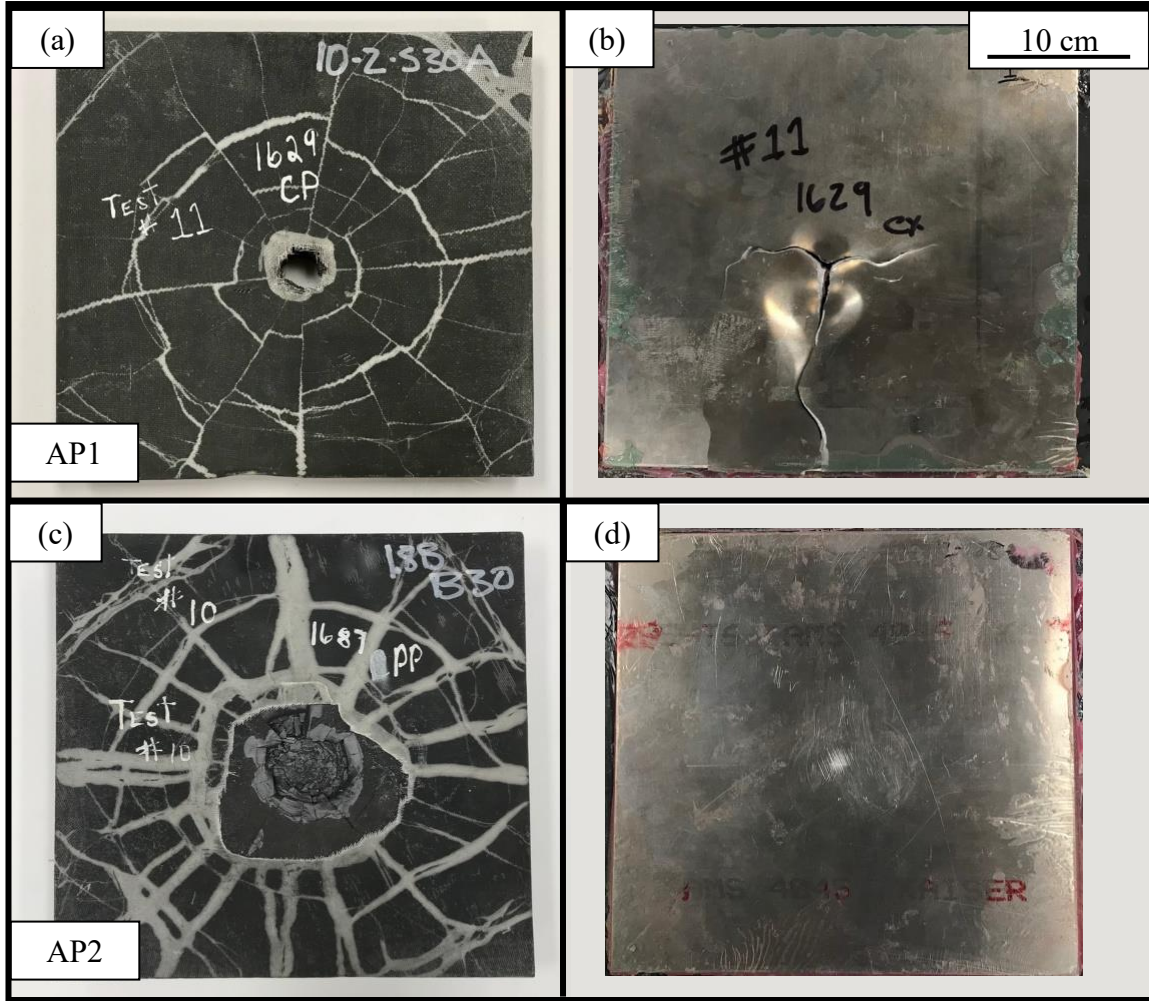


Figure 6-9: Front (a and c) and rear (b and d) images of the initial tests run of CMF hard armors against 12.7 mm AP threats.

The second round of testing was completed at higher impact velocities on samples with an increased areal density (Samples AP3-AP13). Figure 6-10(a-d) shows some of the panels that were tested at velocities below 800 m/s. Similar to the first round of testing, the damage on the ceramic is isolated to the primary point of impact with radial cracks extending toward the edge of the panel. The radial cracks are caused by the reflective shock wave created by the impedance mismatch between the ceramic and the CMF. The radial cracking on the CMF armors is minimal as can be seen in Figure 6-10. Below the removed ceramic we can see the

depressed surface of the CMF, evidence of the yielding and impact energy absorption of the CMF layer. These samples have a consistent BFS with minimal bulging and no apparent cracking of the aluminum backplate. AP8 is used as a representative of the three PP panels tested at speeds above 800 m/s (AP8-AP10). Front and back images of AP8 are presented in Figure 6-10(e-f). As can be seen, the ceramic interaction with the hard steel core of the bullet remains similar to the previous CMF armors. The diameter of impact on the front and back of the armor are consistent while the BFS remains negligible. The BFS increases slightly as the kinetic energy of the bullet reaches the upper limits of what can be absorbed by the current CMF layer. In samples AP3-AP6, there is limited deformation in the back plate as the CMF layer was able to absorb the bullet's kinetic energy without reaching its full densification strain of 55-60%, as shown in Figure 6-6. In AP8-AP10, the CMF layer approaches its maximum energy absorption and strain limit as can be seen by the increased residual energy shared with the aluminum backing (Figure 6-10(e-f)). The slight increase in BFS at impacts above 800 m/s is evident of complete compression and densification of the CMF layer. These samples present the effectiveness of the CMF layer's high energy absorption during high-strain rate impacts by the limited deformation and failure of the ceramic faceplate and aluminum backplate.

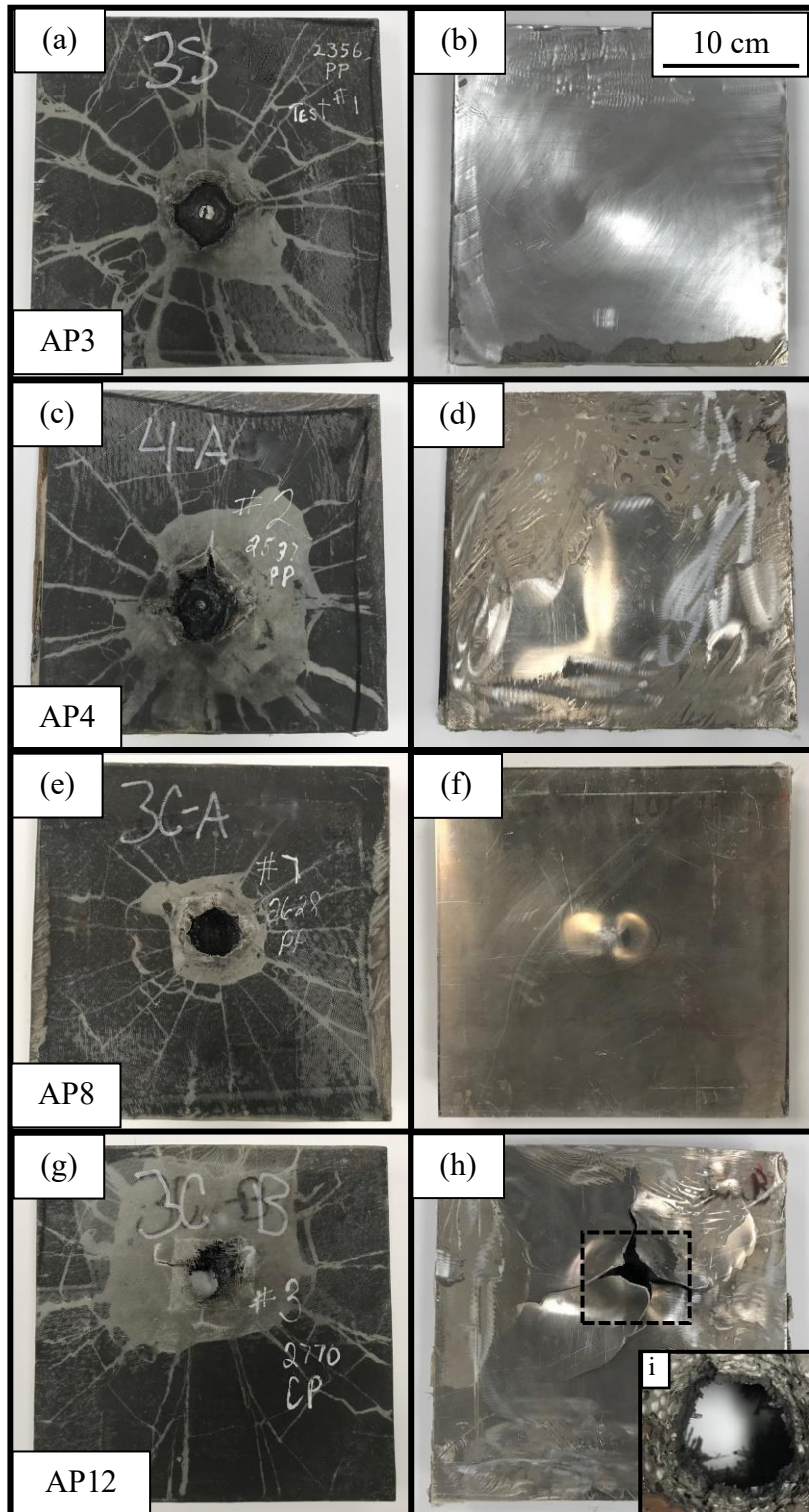


Figure 6-10: Front (a, c, e, g) and rear (b, d, f, h) images of CMF hard armors impacted by 12.7 x 99 mm AP threat with a zoom in of the crushed spheres found below the backplate of AP12 (i).

Figure 6-10(g-h) shows AP12 armor after testing above 820 m/s resulting in complete penetration. The aluminum backplate experiences a mixed mode of tensile and shear fracture about the point of impact. Further optimization of CMF armors followed by repeated testing is required to create CMF armors that can stop the 12.7 x 99 mm AP threat at impacting velocities above 820 m/s. The total CMF armor has yet to be optimized to ensure the maximum amount of erosion within the ceramic, maximum energy absorption by the CMF, optimal support provided by the aluminum backing and adhesive bonds between each layer while minimizing the overall weight. It should be noted that some of the AP samples experienced varying degrees of delamination between the CMF and aluminum backing at higher impact velocities. The tested panels herein used simple assembly techniques with minimum control over the thickness of the adhesive layer that can be further optimized for commercial implementation and eliminate the delamination issues. In Figure 6-10(h) partial delamination and cracking of the back plate can be seen extending to the edge of the panel. This type of failure hinders the overall performance of the armor by allowing the CMF layer to be prematurely separated from the aluminum backing prior to being completely compressed. The tests do not result in the preferred outcome but do show some insight to the working mechanisms within the armor and more specifically, the CMF layer.

Figure 6-10(i) shows the crush zone of AP12 with compressed hollow spheres under and around the primary impact area indicating the key mechanism of energy absorption in CMFs, which is the compression and densification of porosities in the material. The aluminum layer can better support the CMF during compression with improved bonding and optimization of the epoxy layer. Grujicic *et al.* determined the thickness and type of the adhesive layer has significant impact on the performance of a hybrid armor system [167]. In this case a structural

epoxy was used for the adhesive layer, while future arrangements may benefit from the use of elastomeric based adhesives. Elastomeric adhesives allow for more isolated cracking and failure of the ceramic faceplate and limit the in-service loads experienced by the armor when applied to the exterior of a vehicle [167], [168].

The V_{50} for the CMF hard armors was calculated using the impact velocities and areal densities of targets AP8 - AP13. The V_{50} is needed to compare the performance of CMF hard armor to commercially available RHA and other high performing steel armors. The V_{50} of these armors is approximately 830 m/s with an average areal density of 10.06 g/cm². The mass efficiency ratio was calculated in comparison to RHA's performance at the same impact velocity as per MIL-DTL-12560K [35]. The mass efficiency ratio (MER) is calculated by dividing the areal density of RHA, required to stop the bullet at a specific impact velocity, by the areal density of the tested armor at the same velocity. The calculated MER are plotted in Figure 6-11 for PP (triangle), CP (circle), and the V_{50} value (X) as a function of the impact velocity. Ultra-high hardness (UHH) Bisalloy steel armor has also been tested against 12.7 mm AP threats by Ryan *et al.* [45]. The results of their testing are plotted alongside CMF's MER for further comparison and are denoted by black squares. The UHH armors offer partial penetration and a MER at lower impacting velocities [45]. Conversely for the CMF armors, the mass efficiency increases alongside higher impact velocity. The V_{50} result yields a MER of approximately 2.1 for the 12.7 x 99 mm AP impact of CMF armors at velocities above 800 m/s, meaning the CMF hard armors can stop the round at less than half the weight required by the equivalent RHA. It is notable that these results are from a completely unoptimized armor structure with off-the-shelf ceramic, aluminum, adhesive and rudimentary assembly techniques. A higher MER would be expected with further optimization of each element in the

CMF armors. The weight reduction is primarily due to the lower density of the armor and its constituents as well as the extraordinary energy absorption and toughness of CMF during high-strain rate impacts.

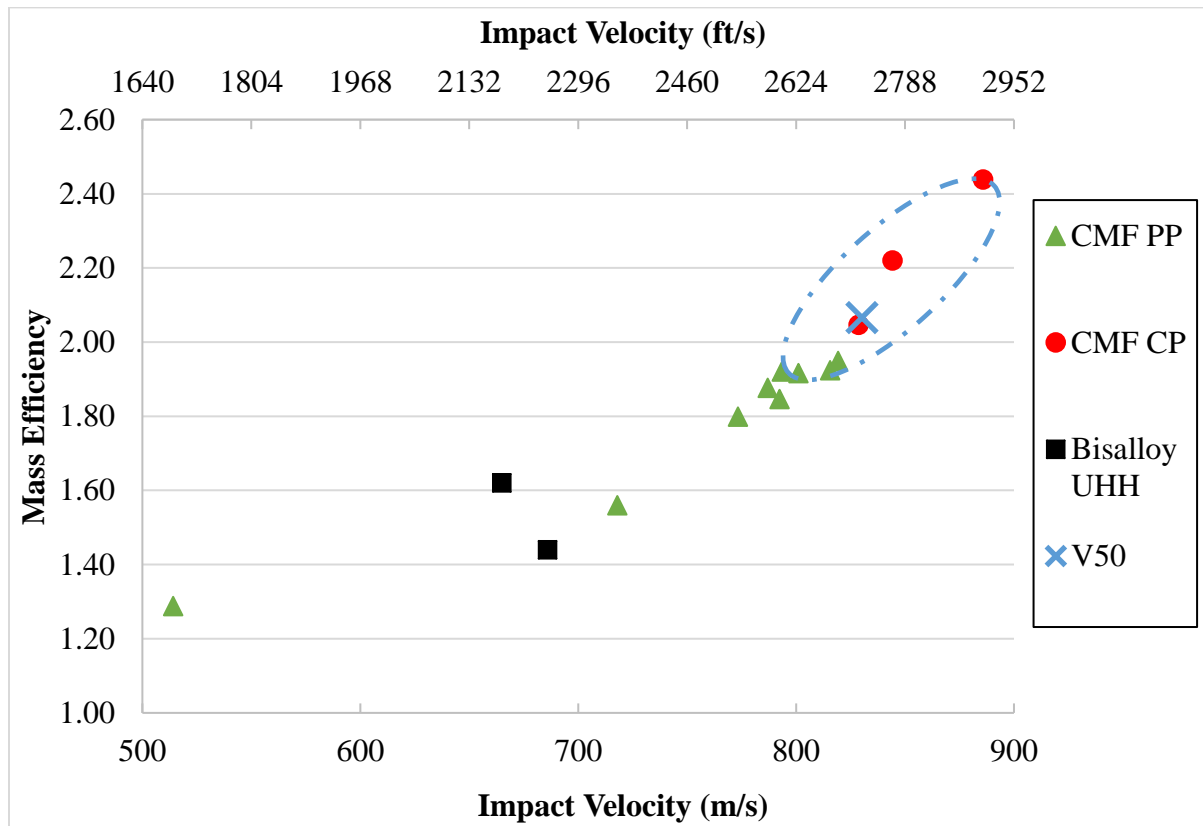


Figure 6-11: Mass efficiency of CMF hard armors and commercially available Bisalloy ultra-high hardness steel plate [45]. The blue dotted line encompasses the samples that were used to calculate the V₅₀.

6.2.2. Computational Results

Analytical Energy Absorption

Table 6-5: Percent of energy absorbed by each layer in the CMF hard armor system for all PP impacts.

Panel	Projectile Type	Impact Velocity (m/s)	Bullet Energy (J)	Ceramic and Fragment Motion %	Bullet %	Backplate %	CMF %
B1	Ball	717	10802	16	3	5	76
B2	Ball	730	11200	20	3	4	73
AP2	AP	514	6213	24	4	3	69
AP3	AP	718	12118	24	2	3	71
AP4	AP	773	14052	22	2	2	74
AP5	AP	787	14555	17	2	4	77
AP6	AP	792	14759	20	2	3	75
AP7	AP	793	14793	16	2	4	78
AP8	AP	801	15078	16	2	4	78
AP9	AP	816	15634	16	2	3	79
AP10	AP	819	15775	16	2	4	78

The percent of energy absorbed by each layer of the CMF armor when tested against 12.7 x 99 mm ball and AP were calculated using the analytical approximation discussed in Section 2.3 of this article and are presented in Table 6-5. Only the energy absorption of PP impacts is calculated as the exit velocity of the round was not measured for CP tests, and therefore the energy absorption cannot be accurately estimated. The energy absorption assigned to the bullets is approximated following analysis of the remaining cores that were retrieved following testing. The mild steel cores (Figure 6-12(a)) reveal plastic deformation of approximately 50% of their volume while the retrieved fragments of the AP round (Figure 6-12(b)) show brittle fracture of the hard core and plastic deformation of the copper casing. The motion of the ceramic and bullet fragments ejected from the surface of the armor is assumed to make up 4-5% of the overall energy of the impact given the sizing of the ceramic and bullet fragments found following testing and is included in the energy attributed to the ceramic faceplate ($E_{Ceramic}$) [152], [169], [170]. Using the methods described in Section 2.3, the bullets absorb up to 4% and 5.5% of the AP and ball round's kinetic energy respectively and CMF layer was calculated to absorb 72-75% of the ball round's kinetic energy and 68-78% of the AP round's kinetic energy (Table 6-5). The variation in energy absorption is due to the volume of shattered ceramic and the resulting volume of CMF that is compressed underneath during impact. There is a larger percentage of energy absorbed by the ceramic layer in AP3 and AP4 when compared to AP7-AP10. This is evident by the larger diameter, and overall volume, of ceramic fractured in Figure 6-10(a) and (c) compared to Figure 6-10(e). The larger volume is due to a small variation in the thickness of the ceramic faceplates used for some samples. The thinner ceramic faceplates on AP7-AP10 have a smaller impact zone in the

ceramic face plate with its less overall damage. This is compensated by additional plastic deformation in the CMF and aluminum backplate.

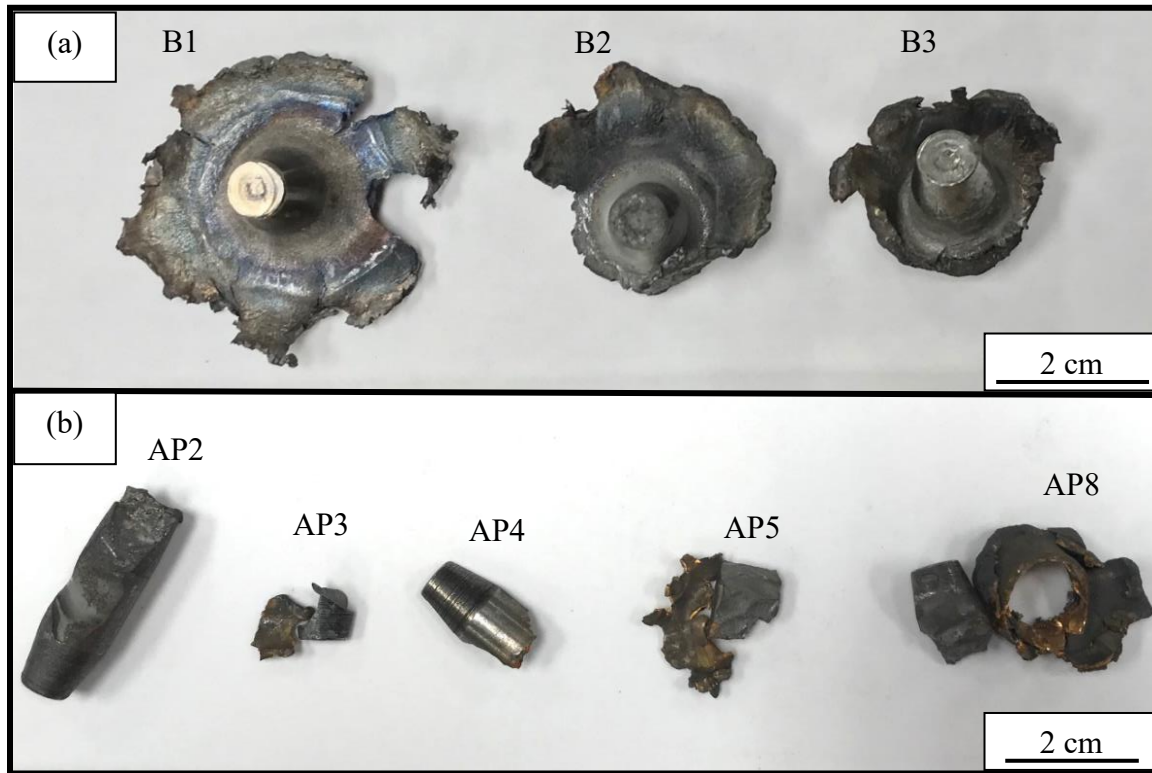


Figure 6-12: Images of the residual core fragments and casings retrieved after testing for the (a) ball and (b) AP rounds.

The volumetric strain energy of the CMF layer can be approximated by dividing the energy absorbed (E_{CMF}) by the volume of CMF deformed during impact. The volumetric energy absorption of CMF under impact of 12.7 x 99 mm ball and AP rounds are calculated to be 176 MJ/m³ and 213 MJ/m³, respectively. The volumetric energy absorption of the CMF depends on the type of impacting round as both have very different yielding behaviors and interaction with the armor as can be seen when comparing Figure 6-7 and Figure 6-10. The energy absorption at such high ballistic velocities is 3-4 times larger than under quasi-static compressive loading [122]. The strengthening is due to the high strain rate sensitivity of CMF

caused by many factors including the back pressure created within the spheres as they burst and resist against the sudden compressive load [107], [122], [123]. This mechanism directly increases the volumetric energy absorption of the CMF layer as discussed in regard to the stress-strain curves in Figure 6-6. The multilinear stress-strain curve used in the FEA model was influenced by the calculated volumetric energy absorption of the CMF. The multilinear stress-strain curve in this work to represent the CMF layer is presented in Figure 6-13 alongside the multilinear model used in our previous studies [122]. The updated stress-strain curve has an ever-increasing slope as required for material model input into ANSYS/AUTODYN and has a similar shape to the dynamic and quasi-static load paths obtained from experimental tests.

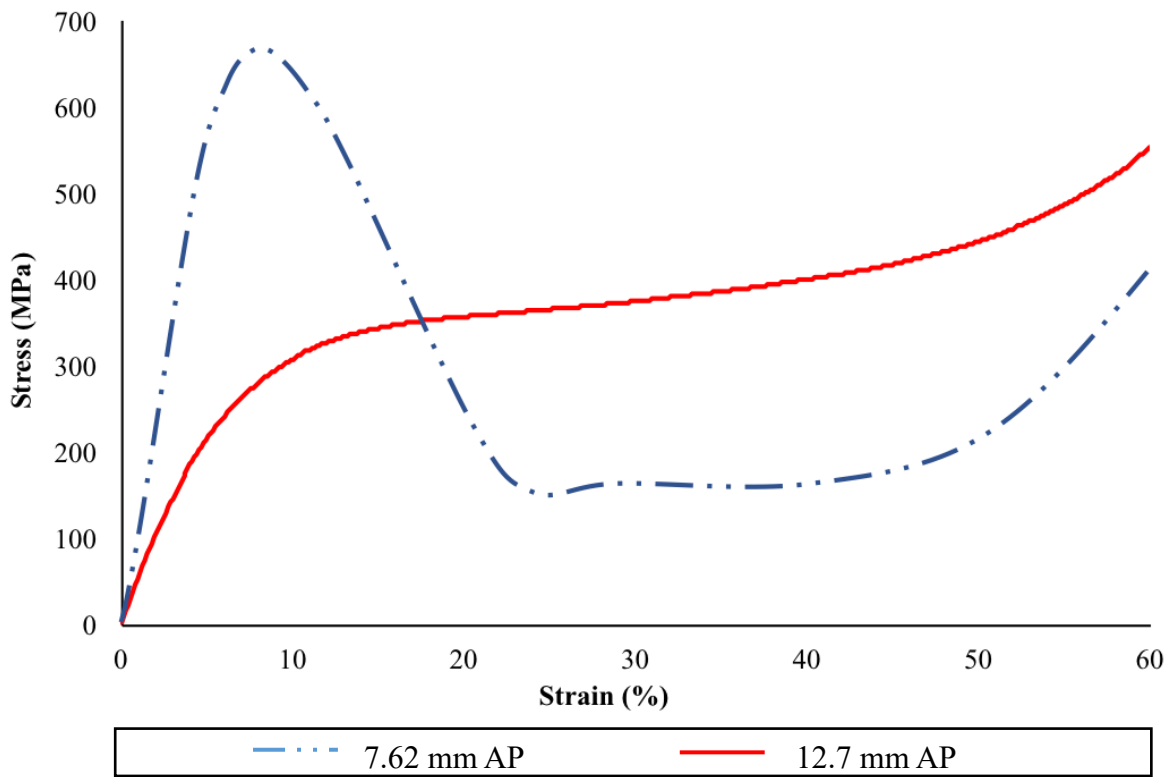


Figure 6-13: Multilinear stress-strain curves used to represent CMF in finite element analysis during ballistic impact of 7.62 [122] and 12.7 mm AP threats.

Finite Element Analysis Results

Figure 6-14 plots the evolution of the kinetic energy for the simulated impact of the AP projectile. As can be seen from the plot, the energy of the bullet is absorbed in a total of $140\mu\text{s}$ in the FEA model. Figure 6-14 shows a large portion of the kinetic energy is absorbed between 40 and $90\mu\text{s}$ during penetration through the CMF hard armor. The simulation modeled the entire panel, but for further detail, a cross-section of the armor is used to present the results. The maximum principal stress in the armor system at varying time intervals is shown in Figure 6-15. Although multiple layers are interacting at the same time, the main energy absorption occurs between $30\text{-}90\mu\text{s}$ (Figure 6-14) which coincides with the bullet's contact with the CMF layer in Figure 6-15(b) and (e). Peak stresses are found at the tip of the bullet as it penetrates through the armor and falls off radially away from the point of impact. As the bullet reaches the backplate, a majority of the kinetic energy has already been absorbed by the CMF, ceramic faceplate, and the various components of the bullet itself. The ceramic layer effectively models the initial impact, but elements become eroded and removed before the hardened core is eroded to a size similar to that found during experimental testing (Figure 6-12(b)). Minor discrepancies between the experimental and numerical results may be due to the criteria used for the boundary conditions between layers. The armor uses a high strength epoxy to hold the layers together while the model uses general contacts between layers, which allows for an increased area of debonding in the model with no inherent strength between layers. Although this does not greatly affect the results, by introducing a bonding criterion between the armor's layers, it may reduce the radial spread and better mimic the experimental BFS. The results can be optimized in future works by implementing a more sophisticated element erosion criteria or meshless bodies that retain the inertia of the eroded particles [171]. The interaction of

composite metal foam within a sandwich panel armor is a complex problem and requires further refinement to establish a consistent strengthening model useful for a variety of loading conditions.

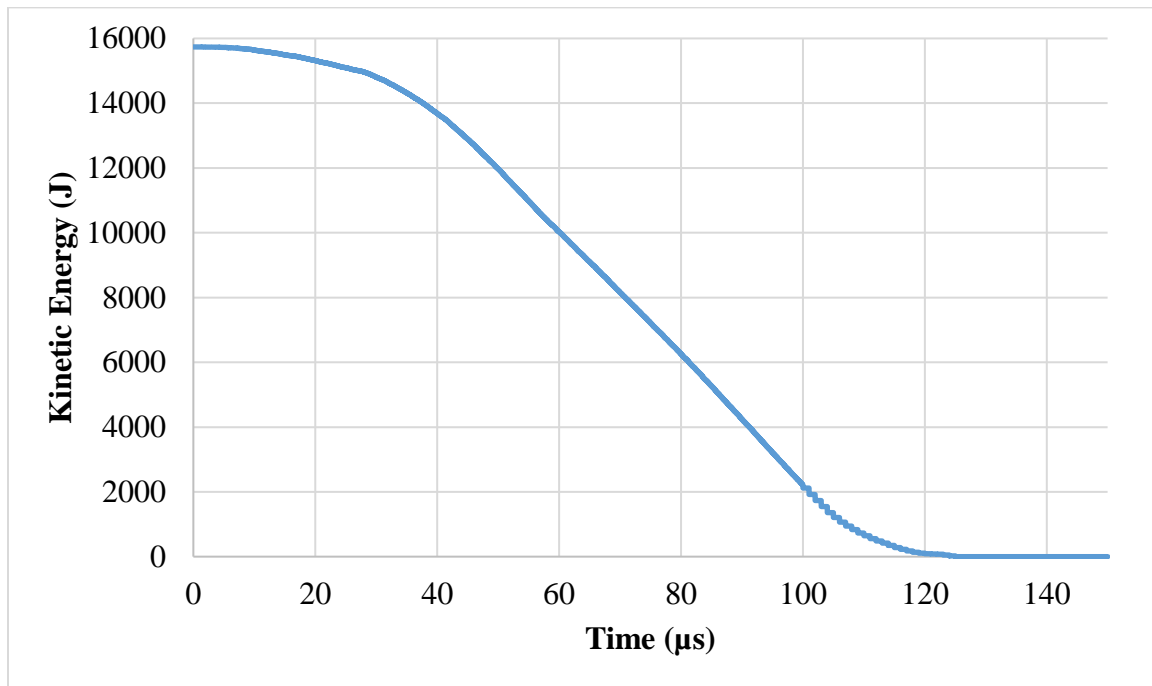


Figure 6-14: Kinetic energy of the 12.7 x 99 mm AP core resulted from FEA modeling of 800 m/s impact.

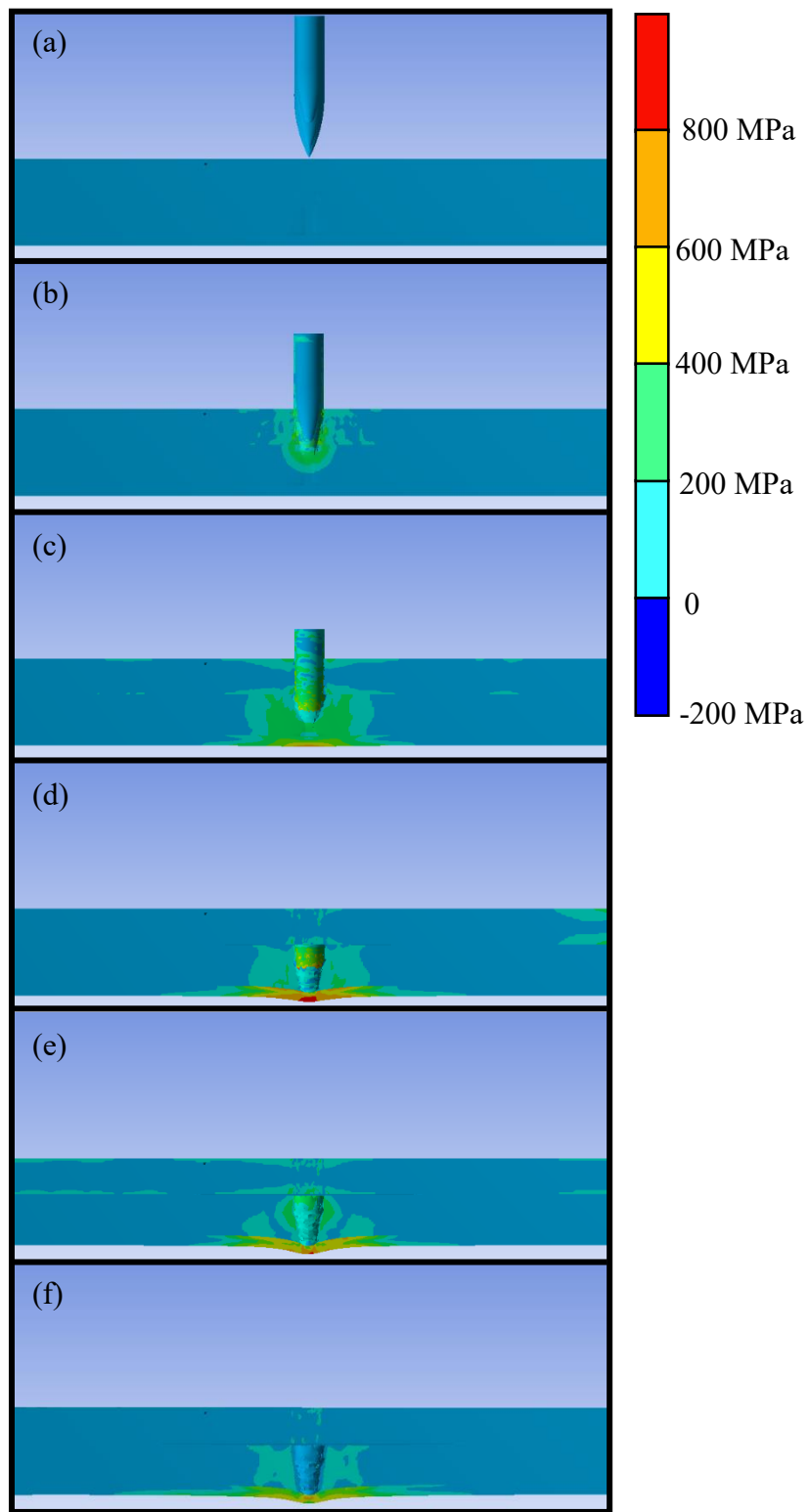


Figure 6-15: ANSYS maximum principal stress distribution of all layers of the CMF armor during the simulated ballistic impact of the 12.7 mm AP round with a velocity of 800 m/s at (a) 0 μ s, (b) 30 μ s, (c) 60 μ s, (d) 90 μ s, (e) 120 μ s, and (f) 150 μ s.

6.3. Summary of CMF Armors Against Large Ballistic Threats (0.50 Cal)

The performance of SS-CMF armors tested against 12.7 x 99 mm (0.50 Cal) ball and AP rounds at a range of impact velocities was reported and discussed. The mild steel cores of the ball rounds penetrated one of the three samples but reveal the benefits of using multiple tiles over a single ceramic faceplate to limit the spread of damage. The hardened steel core of the AP rounds penetrated deep into the ceramic faceplate, compressing the CMF layer until the projectile is either stopped and embedded within the armor, or can fully penetrate and exit the backing plate. The energy absorption and mass efficiency of the SS-CMF hard armors was reported and compared to conventional armors against similar threats and show potential weight savings. Finite element analysis of the armor system was created using ANSYS/AUTODYN. The simulation closely predicts the experimental results and verifies the energy absorption model implemented for the CMF layer. The numerical modeling results are in good agreement with the experimental results given the complexity of the multilayered armor and unique yielding of CMF.

CHAPTER 7: COMPARING THE PERFORMANCE OF COMPOSITE METAL FOAM ARMORS AGAINST VARIOUS THREAT SIZES

The previous chapter analyzed the effectiveness of CMF hard armors when facing a larger threat size by testing the 12.7 mm ball and AP threats [138]. This work presents the results of CMF hard armors against the 14.5 x 114 mm B32 API (a much larger threat than the previous rounds with a very high dynamic energy) and compares the initial results to previous findings against smaller threats with hardened steel cores. The efficiency of one single ceramic face sheet compared to smaller tiles covering the armor as well as the presence of a thin layer of steel RHA on top of the ceramic face sheet will be compared and discussed.

7.1. Materials and Processing

The steel-steel composite metal foam (SS-CMF) samples were manufactured using the same powder metallurgy technique as the previous chapter. The CMF panels were manufactured in 25 x 25 cm and 30 x 30 cm sizes with a density between 2.8 and 3 g/cm³. The CMF is layered between a ceramic face made of boron carbide (B₄C) and an aluminum 7075-T6 backplate. The boron carbide (B₄C) ceramic tiles were purchased in two sizes from two separate companies, Saint-Gobain and M Cubed Technologies Inc.

The layered armors are assembled using a vacuum bagging technique and a thin layer of high strength epoxy between each component. The epoxy used to adhere the layers was a two-part Loctite EA 9309NA aerospace grade epoxy with a high tensile and peel strength. Three armors, each with a different arrangement, were tested against the 14.5 mm B32 API round. Armor 1 was manufactured using a dual-layered ceramic faceplate on top of a CMF core and a thin aluminum backplate. A dual ceramic is used to limit crack mitigation to the top ceramic layer, protecting the secondary ceramic from complete fracture. The second layer of

ceramic helps to further break down the larger core of the 14.5 mm API round and potentially improve the performance of the CMF core by further distributing the load of the projectile. The second armor (Armor 2) had a thin layer of RHA over a single ceramic plate followed by the CMF core and a thin aluminum backing, in attempts to protect the ceramic face sheet from shattering upon impact. The RHA layer can absorb some of the shock of the incendiary explosive and limit fragmentation of the ceramic layer. Armor 3 is arranged much like Armor 2 but used multiple 10 × 10 cm ceramic tiles in place of a single ceramic layer. Armor 3 is assembled using the 30 × 30 cm CMF panel in order to evenly distribute the ceramic tiles, while Armor 1 and 2 were both arranged using panels with a size of 25 × 25 cm. The multiple tile arrangement can be useful for dissipating the energy of the incoming threat by transferring energy between surrounding tiles and protecting those away from the point of impact [172]. An exploded-view diagram of the three different layups are shown in Figure 7-1, note that the thicknesses and sizes in this figure are not to scale. The second and third arrangement (Figure 7-1(b) and (c)) test the viability of an armor with an outer layer that is more durable than the ceramic faceplate while also comparing the performance of one large ceramic plate against multiple square tile arrangements. Each of the three armors present an alternative armor solution to stopping the 14.5 mm threat that can be further optimized for future tests at higher velocities closer to the muzzle velocity expected for such rounds.

14.5 x 114 mm AP-I

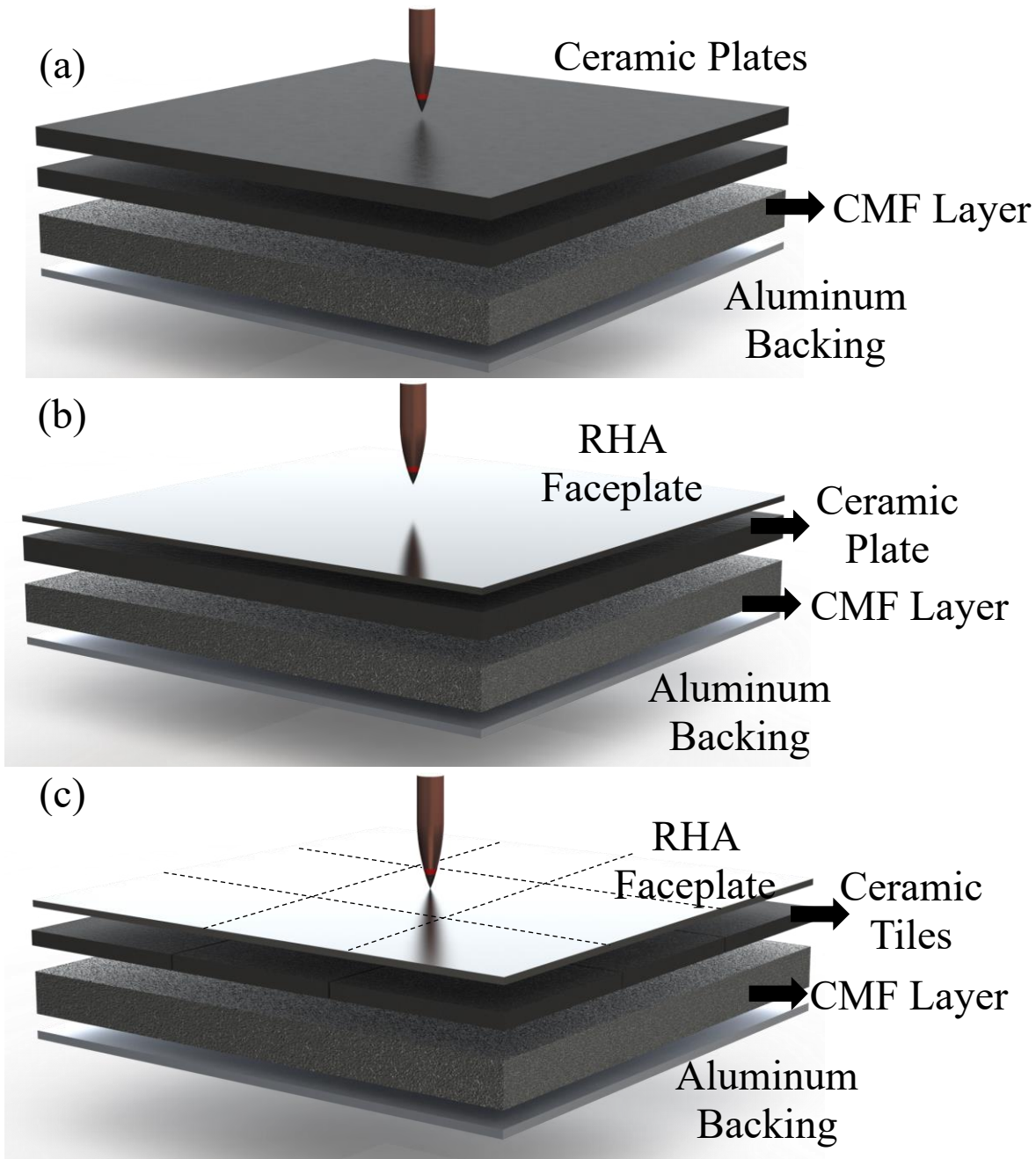


Figure 7-1: Exploded view diagram showing the arrangement of the CMF armors using (a) a ceramic face sheet, (b) a thin RHA faceplate above the ceramic, and (c) RHA above a layer of individual ceramic tiles. Note that the thicknesses and sizing are not to scale.

7.2. Ballistic Testing and Procedures

The CMF layered hard armors were placed onto a testing mount 5 m down range from a Mann gun used to fire the ballistic threats, shown in Figure 7-2(a). Three velocity chronographs are used to measure the impact velocity of the bullet as it approaches the sample. The samples are clamped to a heavy-duty steel structure to support the armors about its outer edges as can be seen marked in Figure 7-2(b). A high-speed camera was placed facing the target panel to record the impact of the projectile while also confirming the obliquity and impact velocity. A single shot was fired at the center of each armor with a zero degree obliquity.

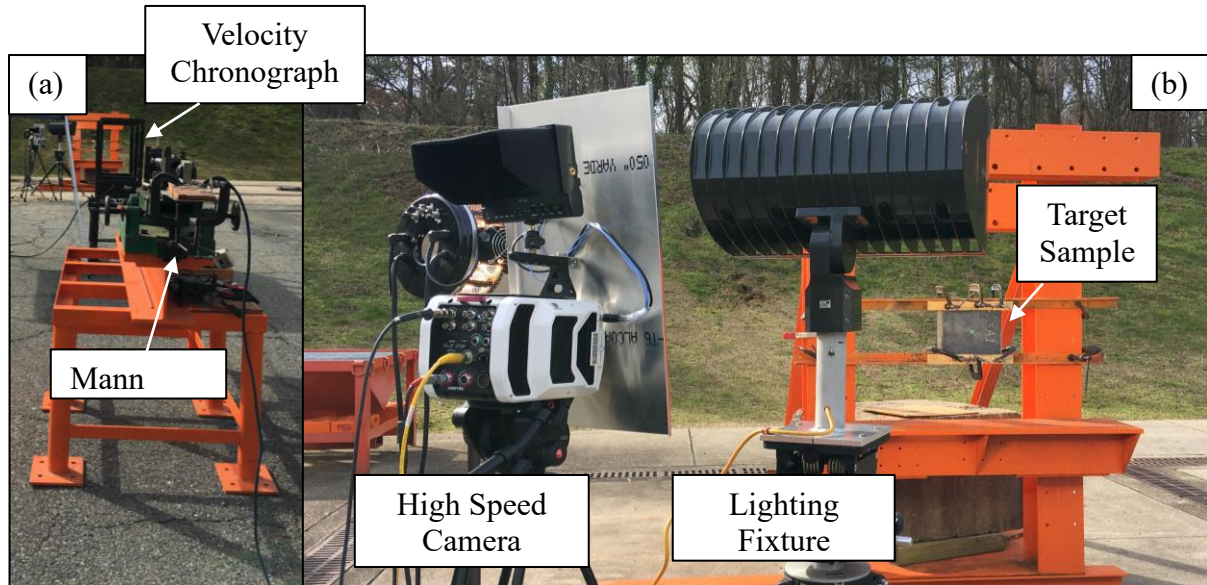


Figure 7-2: Digital images of the (a) Mann gun used to fire the rounds and (b) the target sample and high-speed camera setup used to record the impact.

The 14.5 x 114 mm B32 API was chosen for testing in accordance with the NATO standard agreement (STANAG) 4569 Level IV protection [173]. This standard is created for logistic and light armor vehicle (LAV) protection systems and includes larger caliber threats

not accounted for in the NIJ body armor standards [124]. A cross sectional drawing of the 7.62 mm AP, 12.7 mm AP, and 14.5 mm B32 is presented in Figure 7-3. Each round has a hardened steel core (HRC61-66) surrounded by a lead filler and a brass casing. In addition to the AP penetrator, the 14.5 mm also includes an incendiary charge located at the tip of the projectile that ignites upon impact. Table 7-1 includes the size and impact energy of the B32 API and compares it with the previously tested 7.62 and 12.7 mm M2 AP [24].

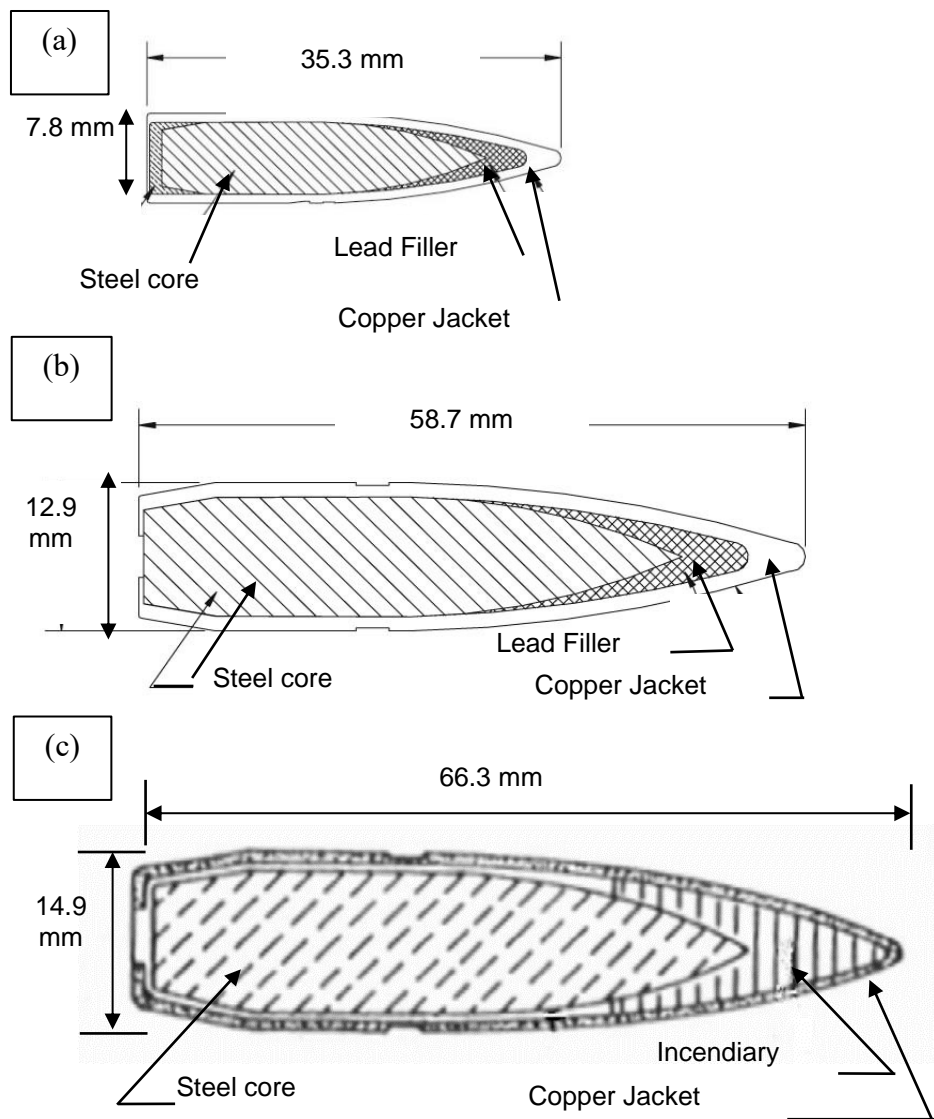


Figure 7-3: Cross section drawing of the (a) 7.62 x 63 mm M2 AP, (b) 12.7 x 99 M2 AP, and (c) 14.5 x 114 mm B32 API projectiles [24] that are used for testing CMF armors.

The results of the ballistic impacts against the CMF armors are analyzed using MIL-STD-622F testing procedures and are categorized as either complete penetration (CP) or partial penetration (PP) [151]. The impact is considered PP when the armor is able to stop the impending round while the test is considered CP when the projectile creates a hole large enough for light to penetrate through the armor. The most popular method of analyzing

potential light armors is to determine a V₅₀ as per MIL-STD-622F. The V₅₀ is determined by calculating the arithmetic mean of at least two partial and two complete penetrations of armors with similar areal densities. The result represents the velocity at which a round has an equal probability of both penetrating and being stopped by the armor. A preliminary average of the CMF armors against the 14.5 x 114 mm B32 API impact velocity, areal density, and efficiency were calculated for the tests conducted in this study and is compared to the results of prior works.

Table 7-1: Projectile and core sizes for each of the tested ballistic rounds [24].

Threat	Projectile Length (mm)	Projectile Diameter (mm)	Projectile Mass (g)	Core Length (mm)	Core Diameter (mm)	Core Mass (g)	Impact Energy (kJ) (750-900 m/s)
7.62 x 63 mm AP (0.30 Cal)							
	35.3	7.85	10.8	27.4	6.2	5.3	3-4
12.7 x 99 mm AP (0.50 Cal)							
	58.7	12.98	45.9	45.9	10.9	25.9	13-19
14.5 x 114 mm B32 API							
	66.3	14.9	64.2	53.1	12.4	41.0	18-26

7.3. Results and Discussion

7.3.1. 14.5 mm Test Results

The results of the ballistic testing of CMF hard armors against 14.5 mm threats are presented in Table 7-2. The tested armors are listed in order of their impact velocity and configuration and compared to standard armors such as RHA and HHA that are established in their military testing standards, MIL-A-12560 [35] and MIL-A-46100 [42], respectively. The kinetic energy of the 14.5 mm round during these tests was approximately 20 kJ at impact velocities just under 800 m/s. The current test speeds are equivalent to impact of the 14.5 mm B32 round at a standoff distance of 500 m [151], [173]. Two of the tests resulted in partial penetration, while Armor 3 was unable to stop the round partly due to premature separation of the backing plate. Images of the front and back of each armor are shown in Figure 7-4. The results are split into two sections where the armor arrangements tested herein are first analyzed and compared for their benefits and drawbacks. The second section uses previously published data to investigate the performance of CMF armors against increasing threat sizes.

Table 7-2: Summary of ballistic testing of CMF armors against the 14.5 x 114 mm B32 round.

	Areal Density (g/cm ²) [lbs/ft ²]	Impact Velocity (m/s)	Bullet Kinetic Energy (J)	PP/CP
Armor 1	16.3 [33.5]	769	19,057	PP
Armor 2	17.2 [35.2]	769	19,057	PP
Armor 3	16.1 [32.9]	791	20,129	CP
Average	16.5 [33.8]	776	19,274	-

Table 7-2: (continued).

HHA	19.4 [39.7]	744	17,823	V ₅₀ [38]
RHA	24.3 [49.8]	835	22,451	V ₅₀ [38]

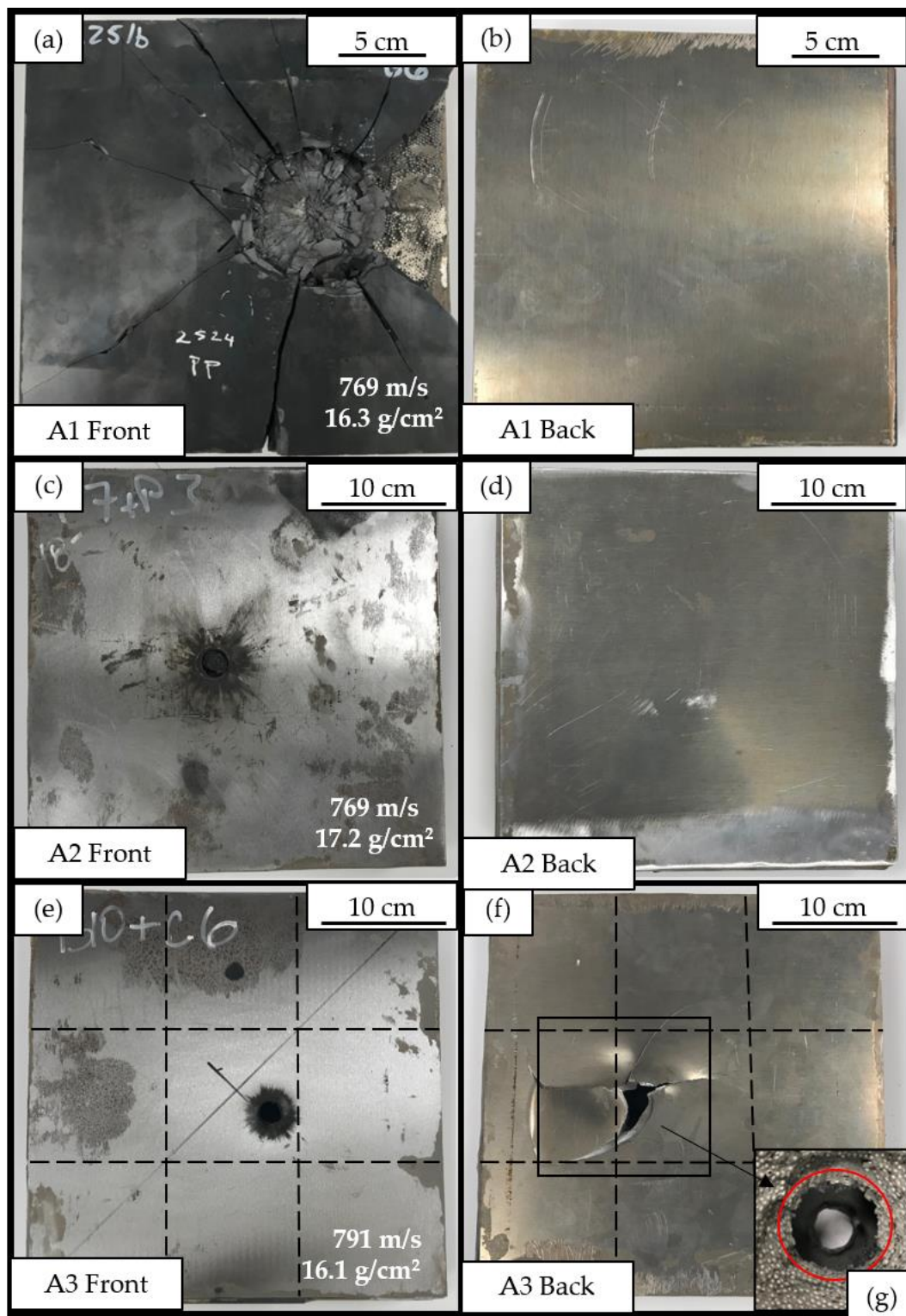


Figure 7-4: Digital images of the front and back (a-f) of Armor 1, 2, and 3 following ballistic testing as well as additional images of the compressed spheres (g) in Armor 3.

Armor 1: Double Layered Ceramic

Testing of Armor 1 resulted in partial penetration of the 14.5 mm API at an impact speed of 769 m/s. The front and back of Armor 1 are presented in Figure 7-4(a) and (b). As can be seen, the top ceramic faceplate shattered upon impact with cracks propagating across the entire surface of the panel. The lower ceramic also fractures to a similar extent and is not protected from the impact using a dual ceramic arrangement. Large fragments of ceramic are removed from the first layer about the point of impact, while the broken parts of the second layer have remained intact with the CMF core. The ceramic layer experiences higher levels of fracture due to the incendiary found at the head of the 14.5 mm API. This creates larger fragments along the surface of the armor compared to testing of previous AP rounds which leads to delamination of the faceplate, as can be seen along the right side of the armor's surface. The aluminum backplate shows no sign of the impact, confirming that the CMF core was more than enough in conjunction with the double layer ceramic to stop the API round. This armor seems to be over-designed and a much lower areal density is expected to perform in similar conditions. The fracture of the ceramic may be reduced by replacing the top ceramic with a thin RHA plate to absorb the initial shock and create an armor more compatible with conventional vehicle designs. Amor 2 explores this by using an RHA face sheet in place of one of the ceramic layers.

Armor 2: RHA-Ceramic-CMF-Al

The front and back of Armor 2 are shown in Figure 7-4(c) and (d). As can be seen by the results of the impact on Armor 2, the replacement of one of the ceramic face sheets with a thin RHA layer improves retention of the ceramic fragments and reduced the overall fragmentation of the armor. The effects of the incendiary charge are shown by the black

charring around the impact point, and front petaling of the RHA plate (Figure 7-4(c)). Armor 1 and 2 were tested at approximately the same impact velocity, 769 m/s. Similar to Armor 1, Armor 2 shows no apparent signs of the impact on the aluminum backplate (Figure 7-4(d)) and both armors were able to stop the bullet within the CMF layer. Armor 2 is also over-designed and much less areal density may perform in similar conditions. Fragments of the hardened core are captured within the CMF layer and no major cracking or failure of the armor can be found away from the point of impact. This is primarily due to the initial mitigation of the incendiary charge by the RHA face sheet and the absorption of the kinetic energy primarily within the CMF layer. The RHA layer increases the areal density of the armor, when compared to Armor 1, but may be used in future CMF armor designs to improve retention of the ceramic layer and can be further optimized to create similar armors with a higher efficiency.

Armor 3: RHA-Ceramic (Tiles)-CMF-Al

Armor 3 was tested at an impact velocity of 790 m/s, slightly higher than the previous armors, and was unable to stop the impending round as the core penetrated the aluminum backplate. The armor had a similar areal density to Armor 1, but with a different face sheet arrangement. Armor 3 has a thinner ceramic layer than Armor 1, replaced partially by the RHA faceplate, but was unable to stop the round at 790 m/s. However, both Armors 2 and 3 have similar arrangements of components using steel face sheets. The main factor causing complete penetration in Armor 3 was the close proximity of the impact to the seam line between ceramic tiles. The effectiveness of the tiles was limited by the impact close to the seam, leading to premature delamination of the back plate. Separation of the backplate prevented the CMF from fully compressing and maximizing its energy absorption capabilities. The impact and exit points of the round are shown in Figure 7-4(e) and (f) with the dotted lines representing the

location of the seams between ceramic tiles that are placed below the RHA faceplate. The multi-tile arrangement has potential to improve the ceramic layer's energy absorption and crack propagation between tiles, but as can be seen, are vulnerable to impacts at the seam between tiles making it less effective than a monolithic ceramic plate. The separation of the backplate from Armor 3 allowed a better look at the extent of deformation in the CMF layer as seen in Figure 7-4(g). At the interface with the aluminum plate the initial point of impact at the center of the frame can be seen. The compressed layer of the CMF core is highlighted by the red circle in Figure 7-4(g). Surrounding the primary point of impact, the CMF layer is compressed and gradually sheared between the matrix and the sphere walls, similar to what has been seen in testing of CMF armors against the 12.7 mm M2 AP [138]. The sheared layers of the CMF failed before they were able to help absorb the kinetic energy of the ballistic impact. The use of two layers of ceramic is not directly beneficial nor was the use of multiple ceramic tiles. Even though many researchers have tried using multiple tiles and multi-layered ceramics in the structure of their armors in attempts to reduce the extent of the ceramic layer damage, the CMF absorbs the majority of the impact energy, in these armors, and leaves the ceramic less damaged inherently. The use of individual tiles or multiple layers of ceramic tile does not provide much benefit given the unique energy absorption of the CMF layer. On the contrary, such arrangements can create weak areas (as observed in Armor 3) that can defeat their intended purpose and cause further penetration risks. Future testing is expected to optimize the interfacial bonding, the design of the lay-up of the armor, and its resulting total mass and efficiency of the armors. It is emphasized that these are the preliminary results of CMF hard armors against the 14.5 x 114 mm B32 API threat and further optimization and

testing would allow for improvement in performance of the CMF hard armor system towards finalizing an accurate V_{50} .

CMF also has other benefits that meet STANAG armor requirements in addition to its use in ballistic armors against the 14.5 mm B32 API rounds and similar threats. CMF also has a lower thermal conductivity over standard materials often used for combat vehicles and additional radiation shielding that are passive benefits applicable to combat scenarios and war zones [41,42]. The insulating properties of CMF give military personnel more time to dismount during internal and external fires in combat. Future work should focus on the implementation to vehicle designs and full-scale testing that includes attachment options for both CMF panels and possible applique armors that can bolt or adhere to the exterior of the vehicle's vulnerable points.

7.3.2. Mass Efficiency Ratio (MER)

In order to assess the effectiveness of the CMF armors and compare it to RHA, a mass efficiency ratio (MER) is calculated. The MER compares the armor's performance to that of RHA at a similar impact velocity and determines the armor's weight savings. In this study, the MER is calculated by dividing the areal density of RHA (ρ_{RHA}) required to stop the impending round at a specified velocity by the areal density of the CMF armor (ρ_{CMF}) shown by the equation below:

$$MER = \rho_{RHA}/\rho_{CMF} \quad (1)$$

Armors with an overall weight savings (MER greater than 1) would potentially improve military vehicles with an increased fuel efficiency, maneuverability, and ability to carry larger payloads.

An approximate V_{50} , noted by V_{50*} , of the CMF armors against the 14.5 x 114 mm B32 API is calculated by finding the arithmetic mean of Armor 2 and Armor 3. The V_{50*} is denoted by an asterisk as only two rounds are used in its calculation and does not meet the required number of tests for the V_{50} specifications in MIL-STD-622F. The initial results suggest an average areal density of 16.2 g/cm^2 at an impact velocity of approximately 780 m/s. These values require quadruple testing in order to calculate a more accurate V_{50} value and validate the current findings. An improvement is expected as the current work can be used to infer the needed areal density to defeat the threat at higher impact velocities. The average performance of the unoptimized CMF armors can be compared to RHA and HHA against the same threat. According to Gooch *et al*, RHA with an areal density of 24.3 g/cm^2 has a V_{50} of approximately 835 m/s against the 14.5 mm B32 API while HHA has a measured areal density of 19.4 g/cm^2 at 744 m/s [46]. The areal density and impact velocity of these armors are plotted in Figure 7-5 alongside the CMF armors tested in this study for comparison. Although the CMF armors were tested in their unoptimized state and a different impact velocity, the advantage of the CMF armors is apparent. The CMF average is tested at a higher impact velocity than the HHA and is 20% lighter than the bulk metal armor. The MER for the tested CMF armors is calculated to be 1.2 and 1.5 when compared to the HHA and RHA, respectively.

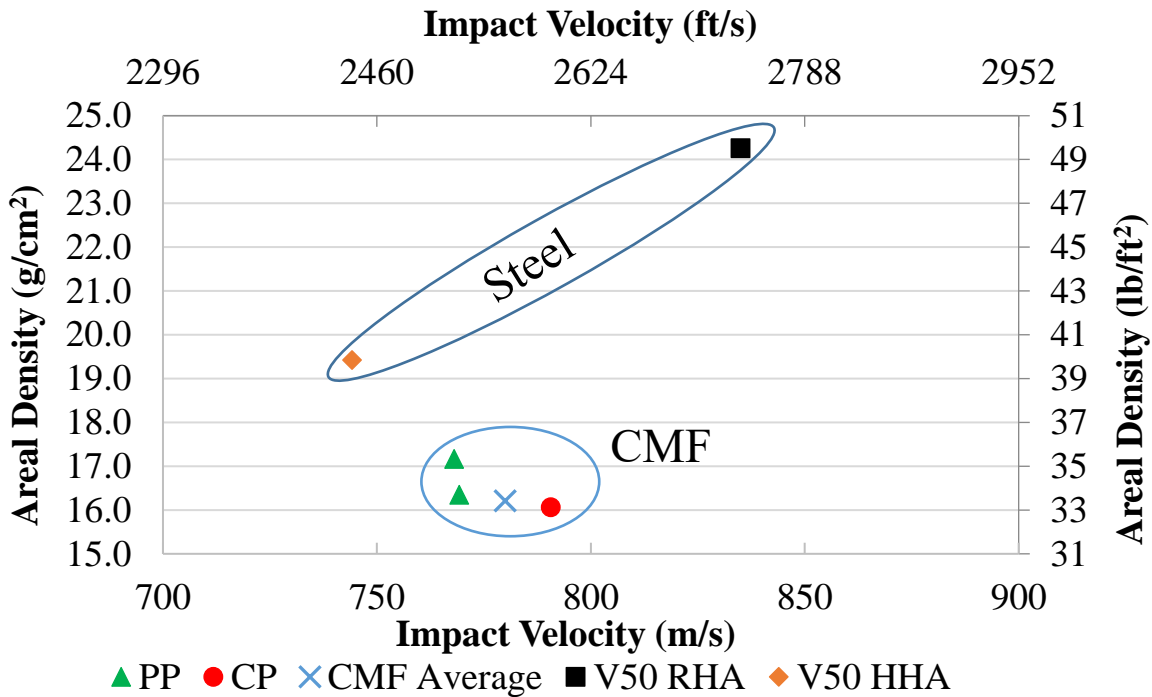


Figure 7-5: Results of the 14.5 x 114 mm B32 API testing plotted alongside V_{50} values for both RHA and HHA [35], [42], [46].

7.3.3. Analytical Energy Absorption

The energy absorption of the CMF layer can be calculated using an analytical method developed and described in detail in previous publications and outlined in Section 6.1.3. [122], [123], [138]. First the kinetic energy of the impacting round is calculated using classical mechanics assuming a projectile mass of 64.4 g for the 14.5 mm B32 API and the round's impact velocity. The material parameters for the ceramic and aluminum backplate are taken from a previous work [122]. The mechanical properties of the RHA under compressive loads, as it is being used as a faceplate, are approximated using data by Bassim *et al.* [174].

Table 7-3: Percent of energy absorbed by each layer for PP impacts against multiple sized rounds.

Armor	Areal Density [g/cm ²] [lb/ft ²]	Average Round Velocity (m/s)	Total Energy of the round (J)	Percentage of the round's energy absorbed by:				
				Ceramic and Motion of Fragment Cloud %	Bullet %	Backplate %	RHA %	CMF %
Armor 1	16.3 [33.5]	769	19057	27	2	1	-	70
Armor 2	17.2 [35.2]	769	19057	13	2	1	1	83
7.62 x 63 mm M2 AP [122]	5.9 [12.1]	867	4081	9	15	16	-	60
12.7 x 99 mm M2 AP [138]	10.3 [21.1]	804	15208	17	2	4	-	77

The energy absorption results calculated using the above mentioned approximation are listed in Table 7-3. The hardened steel core fragments retrieved from Armor 2 are used to calculate the amount of energy absorbed by erosion and fracture of the AP core attributed to E_{Bullet} . The fragments from Armor 1 were unable to be fully retrieved as both the hardened core and ceramic fragments were ejected from the surface during testing and were not found after testing. The retrieved fragments account for 12.16g or 30% of the core's initial mass and are shown in Figure 7-6. The fractured core provides evidence of the armor appropriately eroding the steel core and casing being deformed upon impact and is used in calculating the amount of energy attributed to the erosion of the bullet. The calculations indicated that the CMF layer in Armor 1 absorbs 70% of the bullet's kinetic energy and a volumetric energy absorption of 180 MJ/m³. Similarly, the CMF layer of Armor 2 was calculated to absorb 83% of the kinetic energy which is equal to a volumetric energy absorption of 243 MJ/m³. The reduced energy

absorbed by the CMF is due to the double layer ceramic used in Armor 1. There is a benefit to having thinner single layer ceramic in Armor 2 as the bullet is cradled within the armor, and more specifically the CMF layer. It appears that both Armor 1 and Armor 2 are slightly overdesigned for the 14.7 mm B32 at the tested impact velocity as the aluminum backplate shows no signs of indentation or fracture.

Armor 2



Figure 7-6: Fragments of the fractured steel core retrieved from Armor 2 (PP) following testing.

7.3.4. Comparison of CMF Armors against Various AP Threats

The data collected was also used to compare the CMF armor's ability to stop AP threats of different sizes and how it changes with increasing size. The percent energy absorbed by each layer is compared for the PP tests and their averages calculated for the previous testing of 7.62 [122] and 12.7 mm M2 AP rounds [138] in Table 7-3 and the energy absorbed by the CMF is plotted in Figure 7-7 as a function of the kinetic energy of the round. It can be seen that as the projectile size and impact energy increases so does the effectiveness of the CMF layer. As the areal density of the armor increases, the percent of energy absorbed by the CMF

also increases linearly from approximately 60% for the 7.62 mm to above 83% for the 14.5 mm rounds. The linear trend is due to the following factors:

- a) The increasing impact area of the larger bullets engages a greater number of spheres, improving the cushion-ability of the armor.
- b) The increased thickness of the CMF layer in the armor design further helps spread the load through the thickness of the armor, strengthening its performance under compression.
- c) A larger secondary impact zone is created as a result of the reflected stress waves in the thicker armors. The secondary impact region supports the primary impact zone around the projectile cores.

Additional information on the armor arrangements tested against the 7.62-, 12.7- and 14.5 mm AP threats, including the areal densities and total thicknesses, are compared in Table 7-4. Due to confidentiality, the exact thicknesses cannot be reported, but a normalized value can be used for comparison. The normalized values are calculated by first finding an average of equal number of PP and CP tests for 12.7 mm and 14.5 mm and dividing them by the average values for the 7.62 mm armors. This gives a direct comparison of the kinetic energy of the round, thickness of the armors, and areal density. From this data we can see the kinetic energy of the round increases by 3.4 and 4.8 for the 12.7 mm and 14.5 mm threat, respectively. Whereas the areal density and total thickness of the armor increase at a slower rate. The total thickness and areal density follow a similar trend for the 12.7 mm AP threat. It can be seen that the capabilities of the armors do not increase linearly with the kinetic energy of the round due to multiple factors. The larger threats carry not only a greater kinetic energy, but also influence a larger volume of material to deform under impact. By incorporating more spheres within the

CMF layer and increasing the thickness of each constituent, the armor's capabilities change depending on the threat size. An important factor to note is that the ceramic, CMF, and backplate thicknesses all remained proportional (excluding Armor 1 using a double ceramic layer). The increase in the impact volume can be seen by analyzing PP and CP of all three threat types: 7.62, 12.7 mm M2 AP, and the 14.5 mm API.

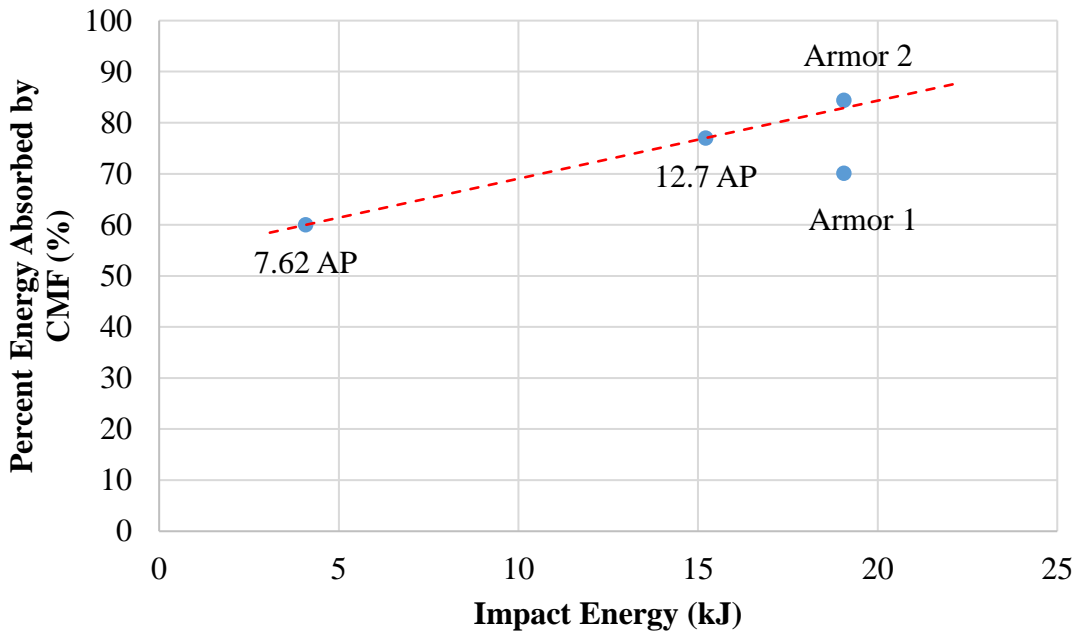


Figure 7-7: Percent of energy absorbed by the CMF layer as a function of the impact energy imparted by each ballistic threat. A linear fit between the 7.62 [122] and 12.7 mm [138] AP data shows how the 14.5 x 114 mm B32 API data currently compares with its higher impact energy.

Table 7-4: Properties of CMF armors against the 12.7 mm and 14.5 mm AP threats when normalized by the 7.62 mm AP armors.

Threat Type	Normalized Energy of the round	Normalized Total Thickness	Normalized Areal Density
7.62 × 63 mm M2 AP [15]	1.00	1.00	1.00
12.7 × 99 mm M2 AP [16]	3.92	1.60	1.77
14.5 × 114 mm B32 API	4.72	2.31	2.90

Samples tested against 7.62 mm M2 AP, 12.7 mm M2 AP, and 14.5 mm API are shown next to each other in Figure 7-8. Further information on the performance of CMF armors against the individual threats can be found in prior publications [122], [138]. The first row of Figure 7-8 shows the front and back of a 25x25 cm CMF armor (with an areal density of 6.0 g/cm²) tested against two impacting 7.62 mm AP both resulting in PP. Figure 7-8(a) shows both bullets cradled within the top layer of the armor. A close up view of the center impact is shown in Figure 7-8(c). The impact area is slightly larger than the diameter of the bullet as the load was spread by the top ceramic layer and creates a primary and secondary impact region in the armor as highlighted by the white and red circles, respectively. The secondary impact region is not much larger than the bullet's diameter given the relatively thin layer of ceramic. Moreover, tensile stresses created due to the sudden changes in mechanical impedance between various layers of the armor are reflected from the back into the armor towards the impact face. The size of the secondary impact zone is a function of the armor thickness and the mechanical impedance of the components. Since all components are the same in different CMF armors, their mechanical impedance would be similar and as the result, the only factor affecting the

secondary impact area is the thickness of different components of the armor, especially the CMF layer (and its areal density). The thicker the CMF (or higher areal density), the larger the secondary impact zone which leads to a higher energy absorption percentage in the CMF layer. Since the armor against 7.62 rounds are the thinnest, the secondary impact zone is the smallest as can be seen in Figure 7-8(c). The CMF armor also offers multi-shot capability that is unique to the yielding of CMF as neither soft nor hard-armors can offer such extensive multi-shot capability.

Figure 7-8(d)-(f) present similar images of a slightly thicker CMF armor (with an areal density of 10.7 g/cm^2) tested against the 12.7 mm M2 AP threat with PP. The same cradle behavior is seen, but additional ceramic on the top surface of the armor is removed with a larger crater surrounding the AP core. The secondary region of compressed CMF is created as the load is reflected from the back into the armor. The secondary region is larger than that seen in the 7.62 mm round. There are two mechanisms at work that lead to a larger primary and secondary loading region in the CMF layer. First, the armors facing the 12.7 mm AP threats used a thicker ceramic layer (as can be seen by the higher areal density of the armor) that spreads the load to a larger surface area of CMF due to the Hertzian cone formation through the ceramic's thickness [122], [175]. Second, the blast waves from a larger caliber threat carries a higher kinetic energy that is reflected within the thicker armor (with higher areal density). An increase can be seen in both the secondary impact area and energy absorbed by the CMF when compared to the 7.62 mm round.

Images of Armor 3 after impact with the 14.5 mm API are once again presented in Figure 7-8(g)-(i) with a larger image of the exposed CMF layer on the back of the armor in Figure 7-8(i). Similar to the 12.7 mm AP round, the number of spheres affected by the impact

further increases when facing a large threat such as the 14.5 mm round with a thicker ceramic and CMF. The increased size of the round along with the use of a thicker ceramic layer spreads the impact energy over a larger area of CMF engaging a greater number of hollow spheres to absorb the impact energy. The secondary impact area is affected by the larger thickness of CMF layer as well as the additional incendiary charge that is ignited upon impact. The explosive tip releases a shock wave that travels through the armor, further expanding the Hertzian cone formation in the ceramic layer. A constant trend can be seen once again when comparing the armors against smaller threats as the secondary impact region grows with threat size and is thought to be one of the main reasons for the increase in percent energy absorbed by the CMF layer. As the secondary impact region grows from the reflected load within the armor, more spheres are incorporated in the deformation and support the primary impact region.

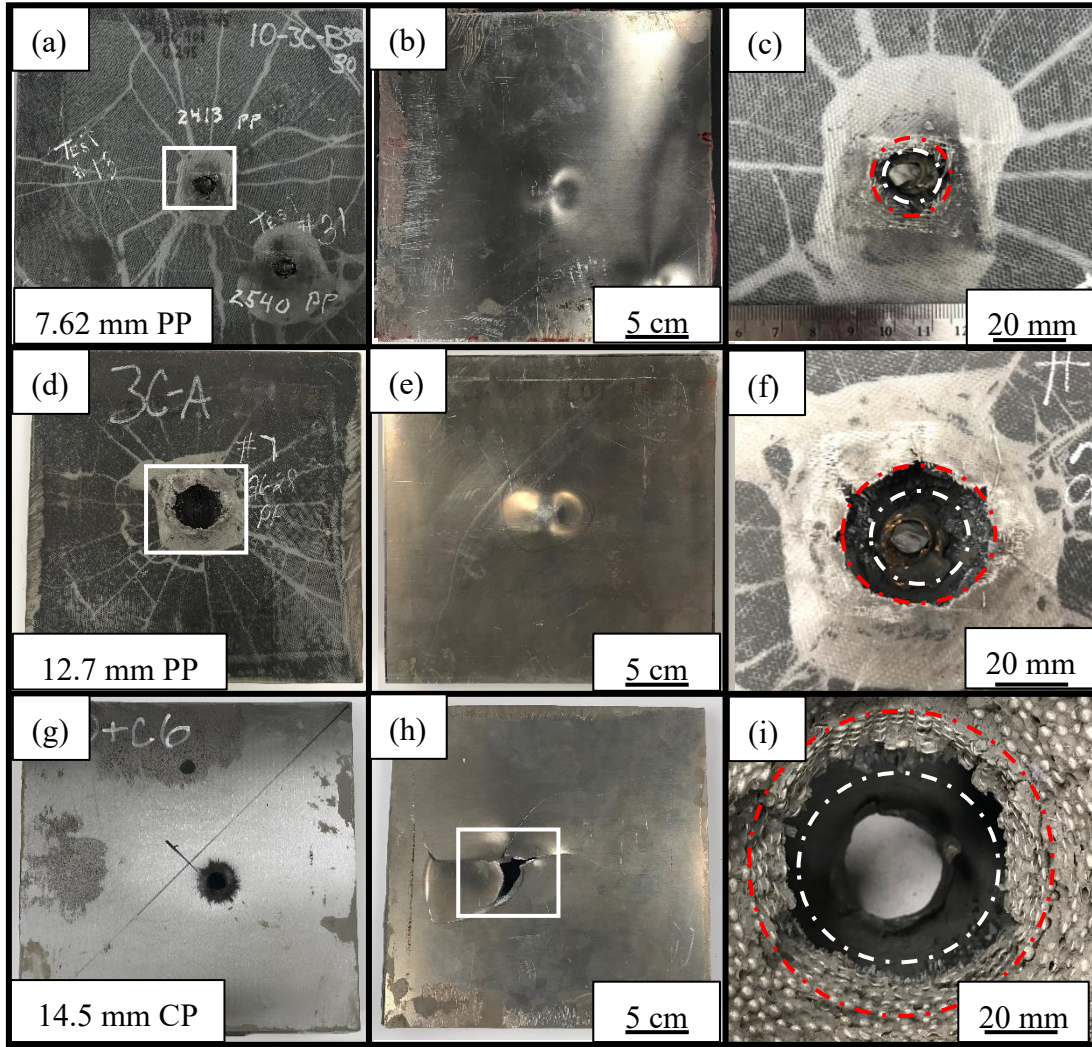


Figure 7-8: Digital images of the front and back of the layered SS-CMF armors with a highlight of the impact region after testing against a (a)-(c) 7.62 mm M2 AP, (d)-(f) 12.7 mm M2 AP, and (g)-(i) 14.5 mm B32 API.

7.4. Summary of CMF Armors Against Increasing Ballistic Threat Size

SS-CMF hard armors were manufactured and tested against 14.5 x 114 mm B32 API ballistic threats. Three arrangements were tested and two were able to stop the tested rounds at impact speeds between 770 and 790 m/s. The RHA layer is able to mitigate the incendiary impact of the round while the ceramic and CMF layers absorb the AP core's kinetic energy.

The average mass efficiency of the unoptimized CMF armor is calculated from the initial results with a MER of 1.5 at 780 m/s impact velocity when compared to RHA. The CMF layer was calculated to absorb between 70-83% of the bullet's kinetic energy using an analytical approximation. When compared to a variety of ballistic threats, the CMF armors continue to show strengthening as the size and impact energy of the round increases. The increasing impact area of the larger bullets also engages a higher number of spheres, improving the cushionability of the armor. As the impact area increases, the hardened steel core is less likely to pierce the CMF layer and is stopped within the armor due to the growth of the secondary impact region. The spheres within the secondary impact region help support the primary point of impact of the projectile core and improve the overall performance of the CMF layer.

CHAPTER 8: A STUDY ON BLAST AND FRAGMENT RESISTANCE OF COMPOSITE METAL FOAMS THROUGH EXPERIMENTAL AND MODELING APPROACHES

The previous chapters investigated the ballistic performance of CMF armors to protect from multiple threat types. One major concern for military systems in addition to ballistic impacts, is IED detonations that release high speed fragments and blast waves. This chapter presents the recent progress in the performance of CMF against blast and fragment impacts through both experimental and numerical approaches for armor applications [176]. A High Explosive Incendiary (HEI) round was used to create the blast wave and high speed fragments for testing. This study is an initial step towards the application of CMF in vehicular armors to protect against full scale improvised explosive device (IED). The HEI was selected as a scaled option to IED threats due to its ease of set up and test against multiple panels. The experimental performance is presented and compared to the advanced finite element simulations.

8.1. Materials and Processing

Steel-steel composite metal foam (SS-CMF) panels of 25 x 25 cm dimension with two different thicknesses of approximately 9.5 and 16.75 mm were manufactured. Figure 8-1 shows a surface image of a SS-CMF panel with a close up of the internal structure and arrangement of spheres. Hollow steel spheres (Hollomet GmbH, Dresden, Germany) of two sphere diameters of 2 mm and 3.5 mm were used. The 2mm spheres have a wall thickness of 100 μm and were used to manufacture the 9.5 mm thick CMF panels, while the 3.25 mm spheres are thin-walled and have a wall thickness of 88 μm . It is proven that the average wall thickness to sphere diameter ratio of 5% can provide sphere stability in the structure of CMFs. In addition, CMF manufactured using the 3.5 mm spheres, which is a lower sphere wall thickness to

diameter ratio (2.5%), was also designed to reduce the density of the CMF and evaluate the ratio's impact on the blast performance of the material. These spheres were used for manufacturing the 16.75 mm thick CMF panel. The panel thicknesses were chosen to include at least 4-5 layers of spheres throughout the panel's thickness. No additional secondary treatment was used, and the panels were tested as processed. The exact densities and thicknesses of each panel were measured prior to testing and are presented in Table 8-1.

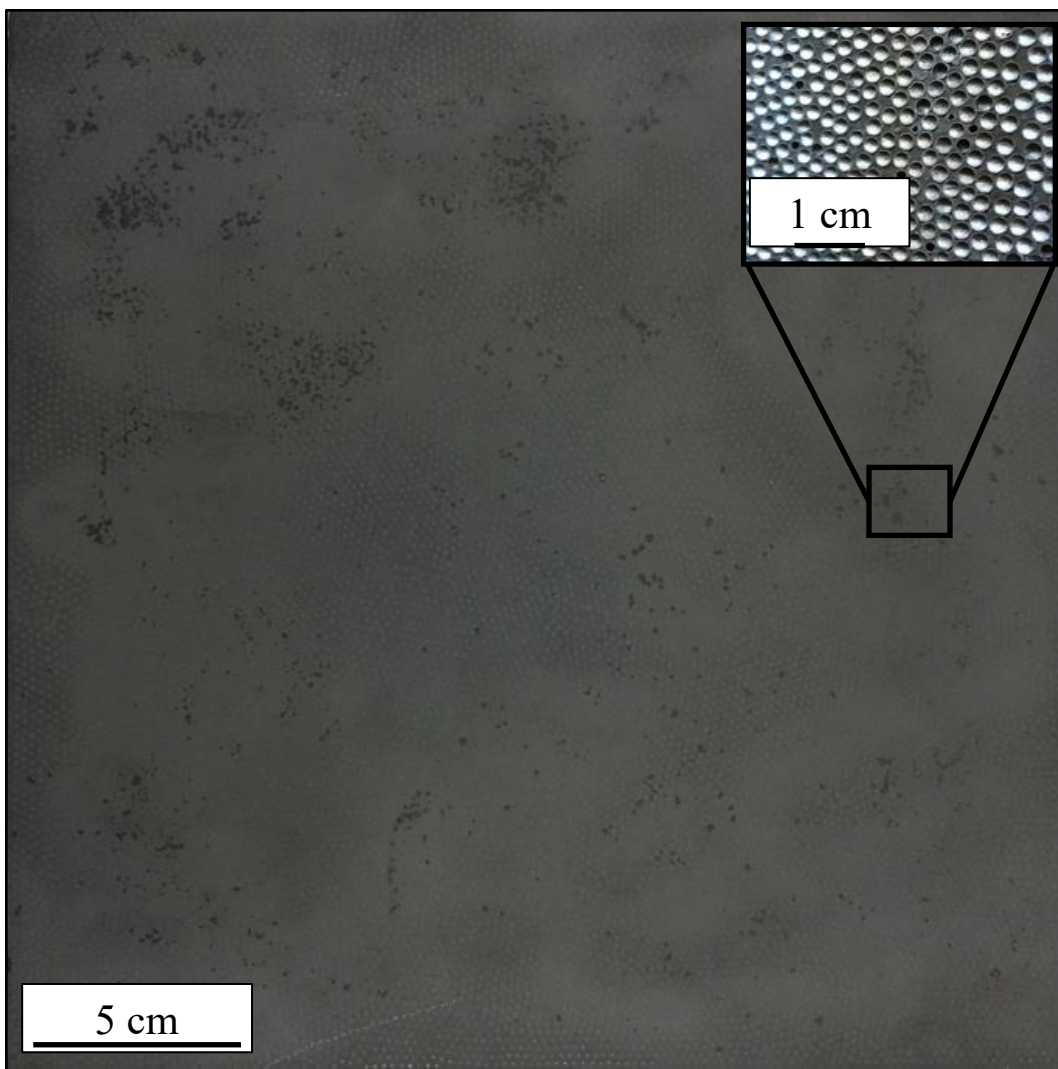


Figure 8-1: Manufactured 25 x 25 cm SS-CMF panel with a zoom in of the sphere arrangement on the top corner.

Table 8-1: CMF Panels and their corresponding thickness, density, and sphere diameters used to test against HEI rounds.

CMF Panel	Thickness (mm)	Density (g/cm ³)	Sphere Diameter (mm)	Sides Tested
Panel 1	9.4	3.4	2	Both
Panel 2	9.5	2.9	2	Single
Panel 3	9.7	2.9	2	Both
Panel 4	10.0	3.5	2	Single
Panel 5	16.7	3.1	3.5	Single

8.2. Experimental Set Up and Testing Procedures

The blast tests were conducted at the Aviation Applied Technology Directorate in Fort Eustis, Virginia. Three 23 x 152 mm High Explosive Incendiary (HEI) rounds were used. An image of the HEI threat is shown in Figure 8-2. The HEI round imparts its energy in the form of a high-pressure blast wave and fragmentations traveling at supersonic speeds. The round uses a percussion primed cartridge with a large steel body partially filled with 13.35g of the explosive mixture hexal (A-IX-2) made up of cyclotrimethylenetrinitramine (RDX) (74%), aluminum (22%), and wax (4%). The explosive is equivalent to approximately 21g of trinitrotoluene (TNT) given that A-IX-2 has a TNT relative effectiveness factor of 1.54. The head of the round is fitted with a delayed-action self-destruct fuse used to ignite the explosive mixture following initial penetration of an aluminum striker plate placed in front of the CMF panels. Ignition of the self-destruct fuse results in a high-pressure blast wave and fragments aimed towards the CMF panels that surround the center of the blast.



Figure 8-2: Image of 23 x 152 mm high explosive incendiary rounds used to test CMF panels against blast wave and fragment impact.

The test set up used a Mann gun to fire the HEI round towards a thin aluminum 2024-T3 target with a thickness of 2.3 mm. The aluminum target was attached to a heavy steel frame placed down range of the Mann gun and was used to activate the self-destruct fuse at the head

of the HEI round. Two heavy-duty steel frames were located behind the aluminum target and faced at an angle of approximately 15° as shown in Figure 8-3 and Figure 8-4. These heavy-duty frames have the ability to hold up to four CMF panels, two on either side. The CMF panels were distanced approximately 46 cm away from the aluminum target and clamped in place against the frames to constrain edge deformation of the panels. A diagram of the test setup can be seen in Figure 8-3, while digital images in Figure 8-4 show the actually setup. Once the HEI impacts the aluminum target, with a barrel speed of approximately 970 m/s, the self-destruct fuse is set off and a high-pressure blast wave and a cloud of fragments traveling at supersonic speeds impact the CMF panels. The fragment cloud is a mixture of the copper and steel that make up the HEI round and aluminum from the target panel. Two PhantomTM v1210 digital high-speed cameras were placed to the left of the aluminum target. The cameras were used to record up to 40,000 frames per second and help to determine the incident speed of the fragments by measuring the time it takes to reach the CMF panels from a calibrated distance. Thin white sheets of paper are placed over the face of the CMF panels in order to easily track the frags as they pass through the cameras' field of view. The sheets of paper block background images and improve the accuracy and focus of the high-speed camera footage. In total, three HEI rounds were fired at a total of 5 CMF panels with some panels being tested on both sides, or multiple tests on one side.

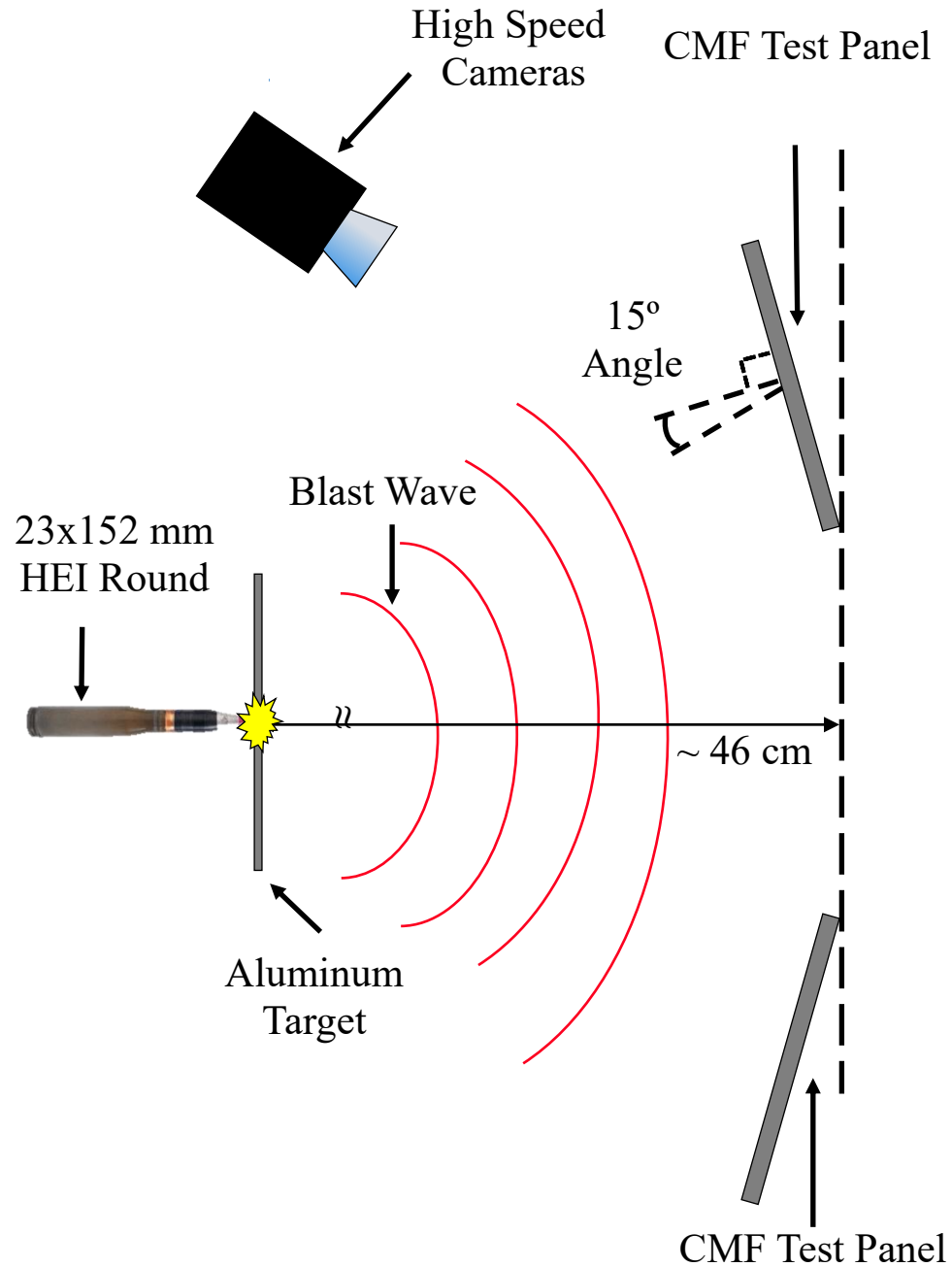


Figure 8-3: Diagram of the experimental setup for HEI blast against CMF panels.

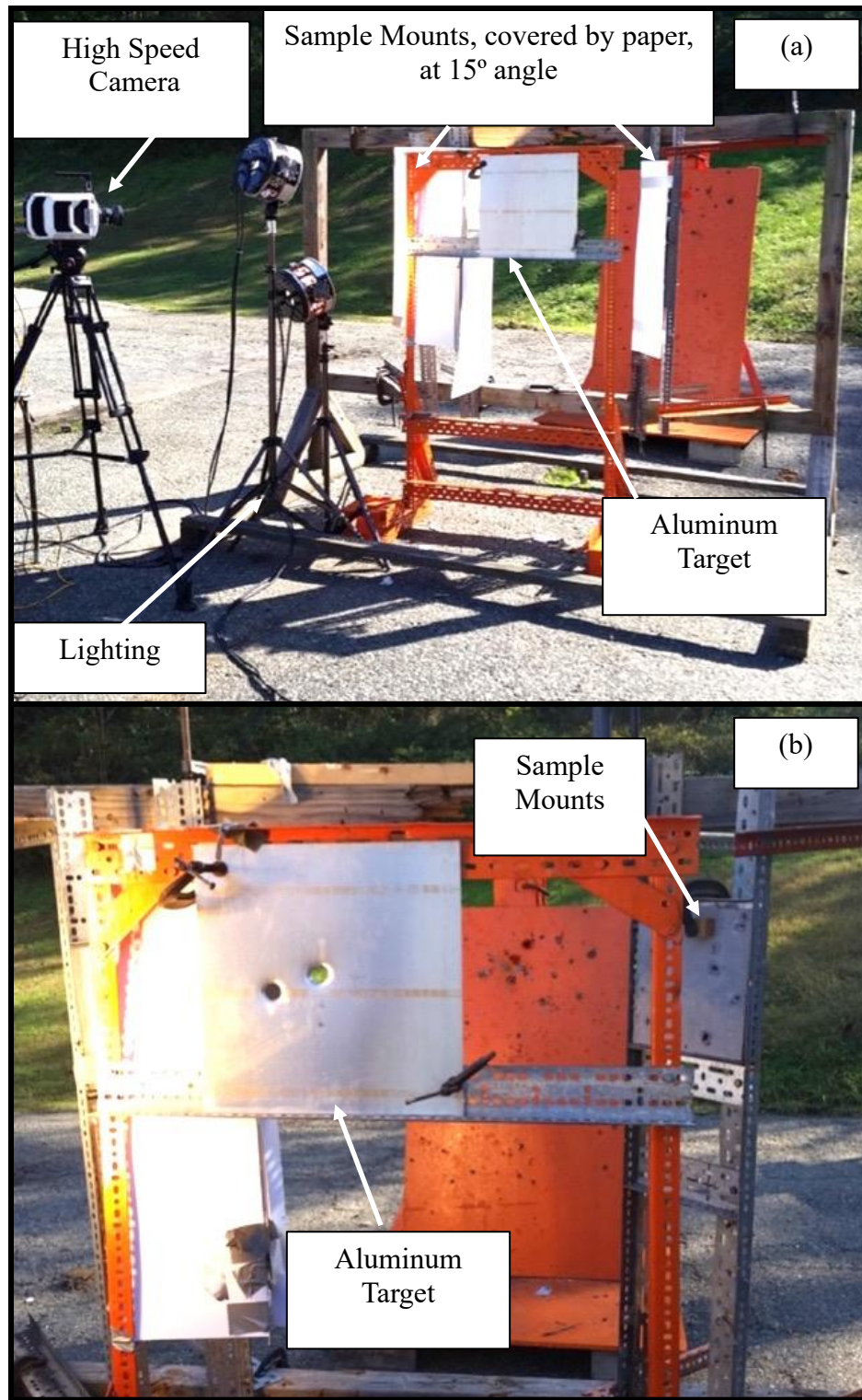


Figure 8-4: Experimental set up showing the positioning of cameras and CMF panels in relation to the thin aluminum target.

Following testing, the panels were analyzed for their flatness and extent of damage on the front and back surfaces using digital imaging. The mass of each panel was measured and compared with their original mass to evaluate the increase due to the arrested fragments. The approximate area of impact and depth of penetration of each fragment was also measured and recorded. The measurements were approximated, as a majority of the fragments were welded to the CMF panels and were unable to be removed without further machining. The fragments found in the panels ranged in size and were grouped by their approximate area of impact. Three groupings of small ($< 50 \text{ mm}^2$), medium ($50\text{-}90 \text{ mm}^2$), and large ($> 90 \text{ mm}^2$) fragments were defined by the measured areas of impact. The density of the fragments was approximated by dividing the total average volume of the fragments by the mass gained in each panel. The approximated density was found to be 6250 kg/m^3 , leading one to believe the fragments are made of a mixture of steel (with a density of 7870 kg/m^3) and copper (with a density of 8960 kg/m^3) from the projectile casing, plus some aluminum (with a density of 2660 kg/m^3) from the aluminum target.

Fragment speed was measured using the high-speed camera, while the blast wave properties are calculated based on the TNT equivalent of the A-IX-2 that fills the HEI round. According to Hopkinson-Cranz, a blast overpressure can be characterized by the distance from the detonation source and mass of the explosive charge [27]. One can calculate the scaled distance, Z, of an explosive given by:

$$Z = \frac{R}{\sqrt[3]{W}} \quad (1)$$

where R is the distance from the detonation source in meters [m] and W is the mass of the explosive in kilograms [kg]. The scaled distance is used to calculate the effective blast wave parameters created by the explosion. The blast wave is primarily characterized by the

peak wave overpressure, shock front velocity, and blast energy. The peak overpressure is defined as the initial and instantaneous rise in pressure that occurs upon arrival of the blast wave at a given distance. A negative wave phase follows the peak pressure rise and causes the structure to undergo a suction force. The negative phase of the pressure wave is ignored during structural calculations as critical damage is found to occur during the positive wave. Although the negative wave phase is ignored, a reflected wave is created by the particles bouncing off of the surrounding structures' surfaces. In an ideal elastic collision, the reflected wave pressure is equal to the incident pressure. To take this into account, the equivalent TNT mass used to calculate the scaled distance is doubled, assuming the structure undergoes impact by both an initial and reflected wave pulse initiated from the steel frame that holds the aluminum impact panel. The peak pressure can be calculated using the scaled distance through a number of different numerical methods. The equations used for calculation of the blast wave parameters were developed by Kingery-Bulmash [177]. The Kingery report fits a high order polynomial equation to data collected for large air blast events created by hemispherical charges ranging in mass from 5-500 tons of TNT. Equation 2 gives the high order polynomial used for calculation of the peak overpressure and shock wave front velocity.

$$\text{Function} = \text{EXP}(A + B * (\ln Z) + C * (\ln Z)^2 + D * (\ln Z)^3 + E * (\ln Z)^4 + F * (\ln Z)^5 + G * (\ln Z)^6) \quad (2)$$

Z is the scaled distance given by equation 1 and A, B, C, D, E, F, and G are the coefficients determined and reported by Kingery-Bulmash. The coefficients used to calculate the blast wave peak overpressure and shock front velocity are given in Table 8-2. The blast wave energy is calculated by the explosive's TNT equivalent to determine the energy released by a given weight of an explosive product.

Table 8-2: Simplified Kingery-Bulmash Airblast Coefficients.

	A	B	C	D	E	F	G
Peak							
Overpressure (kPa)	7.2106	-2.1069	-0.3229	0.117	0.0685	0	0
Shock Front Velocity (km/s)	0.1794	-0.956	-0.0866	0.109	0.0699	0.01218	0

8.3. Finite Element Model Conducted by an External Company to Initialize and Run the Model

Finite element analysis (FEA) offers a broad understanding of the blast armor systems and their limitations. In this study, the modeling efforts for blast and frag resistance of CMF into three subgroups including the material model, fragment model, and the blast wave and particle model. Two modeling scenarios were run in IMPETUS Afea: 1) fragment impact on the test panel and 2) fragment impact coupled with the blast wave. The model was compiled and run by an outside service provider. The results are analyzed and used for comparison to the experimental work.

8.3.1. Material Model Conducted by an External Company

The model uses the fracture criteria developed by Yuanli Bai and Tomasz Wierzbicki [178]. The Bai-Wierzbicki model is an empirical expansion on the constitutive model built by Gordon Johnson and William Cook. The Johnson-Cook failure criteria is the standard model used for modeling ductile materials under high strain rates [157]. Yet, the J2 plasticity theory that the Johnson-Cook strength model uses, assumes hydrostatic pressure has little to no effect on the material strain hardening or flow stress the material undergoes. Bai-Wierzbicki (B-W) found under hydrostatic pressures the third deviatoric stress invariant becomes relevant to the plasticity of metals. They reported that in low triaxiality situations the fracture locus of certain

metals shifts and becomes correlated to the Lode angle and triaxiality ratio [178]–[180]. These conditions modify the material's strengthening parameters and under certain types of loading, such as high strain rate ballistic and blast loading, where each iteration undergoes large deformations, the B-W model can be more accurate than J2 plasticity models, such as the Johnson-Cook plasticity model [180].

The Bai-Wierzbicki model calculates the evolution of the stress tensor and plastic strain in each element through integral steps. At each integration point within an element, the stress triaxiality, σ_i^* , and Lode parameter, μ_i , are calculated as:

$$\sigma_i^* = \frac{\sigma_{I,i} + \sigma_{II,i} + \sigma_{III,i}}{3\sigma_{VM,i}} \quad (3)$$

$$\mu_i = \frac{2\sigma_{II,i} - \sigma_{I,i} - \sigma_{III,i}}{\sigma_{I,i} - \sigma_{III,i}} \quad (4)$$

where σ_{VM} is the von Mises equivalent stress and σ_I , σ_{II} , σ_{III} are the three primary stresses. The subscript i denotes the integration point within a given element. These values are used to determine the average plastic strain ε_p , average stress triaxiality σ^* , and average Lode parameter μ within a given element shown in equations 5-7.

$$\varepsilon_p = \frac{1}{V} \sum_{i=1}^{n_{ip}} V_i \varepsilon_p \quad (5)$$

$$\mu = \frac{1}{V} \sum_{i=1}^{n_{ip}} V_i \mu_i \quad (6)$$

$$\sigma^* = \frac{1}{V} \sum_{i=1}^{n_{ip}} V_i \sigma_i^* \quad (7)$$

The material properties for composite metal foam are based on previous experimental work conducted on 2 mm SS-CMF under high strain rate conditions [107], [122]. The CMF properties that were used in this modeling work are determined through prior experimental studies and are reported in Table 8-3. The CMF panel was modeled as a homogenized 16 mm

thick panel, with all of the determined properties, disregarding the geometry of the spheres within the body.

A comparison simulation using a 5083-H116 aluminum panel with the same mass as the 16 mm CMF was run under the same blast and fragment impact conditions. Aluminum 5083 is an aluminum-magnesium alloy that is used in ship hulls and naval structures. It was chosen for its similar density to CMF, as well as its current use in armor system studies [52], [181]–[183]. The thickness of the aluminum plate was determined to be 16.85 mm in order to have the same mass as the 16 mm SS-CMF panel. The mechanical properties of AA5083-H116 were taken from ASTM-B928 [184]. The edges of the panels are constrained against motion, similar to the experimental setup.

Table 8-3: Material properties for the composite metal foam, aluminum armor, aluminum, low carbon steel, and copper fragments.

	Density ρ (kg/m ³)	Modulus of Elasticity E (GPa)	Poisson's Ratio ν	Failure Tensile Strain ε_f (%)	Tensile Strength (MPa)
SS-CMF [73], [93], [94], [96], [100], [107], [122]	2800	13.0	0.20	5	86
AA 5083-H116 [183]	2660	70.3	0.33	25	441
22000					
Copper Alloy [185]	8960	200	0.31	45	425
Al 2024-T3 [186]	2700	196	0.33	17	483
Low Carbon Steel [187]	7870	205	0.29	30	440

8.3.2. Fragment Model Conducted by an External Company

To create the fragments of representative geometries, a fragment cloud was initialized in IMPETUS using previous work of an exploded 120 mm M62 mortar projectile. The fragment cloud was analyzed, and three fragments were chosen to represent those seen during experimental testing, one from each size group of small ($< 50 \text{ mm}^2$), medium ($50\text{-}90 \text{ mm}^2$), and large ($> 90 \text{ mm}^2$). The fragments were meshed using cubic-tetrahedral elements for each of the three fragment sizes. Each fragment size was given a different material property to compare and determine which material best represents the fragments from the experimental testing. The small fragment was treated as shrapnel created from the low carbon steel jacket of the bullet, medium was given the properties of the aluminum impact panel, and the large fragment was treated as copper from the HEI round. The mechanical properties, at room temperature, of the low carbon steel, aluminum 2024-T3, and copper alloy 22000 are taken from the ASM Handbook and presented here in Table 3 [185]–[187]. The fragments were given an initial velocity of 1525 m/s, the highest speed measured by the high-speed video cameras used in the experimental testing, in order to simulate a “worst-case” scenario. The initial velocity was angled at 15°, to best match the impact parameters experienced during the live round testing.

8.3.3. Particle Blast Model Conducted by an External Company

The air particles in the IMPETUS Afea Solver were modeled as rigid particles using the corpuscular method, also known as the discrete particle method. The air particles were modeled in IMPETUS as an ideal gas, with a density of $\rho=1.3\text{kg/m}^3$, internal energy of $E_0=253\text{kJ/m}^3$, and ratio of specific heats $\gamma= 1.4$. The blast wave is modeled after the shock front statistics expected from a high-explosive incendiary shell made of 13.35g of A-IX-2. The

blast wave parameters for the discrete particle model include the peak overpressure, particle velocity, and blast wave energy. In this study, we have increased the explosive mass to 15 times its initial amount to consider an amplified worst-case scenario. It is notable that the speed of fragments stayed the same and is equivalent to what was recorded during the experimental testing using the high-speed cameras. The blast parameters are calculated using equations 1-2 and the results of which are shown in Table 8-4. Figure 8-5 gives a visual representation of the initialized blast wave with the impending fragments. The blast model allows for an in depth understanding of the energy dissipation capabilities of CMF panels and a more precise calculation of the blast wave interaction when coupled with the fragment impact.

Table 8-4: HEI blast wave properties arriving at the CMF and aluminum 5083-H116 panels.

Particle Velocity	2075 m/s
Peak Wave Overpressure	4.3 MPa
Blast Energy	600 kJ

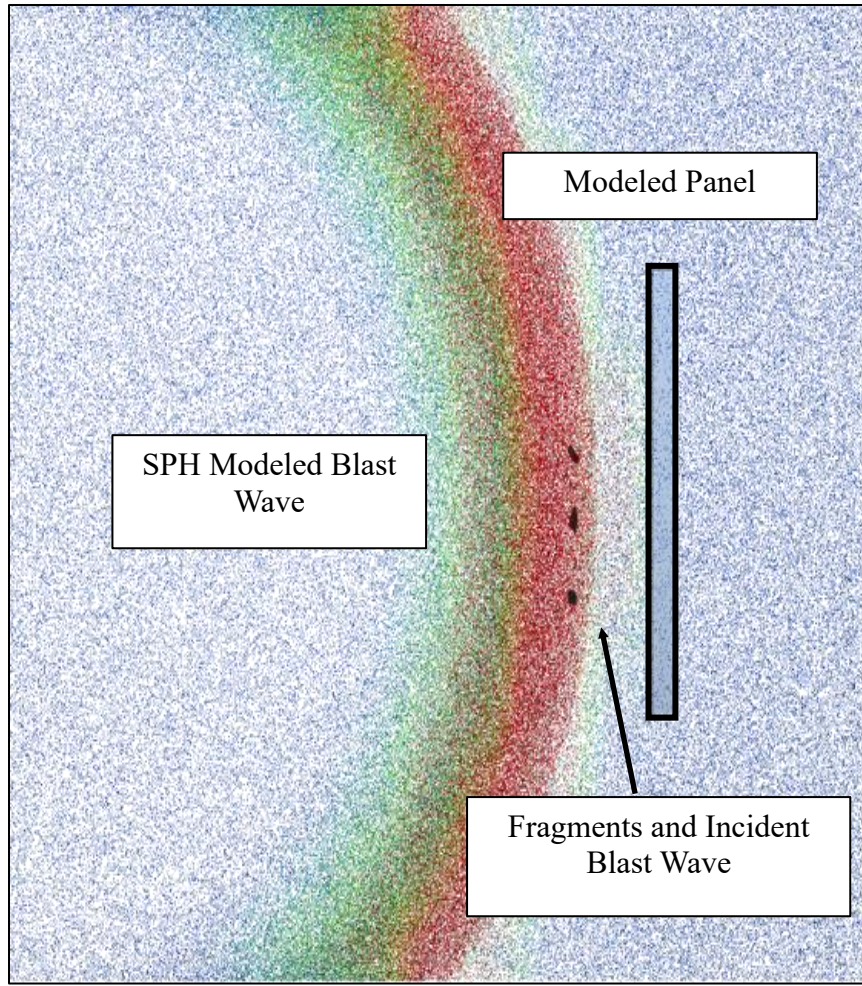


Figure 8-5: Initialized blast wave and fragments modeled in IMPETUS Afea Solver.

8.4. Results and Discussion

8.4.1. Experimental Results

The speed of the fragments arriving at the CMF panels was measured by the high-speed cameras and found to be between 1400-1524 m/s (4600-5000 ft/s). The fragment sizes varied with each shot but were grouped into three sizes for ease of analysis and comparison. Images of the CMF panels following testing are shown in Figure 8-6. It can be noted that all of the panels remained intact with no cracking or warping due to the impacts. Figure 8-6(a)-(d)

includes all of the 9 mm CMF panels tested. Figure 8-6(e) shows panel 5 with a close up of a large fragment and its impact area in 8(f). Figure 8-7 shows the depth of penetration of all fragments as a function of their areal impact size. The two graphs show the general groupings (by color) of the fragments, where small fragments are represented with yellow bars, medium with red, and large fragments with blue for both the 9 mm and 16.75 mm CMF panels. Fragments that penetrated the panels are shown at the top of the graph labeled as “complete penetration” in Figure 8-7(a). Panel 5, the thicker CMF panel, following three complete tests against the explosive threat, stopped all fragments except for two that impacted at the edge of the panel. Due to their impact lying along the edge, these data points are excluded as outliers in the graphical representations. The locations of these fragments on panel 5 are highlighted in Figure 8-6(e).

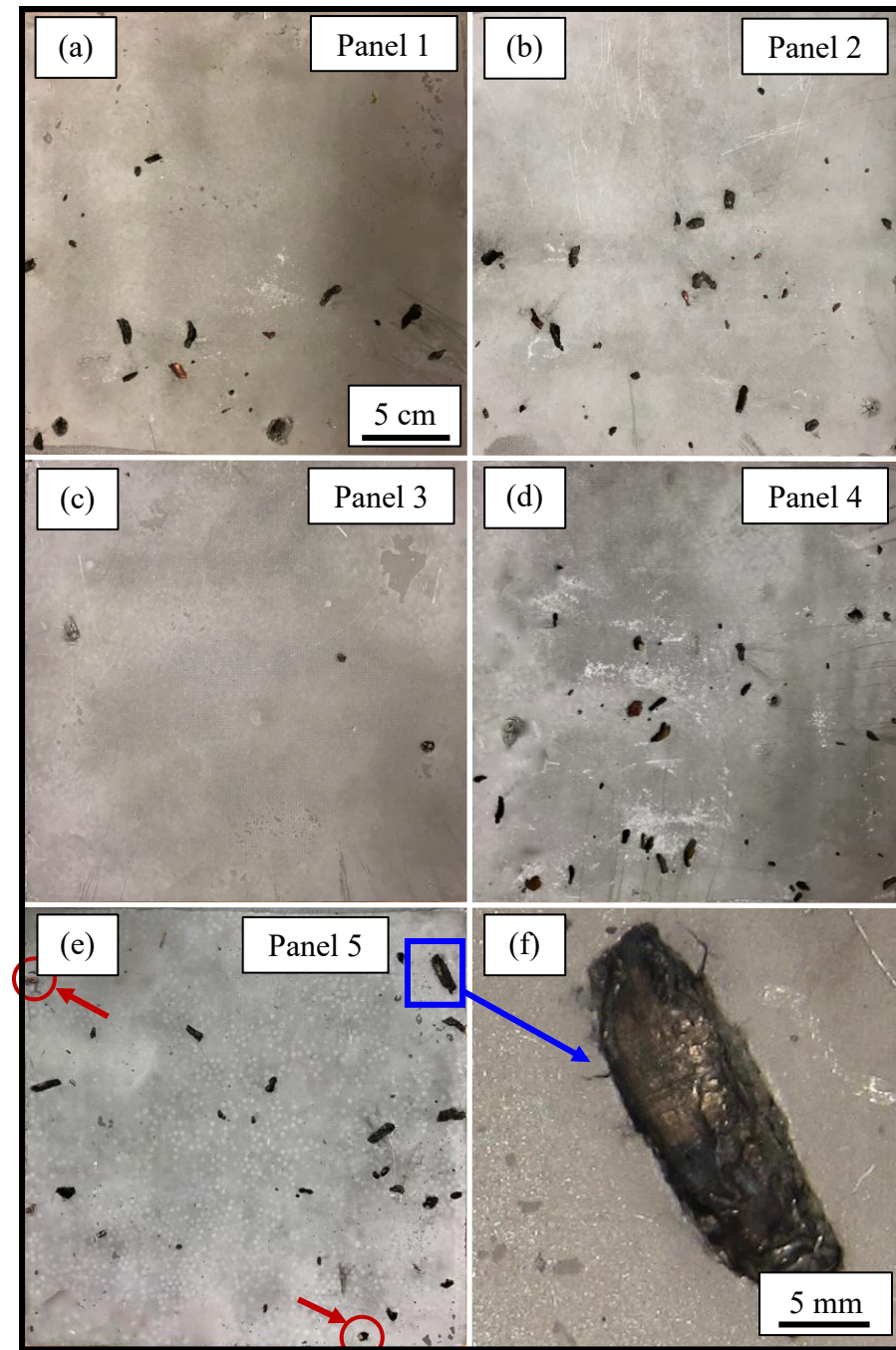
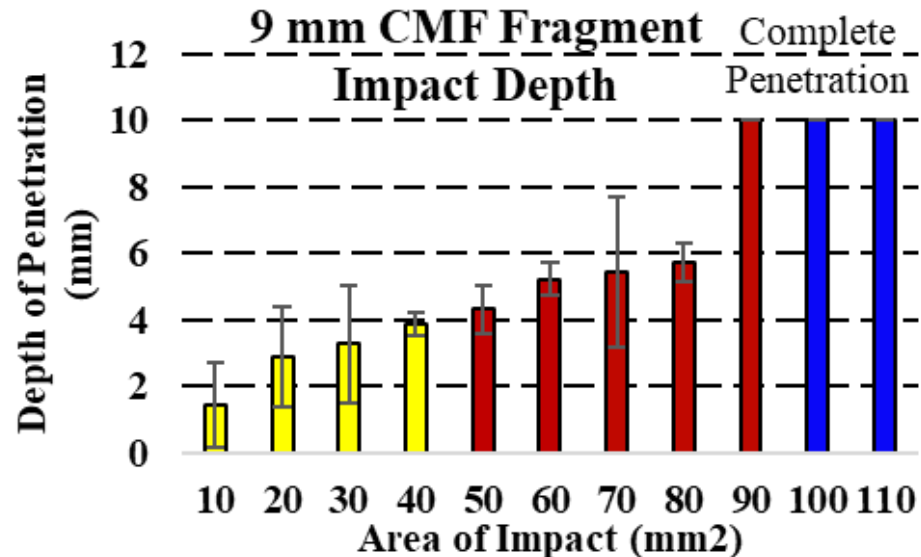


Figure 8-6: Digital images of the surface of SS-CMF panels with thickness of (a)-(d) 9 mm and (e) 16.75 mm following testing against three 23 x 152 mm HEI rounds with a close up (f) of a large fragment impacted on the 16.75 mm thick SS-CMF.

The thinner CMF panels had few fragments penetrate through the entire thickness but did not crack or bulge. The entirety of each CMF panel remained intact following all tests. The

fragments, which did penetrate the panel, have a variety of impact areas, and cause slight petaling at their point of exit. The thinner panels, although able to stop a majority of the fragments, were too thin to fully defeat all of the fragments created by the 23 x 152mm HEI round at such close proximity. A compilation of the findings and average values for each fragment size is presented in Table 8-5.

(a)



(b)

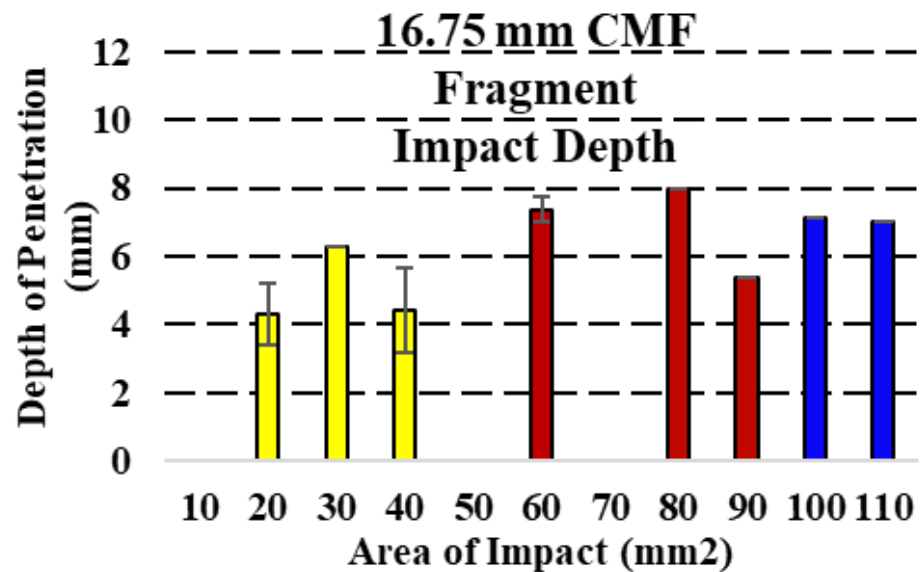


Figure 8-7: Fragment depth of penetration based on the area of impact of small (yellow), medium (red) and large (blue) fragments for: (a) thin CMF panels and (b) thick CMF panel.

The depth of penetration of the fragments for both CMF panels differs slightly for fragments of a similar size. The thinner CMF panels are able to stop a majority of the incident fragments between 2 and 6 mm thickness, while the thicker panel stopped a similar distribution of fragments between 3 and 8 mm thickness. The small sized fragments are stopped at similar depths between the thin and thick CMF panels. Yet, for medium and large sized fragments, the penetration is consistently deeper in the 16.75 mm thick CMF panel (panel 5). There is little deviation in penetration depth between medium size and large size fragments in both types of CMF panels. Although the large fragments carry more energy, they also cause more spheres to compress, resulting in more efficient absorption of additional energy.

Table 8-5: Average depth of penetration for each fragment size comparing experimental and numerical modeling findings.

Modeled Fragment Area of Impact (mm ²)	Real Fragment Area of Impact Range (mm ²)	Experimental Depth of Penetration (mm)		Depth of Penetration in CMF panel resulted from IMPETUS modeling (mm)
		Thin Panels of CMF with 5 layers of 2mm spheres	Thick Panel of CMF with 5 layers of 3.5mm spheres	
Small (7 x 4 mm)	0-10	2.4	4.6	
	10-20	2.3	4.5	
	20-30	4.5	6.2	6.3
	30-40	4.0	4.0	
	40-50	4.5	6.2	
	50-60	4.4	7.6	
Medium (16 x 6 mm)	60-70	5.6	12.3	6.5
	70-80	-	7.2	
Large (22 x 7 mm)	> 90	-	6.6	7.8

The primary difference between the thin and thick CMF panels (panels 1-4 versus panel 5), other than their manufactured thicknesses, is the size and type of the spheres used during

their processing. Panel 5 uses spheres with an outer diameter of 3.5 mm, while panels 1-4 use spheres with a 2 mm outer diameter. Upon further investigation of the findings, it can be seen that the fragments are brought to rest in increments of sphere diameters. One sphere layer is required to stop small fragments, while medium fragments require compressing approximately two layers (two sphere diameters) before completely coming to rest. This interaction can be attributed to the air that is displaced within the spheres, dissipating energy upon impact, a characteristic unique to composite metal foams. These observations would explain the deviation in the fragments' depth of penetration between the thinner and thicker CMF panels tested and will be the focus of future experimental and modeling studies to design the material in such a way that the fragment penetration is minimized using the lightest possible design of CMF.

8.4.2. Modeling Results Conducted by an External Company

The depth of penetration for each fragment size resulted from the IMPETUS Afea model and the experimental tests are presented in Figure 8-8 and Table 5. These findings are used to analyze the effectiveness of the SS-CMF panel when compared to 5083-H116 aluminum armor. Figure 8-8 shows the depth of penetration of each fragment based on its approximated area of impact. The CMF is shown to require less depth to stop various fragment sizes, when compared to the modeled AA5083-H116 armor in both conditions with and without the presence of the blast wave. The bulk aluminum armor requires a larger thickness to halt the fragments. Moreover, the petaling and bulging damage to the aluminum armor panel is more severe. Comparing the two panels, the small fragments penetrate 2 mm deeper into the aluminum armor than the CMF panel. This trend remains consistent with the larger and denser copper fragments, where the aluminum armor requires approximately 11 mm of material to

stop the fragment, versus the 7 mm of the CMF (a little over half of what is required for the aluminum panel). The depth of penetration for the aluminum 2024-T3 fragments is similar for both the CMF and aluminum models. This can be due to the lower density of the impacting fragments as there is less energy to be absorbed by the panels and both the CMF and aluminum perform similarly. The modeled depths of penetration for the medium fragments also fall below experimental findings, providing reason to believe the fragments created during experimental testing are better represented by the steel and copper material properties.

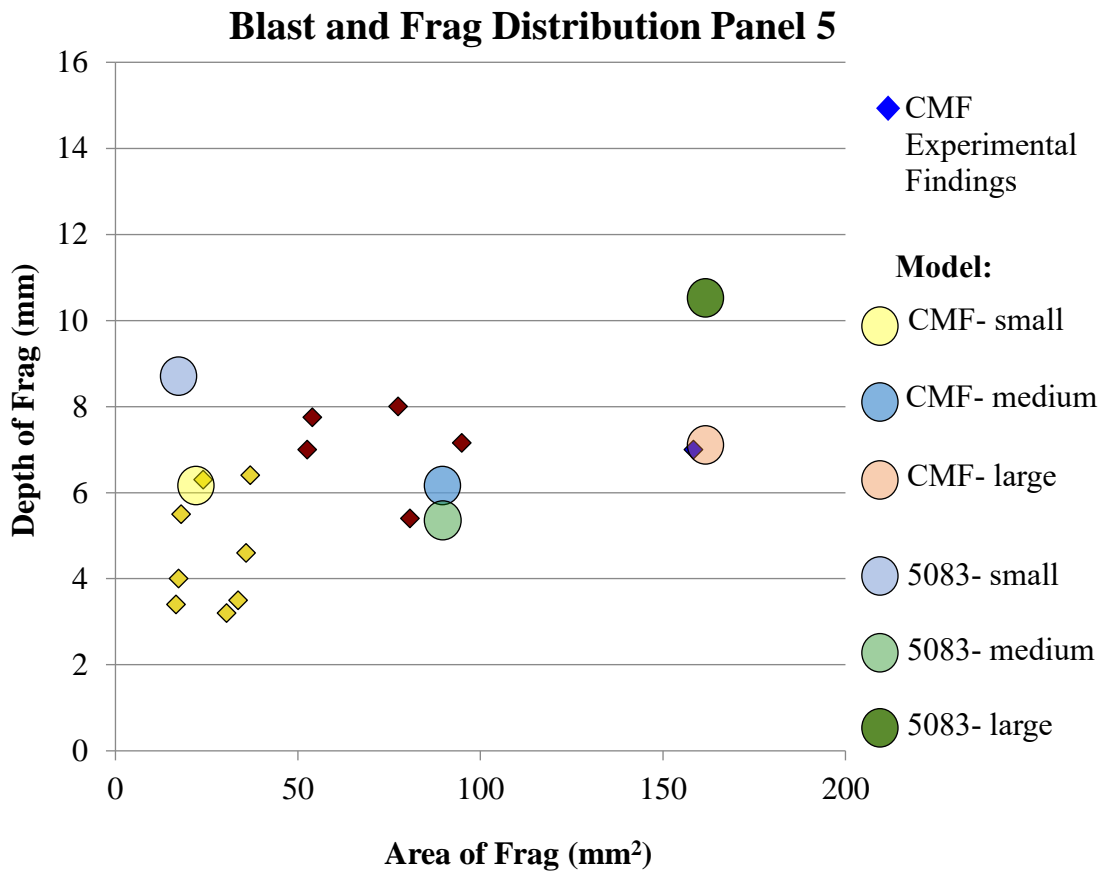


Figure 8-8: Comparison of the experimental and modeling results for a 16 mm thick CMF panel and 16.85 mm thick aluminum 5083 armor panel against HEI blast and frag.

The CMF and aluminum 5083-H116 panels were also modeled against impact of the fragments coupled with the blast wave. A comparison of the CMF and AA5083-H116 effective stress distributions at 50 and 180 μ s is presented in Figure 8-9. As can be seen, the composite metal foam, Figure 8-9(a) and (c), locally deforms and compresses below the fragments and absorbs the blast wave efficiently. This phenomenon is possibly due to the deformation/compression of the micro- and macroporosities, which dissipate the fragment impact load and blast wave energy. It can be seen, following the impact of the fragments and blast wave, the aluminum panel is affected across the entirety of the panel and remains in a high state of stress. The aluminum plate also accumulates front radial petaling, as well as bulging at the rear of the panel, whereas the CMF panel shows minimal signs of bulging and petaling. The CMF, on the other hand, is under much less stress throughout the entire panel and the high stress areas are limited to the fragment's impact zone. The aluminum panel not only experiences a high stress state across the entire panel but also takes longer to dissipate the incident energy, making the aluminum less efficient at absorbing blast waves and more prone to transferring the blast energy to structures and occupants behind it.

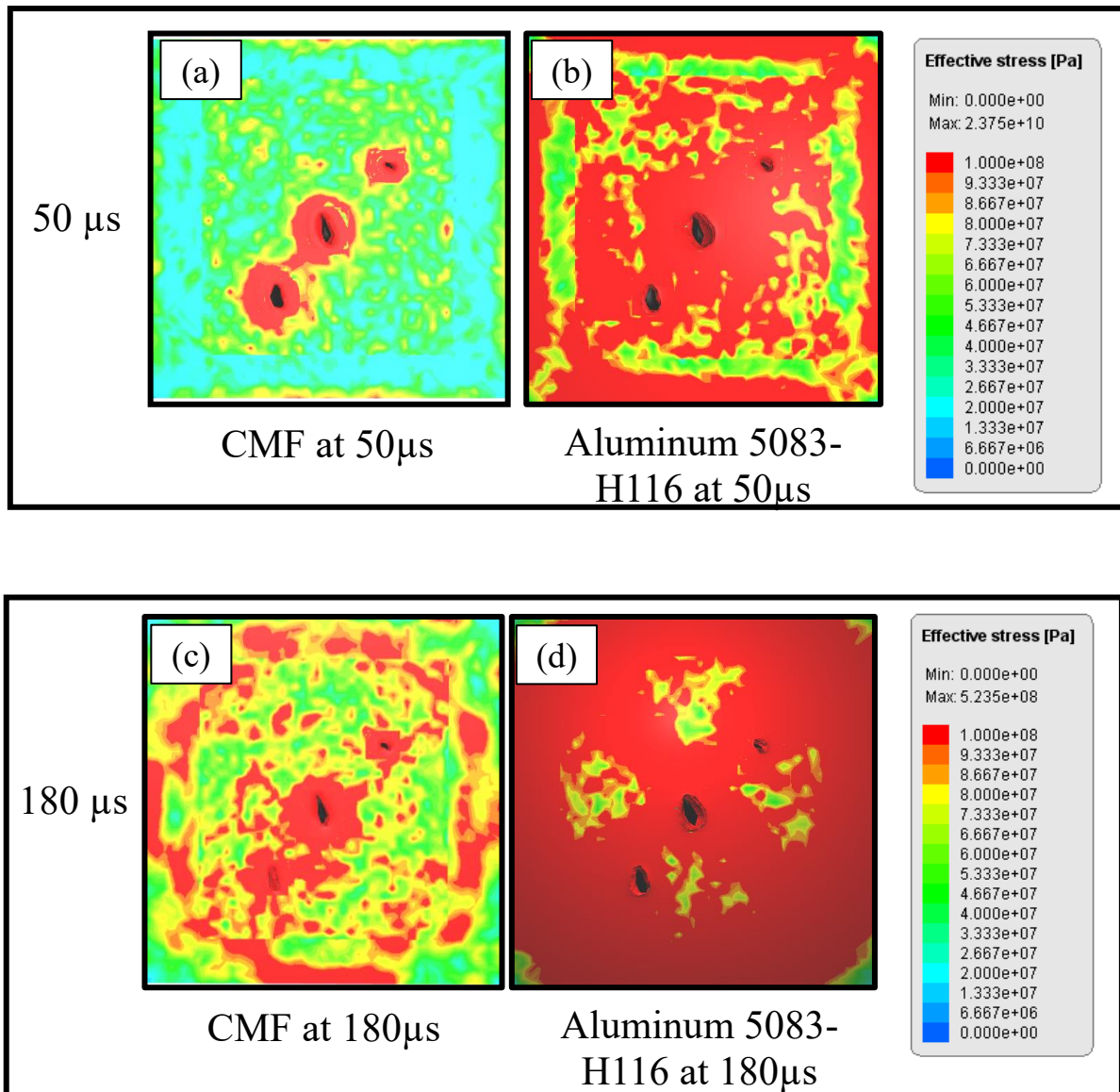


Figure 8-9: Comparison of the stress distribution in CMF (a,c) and aluminum 5083-H116 (b,d) panels upon interaction with blast wave and fragment impacts resulted from HEI round at 50 μ s (a,b) and 180 μ s (c,d).

8.5. Summary of Blast and Frag Testing of SS-CMF

Steel-steel composite metal foam armor panels were manufactured using powder metallurgy technique in multiple thicknesses and tested against 23 x 152 mm high explosive incendiary rounds that release a high-pressure blast wave and metal fragments at speeds up to

1524 m/s. The CMF panels were able to withstand the blast and frag impacts without bowing or cracking. The thicker sample was able to completely stop various sized fragments from three separate HEI tests. These initial tests provide valuable blast and frag data, which can be used to calculate the effective thicknesses required to defeat additional explosive ordnances and potentially protect against full scale IEDs. A finite element analysis was conducted by an external company using IMPETUS Afea Solver and was able to efficiently predict the behavior and energy absorption capabilities of composite metal foam. The simulations successfully model the blast and fragment impact created by the HEI threat and show the superior energy absorption capabilities of CMF when compared to a conventional armor.

CHAPTER 9: CONCLUSIONS

9.1. Mechanical Testing of SS-CMF and SS-CMF-CSP

Advanced materials are needed to perform under extreme environments such as those required to protect tank cars, military personnel, and vehicles under extreme loading. Tank cars require additional protections under accident conditions to reduce puncture and subsequent spilling of hazardous materials. CMF has unique energy absorption, thermal insulating, and radiation shielding properties that can be used to improve future tank car designs. In the first phase of this study, CMF sandwich panels were manufactured and characterized for potential use in future tank car designs. SS-CMF core sandwich panels (SS-CMF-CSP) were manufactured by adhesively and diffusion bonding stainless steel face sheets to the surface of an SS-CMF core. Samples were cut from the panels and tested under quasi-static compression and tension. The bond interface and microstructure of the SS-CMF-CSP were investigated using SEM and EDS analysis prior to mechanical testing.

The mechanical properties of the SS-CMF and SS-CMF-CSP were reported under compression and tension. The adhesively bonded samples were found to have little effect on the compressive properties of the CMF. Strengthening in the diffusion bonded samples was experienced under compression and is attributed to the secondary heat cycle that led to additional microstructural changes such as twin formation and diffusion of carbon from the sphere wall to the surrounding matrix. The diffusion bonded SS-CMF-CSP had a 17% higher plateau stress and 10% higher densification stress with uniform deformation under compression. Finite element analysis results show good agreement with the experimental work.

The tensile properties of SS-CMF and SS-CMF-CSP were reported as well. The ultimate tensile strength for the bare SS-CMF samples was between 75-85 MPa with a failure strain of

7.5-8%. The SS-CMF-CSP showed strengthening provided by the bulk metal face sheets with a 115% increase in tensile strength and average failure strain of 23%. The normalized stress values of the sandwich panel showed improvement over the bare samples, due to strengthening afforded by the bulk metal face sheets without greatly increasing the density. The fracture surfaces of the samples were investigated and revealed a change in failure mode under tension between the bare samples and sandwich panels due to microstructural changes during the diffusion bonding heat cycle. The elastic modulus of the SS-CMF and SS-CMF-CSP were approximated using the rule of mixtures and found to lie within the calculated lower and upper bounds.

9.2. Ballistic Performance of Composite Metal Foam Armors

Ballistic testing of CMF armors was completed on threats larger than previously tested. CMF layered armors were manufactured by sandwiching SS-CMF between a ceramic face plate and high strength aluminum backing and tested against 12.7 x 99 mm Ball/M2 AP and 14.5 x 115 mm B32 API. Rolled homogeneous armor was also used in the armor arrangements when testing against the largest caliber threat. The CMF armors were able to arrest all round types. The CMF layer absorbed between 77% and 83% of the impacting round's kinetic energy for the 12.7 mm and 14.5 mm rounds, respectively. The CMF armors show a strengthening behavior when facing increasing threat sizes due to the secondary impact region that forms around the core of the bullet. Further testing and optimization of CMF armors is expected to improve their mass efficiency against both threats. However, it is important to note, given the current data the armor shows improvement over conventional RHA and offer a weight reduction that can be vital for the advancement of today's military vehicles. Future armors can be built to maximize the advantages of CMF due to its high energy absorption capabilities and

cushioning of the AP core. The results from these studies will help to model and predict the performance of CMF armors against various threat sizes and energies.

9.3. Blast and Fragment Resistance of CMF

Composite metal foam armors were manufactured and tested against blast and fragment impact by detonation of a 23 x 152 mm high explosive incendiary round. The bare CMF panels faced a blast wave and fragment impact at speeds up to 1524 m/s. The CMF panels were able to withstand the impacts without cracking or bowing. Although the fragments possess high impact energies, the CMF panels were able to locally absorb the fragments and dissipate the blast wave energy. Finite element analysis of the CMF panels was able to accurately predict the panels' performance and provide further insight to the superior energy absorption capabilities of CMF when compared to bulk aluminum armor.

CHAPTER 10: INSIGHT FOR FUTURE WORK

In this work it has been shown that composite metal foam sandwich panels can be manufactured using both diffusion and adhesive bonding. The face sheets were found to improve the strength of the core under tension. Microstructural changes due to the additional heat cycle also strengthened the sandwich panels under both compression and tension. Future studies can improve the diffusion bonding process and test the panels under beam flexure, shear, and dynamic tensile loading. The diffusion bonding process can be improved by adding an interface between the open hollow spheres of the CMF and the stainless steel face sheets. By creating a solid bond in these areas, the interfacial bond strength of the sandwich panel will be improved without greatly modifying the structure of the CMF core. These tests can also focus on strength optimization of the face sheet thicknesses in each case. The optimization can also consider weight efficiency of the panel and revisit tensile testing of various face sheet thicknesses. The strain failure of the CMF core under tension should be analyzed using advanced strain mapping techniques, such as Digital Image Correlation (DIC), for further understanding of crack initiation and propagation.

The blast and ballistic testing of SS-CMF armors was successful against various threats and showed a weight efficiency improvement from the standard armors. The blast and fragment testing of SS-CMF can be expanded upon by testing panels against explosive shape charges with fragments planted below the panel to better simulate the detonation of improvised explosives against the panels and study the effects as if they represented the hull of a vehicle. The ballistic panels should be further optimized using large scale manufacturing techniques and obtain an improved mass efficiency ratio by incorporating other materials into the layered

armors and eliminating those that proved inefficient such as the individual ceramic tile arrangement.

In order to fully understand SS-CMF armor's application in the field, work discussing the weldability and attachment of SS-CMF panels to the exterior of vehicle designs is needed. The weldability and potential attachment of CMF panels would be applicable for both tank car and military vehicle applications. This can be tested on bare CMF panels as well as sandwich panels using an improved diffusion bonding technique with various metal such as TC-128 and RHA (the current tank car and armor standards).

LIST OF PUBLICATIONS

1. Marx, J., & Rabiei, A. (2017). Overview of composite metal foams and their properties and performance. *Advanced Engineering Materials*, 19(11), 1600776.
2. Marx, J., Portanova, M., & Rabiei, A. (2018). A study on blast and fragment resistance of composite metal foams through experimental and modeling approaches. *Composite Structures*, 194, 652-661.
3. Marx, J., Portanova, M., & Rabiei, A. (2019). Ballistic performance of composite metal foam against large caliber threats. *Composite structures*, 225, 111032.
4. Marx, J. C., Robbins, S. J., Grady, Z. A., Palmieri, F. L., Wohl, C. J., & Rabiei, A. (2020). Polymer infused composite metal foam as a potential aircraft leading edge material. *Applied Surface Science*, 505, 144114.
5. Marx, J., & Rabiei, A. (2020). Tensile properties of composite metal foam and composite metal foam core sandwich panels. *Journal of Sandwich Structures & Materials*. Online Publication.
6. Marx, J., & Rabiei, A. (2020) Study on the Microstructure and Compression of Composite Metal Foam Core Sandwich Panels, *Metallurgical and Materials Transactions A*. Online Publication.
7. Chen, S., Marx, J., & Rabiei, A. (2016). Experimental and computational studies on the thermal behavior and fire retardant properties of composite metal foams. *International Journal of Thermal Sciences*, 106, 70-79.
8. Rabiei, A., Portanova, M., Marx, J., Scott, C. and Schwandt, J. (2020), A Study on Puncture Resistance of Composite Metal Foam Core Sandwich Panels. *Advanced Engineering Materials*. Online Publication.

Conference Proceedings

1. Marx, J., Portanova, M., & Rabiei, A. (2017). Blast and Frag Response of Composite Metal Foam Armor Systems. In *Proceedings of the American Society for Composites—Thirty-second Technical Conference*.
2. Robbins, S. J., Marx, J. C., Grady, Z. A., Palmieri, F. L., Wohl, C. J., & Rabiei, A. (2020). Polymer infused composite metal foam as a potential aircraft leading edge material. In: *41st 2018 Annual Meeting of the Adhesion Society*. Adhesion Society, Inc.; Blacksburg, VA.
3. Marx J., Rabiei A. (2020) Study on the Mechanical Properties of Composite Metal Foam Core Sandwich Panels. In: *Proceedings of the 11th International Conference on Porous Metals and Metallic Foams (MetFoam 2019)*. The Minerals, Metals & Materials Series. Springer, Cham.

REFERENCES

- [1] R. S. Institute, “Tank Car 101,” 2017.
<https://tankcarresourcecenter.com/tankcar101/#1499693534177-d720d234-3972>.
- [2] Gouda Hazem, “41 Killed, 179 Injured in Egypt’s Alexandria Train Collision,” *Irish Times*, 2017. <https://wwwirishtimes.com/news/world/middle-east/at-least-40-people-killed-after-train-crash-in-egypt-1.3183808>.
- [3] A. Barnett, “Why you won’t die in a plane crash,” *CNN*, Jul. 09, 2013.
- [4] P. Chiasson, “Feed Loader,” *Star Tribune*, 2013. <https://www.startribune.com/jan-8-oil-train-accidents-prompt-review-of-tank-car-safety/239194271/>.
- [5] C. A. Reschovsky, M. Flowers, D. Smallen, and J. Sharp, “Fleet Composition of Rail Tank Cars Carrying Flammable Liquids: 2018 Report,” United States. Department of Transportation. Bureau of Transportation Statistics, 2018.
- [6] J. Murphy, “Lac-Mégantic: The runaway train that destroyed a town,” *BBC News*, Toronto, Jan. 19, 2018.
- [7] T. L. Anderson, *Fracture Mechanics: Fundamentals and Applications, Fourth Edition*. 2017.
- [8] P. Springer, “‘We would have been history’: 5 years later, Casselton train blast still echoes with lessons learned, regulatory changes,” *Grand Forks Herald*, Grand Forks, Dec. 29, 2018.
- [9] P. Rakoczy, M. Carolan, T. Gorham, and S. Eshraghi, “Side Impact Test and Analyses of a DOT-117 Tank Car.” [Online]. Available:
<https://rosap.ntl.bts.gov/view/dot/40276>.
- [10] R. S. Institute, “Tank Car Standards in North America,” 2017.
<https://tankcarresourcecenter.com/standards/>.
- [11] A. of A. Railroads’, “Section C-III: Specifications for Tank Cars,” in *Manual of Standards and Recommended Practices*, Pueblo, CO, 2014.
- [12] R. L. Bodnar, F. Hamad, C. Penniston, and S. Roysum, “As-Rolled Plate Product with Improved Yield Strength, Toughness, and Weldability for Pressurized Railroad Tank Cars,” *Mater. Sci. Technol. IRON STEEL Technol.*, vol. 6, p. 3502, 2007.
- [13] T. L. Anderson and S. W. Kirkpatrick, “Quantifying and Enhancing Puncture Resistance in Railroad Tank Cars Carrying Hazardous Materials,” Arlington, VA, 2006.
- [14] National Transportation Safety Board, “Derailment of Canadian Pacific Railway Freight Train 292-16 and Subsequent Release of Anhydrous Ammonia near Minot North Dakota January 18, 2002.No Title,” 2004.
- [15] S. Abotula, B. R. Konda, W. J. Walsh, V. S. A. Challa, T. Ros, and M. Manohar, “Analysis of Puncture Resistant Steel for Tank Cars,” *Steel Res. Int.*, vol. 90, no. 4, p. 1800339, Apr. 2019, doi: 10.1002/srin.201800339.
- [16] S. W. Kirkpatrick, J. M. Munaretto, V. Phan, and R. A. MacNeill, “Development of Analytical Models for Railroad Tank Car Impact and Puncture Behaviors,” in *Rail Transportation Division Conference*, 2012, vol. 45073, pp. 75–84.
- [17] M. E. Carolan *et al.*, “Application of welded steel sandwich panels for tank car shell impact protection.” 2013, [Online]. Available:
<https://rosap.ntl.bts.gov/view/dot/26243>.
- [18] R. Ash, *Lightweight ballistic composites: military and law-enforcement applications*:

- Vehicle Armors*, Second. Sawston, Cambridge: Woodhead Publishing, 2016.
- [19] P. J. Hazell, *Armour: materials, theory, and design*. Boca Raton, FL: CRC press, 2016.
- [20] L. F. da Silva, A. Lavoratti, I. M. Pereira, R. R. Dias, S. C. Amico, and A. J. Zattera, “Development of multilaminar composites for vehicular ballistic protection using ultra-high molecular weight polyethylene laminates and aramid fabrics,” *J. Compos. Mater.*, 2019, doi: 10.1177/0021998318815959.
- [21] G. M. Bochene, “Directions in Engine-Efficiency and Emissions Research (DEER),” 2011. [Online]. Available: <https://www.energy.gov/eere/vehicles/2011-directions-engine-efficiency-and-emissions-research-deer-conference-presentations>.
- [22] W. Gooch, M. Burkins, D. Mackenzie, and S. Vodenicharov, “Ballistic analysis of bulgarian electroslag remelted dual hard steel armor plate,” in *Proc. of 22nd International Symposium on Ballistics*, 2005.
- [23] G. Campbell, A. Protection, and N. B. C. Protection, “Titanium applications for the abrams main battle tank,” in *International Titanium Association Meeting, Las Vegas, NV*, 1996, vol. 2.
- [24] W. Gooch *et al.*, “Development and ballistic testing of a new class of auto-tempered high hard steels under military specification MIL-DTL-46100E,” *TMS Annu. Meet.*, vol. 3, no. September, pp. 321–328, 2009.
- [25] A. F. P. Service, “Coalition, Iraqi Forces Discover Multiple Weapons Caches,” *American Forces Information Service, Department of Defense*, 2005. http://www.defenselink.mil/news/Nov2005/20051109_3279.html.
- [26] C. Department of Health and Human Services, “Explosions and Blast Injuries: A Primer for Clinicians,” 2013. doi: 10.1056/NEJMcm1203842.
- [27] V. Karlos and G. Solomon, *Calculation of blast loads for application to structural components*. 2013.
- [28] IATG and UN ODA, “International Ammunition Technical Guideline: Formulae for ammunition management,” New York, NY, 2016. [Online]. Available: <https://s3.amazonaws.com/unoda-web/wp-content/uploads/2019/05/IATG-01.80-Formulae-for-Ammunition-Management-V.2.01.pdf>.
- [29] J. Shin, A. S. Whittaker, and D. Cormie, “TNT Equivalency for Overpressure and Impulse for Detonations of Spherical Charges of High Explosives,” *Int. J. Prot. Struct.*, vol. 6, no. 3, pp. 567–579, Sep. 2015, doi: 10.1260/2041-4196.6.3.567.
- [30] T. Krauthammer and T. Krauthammer, *Modern Protective Structures*. Boca Raton, FL: CRC Press, 2008.
- [31] Major Rodney H. Lipscomb II, “MRAPs in the Brigade Combat Team,” *Army Sustainment*, 2011. https://alu.army.mil/alog/issues/sepoct11/MRAP_Combat_Team.html.
- [32] J. Montgomery and E. Chin, “Protecting the future force: a new generation of metallic armors leads the way,” *Amcpiac Q*, 2004.
- [33] J. Prifti, M. Castro, R. Squillaciotti, and R. Cellitti, “Improved Rolled Homogeneous Armor (IRHA) Steel Throughh Higher Hardness,” Aberdeen Proving Ground, 1997.
- [34] Department of Defense, “Military Specification MIL-DTL-46027K , ARMOR PLATE, ALUMINUM ALLOY, WELDABLE 5083, 5456, & 5059,” 2007.
- [35] U. S. Military, “Armor Plate, Steel, Wrought, Homogeneous, MIL-DTL-12560K (MR) (For use in Combat-Vehicles and for Ammunition Testing),” Aberdeen Proving

- Ground, 2013.
- [36] W. J. Nam and H. C. Choi, “Effect of Si on mechanical properties of low alloy steels,” *Mater. Sci. Technol.*, 1999, doi: 10.1179/026708399101506238.
 - [37] W. R. Whittington *et al.*, “Capturing the effect of temperature, strain rate, and stress state on the plasticity and fracture of rolled homogeneous armor (RHA) steel,” *Mater. Sci. Eng. A*, vol. 594, pp. 82–88, 2014, doi: <https://doi.org/10.1016/j.msea.2013.11.018>.
 - [38] K. Maweja and W. Stumpf, “The design of advanced performance high strength low-carbon martensitic armour steels. Microstructural considerations,” *Mater. Sci. Eng. A*, 2008, doi: 10.1016/j.msea.2007.07.078.
 - [39] R. cheng Yi, L. kui Yin, J. ru Wang, Z. gang Chen, and D. qi Hu, “Study on the performance of ceramic composite projectile penetrating into ceramic composite target,” *Def. Technol.*, 2017, doi: 10.1016/j.dt.2017.05.009.
 - [40] R. Orgorie, “Armor for Combat Vehicles - New Armor Materials,” *Mach. Des.*, vol. 41, no. 27, p. 36, 1969.
 - [41] R. L. Woodward, “RATIONAL BASIS FOR THE SELECTION OF ARMOUR MATERIALS.,” *J Australas Inst Met*, 1977.
 - [42] “Military Specification MIL-DTL-46100E (MR), Armor Plate, Steel, Wrought, High-Hardness,” U.S. Army Research Laboratory, Aberdeen Proving Ground, 2008.
 - [43] “Military Specification MIL-DTL-32332 (MR), Armor Plate, Steel, Wrought, Ultra-High-Hardness,” U.S. Army Research Laboratory, Aberdeen Proving Ground, 2009.
 - [44] P. K. Jena *et al.*, “Effect of heat treatment on mechanical and ballistic properties of a high strength armour steel,” *Int. J. Impact Eng.*, 2010, doi: 10.1016/j.ijimpeng.2009.09.003.
 - [45] S. Ryan, H. Li, M. Edgerton, D. Gallardy, and S. J. Cimpoeru, “The ballistic performance of an ultra-high hardness armour steel: An experimental investigation,” *Int. J. Impact Eng.*, vol. 94, pp. 60–73, 2016, doi: 10.1016/j.ijimpeng.2016.03.011.
 - [46] W. Gooch, M. Burkins, R. Squillaciotti, R.-M. S. Koch, H. Oscarsson, and C. Nash, “Ballistic Testing of Swedish Steel ARMOX Plate for US Armor Applications BALLISTIC TESTING OF SWEDISH STEEL ARMOX ® PLATE FOR U . S . ARMOR APPLICATIONS,” in *21st International Symposium on Ballistics*, 2004, pp. 19–23.
 - [47] W. a. Gooch, M. S. Burkins, and R. J. Squillaciotti, “Ballistic testing of commercial aluminum alloys and alternate processing techniques to increase the availability of aluminum armor,” *23rd Int. Symp. Ballist.*, no. April, pp. 981–988, 2007.
 - [48] “Yarrow Shipbuilders,” 2020. https://en.wikipedia.org/wiki/Yarrow_Shipbuilders.
 - [49] Lincoln Electric, “Aluminum: Experience in Application,” 2020. <https://www.lincolnelectric.com/en-au/support/process-and-theory/Pages/aluminum-application-detail.aspx>.
 - [50] T. L. Jones and B. E. Placzankis, “The Examination of the Aluminum Alloy 7017 as a Replacement for the Aluminum Alloy 7039 in Lightweight Armor Systems,” 2016.
 - [51] Department of Defense, “MIL-DTL-46063H, ARMOR PLATE, ALUMINUM ALLOY 7039,” no. September, 1998.
 - [52] T. Børvik, M. J. Forrestal, and T. L. Warren, “Perforation of 5083-H116 Aluminum Armor Plates with Ogive-Nose Rods and 7.62 mm APM2 Bullets,” *Exp. Mech.*, no. 50, pp. 969–978, 2010, [Online]. Available: 10.1007/s11340-009-9262-5.

- [53] M. J. Forrestal, T. Børvik, and T. L. Warren, “Perforation of 7075-T651 aluminum armor plates with 7.62 mm APM2 bullets,” *Proc. Soc. Exp. Mech. Inc.*, vol. 67, pp. 1245–1251, 2010, doi: 10.1007/s11340-009-9262-5.
- [54] J. K. Holmen, J. Johnsen, S. Jupp, O. S. Hopperstad, and T. Børvik, “Effects of heat treatment on the ballistic properties of AA6070 aluminium alloy,” *Int. J. Impact Eng.*, 2013, doi: 10.1016/j.ijimpeng.2013.02.002.
- [55] C. Mondal, B. Mishra, P. K. Jena, K. Siva Kumar, and T. B. Bhat, “Effect of heat treatment on the behavior of an AA7055 aluminum alloy during ballistic impact,” *Int. J. Impact Eng.*, 2011, doi: 10.1016/j.ijimpeng.2011.03.001.
- [56] M. A. Khan *et al.*, “Ballistic behaviour of spray formed AA7055 aluminum alloy against tungsten core projectile impact,” *Vacuum*, 2019, doi: 10.1016/j.vacuum.2018.10.073.
- [57] T. L. Jones, R. D. DeLorme, M. S. Burkins, and W. A. Gooch, “Initial ballistic evaluation of the magnesium alloy AZ31B,” in *Magnesium Technology*, 2007.
- [58] R. Perkins and R. Rennhack, “Processing and ballistic evaluation of dual-hardness titanium armor: AD-777 809,” Springfield, VA, 1974.
- [59] J. D. Beal, R. Boyer, D. Sanders, and T. B. Company, “Forming of titanium and titanium alloys,” in *ASM Handbook, vol. 14B, Metalworking: Sheet Forming*, 2006, pp. 656–669.
- [60] R. R. Boyer, “Attributes, characteristics, and applications of titanium and its alloys,” *JOM*, 2010, doi: 10.1007/s11837-010-0071-1.
- [61] J. S. Montgomery and M. G. H. Wells, “Titanium armor applications in combat vehicles,” *JOM*, 2001, doi: 10.1007/s11837-001-0144-2.
- [62] B. McLaurin, “DUAL- HARDNESS TITANIUM BODY ARMOR FOR CONCEALABLE APPLICATIONS,” Naval Postgraduate School, 2018.
- [63] E. Medvedovski, “Ballistic performance of armour ceramics: Influence of design and structure. Part 1,” *Ceram. Int.*, vol. 36, no. 7, pp. 2103–2115, 2010, doi: 10.1016/j.ceramint.2010.05.021.
- [64] E. Medvedovski, “Ballistic performance of armour ceramics: Influence of design and structure. Part 2,” *Ceram. Int.*, vol. 36, no. 7, pp. 2117–2127, 2010, doi: 10.1016/j.ceramint.2010.05.022.
- [65] M. Übeyli, H. Deniz, T. Demir, B. Ögel, B. Gürel, and Ö. Keleş, “Ballistic impact performance of an armor material consisting of alumina and dual phase steel layers,” *Mater. Des.*, vol. 32, no. 3, pp. 1565–1570, 2011, doi: 10.1016/j.matdes.2010.09.025.
- [66] A. K. Bandaru, V. V. Chavan, S. Ahmad, R. Alagirusamy, and N. Bhatnagar, “Ballistic impact response of Kevlar® reinforced thermoplastic composite armors,” *Int. J. Impact Eng.*, vol. 89, pp. 1–13, 2016, doi: 10.1016/j.ijimpeng.2015.10.014.
- [67] N. K. Naik and P. Shrirao, “Composite structures under ballistic impact,” *Compos. Struct.*, vol. 66, no. 1–4, pp. 579–590, 2004, doi: 10.1016/j.compstruct.2004.05.006.
- [68] D. Fecko, P. D. Lyle, and D. Murray, “The Synergistic Roles of High Strength Glass Composite and Alumina Ceramic Facing in Lightweight Composite Armor Against Armor Piercing Projectiles,” in *International SAMPE Symposium*, 2004, pp. 469–474.
- [69] D. Hu, Y. Zhang, Z. Shen, and Q. Cai, “Investigation on the ballistic behavior of mosaic SiC/UHMWPE composite armor systems,” *Ceram. Int.*, vol. 43, no. 13, pp. 10368–10376, 2017, doi: 10.1016/j.ceramint.2017.05.071.
- [70] W. Liu, Z. Chen, X. Cheng, Y. Wang, A. R. Amankwa, and J. Xu, “Design and

- ballistic penetration of the ceramic composite armor," *Compos. Part B Eng.*, 2016, doi: 10.1016/j.compositesb.2015.08.071.
- [71] J. Venkatesan, M. A. Iqbal, and V. Madhu, "Ballistic Performance of Bilayer Alumina/Aluminium and Silicon Carbide/Aluminium Armours," *Procedia Eng.*, vol. 173, pp. 671–678, 2017, doi: 10.1016/j.proeng.2016.12.141.
 - [72] K. Krishnan, S. Sockalingam, S. Bansal, and S. D. Rajan, "Numerical simulation of ceramic composite armor subjected to ballistic impact," *Compos. Part B Eng.*, vol. 41, no. 8, pp. 583–593, 2010, doi: 10.1016/j.compositesb.2010.10.001.
 - [73] J. Marx and A. Rabiei, "Overview of Composite Metal Foams and Their Properties and Performance," *Adv. Eng. Mater.*, vol. 19, no. 11, p. 1600776, Nov. 2017, doi: 10.1002/adem.201600776.
 - [74] C. Y. Zhao, "Review on thermal transport in high porosity cellular metal foams with open cells," *Int. J. Heat Mass Transf.*, vol. 55, no. 13, pp. 3618–3632, 2012, doi: <https://doi.org/10.1016/j.ijheatmasstransfer.2012.03.017>.
 - [75] K. Y. G. McCullough, N. A. Fleck, and M. F. Ashby, "Uniaxial stress-strain behaviour of aluminum alloy foams," *Acta Mater.*, 1999, doi: 10.1016/S1359-6454(99)00128-7.
 - [76] L. J. Gibson and M. F. Ashby, *Cellular solids: Structure and properties, second edition*. Second. Cambridge: Cambridge University Press, 1997.
 - [77] M. Ashby, A. Evans, N. Fleck, L. Gibson, J. Hutchinson, and H. Wadley, *Metal Foams: A Design Guide*. London: Butterworth Heimann, 2000.
 - [78] X.-H. Han, Q. Wang, Y.-G. Park, C. T'Joen, A. Sommers, and A. Jacobi, "A Review of Metal Foam and Metal Matrix Composites for Heat Exchangers and Heat Sinks," *Heat Transf. Eng.*, vol. 33, no. 12, pp. 991–1009, Sep. 2012, doi: 10.1080/01457632.2012.659613.
 - [79] Y. Sugimura, A. Rabiei, A. G. Evans, A. M. Harte, and N. A. Fleck, "Compression fatigue of a cellular Al alloy," *Mater. Sci. Eng. A*, 1999, doi: 10.1016/s0921-5093(99)00147-1.
 - [80] U. Ramamurty and A. Paul, "Variability in mechanical properties of a metal foam," *Acta Mater.*, 2004, doi: 10.1016/j.actamat.2003.10.021.
 - [81] O. Sadot *et al.*, "Experimental investigation of dynamic properties of aluminum foams," *Journal of Structural Engineering*. 2005, doi: 10.1061/(ASCE)0733-9445(2005)131:8(1226).
 - [82] T. J. Lim, B. Smith, and D. L. McDowell, "Behavior of a random hollow sphere metal foam," *Acta Mater.*, 2002, doi: 10.1016/S1359-6454(02)00111-8.
 - [83] W. S. Sanders and L. J. Gibson, "Mechanics of hollow sphere foams," *Mater. Sci. Eng. A*, 2003, doi: 10.1016/S0921-5093(02)00583-X.
 - [84] A. Rabiei, "Composite metal foam and methods of preparation thereof," US9208912 B2, 2015.
 - [85] A. Rabiei, "COMPOSITE METAL FOAM AND METHOD OF PREPARATION THEREOF," US2016011815 A1, 2016.
 - [86] E. Rizzi, E. Papa, and A. Corigliano, "Mechanical behavior of a syntactic foam: Experiments and modeling," *Int. J. Solids Struct.*, 2000, doi: 10.1016/S0020-7683(99)00264-4.
 - [87] N. Gupta, Kishore, E. Woldeisenbet, and S. Sankaran, "Studies on compressive failure features in syntactic foam material," *J. Mater. Sci.*, 2001, doi: 10.1023/A:1017986820603.

- [88] L. Bardella and F. Genna, “On the elastic behavior of syntactic foams,” *Int. J. Solids Struct.*, 2001, doi: 10.1016/S0020-7683(00)00228-6.
- [89] P. K. Rohatgi, J. K. Kim, N. Gupta, S. Alaraj, and A. Daoud, “Compressive characteristics of A356/fly ash cenosphere composites synthesized by pressure infiltration technique,” *Compos. Part A Appl. Sci. Manuf.*, 2006, doi: 10.1016/j.compositesa.2005.05.047.
- [90] D. P. Mondal, S. Das, N. Ramakrishnan, and K. Uday Bhasker, “Cenosphere filled aluminum syntactic foam made through stir-casting technique,” *Compos. Part A Appl. Sci. Manuf.*, 2009, doi: 10.1016/j.compositesa.2008.12.006.
- [91] I. N. Orbulov and J. Ginszler, “Compressive characteristics of metal matrix syntactic foams,” *Compos. Part A Appl. Sci. Manuf.*, 2012, doi: 10.1016/j.compositesa.2012.01.008.
- [92] L. Peroni, M. Scapin, M. Avalle, J. Weise, and D. Lehmhus, “Dynamic mechanical behavior of syntactic iron foams with glass microspheres,” *Mater. Sci. Eng. A*, 2012, doi: 10.1016/j.msea.2012.05.053.
- [93] A. Rabiei and A. T. O’Neill, “A study on processing of a composite metal foam via casting,” *Mater. Sci. Eng. A*, vol. 404, no. 1–2, pp. 159–164, 2005, doi: 10.1016/j.msea.2005.05.089.
- [94] A. Rabiei, L. Vendra, N. Reese, N. Young, and B. P. Neville, “Processing and characterization of a new composite metal foam,” *Mater. Trans.*, vol. 47, no. 9, pp. 2148–2153, 2006, doi: 10.2320/matertrans.47.2148.
- [95] L. J. Vendra and A. Rabiei, “A study on aluminum-steel composite metal foam processed by casting,” *Mater. Sci. Eng. A*, vol. 465, no. 1–2, pp. 59–67, 2007, doi: 10.1016/j.msea.2007.04.037.
- [96] B. P. Neville and A. Rabiei, “Composite metal foams processed through powder metallurgy,” *Mater. Des.*, vol. 29, no. 2, pp. 388–396, 2008, doi: 10.1016/j.matdes.2007.01.026.
- [97] J. A. Brown, L. J. Vendra, and A. Rabiei, “Bending properties of Al-steel and steel-steel composite metal foams,” *Metall. Mater. Trans. A Phys. Metall. Mater. Sci.*, vol. 41, no. 11, pp. 2784–2793, 2010, doi: 10.1007/s11661-010-0343-y.
- [98] L. J. Vendra, J. A. Brown, and A. Rabiei, “Effect of processing parameters on the microstructure and mechanical properties of Al-steel composite foam,” *J. Mater. Sci.*, vol. 46, no. 13, pp. 4574–4581, 2011, doi: 10.1007/s10853-011-5356-4.
- [99] A. Rabiei and L. J. Vendra, “A comparison of composite metal foam’s properties and other comparable metal foams,” *Mater. Lett.*, vol. 63, no. 5, pp. 533–536, 2009, doi: 10.1016/j.matlet.2008.11.002.
- [100] M. Garcia-Avila and A. Rabiei, “Effect of sphere properties on microstructure and mechanical performance of cast composite metal foams,” *Metals (Basel)*, vol. 5, no. 2, pp. 822–835, 2015, doi: 10.3390/met5020822.
- [101] L. Vendra and A. Rabiei, “Evaluation of modulus of elasticity of composite metal foams by experimental and numerical techniques,” *Mater. Sci. Eng. A*, vol. 527, no. 7–8, pp. 1784–1790, 2010, doi: 10.1016/j.msea.2009.11.004.
- [102] S. Chen, J. Marx, and A. Rabiei, “Experimental and computational studies on the thermal behavior and fire retardant properties of composite metal foams,” *Int. J. Therm. Sci.*, vol. 106, pp. 70–79, 2016, doi: 10.1007/bf00354407.
- [103] A. Rabiei, A. T. O’Neill, and B. P. Neville, “Processing and development of a new

- high strength metal foam,” in *Materials Research Society Symposium Proceedings*, 2005, doi: 10.1557/proc-851-nn11.4.
- [104] B. H. Smith, S. Szyniszewski, J. F. Hajjar, B. W. Schafer, and S. R. Arwade, “Characterization of steel foams for structural components,” *Metals (Basel)*., vol. 2, no. 4, pp. 399–410, 2012, doi: 10.3390/met2040399.
 - [105] D. Ruan, G. Lu, F. L. Chen, and E. Siories, “Compressive behaviour of aluminium foams at low and medium strain rates,” *Compos. Struct.*, vol. 57, no. 1–4, pp. 331–336, 2002, doi: 10.1016/S0263-8223(02)00100-9.
 - [106] T. Miyoshi, M. Itoh, S. Akiyama, and A. Kitahara, “Aluminum foam, ‘ALPORAS’: the production process, properties and applications,” *Mater. Res. Soc. Symp. - Proc.*, vol. 521, no. 4, pp. 133–137, 1998.
 - [107] Y. Alvandi-Tabrizi, D. A. Whisler, H. Kim, and A. Rabiei, “High strain rate behavior of composite metal foams,” *Mater. Sci. Eng. A*, vol. 631, pp. 248–257, 2015, doi: 10.1016/j.msea.2015.02.027.
 - [108] X. Xia *et al.*, “Compressive properties of closed-cell aluminum foams with different contents of ceramic microspheres,” *Mater. Des.*, 2014, doi: 10.1016/j.matdes.2013.11.040.
 - [109] X. Xia, H. Feng, X. Zhang, and W. Zhao, “The compressive properties of closed-cell aluminum foams with different Mn additions,” *Mater. Des.*, 2013, doi: 10.1016/j.matdes.2013.05.008.
 - [110] J. Banhart, W. Brinkers, and Fraunhofer-Institute, “Fatigue behaviour of aluminium foams J.,” *J. Mater. Sci. Lett.*, 2002, doi: 10.1023/A.
 - [111] A. Rabiei, B. Neville, N. Reese, and L. Vendra, “New composite metal foams under compressive cyclic loadings,” *Mater. Sci. Forum*, vol. 539–543, no. PART 2, pp. 1868–1873, 2007, doi: 10.4028/www.scientific.net/MSF.539-543.1868.
 - [112] L. Vendra, B. Neville, and A. Rabiei, “Fatigue in aluminum-steel and steel-steel composite foams,” *Mater. Sci. Eng. A*, vol. 517, no. 1–2, pp. 146–153, 2009, doi: 10.1016/j.msea.2009.03.075.
 - [113] S. Chen, M. Bourham, and A. Rabiei, “Novel light-weight materials for shielding gamma ray,” *Radiat. Phys. Chem.*, 2014, doi: 10.1016/j.radphyschem.2013.08.001.
 - [114] S. Chen, M. Bourham, and A. Rabiei, “Attenuation efficiency of X-ray and comparison to gamma ray and neutrons in composite metal foams,” *Radiat. Phys. Chem.*, vol. 117, pp. 12–22, 2015, doi: 10.1016/j.radphyschem.2015.07.003.
 - [115] S. Chen, M. Bourham, and A. Rabiei, “Neutrons attenuation on composite metal foams and hybrid open-cell Al foam,” *Radiat. Phys. Chem.*, 2015, doi: 10.1016/j.radphyschem.2014.11.003.
 - [116] W. J. Weber, R. C. Ewing, and W. Lutze, “Performance assessment of zircon as a waste form for excess weapons plutonium under deep borehole burial conditions,” in *Materials Research Society Symposium - Proceedings*, 1996.
 - [117] S. Chen, M. Bourham, and A. Rabiei, “Attenuation efficiency of X-ray and comparison to gamma ray and neutrons in composite metal foams,” *Radiat. Phys. Chem.*, 2015, doi: 10.1016/j.radphyschem.2015.07.003.
 - [118] W. H. Hsieh, J. Y. Wu, W. H. Shih, and W. C. Chiu, “Experimental investigation of heat-transfer characteristics of aluminum-foam heat sinks,” *Int. J. Heat Mass Transf.*, 2004, doi: 10.1016/j.ijheatmasstransfer.2004.04.037.
 - [119] A. Rabiei and M. Garcia-Avila, “Effect of various parameters on properties of

- composite steel foams under variety of loading rates," *Mater. Sci. Eng. A*, vol. 564, pp. 539–547, 2013, doi: 10.1016/j.msea.2012.11.108.
- [120] Y. Alvandi-Tabrizi and A. Rabiei, "Use of Composite Metal Foam for Improving Absorption of Collision Forces," *Procedia Mater. Sci.*, vol. 4, no. 2004, pp. 377–382, 2014, doi: 10.1016/j.mspro.2014.07.577.
- [121] N. Prat, F. Rongieras, J. C. Sarron, A. Miras, and E. Voiglio, "Contemporary body armor: Technical data, injuries, and limits," *European Journal of Trauma and Emergency Surgery*. 2012, doi: 10.1007/s00068-012-0175-0.
- [122] M. Garcia-Avila, M. Portanova, and A. Rabiei, "Ballistic performance of composite metal foams," *Compos. Struct.*, vol. 125, pp. 202–211, 2015, doi: 10.1016/j.compstruct.2015.01.031.
- [123] M. Garcia-Avila, M. Portanova, and A. Rabiei, "Ballistic Performance of a Composite Metal Foam-ceramic Armor System," *Procedia Mater. Sci.*, vol. 4, no. 2010, pp. 151–156, 2014, doi: 10.1016/j.mspro.2014.07.571.
- [124] US Department of Justice, "Ballistic Resistance of Body Armor NIJ Standard 0101.06," 2008.
- [125] J. Banhart, "Manufacture , characterisation and application of cellular metals and metal foams," *Prog. Mater. Sci.*, vol. 46, pp. 559–632, 2001.
- [126] J. Banhart, "Metal Foams: Production and Stability," *Adv. Eng. Mater.*, vol. 8, no. 9, pp. 781–794, Sep. 2006, doi: 10.1002/adem.200600071.
- [127] K. Kitazono, A. Kitajima, E. Sato, J. Matsushita, and K. Kuribayashi, "Solid-state diffusion bonding of closed-cell aluminum foams," *Mater. Sci. Eng. A*, vol. 327, no. 2, pp. 128–132, 2002, doi: 10.1016/S0921-5093(01)01766-X.
- [128] H. N. G. Wadley, N. A. Fleck, and A. G. Evans, "Fabrication and structural performance of periodic cellular metal sandwich structures," *Compos. Sci. Technol.*, vol. 63, no. 16, pp. 2331–2343, 2003, doi: 10.1016/S0266-3538(03)00266-5.
- [129] K. P. Jackson, J. M. Allwood, and M. Landert, "Incremental forming of sandwich panels," *J. Mater. Process. Technol.*, vol. 204, no. 1–3, pp. 290–303, 2007, doi: 10.1016/j.jmatprotec.2007.11.117.
- [130] A. Nabavi and J. V. Khaki, "Manufacturing of aluminum foam sandwich panels : comparison of a novel method with two different conventional methods," *J. Sandw. Struct. Mater.*, vol. 13, no. 2, pp. 177–187, 2010, doi: 10.1177/1099636210374270.
- [131] M. A. Yahaya, D. Ruan, G. Lu, and M. S. Dargusch, "Response of aluminium honeycomb sandwich panels subjected to foam projectile impact – An experimental study," *Int. J. Impact Eng.*, vol. 75, pp. 100–109, Jan. 2015, doi: 10.1016/J.IJIMPENG.2014.07.019.
- [132] H. Lin, H. Luo, W. Huang, X. Zhang, and G. Yao, "Diffusion bonding in fabrication of aluminum foam sandwich panels," *J. Mater. Process. Technol.*, vol. 230, pp. 35–41, 2016, doi: 10.1016/j.jmatprotec.2015.10.034.
- [133] J. Marx and A. Rabiei, "Study on the Microstructure and Compression of Composite Metal Foam Core Sandwich Panels," *Metall. Mater. Trans. A*, 2020, doi: 10.1007/s11661-020-05964-1.
- [134] A. Rabiei, "Materials with Improved Absorption of Collision Forces for Railroad Cars," Washington, DC, 2014.
- [135] T. Materials, *ASM Handbook, Volume 9, Metallography and Microstructures*. 2004.
- [136] S. L. Lopatnikov, B. A. Gama, and J. W. Gillespie, "Modeling the progressive

- collapse behavior of metal foams,” *Int. J. Impact Eng.*, vol. 34, no. 3, pp. 587–595, 2007, doi: 10.1016/j.ijimpeng.2005.12.004.
- [137] L. Li, P. Xue, and G. Luo, “A numerical study on deformation mode and strength enhancement of metal foam under dynamic loading,” *Mater. Des.*, vol. 110, pp. 72–79, 2016, doi: 10.1016/j.matdes.2016.07.123.
- [138] J. Marx, M. Portanova, and A. Rabiei, “Ballistic performance of composite metal foam against large caliber threats,” *Compos. Struct.*, vol. 225, p. 111032, Oct. 2019, doi: 10.1016/j.compstruct.2019.111032.
- [139] J. C. Marx, S. J. Robbins, Z. A. Grady, F. L. Palmieri, C. J. Wohl, and A. Rabiei, “Polymer Infused Composite Metal Foam as a Potential Aircraft Leading Edge Material,” *Appl. Surf. Sci.*, vol. 505, p. 144114, Oct. 2019, doi: 10.1016/j.apsusc.2019.144114.
- [140] J. K. L. Lai, “A review of precipitation behaviour in AISI type 316 stainless steel,” *Mater. Sci. Eng.*, vol. 61, no. 2, pp. 101–109, Nov. 1983, doi: 10.1016/0025-5416(83)90191-X.
- [141] C. Motz and R. Pippin, “Deformation behaviour of closed-cell aluminium foams in tension,” *Acta Mater.*, vol. 49, no. 13, pp. 2463–2470, 2001, doi: 10.1016/S1359-6454(01)00152-5.
- [142] E. Andrews, W. Sanders, and L. J. Gibson, “Compressive and tensile behaviour of aluminum foams,” *Mater. Sci. Eng. A*, 1999, doi: 10.1016/S0921-5093(99)00170-7.
- [143] O. B. Olurin, N. A. Fleck, and M. F. Ashby, “Deformation and fracture of aluminium foams,” *Mater. Sci. Eng. A*, vol. 291, no. 1–2, pp. 136–146, 2000, doi: 10.1016/S0921-5093(00)00954-0.
- [144] S. T. Szyniszewski, B. H. Smith, J. F. Hajjar, B. W. Schafer, and S. R. Arwade, “The mechanical properties and modeling of a sintered hollow sphere steel foam,” *Mater. Des.*, vol. 54, pp. 1083–1094, 2014, doi: 10.1016/j.matdes.2013.08.045.
- [145] J. Marx and A. Rabiei, “Tensile properties of composite metal foam and composite metal foam core sandwich panels,” *J. Sandw. Struct. Mater.*, p. 1099636220942880, 2020.
- [146] ASTM E8, “ASTM E8/E8M standard test methods for tension testing of metallic materials 1,” *Annu. B. ASTM Stand.* 4, 2010, doi: 10.1520/E0008.
- [147] E. Andrews, W. Sanders, and L. J. Gibson, “Compressive and tensile behaviour of aluminum foams,” *Mater. Sci. Eng. A*, vol. 270, no. 2, pp. 113–124, Sep. 1999, doi: 10.1016/S0921-5093(99)00170-7.
- [148] H. von Hagen and W. Bleck, “Compressive, tensile and shear testing of melt-foamed aluminium,” in *Materials Research Society Symposium - Proceedings*, 1998, doi: 10.1557/proc-521-59.
- [149] O. Andersen, U. Waag, L. Schneider, G. Stephani, and B. Kieback, “Novel metallic hollow sphere structures,” *Adv. Eng. Mater.*, vol. 2, no. 4, pp. 192–195, 2000, doi: 10.1002/(SICI)1527-2648(200004)2:4<192::AID-ADEM192>3.0.CO;2-#.
- [150] A. Falkowska and A. Seweryn, “Fatigue of sintered porous materials based on 316l stainless steel under Uniaxial loading,” *Mater. Sci.*, vol. 51, no. 2, pp. 200–207, 2015, doi: 10.1007/s11003-015-9829-5.
- [151] D. of Defense, “Mil-Std-662F Test Method Standard V 50 Ballistic Test for Armor,” 1997.
- [152] N. K. Naik, S. Kumar, D. Ratnaveer, M. Joshi, and K. Akella, “An energy-based

- model for ballistic impact analysis of ceramic-composite armors,” *Int. J. Damage Mech.*, vol. 22, no. 2, pp. 145–187, 2013, doi: 10.1177/1056789511435346.
- [153] M. A. Iqbal, K. Senthil, P. Bhargava, and N. K. Gupta, “The characterization and ballistic evaluation of mild steel,” *Int. J. Impact Eng.*, vol. 78, pp. 98–113, 2015, doi: 10.1016/j.ijimpeng.2014.12.006.
- [154] T. Fras, A. Murzyn, and P. Pawłowski, “Defeat mechanisms provided by slotted add-on bainitic plates against small-calibre 7.62 mm × 51 AP projectiles,” *Int. J. Impact Eng.*, vol. 103, pp. 241–253, 2017, doi: 10.1016/j.ijimpeng.2017.01.015.
- [155] J. K. Holmen, J. Johnsen, O. S. Hopperstad, and T. Børvik, “Influence of fragmentation on the capacity of aluminum alloy plates subjected to ballistic impact,” *Eur. J. Mech. A/Solids*, vol. 55, pp. 221–233, 2016, doi: 10.1016/j.euromechsol.2015.09.009.
- [156] G. Johnson and W. Cook, “A constitutive model and data for metals subjected to large strains, high strain rates and high temperatures.,” *Proc 7th Int Symp Ballist.*, vol. The Hague, no. Netherlands, 1983.
- [157] G. R. Johnson and W. H. Cook, “Fracture characteristics of three metals subjected to various strains, strain rates, temperatures and pressures,” *Eng. Fract. Mech.*, vol. 21, no. 1, pp. 31–48, 1985, doi: 10.1016/0013-7944(85)90052-9.
- [158] T. Dennis, W. S. Dx, and A. S. D. X. X, “International Journal of Impact Engineering Effect of composite covering on ballistic fracture damage development in ceramic plates,” vol. 99, pp. 58–68, 2017, doi: 10.1016/j.ijimpeng.2016.09.010.
- [159] X. Guo, X. Sun, X. Tian, G. J. Weng, Q. D. Ouyang, and L. L. Zhu, “Simulation of ballistic performance of a two-layered structure of nanostructured metal and ceramic,” *Compos. Struct.*, vol. 157, pp. 163–173, 2016, doi: 10.1016/j.compstruct.2016.08.025.
- [160] A. You, M. A. Y. Be, and I. In, “CONSTITUTIVE MODEL CONSTANTS FOR Al7075-T651 and Al7075-T6,” vol. 945, no. January 2010, 2016, doi: 10.1063/1.3295300.
- [161] G. Johnson and T. Holmquist, “A computational constitutive model for brittle materials subjected to large strains, high strain rates and high pressures.,” *Shock wave high-strain-rate Phenom. Mater.*, pp. 1075–1081, 1992.
- [162] G. R. Johnson and T. J. Holmquist, “An improved computational constitutive model for brittle materials,” vol. 981, no. May, pp. 981–984, 2008, doi: 10.1063/1.46199.
- [163] W. H. Gust and E. B. Royce, “Dynamic yield strengths of B4C, BeO, and Al₂O₃ceramics,” *J. Appl. Phys.*, vol. 42, no. 1, pp. 276–295, 1971, doi: 10.1063/1.1659584.
- [164] G. R. Johnson and T. J. Holmquist, “Response of boron carbide subjected to large strains, high strain rates, and high pressures,” *J. Appl. Phys.*, vol. 85, no. 12, pp. 8060–8073, 1999, doi: 10.1063/1.370643.
- [165] P. Lundberg, “Interface Defeat and Penetration: Two Modes of Interaction between Metallic Projectiles and Ceramic Targets,” *Fac. Sci. Technol.*, p. 53, 2004.
- [166] J. Marx, M. Portanova, and A. Rabiei, “A study on blast and fragment resistance of composite metal foams through experimental and modeling approaches,” *Compos. Struct.*, vol. 194, pp. 652–661, Jun. 2018, doi: 10.1016/j.compstruct.2018.03.075.
- [167] M. Grujicic, B. Pandurangan, and B. d’Entremont, “The role of adhesive in the ballistic/structural performance of ceramic/polymer-matrix composite hybrid armor,” *Mater. Des.*, vol. 41, pp. 380–393, 2012, doi: 10.1016/j.matdes.2012.05.023.

- [168] R. Zaera, S. Sánchez-Sáez, J. L. Pérez-Castellanos, and C. Navarro, “Modelling of the adhesive layer in mixed ceramic/metal armours subjected to impact,” *Compos. Part A Appl. Sci. Manuf.*, vol. 31, no. 8, pp. 823–833, 2000, doi: 10.1016/S1359-835X(00)00027-0.
- [169] I. S. Chocron Benloulo and V. Sánchez-Gálvez, “A new analytical model to simulate impact onto ceramic/composite armors,” *Int. J. Impact Eng.*, vol. 21, no. 6, pp. 461–471, 1998, doi: 10.1016/S0734-743X(98)00006-2.
- [170] J. López-Puente, A. Arias, R. Zaera, and C. Navarro, “The effect of the thickness of the adhesive layer on the ballistic limit of ceramic/metal armours. An experimental and numerical study,” *Int. J. Impact Eng.*, vol. 32, no. 1–4, pp. 321–336, 2005, doi: 10.1016/j.ijimpeng.2005.07.014.
- [171] G. Sabadin, M. Gaiotti, C. M. Rizzo, and A. Bassano, “Development and validation of a numerical model for the simulation of high-velocity impacts on advanced composite armor systems,” *Nonlinear Dyn.*, vol. 91, no. 3, pp. 1791–1816, 2018, doi: 10.1007/s11071-017-3981-4.
- [172] W. Liu *et al.*, “Influence of different back laminate layers on ballistic performance of ceramic composite armor,” *Mater. Des.*, vol. 87, pp. 421–427, 2015, doi: 10.1016/j.matdes.2015.08.024.
- [173] NATO, *NATO: Protection Levels for Occupants of Armoured Vehicles, STANAG 4569*. 2014, p. 3rd Edition.
- [174] M. N. Bassim, A. G. Odehy, and M. Bolduc, “Deformation and failure of a rolled homogeneous armour steel under dynamic mechanical loading in compression,” *12th Int. Conf. Fract. 2009, ICF-12*, vol. 5, pp. 3464–3473, 2009.
- [175] C. G. Fountzoulas and J. C. LaSalvia, “Simulation of the Ballistic Impact of Tungsten-Based Penetrators on Confined Hot-Pressed Boron Carbide Targets,” in *Advances in Ceramic Armor VII: Ceramic Engineering and Science Proceedings, Volume 32*, Sep. 2011, pp. 261–269, doi: doi:10.1002/9781118095256.ch23.
- [176] J. Marx, M. Portanova, and A. Rabiei, “A study on blast and fragment resistance of composite metal foams through experimental and modeling approaches,” *Compos. Struct.*, vol. 194, no. February, pp. 652–661, 2018, doi: 10.1016/j.compstruct.2018.03.075.
- [177] C. Kingery and G. Bulmash, “Airblast parameters from TNT spherical air burst and hemispherical surface burst.,” Ballistic Research Laboratory, 1984.
- [178] Y. Bao and T. Wierzbicki, “A comparative study on various ductile crack formation criteria,” *J. Eng. Mater. Technol. ASME*, vol. 126, no. 3, pp. 314–324, 2004, doi: 10.1115/1.1755244.
- [179] Y. Bao and T. Wierzbicki, “On fracture locus in the equivalent strain and stress triaxiality space,” *Int. J. Mech. Sci.*, vol. 46, no. 1, pp. 81–98, 2004, doi: 10.1016/j.ijmecsci.2004.02.006.
- [180] Y. Bai and T. Wierzbicki, “A new model of metal plasticity and fracture with pressure and Lode dependence,” *Int. J. Plast.*, vol. 24, no. 6, pp. 1071–1096, 2008, doi: 10.1016/j.ijplas.2007.09.004.
- [181] M. J. Forrestal, B. Lim, and W. Chen, “A Scaling Law for APM2 Bullets and Aluminum Armor Plates,” *Exp. Mech.*, vol. 59, no. 1, pp. 121–123, 2019, doi: 10.1007/s11340-018-00442-7.
- [182] T. L. Jones and B. E. Placzankis, “ARL-TR-7727: The Examination of the Aluminum

- Alloy 7017 as a Replacement for the Aluminum Alloy 7039 in Lightweight Armor Systems,” 2016.
- [183] M. J. Pawar *et al.*, “Comparison of ballistic performances of Al₂O₃ and AlN ceramics,” *Int. J. Impact Eng.*, vol. 98, pp. 42–51, 2016, doi: 10.1016/j.ijimpeng.2016.08.002.
 - [184] ASTM Standard B928/B928M, “Standard Specification for High Magnesium Aluminum-Alloy Sheet and Plate for Marine Service and Similar Environments,” *ASTM B. Stand.*, no. February 2004, pp. 1–12, 2009, doi: 10.1520/B0928.
 - [185] D. Tyler and W. Black, *Introduction to Copper and Copper Alloys, Properties and Selection: Nonferrous Alloys and Special-Purpose Materials, ASM Handbook*. ASM International, 1990.
 - [186] A. International, *Properties of Wrought Aluminum and Aluminum Alloys, Properties and Selection: Nonferrous Alloys and Special-Purpose Materials, ASM Handbook*. 1990.
 - [187] A. International, *Carbon and Low-Alloy Steel Sheet and Strip, Properties and Selection: Irons, Steels, and High-Performance Alloys, ASM Handbook*. 1990.